— Project Review —

Consortium Project on
Seismic Inverse Methods for Complex Structures

Golden, Colorado, May 21-24, 2007

2006-07 CWP Students and Research Leaders:

Laxmidhar Behera	Kurang Mehta	John Stockwell
Jyoti Behura	Gabi Melo	Ilya Tsvankin
Norm Bleistein	Masatoshi Miyazawa	Ivan Vasconcelos
Yuanzhong Fan	Derek Parks	Xiaoxiang Wang
Rodrigo Fuck	Paul Sava	Greg Wimpey
Dave Hale	Steve Smith	Xiaoxia Xu
Ken Larner	Roel Snieder	Jia Yan
John Mathewson		

Associated Faculty:

Feng (Suzie) Su

CWP Staff:

Michelle Szobody, Program Assistant
Barbara McLenon, Publications Specialist

Center for Wave Phenomena
Colorado School of Mines
Golden, Colorado 80401
(303) 273-3557 fax: (303) 273-3478
email: cwpcsm@dix.mines.edu
http://www.cwp.mines.edu

Contents

Interferometry by Correlation

Interferometry by Deconvolution

Acknowledgments

This project review book is prepared for the sponsors of the Consortium Project at the Center for Wave Phenomena. The Consortium Project provides substantial funding for the overall research and educational program at the Center. The Center has also received funds from the following agencies:

- American Chemical Society, Petroleum Research Fund
- Australian Research Council
- Chemical Sciences, Geosciences and Biosciences Division, Office of Basic Energy Sciences, U.S. Department of Energy
- ExxonMobil Upstream Research Company
- Landmark Graphics Corporation
- National Science Foundation
- Shell Gamechanger Program
- Statoil
- United States Geological Service (USGS)

We are extremely grateful for the support of these agencies during the past year and for that of the Consortium sponsors who are listed here.

Anadarko Petroleum Corporation
Aramco
BHP Billiton Petroleum
BP America Inc.
Bureau of Geophysical Prospecting
CGGVeritas
Chevron Energy Technology Company
ConocoPhillips Company
Devon Energy Corporation
EnCana Corporation
ENI-AGIP E & P Division
ExxonMobil Upstream Research Co.
GX Technology
Hess Corporation
Hydro Gulf of Mexico
Landmark Graphics Corporation
Petrobras America Inc.
PGS Inc.
Shell International E & P
Statoil Research Centre
Talisman Energy Inc.
Total E & P Services
WesternGeco

CWP Policy on Proprietary Printed Material

New printed material that is produced at the Center for Wave Phenomena under Consortium support is presented to Sponsors before it is released to the general public. We delay general publication by at least 60 days so that Sponsors may benefit directly from their support of the Center for Wave Phenomena.

During this delay, Sponsors may make whatever use of the material inside their organization that they deem proper. However, we expect that all Sponsors will respect the rights of other Sponsors, and of CWP, by not publishing these results externally and independently, in advance of this 60-day delay (even with attribution to CWP). Please refer to your Consortium Membership Agreement under the paragraph entitled "Sponsor Confidentiality Obligation."

Those reports in this book that were produced primarily under consortium support and have not been previously distributed or submitted for publication, will be available for general distribution by October 1, 2007.

If you have independently generated results that duplicate or overlap these, and plan to submit them for publication under your own name before this date, please notify us immediately, so that misunderstandings do not arise.

INTRODUCTION

This edition of the report on the Consortium Project at the Center for Wave Phenomena summarizes much of the research conducted within CWP after the 2006 Project Review Meeting. Note that the papers in this report and those presented orally during the Annual Project Review Meeting, May 21–24, 2007, only partially overlap. Also, in addition to these papers, several last-minute manuscripts will be distributed during the Meeting and mailed to representatives of sponsor companies.

Papers in This Report

The 22 papers in this volume are grouped into the following five categories: imaging and velocity analysis, time-lapse methods and image processing, azimuthal AVO and moveout analysis, interferometry by correlation, and interferometry by deconvolution. These categories show both similarities to and differences from those of the past few years, indicative of both the continuity and expanding breadth of our research program.

Imaging and velocity analysis

The section on imaging and velocity analysis includes three papers. In his first paper, *Sava* introduces a new imaging condition based on interferometric correlations of extrapolated wavefields with the goal of reducing imaging artifacts caused by unknown small-scale velocity variations. The new condition should be particularly beneficial for models with rapid velocity variations typical for salt, anhydrite, and basalt environments. The topic of *Sava*'s second paper is another extended imaging condition that differentiates among wavefields based on multiple attributes (time, propagation direction) in order to avoid cross-talk between unrelated events. Applications include imaging with multiple seismic experiments (shots), multiple attenuation during imaging, etc. *Behera and Tsvankin* present an efficient methodology for P-wave prestack depth imaging in tilted transversely isotropic (TTI) media that properly accounts for the tilt of the symmetry axis as well as for spatial velocity variations. The algorithm is successfully tested on several TTI models typical for active tectonic areas and subsalt exploration plays. The paper also demonstrates that ignoring the tilt of the symmetry axis may lead to significant image distortions and errors in parameter estimation.

Time-lapse methods and imaging processing

Four papers are devoted to time-lapse methods and image processing. *Snieder et al.* present an overview of noninvasive geophysical methods used to measure temporal changes in the subsurface. They focus on monitoring mechanical properties, fluid transport, and biogeochemical processes and present case studies that illustrate detection of time-lapse changes in the associated medium parameters. *Fuck et al.* give a 3D analytic description of stress-related traveltime shifts measured over compacting hydrocarbon reservoirs. Their formalism is not restricted to zero-offset rays and accounts for both stress-induced velocity changes and deformation of reflectors around the reservoir. Numerical tests for a compacting rectangular reservoir show that the excess stress field produces an anisotropic medium with substantial values of the Thomsen parameters and variable orientation of the symmetry axis. The first paper by *Hale* describes a high-fidelity method for estimating three components of apparent displacement vectors from time-lapse seismic images. The method is used to estimate horizontal displacements of only 5 m from two images with horizontal sampling intervals of 25 m. Regions where these displacements are largest are consistent with the shape of the target reservoir. In another paper, *Hale* introduces new algorithms for local dip filtering based on simple and efficient finite-difference approximations to directional Laplacians. Local dip filters attenuate or enhance coherent features having dips that may vary for each image sample. In one application, these filters are tuned to remove strong coherent events while preserving weaker but interesting events that have only slightly different dips.

Azimuthal AVO and moveout analysis

Azimuthal AVO and moveout analysis is the topic of three papers. *Xu and Tsvankin* apply a comprehensive processing sequence designed for layered azimuthally anisotropic media to wide-azimuth P-wave data acquired over a fractured gas sand formation in the Rulison field, Colorado. They identify two strong azimuthal AVO (amplitude-variation-with-offset) anomalies at the bottom of the reservoir, one of which becomes much more pronounced and spatially coherent after application of the moveout-based

anisotropic geometrical-spreading correction (MASC). Both anomalies coincide with the intersections of wrenching fault systems, which suggests that the AVO analysis helped to detect "soft spots" of high fracture density. In their second paper, *Xu and Tsvankin* extend the algorithm of moveout-based anisotropic spreading correction (MASC) to mode-converted PSV-waves in VTI (TI with a vertical symmetry axis) media and symmetry planes of orthorhombic media. They show that for purposes of spreading correction, reflection traveltimes of PSV-waves can be well-approximated by the Tsvankin-Thomsen and Alkhalifah-Tsvankin nonhyperbolic moveout equations, which are widely used for P-waves. Testing on full-wavefield synthetic data confirms that MASC accurately reconstructs the plane-wave conversion coefficient from conventional-spread PSV data. *Yan and Tsvankin* develop a generalized version of the so-called AK semblance method for long-spread, wide-azimuth data. Their algorithm is designed to correct for the influence of polarity reversals on nonhyperbolic moveout analysis for reflections with type 1 and type 2 AVO responses. Synthetic tests confirm that the AK semblance method gives accurate estimates of the NMO ellipse and the azimuthally varying anellipticity parameter η even when the position of the polarity reversal varies with azimuth.

Interferometry by correlation

The two sections on seismic interferometry feature both theoretical work and applications to field data. Seven papers discuss different aspects of interferometry by correlation. An important question that arose at the previous Project Review meeting is to what extent seismic interferometry remains valid for systems that are not invariant for time reversal. The series of papers by *Snieder* demonstrates that seismic interferometry can be applied to the diffusion equation and to damped acoustic waves. In his collaborative work with *Wapenaar* from Delft University of Technology, *Snieder* proves that the principles of seismic interferometry are valid for almost any linear system. The two papers by *Mehta et al.* describe the results of a joint project with Shell Research. In the first paper, they show that suppression of surface-related multiples can be folded into seismic interferometry, and test their algorithm on ocean-bottom data recorded over the Mars field in the Gulf of Mexico. Application of the method to time-lapse data in the second paper proves that the repeatability of virtual-source data is much higher than that of conventional data. *Behura* introduces a method (called "Virtual Real Source") of extracting the seismic source signature using interferometry. The only requirement for the method is that the source location must coincide with a receiver location (not necessarily at zero offset). The source signature of each shot can be extracted reliably if all shots have similar amplitude spectra, even though their phase spectra might be completely different.

Interferometry by deconvolution

The section interferometry by deconvolution includes four papers by *Vasconcelos et al.*, which show that in several applications it is advantageous to employ deconvolution rather than correlation in seismic interferometry. Two papers discuss deconvolution interferometry using the scattering series and prove that this technique accurately recovers primary reflections. In particular, deconvolution interferometry performs better than correlation interferometry for complicated sources of seismic wavefields. For example, this is the case when drill-bit noise or internal multiples play the role of seismic source. Numerical simulations confirm the feasibility of using both drill-bit noise and internal multiples for imaging with deconvolution-based seismic interferometry. Deconvolution interferometry is then applied to imaging of the San Andreas fault zone, and to subsalt imaging with internal multiples. In the final paper, *Thompson and Snieder* analyze multicomponent seismic records from the Millikan Library in Pasadena, CA, to estimate the shear-wave splitting coefficient of the building. Using deconvolution of traces from different floors, they find that shear waves split into the fast mode polarized in the east-west direction and the slow mode polarized in the north-south direction.

OVERVIEW OF DEVELOPMENTS IN CWP

CWP Faculty

There has been no change in the CWP faculty group and administrative staff since the last Project Review Meeting. The full-time CWP academic faculty includes Dave Hale, Paul Sava, Roel Snieder, and

Ilya Tsvankin (director). Ken Larner and Norm Bleistein remain part of the team in their "retirement," and are actively involved in many aspects of our research and educational program.

Students and Post-Docs

During the 2006-2007 academic year, 13 graduate students were doing research in CWP. Since the last Project Review Meeting, three CWP students have successfully completed their studies at CSM. Xiaoxia Xu defended her Ph.D. thesis and graduated in December 2006; Kurang Mehta and Ivan Vasconcelos defended their Ph.D. theses during the Spring 2007 semester.

Two post-doctoral research fellows, Masatoshi Miyazawa from Japan and Laxmidhar Behera from India, have returned to their home countries after their one-year assignments in CWP. Masatoshi was on leave from the Disaster Prevention Research Institute at Kyoto University, where he works as a research associate. The support for Masatoshi was provided by ExxonMobil. Laxmidhar is a scientist with the National Geophysical Research Institute in Hyderabad, India, and was supported by a BOYSCAST Fellowship. Eduardo Filpo Ferreira da Silva joined CWP as a post-doctoral fellow in March 2007 for a 16-month period. Eduardo is a geophysicist with Petrobras, Brazil, and the company provides full support for his post-doctoral position with CWP.

Center Support

This past year the Consortium was supported by 23 companies (24 with TGS-Nopec joining in June 2007). We thank the representatives of our sponsors for their continued support. A full list of sponsor companies over the term of the past year appears on the acknowledgment page at the beginning of this volume.

We have received about $700K of additional support since June 2006 from the Department of Energy, National Science Foundation, Petroleum Research Fund of the American Chemical Society, U.S. Geological Survey, ExxonMobil, Shell, and Statoil (for details, see below). Also, in 2005 Landmark Graphics committed funding to support a research fellowship for a PhD student (currently Derek Parks) in computer science and/or geophysics for four years, toward the goal of developing new methods for modeling the earth's subsurface. Our industrial and government support for research and education complement one another; each gains from, and strengthens, the other. As a net result, for the present annual fee of $48.4K, a company participates in a research project whose total funding level is close to $1.75M, which gives a leverage factor of over 36.

New Government Funding

The National Science Foundation will support Roel Snieder's project on seismic interferometry. In this project, drill-bit noise generated at the San Andreas Fault Observatory at Depth (SAFOD) provides an incoherent broadside illumination of the San Andreas fault, which is used to image the fault structure. Controlled source experiments with the TRex-shaker in the Garner Valley, California, produce 9C data employed in this project to validate the theory of seismic interferometry.

Ilya Tsvankin has received a two-year grant from the Petroleum Research Fund of the American Chemical Society in support of his project "Attenuation analysis for azimuthally anisotropic media." The project, which provides funding for an A-Team student, is aimed at applying the attenuation coefficient as a fracture-detection attribute and devising anisotropic attenuation corrections for AVO analysis and migration.

Joint Projects with Industry

Roel Snieder and his students Kurang Mehta and Yuanzhong Fan continue their collaboration with Andrey Bakulin, Rodney Calvert and Jon Sheiman of Shell International E&P on a project devoted to seismic interferometry. This project, supported by Shell as part of the "Gamechanger" program,

aims at optimizing the use of seismic interferometry for imaging and monitoring reservoirs. Though this project is not strictly part of the CWP Consortium, Shell is willing for CWP to share the results with Consortium sponsors, within constraints of Shell's research agreement.

Roel Snieder also collaborated with Mike Payne and Anupama Venkatarama of ExxonMobil on using induced seismicity to monitor the steam behavior in a heavy-oil reservoir. Through the support of ExxonMobil, CWP attracted Masatoshi Miyazawa (on leave from Kyoto University) to work on this project for one year.

Paul Sava has initiated a three-year project supported by Statoil on wave-equation velocity analysis and imaging for wide-azimuth data. The grant from Statoil provides partial funding for CWP student Gabriela Melo.

CWP encourages directly sponsored research with other companies that could lead to sharing of results with the Consortium.

13th International Workshop on Seismic Anisotropy

Ilya Tsvankin and Ken Larner, along with James Gaiser of GX Technology, are the organizers of the 13th International Workshop on Seismic Anisotropy planned for August 10-15, 2008, in Winter Park. The previous workshops, which proved instrumental in moving seismic anisotropy to the forefront of exploration seismology, have been held every other year since the 1980's at various locations all over the world. If your company is interested in sponsoring 13IWSA (e.g., by providing student travel grants), please contact one of the organizers.

Interaction with Other Research Projects at CSM and Elsewhere

During this past year, as in previous years, faculty and students of CWP have interacted closely with other industry-funded research projects in the CSM Department of Geophysics. These include the Reservoir Characterization Project (RCP), led by Tom Davis; the Center for Rock Abuse, led by Mike Batzle; and the Gravity/Magnetics Project, led by Yaoguo Li.

In addition, various CWP faculty have engaged in collaborative efforts with researchers elsewhere. As part of his ongoing work on coda-wave interferometry, Roel Snieder is engaged in a collaborative project with David Robinson and Malcolm Sambridge from the Australian National University (ANU) in Canberra, Australia. Their goal is to show that changes in the source mechanism of seismic events can be inferred from coda waves. Using data from the Bureau of Reclamation, this technique is applied to monitor seismicity induced by the injection of brine in Paradox Valley (Colorado). This project is funded by a grant from the Australian Research Council.

Other collaborations of the CWP faculty include:

- Norm Bleistein
  - Sam Gray (Veritas DGC)
  - Guanquan Zhang (Chinese Academy of Sciences)
  - Yu Zhang and Xu Sheng (Veritas DGC)
- Paul Sava
  - Sergey Fomel (Bureau of Economic Geology, University of Texas at Austin)
  - Jeff Shragge (Stanford University)
- Roel Snieder
  - Andrey Bakulin, Rodney Calvert and Jon Sheiman (Shell International E&P)
  - Joan Gomberg and Bill Stephenson (US Geological Survey)
  - Peter Malin (Duke University)
  - Malcolm Sambridge (Australian National University)
  - Anupama Venkatarama and Mike Payne (ExxonMobil)

- Kees Wapenaar (Delft Institute of Technology)
- Uli Wegler (University of Leipzig)

- Ilya Tsvankin
  - Andrey Bakulin and Vladimir Grechka (Shell International E&P)
  - Karl Berteussen (Petroleum Institute, Abu Dhabi)
  - James Gaiser (GX Technology)
  - Martin Landrø (Norwegian University of Science and Technology)
  - Peter Leary (Consultant, OYO Geospace)
  - Ivan Pšenčík, Czech Academy of Sciences

Travels and Activities of CWP People

Interactions and collaborations that have taken place away from Golden include the following:

- Norm Bleistein
  - Presented an invited talk at the Geophysical Inversion Workshop at the University of Calgary (August 2006).
  - Presented an invited talk at a workshop of Brazilian Geophysical Society in honor of Martin Tygel's birthday in Campinas, Brazil (November 2006).
  - Presented an invited talk at a workshop honoring retirement of Peter Hubral in Karlsruhe, Germany (February 2007).
  - Presented three talks at a two-day workshop sponsored by CGGVeritas in Paris (Massy), France (March 2007).

- Dave Hale
  - Attended the 68th EAGE Conference in Vienna and gave an invited talk at the workshop on open-source software (June 2006).
  - Traveled to Houston to meet with representatives of prospective sponsor Paradigm Geophysical (April 2007).

- Ken Larner
  - Attended the RPSEA Forum to discuss DOE-sponsored research and meet with potential CWP sponsors (October 2006).
  - Participated as a guest at the Annual Meeting of the Stanford Exploration Project in Oregon (May 2007).

- Paul Sava
  - Worked on joint research projects with Sergey Fomel at the Bureau of Economic Geology, UT Austin (May 2006).
  - Presented a paper at the 68th EAGE Conference in Vienna (June 2006).
  - Participated in the SEG Summer Research Workshop in Snowbird, UT (July 2007).
  - Traveled to Houston to meet with representatives of ExxonMobil (July 2007).
  - Co-organizer of the Workshop on Reproducible Research in Computational Geosciences, Vancouver, BC (August 2006).
  - Attended the AGU Fall Meeting in San Francisco (December 2006).
  - Co-organizer of the mini-symposium on imaging and interferometry at the SIAM Conference on Mathematical and Computational Issues in the Geosciences, Santa Fe, NM (March 2007).
  - Traveled to Houston and Austin, TX, to make a presentation to the Houston Geophysical Society and visit with representatives of CWP sponsor and prospective sponsor companies (TGS-Nopec, BP, 3DGeo, Paradigm; April 2007).

- Roel Snieder
  - Made multiple trips to Shell Research in Houston and Rijswijk and to ExxonMobil in Houston to discuss joint projects.
  - Presented invited lectures at the 3rd SPICE Research and Training Workshop in Kinsale, Ireland (July 2006).
  - Visited the Universidad Nacional Autónoma de México in Mexico City for joint research and seminars (August 2006).
  - Visited Japan to give invited talks at the SEGJ meeting in Kyoto and at the Workshop "Potential Use of Geophysical Techniques for Monitoring CO2 Storage Sites" in Arashiyana (November 2006).
  - Continued his work on the Earth Science Council of the Office of Basic Energy Sciences of the Department of Energy, and attended the semi-annual meetings of the council in Washington, DC (November 2006 and April 2007).
  - Member of the organizing committee and panel leader for the DOE workshop and report "Basic Research Needs in the Geosciences: Facilitating 21st Century Energy Systems," Bethesda, MD (February 2007).
  - Visited Australian National University in Canberra, Australia, for joint research and lectures (December 2006).
  - Served on the selection panel of the Spinoza Prize of the Netherlands Organisation for Scientific Research. Visited Utrecht, The Netherlands, for a meeting of this committee (February 2007).
  - Presented a weekly seminar at the California Institute of Technology, Pasadena (March 2007).
  - Presented an invited talk at the SIAM Conference on Mathematical and Computational Issues in the Geosciences in Santa Fe, NM (March 2007).
- Ilya Tsvankin
  - Presented a paper at the 68th EAGE Conference in Vienna (June 2006). Presented an invited talk at the workshop "Seismic anisotropy – state of the art in parameter estimation and imaging."
  - Taught the two-day SEG Continuing Education Course "Seismic anisotropy: Basic theory and applications in exploration and reservoir characterization" at the SEG Annual Meeting in New Orleans (October 2006).
  - Presented an invited talk and taught a course on anisotropy at the annual meeting of the ROSE Consortium at the Norwegian University of Science and Technology, Trondheim, Norway (April 2007).
- John Stockwell
  - Attended the 68th EAGE Conference in Vienna and gave an invited talk at the workshop on open-source software (June 2006).
- Laxmidhar Behera (post-doc)
  - Traveled to New Delhi, India as an invited nominee for the CSIR Young Scientist Award (June-July 2006).
- Masatoshi Miyazawa (post-doc)
  - Attended the Workshop on Heavy Oils in Calgary, Canada (June 2006).
  - Attended the AGU Fall Meeting in San Francisco (December 2006).
  - Made several trips to ExxonMobil in Houston to work on a joint project.

Our students traveled considerably as well. Most of them gave presentations at the SEG Annual Meeting in New Orleans (October 2006).

- Jyoti Behura and Jia Yan presented papers at the 12th International Workshop on Seismic Anisotropy in Beijing, China (October 2006). Jyoti also gave a presentation at the Workshop on Heavy Oils in Calgary, Canada (June 2006). Jia attended the SEG Summer Research Workshop in Snowbird, Utah (July 2006).
- Yuanzhong Fan and Kurang Mehta made several trips to the Shell Bellaire Research Center in Houston to work on joint projects.
- Ivan Vasconcelos visited Schlumberger in Ridgefield for joint research in imaging with drill-bit data (April 2006). He also traveled to Paulsson Geophysical Services, Brea, CA, to initiate a research collaboration on VSP data acquisition. During the summer of 2006, Ivan visited BP Exploration and Production Technology and Veritas DGC in England to present his latest research results and interact with their personnel. He has also promoted the CWP research and educational programs by giving talks to both graduate and undergraduate students in the Physics and Geoscience Departments of Universitat de Barcelona and Universitat Politecnica de Catalunya.

Visitors to CWP

CWP has benefited again this year from visits by a number of scientists and friends from other universities and industry. We strongly encourage visits from our sponsor representatives, whether it be for a single day, or for an extended period. Dirk Gajewski of the University of Hamburg spent his six-month sabbatical at CSM (March-October 2006). James Gaiser (WesternGeco/GX Technology) has regularly participated in the A(nisotropy)-Team seminar and collaborated with CWP faculty and students.

As mentioned above, Masatoshi Miyazawa from Japan and Laxmidhar Behera from India have completed their one-year visits as post-doctoral fellows with CWP. A new post-doctoral fellow, Eduardo Filpo Ferreira da Silva from Brazil, joined CWP in March 2007.

Yong Zheng and Weitao Wang, scientists from China, came to CSM for a six-month visit (April-October 2007) to do joint research with Roel Snieder. Roel also worked with Sanne Cottaar, exchange student from The Netherlands, who spent the Fall 2006 semester at CSM. Sjoerd de Ridder, a student from Utrecht University, visited with Roel for one month in March-April 2007. Two students from the University of Science and Technology of China, Jun Li and Jianmin Lin, stayed at CSM for six months (May-November 2006) collaborating with Suzie Su and CWP students.

We also had several short-term visitors:

- Uwe Albertin (WesternGeco)
- Andrey Bakulin (Shell)
- Joe Dellinger (BP)
- Vladimir Grechka (Shell)
- Laurent Stehly (Universite Joseph Fourier, Grenoble, France)
- Uli Wegler (University of Leipzig, Germany)

Papers at SEG

Once again, CWP students and faculty presented a large number of papers at the SEG Annual Meeting. During the 2006 Annual Meeting in New Orleans, they had a total of 17 oral presentations, poster papers, and workshop contributions. A number of these presentations result from collaborations with sponsor companies and academic groups.

For other meetings where CWP personnel presented papers, see the section "Travels and Activities of CWP People" above.

Publications

As in past years, a significant number of papers authored or co-authored by CWP faculty and students have been published in leading journals. In your meeting folder, you can find recent CWP reports on the list called "Available Papers." The complete list of CWP papers from 1984 onward is on our web site at http://www.cwp.mines.edu/bookshelf.html. Most papers are available there for downloading as PDF files.

The Ph.D. theses of Xiaoxia Xu was distributed to Sponsors during March 2007, and those of Kurang Mehta and Ivan Vasconcelos will be distributed this summer. If you would like to receive a copy of these, or of any other CWP publications, contact Barbara McLenon at "barbara@dix.mines.edu".

Computing Environment

The CWP research computing environment includes a 32 processor Linux cluster system. Each of the 16 nodes consists of a dual processor Pentium Xeon 2.4 GHz PC system with 2 GB of RAM available per processor, and about 160 GB total of hard-disk storage for each node. We have had this unit for nearly four years.

Each student and faculty member has a desktop system of 2 GHz or faster, running Linux, with 40-250 GB of storage space per desktop. In addition to these desktop systems, we have purchased a 3.0 GHz server with .5 Terabytes of disk space for home directories and other backed-up materials. System backups are now automated to USB disk drives (in the past, backups were performed to Exabyte tape). The total disk space in CWP exceeds 5 Terabytes, though this is not contiguous.

For data transport, our preferred medium consists of USB hard drives, formatted with the ext3 filesystem. CWP faculty and students make regular use of the following commercial packages: Mathematica, Matlab, the Intel C and Fortran compilers, as well as the NAG95 (Fortran 90/95 compiler).

Software Releases

CWP releases open-source software as well as software that is confidential to the Consortium. Most confidential codes depend heavily on the free software environment, so both of these are relevant to the Consortium. The period of confidentiality is three years. Some of the codes developed at CWP are part of government-funded research projects, and are required to be released as open source. Software developed using in-house resources of sponsor companies generally is not available to us for release.

Of interest to Consortium members are codes for nonhyperbolic moveout inversion of wide-azimuth P-wave data by Ivan Vasconselos and for anisotropic geometrical-spreading correction and azimuthal AVO analysis by Xiaoxia (Ellen) Xu. An extension of Ivan's nonhyperbolic moveout inversion code that takes 3D AVO signature into account has been contributed by Jia Yan. Software under development includes Matlab codes by Rodrigo Fuck for modeling excess stress around compacting reservoirs and stress-related traveltime shifts of seismic waves, shell scripts of virtual source and receiver gathers by Kurang Mehta, and code for computing reflection coefficients in anisotropic attenuative media by Jyoti Behura.

A widely used vehicle of *open* software distribution is the CWP/SU:Seismic Un*x (SU) package. This package has been installed at more than 3600 sites in 68 countries (where a country is defined by its independent country code), and has an active worldwide user group. User base is determined by direct email, listserver group membership (524 as of April 1, 2007), and by downloads (more than 10 per day).

Release 40 of SU was issued on April 10, 2007, and contained many updates and new software, including support for the LAS welllog format, and for SEG Rev 1. Prior to that date, there were nine beta releases of SU.

Of particular interest is a new package called the SLT/SU distribution, which is a collection of legacy codes written in the style of SU at Unocal. This package has been made available thanks to the efforts of Reg Beardsley.

The open-source Mines Java Toolkit is available online from Dave Hale's home page at: http://www.mines.edu/ dhale/jtk/. This software is the foundation for most of Dave's teaching and research, and is also being used by commercial software companies. Anyone with a web browser can view and download the always up-to-date source code repository.

Paul Sava and students working with him use Madagascar (formerly known as RSF), an open-source software package for geophysical data processing and reproducible numerical experiments. Its mission is to provide a convenient and powerful environment and a technology transfer tool for researchers working with digital image and data processing. The technology developed using the Madagascar project management system is transferred in the form of recorded processing histories, which become "computational recipes" to be verified, exchanged, and modified by users of the system. This open-source package is available from http://rsf.sourceforge.net/.

Annual Project Review Meeting

This year's Annual Project Review Meeting will be held May 21–24, 2007, on the CSM campus in Golden, Colorado. A tradition of recent years is that, prior to the Meeting, we hold a tutorial for sponsors on a topic of particular interest within CWP. This year, in the afternoon of May 21, Norm Bleistein will give a tutorial entitled "Mathematics of modeling, migration and inversion with Gaussian beams." During the following three days, students and faculty will present more than 20 research papers. In addition, the program will include two guest speakers: Dave Nichols from Schlumberger and John Toldi from Chevron.

WELCOME

With great pleasure, we welcome representatives of our sponsor companies to the 23rd Annual Project Review Meeting, and look forward to the opportunity to exchange with you ideas and thoughts about this past year's projects and plans for the future.

Ilya Tsvankin, Director
Center for Wave Phenomena
May 2007

selected events picked from the data. Examples of techniques in this category are waveform inversion (Tarantola, 1987; Pratt and Worthington, 1990; Pratt, 1990), wave-equation tomography (Woodward, 1992) or wave-equation migration velocity analysis (Sava and Biondi, 2004a; Sava and Biondi, 2004b; Shen et al., 2005). A more accurate velocity model allows for more accurate wavefield reconstruction. Then, wavefields can be used for imaging using conventional procedures, e.g. cross-correlation.

- The second option is to concentrate on the imaging condition, rather than concentrate on wavefield reconstruction. Assuming that the large-scale component of the velocity models is known (e.g. by iterative migration/tomography cycles), we can design imaging conditions that are not sensitive to small inaccuracies of the reconstructed wavefields. Imaging artifacts can be reduced at the imaging condition step, despite the fact that the wavefields incorporate small kinematic errors due to velocity fluctuations.

The two options are complementary to each other, and both can contribute to imaging accuracy. In this paper, we concentrate on the second approach. For purposes of theoretical analysis, it is convenient to model the small-scale variations velocity fluctuations as random but correlated variations superimposed on a smooth known velocity. We assume that we know the smooth background, but we do not know the random fluctuations. The goal is to design an imaging condition that alleviates artifacts caused by those random fluctuations.

Conventional imaging consists of cross-correlations of extrapolated source and receiver wavefields at image locations. Since wavefield extrapolation is performed using an approximation of the true model, the wavefields contain random time delays, or equivalently random phases, which lead to imaging artifacts.

One way of mitigating the effects of the random model on the quality of the resulting image involves using techniques based on acoustic time reversal (Fink, 1999). A well-known result is that, under certain assumptions, a signal sent through a random medium, recorded by a receiver array, time reversed and sent back through the same medium, refocuses at the source location in a statistically stable fashion. Statistical stability means that the refocusing properties (i.e. image quality) are independent of the actual realization of the random medium (Papanicolaou et al., 2004; Fouque et al., 2005).

An equivalent formulation of this result is that statistical stability can be achieved if random phase shifts between signals recorded at nearby locations are removed by cross-correlation, prior to back propagation into the medium. This observation lies at the heart of coherent interferometric imaging (Borcea et al., 2005; Borcea et al., 2006c; Borcea et al., 2006a; Borcea et al., 2006b) or imaging and velocity analysis in presence of uncertain models (Dussaud, 2005). With this approach, local spatial cross-correlations of data traces on the acquisition surface are computed and extrapolated to the image location using standard techniques. Thus, random phase shifts that cause imaging artifacts are removed prior to extrapolation and imaging quality in the smooth background medium increases. This method assumes the existence of a continuous acquisition array with dense receiver layout to ensure coherency of local cross-correlations.

We investigate an alternative way of using time reversal to increase imaging statistical stability. Instead of coherent interferometry applied to data on the acquisition surface, we first extrapolate wavefields to all locations in the imaging volume and then apply local spatial cross-correlations in the vicinity of every image point. Correlations in the image-space damps small random fluctuations in the extrapolated wavefields. The cross-correlations do not relocate energy in space, but simply produce local averages of the extrapolated wavefields.

The procedure closely resemble conventional imaging procedures where wavefields are extrapolated in the image volume and then cross-correlated in time at every image location. Our method uses averaging in three-dimensional local windows around image locations. From implementation and computational cost points of view, our technique does not differ much from conventional imaging, although the imaging properties are improved. Therefore, we use the name *interferometric imaging condition* for our technique to contrast it with conventional imaging condition which represents a special case of this method for infinitely small local windows.

One advantage of using the interferometric imaging condition in wave-equation migration is that it also makes efficient use of the data obtained by a sparse array, since the cross-correlation is performed at an image point on wavefields extrapolated from all data traces simultaneously. Furthermore, local averaging around the image locations is inherently three-dimensional, in contrast with the two-dimensional averaging typical for interferometric imaging parametrized on the surface. This increases signal-to-noise ratio and improves random phase cancellation, although it also increases computational cost proportionally. Processing with image-space coordinates is simpler than processing using data-space coordinates because, after extrapolation, wavefields are simpler since wave propagation complications have been unraveled in the extrapolation process (Stolk and Symes, 2004).

Finally, we note that the proposed method is not an extension, but an alternative to coherent interferometry. When assumptions permit, the two methods can be used simultaneously in an imaging functional, thus taking advantage of the best qualities of both approaches.

2 SEISMIC IMAGING CONDITIONS

Conventional seismic imaging methods share the fundamental assumption of single scattering in the subsurface (Born approximation). Under this assumption, we can represent waves recorded at the surface as a convolution of Green's functions (G) corresponding to sources on the surface and scattering points in the subsurface. Assuming an impulsive source, we can write

$$P(\mathbf{x}_m,\omega_m) = G(\mathbf{x}_s,\mathbf{y}_m,\omega_m)\,G(\mathbf{y}_m,\mathbf{x}_m,\omega_m)\ , \qquad (1)$$

where P denotes recorded acoustic data at coordinates $\mathbf{x}_m$, $\mathbf{x}_s$ are coordinates of the source, $\mathbf{y}_m$ are coordinates of the scattering points, and ω_m is the frequency of the propagating wave.

Interferometric imaging condition for wave-equation migration

Paul Sava* and Oleg Poliannikov†

* *Center for Wave Phenomena, Colorado School of Mines, Golden CO 80401, USA*
† *Department of Mathematical Sciences, Colorado University, Denver, CO 80217, USA*

ABSTRACT

The fidelity of depth seismic imaging depends on the accuracy of the velocity models used for wavefield reconstruction. Models can be decomposed in two components corresponding to large scale and small scale variations. In practice, the large scale velocity model component can be estimated with high accuracy using repeated migration/tomography cycles, but the small scale component cannot. Therefore, wavefield reconstruction does not completely describe the recorded data and migrated images are perturbed by artifacts.

There are two possible ways to address this problem: improve wavefield reconstruction by estimating more accurate velocity models and image using conventional techniques (e.g. wavefield cross-correlation), or reconstruct wavefields with conventional methods using the known smooth velocity model, and improve the imaging condition to alleviate the artifacts caused by the imprecise reconstruction, as suggested in this paper.

In this paper, the unknown component of the velocity model is described as a random function with local spatial correlations. Imaging data perturbed by such random variations is characterized by statistical instability, i.e. various wavefield components image at wrong locations that depend on the actual realization of the random model. Statistical stability can be achieved by local wavefield averaging either in spatial windows defined in the vicinity of the data acquisition locations, or in local windows defined in the vicinity of image points. We use the latter approach and show that the technique is effective in attenuating imaging artifacts without being hampered by some of the limitations of data-space alternatives.

Key words: imaging, interferometry, random media

1 INTRODUCTION

Seismic imaging in complex media requires accurate knowledge of the medium velocity. Assuming single scattering, imaging requires propagation of the recorded wavefields from the acquisition surface, followed by the application of an imaging condition highlighting locations where scattering occurs, i.e. where reflectors are present.

The main requirement for good-quality imaging is accurate knowledge of the velocity model. Errors in the model used for imaging lead to inaccurate reconstruction of the seismic wavefields and to distortions of the migrated images. In a realistic seismic experiment the velocity model is not known exactly. Migration velocity analysis produces large scale approximations of the model, but fine scale variations remain elusive. For example, when geology includes complicated stratigraphic structures, the rapid velocity variations on the scale of the seismic wavelength and smaller cannot be estimated correctly. Therefore, even if the broad kinematics of the seismic wavefields are reconstructed correctly, the extrapolated wavefields also contain distortions that lead to image artifacts obstructing the image of the geologic structure under consideration. While it is certainly true that even the recovery of a long-wave background may prove to be a challenge in some circumstances, we do not attempt to address that issue in this paper. Instead, we concentrate solely on the problem of dealing with the effect of a small scale random variations.

There are two ways in which we can approach this problem:

- The first option is to improve the velocity analysis methods to estimate the small-scale variations in the model. Such techniques take advantage of all information contained in seismic wavefields and are not limited to kinematic information of

Relation (1) can be written in an equivalent form using time instead of frequency variables, but for simplicity we use the frequency-domain notation throughout this paper. The Green's function G characterizes data propagation in the real medium of velocity v.

Imaging with recorded data $P(\mathbf{x}_m, \omega_m)$ is a two-step procedure:

- The first step consists of extrapolation of source and receiver wavefields from the recording surface to image locations. The source wavefield corresponds to simulated waves propagating forward in time from the source location $\mathbf{x}_s$, and the receiver wavefield corresponds to waves propagating backward in time from recording locations $\mathbf{x}_m$.
- The second step consists of an imaging condition evaluating whether the two extrapolated wavefields match kinematically, which indicates whether a reflector is present in the medium.

Wavefield extrapolation and imaging can be implemented in different space and time domains, for example downward continuation with the one-way wave-equation implemented in frequency-wavenumber, frequency-space or mixed domains, or wavefield extrapolation with the two-way wave-equation in time-space, etc. Wavefield extrapolation can also be performed using Kirchhoff integral methods followed by conventional imaging. However, the actual extrapolation method is irrelevant for the discussion in this paper. For simplicity, we represent wavefield extrapolation with Green's functions in the frequency-domain, although our examples use time-domain two-way finite-difference solutions to the acoustic wave-equation, process typically known as reverse-time migration (Kosloff and Baysal, 1983). Any other implementation of Green's functions can be substituted in our discussion with no change to the conclusions.

In real imaging projects, the actual velocity medium is not known in detail, therefore the known velocity model represents a smooth version of the real model. This smooth model does not incorporate rapid variations of the velocity at scales comparable with or smaller than the seismic wavelength. In this paper, we represent the real model with random variations by symbol $v(x,y,z)$, and the approximate (possibly smooth) model by symbol $v_0(x,y,z)$.

When reconstructing wavefields in seismic imaging, we compute Green's functions connecting points on the acquisition surface with image points in the subsurface. We use the symbol G_0 to denote Green's functions computed in the approximate medium of velocity v_0, in contrast with the symbol G which denotes Green's functions representing wave propagation in the real medium of velocity v.

Using these notations and assuming an impulsive source function, the source wavefield reconstructed during imaging by propagation forward in time from the source position is represented as $G_0(\mathbf{x}_s, \mathbf{y}_m, \omega_m)$, and the receiver wavefield reconstructed by propagation backward in time from the receiver positions is represented as $P(\mathbf{x}_m, \omega_m)\overline{G_0(\mathbf{y}_m, \mathbf{x}_m, \omega_m)}$, where the over-line represents complex conjugation for propagation backward in time.

2.1 Conventional imaging condition

The conventional way of implementing the imaging condition for wave-equation migration involves cross-correlation of the source and receiver wavefields, often referred to as the $U\overline{D}$ imaging condition (Claerbout, 1985), where D and U stand for downward and upward propagating wavefields. The image I is evaluated using the relation

$$I(\mathbf{y}_m) = \int_{\omega_m} d\omega_m \int_{\mathbf{x}_m} d\mathbf{x}_m \; \overline{G_0(\mathbf{x}_s, \mathbf{y}_m, \omega_m)} P(\mathbf{x}_m, \omega_m) \overline{G_0(\mathbf{y}_m, \mathbf{x}_m, \omega_m)} \,. \qquad (2)$$

This imaging condition evaluates the match between source and receiver wavefields reconstructed throughout the medium. Maximum energy at zero temporal cross-correlation lag, computed by summation over temporal frequency, indicates the presence of reflectors. Here and for the rest of the paper, summation over multiple seismic experiments (sources) is assumed.

The propagation geometry of the imaging condition (2) is summarized in figure 1(a): source waves are propagated forward in time from the source at $\mathbf{x}_s$ to the scatterer location $\mathbf{y}_m$, and receiver waves are propagated backward in time from the receiver coordinates $\mathbf{x}_m$ to the scatterer location $\mathbf{y}_m$.

The assumption made in this model is that the Green's functions used for reconstruction are accurate representations of the Green's functions describing wave propagation in the real medium. However, for the case of media with random velocity fluctuations, v_0 is a smooth velocity approximating v. Thus, although the general kinematics of wave propagation are accurately described by v_0, the velocity fluctuations induce perturbations of the wavefield leading to imaging artifacts.

For illustration of those imaging artifacts, consider the numerical modeling in figures 3(a)-3(f). Figures 3(a)-3(e), depict in the background the velocity smooth model v_0, and figures 3(b)-3(f) depict in the background the velocity real model v. Overlayed are the seismic wavefields for a point source on the surface at $x = 600$ m which generates secondary waves from 3 scatterers represented in the figures around $x = 600$ m and $z = 700$ m. Panels (b) and (d) simulate Green's functions in the real model with random fluctuations, and panels (a) and (c) simulate the reconstructed Green's functions in the smooth model. Top row panels correspond to an early time prior to the source wavefield interacting with the scatterers, and the bottom row corresponds to a later time and depicts scattered wavefields from the imaging targets. Figures 4(a)-4(b) show the recorded data on the acquisition surface. For the case of media with random fluctuations, we observe that the wavefronts for the scattered wavefields resemble the corresponding wavefronts in the smooth media. Since we are imaging with the smooth velocity, these wavefronts are the only contributions of the recorded data to the image. The random fluctuations (time delays) incorporated in those wavefields are not compensated in the imaging process and lead to artifacts.

The main question we address here is: what is the impact of migrating data simulated in the random model depicted in figures 3(b)-3(f) with the smooth model depicted in figures 3(a)-3(e)?

- Figure 5(a) shows the result of migrating with smooth velocity v_0 data simulated with the same velocity v_0. Panel 5(c) depicts a zoom on the image in figure 5(a). The images show well-focused diffractors and typical truncation artifacts produced by the limited acquisition on the surface.
- Figure 5(b) shows the result of migrating with smooth velocity v_0 data simulated with the random velocity v. Panel 5(d) depicts a zoom on the image in figure 5(b). The images show the 3 diffractors and the truncation artifacts, together with many other artifacts caused by imaging with an incorrect velocity v_0.

Suppressing artifacts exemplified by figures 5(b) and 5(d) is the focus of this paper. If imaging targets correspond to stratigraphy characterized by finely-spaced reflectors, the artifacts caused by random velocity variation can obscure valuable information and hinder geologic interpretation.

2.2 Coherent interferometry

One way of addressing the problem of imaging in models with random fluctuations involves statistical stabilization using phase compensation in windows localized in time and space (Papanicolaou et al., 2004; Fouque et al., 2005). The idea is that small wavefield fluctuations caused by random perturbations of the velocity model are incoherent spatially and temporally and cancel-out by local cross-correlation and averaging.

The idea of statistical stability for imaging in random media is exploited by the technique called *coherent interferometric imaging* (Borcea et al., 2006b). The main idea of this method is to reduce the delay spread caused by the random fluctuations of the medium using averages of local cross-correlations between nearby traces on the acquisition surface. It has been shown that interferometric imaging methods are capable of reducing imaging artifacts and statistically stabilizing the image by averaging locally in space and time (or frequency) the fluctuations caused by the random variations of the medium.

When constructing an imaging functional, the emulated source wavefield reconstructed with the help of the smooth velocity v_0 contains no random fluctuations, and thus requires no stabilization. All random fluctuations are contained through the recorded data to the receiver wavefield. The latter then requires averaging using interferograms localized in space and time, but the former does not. The modified imaging functional takes the form

$$\begin{aligned} I(\mathbf{y}_m) \;=\; & \int_{\omega_m} d\omega_m \int_{|\omega_h|\le\Omega/2} d\omega_h \int_{\mathbf{x}_m} d\mathbf{x}_m \int_{|\mathbf{x}_h|\le X/2} d\mathbf{x}_h \\ & \overline{G_0\left(\mathbf{x}_s,\mathbf{y}_m,\omega_m-\omega_h\right)}\left(P\left(\mathbf{x}_m-\mathbf{x}_h,\omega_m-\omega_h\right)\overline{G_0\left(\mathbf{y}_m,\mathbf{x}_m-\mathbf{x}_h,\omega_m-\omega_h\right)}\right) \\ & \overline{G_0\left(\mathbf{x}_s,\mathbf{y}_m,\omega_m+\omega_h\right)}\left(P\left(\mathbf{x}_m+\mathbf{x}_h,\omega_m+\omega_h\right)\overline{G_0\left(\mathbf{y}_m,\mathbf{x}_m+\mathbf{x}_h,\omega_m+\omega_h\right)}\right), \end{aligned} \tag{3}$$

where $\mathbf{x}_h$ represents a 2D summation variable on the acquisition surface. For seismic experiments without an active source (exploding reflector experiments), the equivalent imaging functional is

$$\begin{aligned} I(\mathbf{y}_m) \;=\; & \int_{\omega_m} d\omega_m \int_{|\omega_h|\le\Omega/2} d\omega_h \int_{\mathbf{x}_m} d\mathbf{x}_m \int_{|\mathbf{x}_h|\le X/2} d\mathbf{x}_h \\ & P\left(\mathbf{x}_m-\mathbf{x}_h,\omega_m-\omega_h\right)\overline{G_0\left(\mathbf{x}_m-\mathbf{x}_h,\mathbf{y}_m,\omega_m-\omega_h\right)} \\ & \overline{P\left(\mathbf{x}_m+\mathbf{x}_h,\omega_m+\omega_h\right)\overline{G_0\left(\mathbf{x}_m+\mathbf{x}_h,\mathbf{y}_m,\omega_m+\omega_h\right)}}. \end{aligned} \tag{4}$$

The relation $P\left(\mathbf{x}_m-\mathbf{x}_h,\omega_m-\omega_h\right)\overline{G_0\left(\mathbf{y}_m,\mathbf{x}_m-\mathbf{x}_h,\omega_m-\omega_h\right)}$ represents data at position $\mathbf{x}_m-\mathbf{x}_h$ relocated to the image location $\mathbf{y}_m$, and the relation $P\left(\mathbf{x}_m+\mathbf{x}_h,\omega_m+\omega_h\right)\overline{G_0\left(\mathbf{y}_m,\mathbf{x}_m+\mathbf{x}_h,\omega_m+\omega_h\right)}$ represents data at position $\mathbf{x}_m+\mathbf{x}_h$ relocated to the image location $\mathbf{y}_m$ using Green's functions computed in the smooth medium. Cross-correlation occurs at image location $\mathbf{y}_m$ and the propagation geometry from the acquisition surface is schematically depicted in figure 1(b). An image is formed by summation of all interferograms computed around image points from data located on the surface within the decoherence length X. We do not need to worry in this implementation about loss of depth (range) resolution since the statistical stability is achieved by cross-correlation and averaging at the image locations from data reconstructed from all points on the acquisition surface.

2.3 Interferometric imaging condition (IIC)

We can also approach the coherent imaging problem in an alternative way: rather than correlating data on the acquisition surface, we can reconstruct wavefields at all locations in the imaging volume from all locations on the acquisition surface and suppress the random fluctuations in the wavefield by local cross-correlations in small windows around the image point.

Image-space processing as an alternative to data-space processing has been employed in other seismic data processing contexts, for example for imaging passive seismic data (Artman, 2006) or for predicting multiple after wavefield extrapolation (Artman et al., 2007). Here we use a similar idea to attenuating artifacts caused by inaccurate knowledge of velocity during wavefield extrapolation.

For coherent imaging after extrapolation, we can define another decoherence length around an image point Y, which is analogous to the decoherence length defined on the acquisition surface X. The imaging functional corresponding to this case can be written analogously to the one in equation (3) as

$$
\begin{aligned}
I(\mathbf{y}_m) \;=\; & \int_{\omega_m} d\omega_m \int_{|\omega_h|\le\Omega/2} d\omega_h \int_{|\mathbf{y}_h|\le Y/2} d\mathbf{y}_h \\
& \overline{G_0(\mathbf{x}_s, \mathbf{y}_m - \mathbf{y}_h, \omega_m - \omega_h)} \int_{\mathbf{x}_m} d\mathbf{x}_m \, P(\mathbf{x}_m, \omega_m - \omega_h) \, \overline{G_0(\mathbf{x}_m, \mathbf{y}_m - \mathbf{y}_h, \omega_m - \omega_h)} \\
& \overline{G_0(\mathbf{x}_s, \mathbf{y}_m + \mathbf{y}_h, \omega_m + \omega_h)} \int_{\mathbf{x}_m} d\mathbf{x}_m \, P(\mathbf{x}_m, \omega_m + \omega_h) \, \overline{G_0(\mathbf{x}_m, \mathbf{y}_m + \mathbf{y}_h, \omega_m + \omega_h)} \,,
\end{aligned}
\tag{5}
$$

where $\mathbf{y}_h$ represents a 3D summation variable around the image point. For seismic experiments without an active source (exploding reflector experiment), the equivalent imaging functional is

$$
\begin{aligned}
I(\mathbf{y}_m) \;=\; & \int_{\omega_m} d\omega_m \int_{|\omega_h|\le\Omega/2} d\omega_h \int_{|\mathbf{y}_h|\le Y/2} d\mathbf{y}_h \\
& \int_{\mathbf{x}_m} d\mathbf{x}_m \, P(\mathbf{x}_m, \omega_m - \omega_h) \, \overline{G_0(\mathbf{x}_m, \mathbf{y}_m - \mathbf{y}_h, \omega_m - \omega_h)} \\
& \overline{\int_{\mathbf{x}_m} d\mathbf{x}_m \, P(\mathbf{x}_m, \omega_m + \omega_h) \, \overline{G_0(\mathbf{x}_m, \mathbf{y}_m + \mathbf{y}_h, \omega_m + \omega_h)}} \,.
\end{aligned}
\tag{6}
$$

The relation $P(\mathbf{x}_m, \omega_m - \omega_h)\,\overline{G_0(\mathbf{y}_m - \mathbf{y}_h, \mathbf{x}_m, \omega_m - \omega_h)}$ represents data at position $\mathbf{x}_m$ relocated to the image location $\mathbf{y}_m - \mathbf{y}_h$, and the relation $P(\mathbf{x}_m, \omega_m + \omega_h)\,\overline{G_0(\mathbf{y}_m + \mathbf{y}_h, \mathbf{x}_m, \omega_m + \omega_h)}$ represents data at position $\mathbf{x}_m$ relocated to the image location $\mathbf{y}_m + \mathbf{y}_h$. Cross-correlation occurs around image location $\mathbf{y}_m$ and the propagation geometry from the acquisition surface is schematically depicted in figure 1(c).

The imaging procedure described by equation (5) exploits two main ideas:

- The first idea is that of extended imaging conditions (Rickett and Sava, 2002; Sava and Fomel, 2006) where multiple space and time lags of the source-receiver wavefield cross-correlation are evaluated. In particular, $\mathbf{y}_h$ is interpreted as a 3D spatial lag of the cross-correlation between the reconstructed source and receiver wavefields. This lag can be used for decomposition of images function of scattering angles (Sava and Fomel, 2003; Fomel, 2004; Biondi and Symes, 2004; Sava and Fomel, 2005). Here, we use $\mathbf{y}_h$ as a summation variable during averaging around image locations.
- The second idea is that we can achieve statistical stability in random media by space and time averaging of wavefield cross-correlations in local windows (Papanicolaou et al., 2004; Fouque et al., 2005). We exploit this idea similarly to the way it is used by (Borcea et al., 2006b) for coherent interferometric imaging in clutter. The local averaging variable $\mathbf{y}_h$ is similar to the local averaging variable $\mathbf{x}_h$, except that $\mathbf{y}_h$ is defined in the image space, around particular image points. Unlike $\mathbf{x}_h$ which is a 2D quantity defined on the acquisition surface, $\mathbf{y}_h$ is a 3D quantity defined in a volume around the image point location. Unlike $\mathbf{x}_h$ which requires close spacing on the acquisition surface, $\mathbf{y}_h$ is defined around image locations and, assuming media with rapid fluctuations that do not introduce large kinematic differences, does not require special sampling assumptions.

Thus, we can describe the imaging method summarized by equation (5) by the name *interferometric imaging condition*, since it acts similarly to the conventional imaging condition, but with robustness with respect to random fluctuations due to local interferometric averaging in windows around image locations.

Using the interferometric imaging functional defined in equation (5) on the simple example described earlier, we obtain the images depicted in figures 6(b) and 6(d). For comparison, figures 5(b) and 5(d) show the equivalent images obtained using the conventional imaging condition defined in equation (2). The images obtained by interferometric imaging show a reduction of the imaging artifacts surrounding the 3 diffractors despite the fact that imaging was performed using a smooth approximation of the random medium.

Even more generally, we can write the interferometric imaging functional by imposing noise cancellation both on the acquisition surface and around the image points. In this case, imaging is performed using a relation like

$$
I(\mathbf{y}_m) \;=\; \int_{\omega_m} d\omega_m \int_{|\omega_h|\le\Omega/2} d\omega_h \int_{|\mathbf{y}_h|\le Y/2} d\mathbf{y}_h \int_{|\mathbf{x}_h|\le X/2} d\mathbf{x}_h
$$

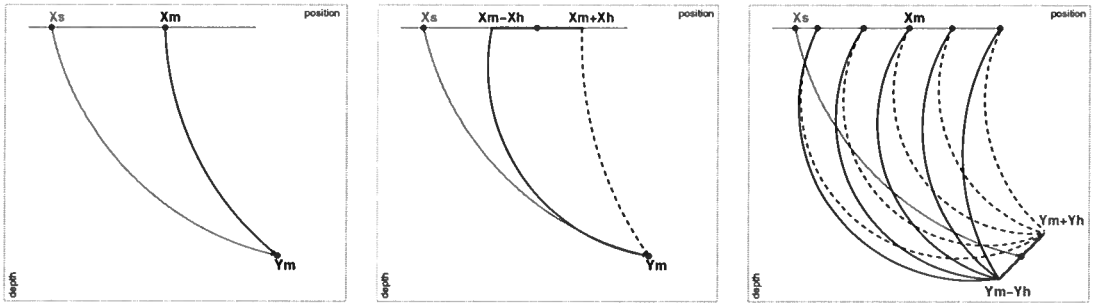

Figure 1. Schematic description of propagation and imaging geometry for various imaging functionals: (a) imaging using equation (2), (b) imaging using equation (3), and (c) imaging using equation (5). Quantity $\mathbf{x}_h$ represents a 1D projection of the 2D averaging variable on the acquisition surface, and quantity $\mathbf{y}_h$ represents a 1D projection of the 3D averaging variable around image points.

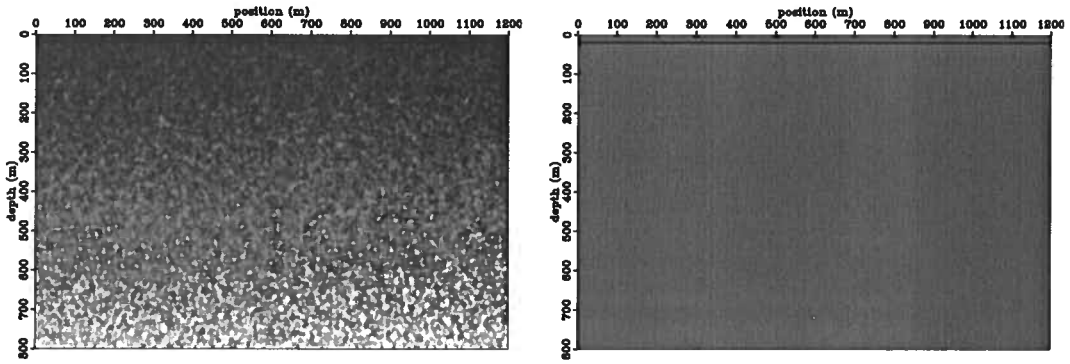

Figure 2. Random velocity model (a) and imaging target located around $x = 600$ m and $z = 700$ m (b).

$$\frac{\overline{G_0\left(\mathbf{x}_s, \mathbf{y}_m - \mathbf{y}_h, \omega_m - \omega_h\right)} \int_{\mathbf{x}_m} d\mathbf{x}_m \, P\left(\mathbf{x}_m - \mathbf{x}_h, \omega_m - \omega_h\right) \overline{G_0\left(\mathbf{x}_m - \mathbf{x}_h, \mathbf{y}_m - \mathbf{y}_h, \omega_m - \omega_h\right)}}{\overline{G_0\left(\mathbf{x}_s, \mathbf{y}_m + \mathbf{y}_h, \omega_m + \omega_h\right)} \int_{\mathbf{x}_m} d\mathbf{x}_m \, P\left(\mathbf{x}_m + \mathbf{x}_h, \omega_m + \omega_h\right) \overline{G_0\left(\mathbf{x}_m + \mathbf{x}_h, \mathbf{y}_m + \mathbf{y}_h, \omega_m + \omega_h\right)}} \,. \tag{7}$$

For seismic experiments without an active source (exploding reflector experiment), the equivalent imaging functional is

$$\begin{aligned} I\left(\mathbf{y}_m\right) \;=\; & \int_{\omega_m} d\omega_m \int_{|\omega_h| \le \Omega/2} d\omega_h \int_{|\mathbf{x}_h| \le X/2} d\mathbf{x}_h \int_{|\mathbf{y}_h| \le Y/2} d\mathbf{y}_h \\ & \int_{\mathbf{x}_m} d\mathbf{x}_m \, P\left(\mathbf{x}_m - \mathbf{x}_h, \omega_m - \omega_h\right) \overline{G_0\left(\mathbf{x}_m - \mathbf{x}_h, \mathbf{y}_m - \mathbf{y}_h, \omega_m - \omega_h\right)} \\ & \overline{\int_{\mathbf{x}_m} d\mathbf{x}_m \, P\left(\mathbf{x}_m + \mathbf{x}_h, \omega_m + \omega_h\right) \overline{G_0\left(\mathbf{x}_m + \mathbf{x}_h, \mathbf{y}_m + \mathbf{y}_h, \omega_m + \omega_h\right)}} \,. \end{aligned} \tag{8}$$

The relation $P\left(\mathbf{x}_m - \mathbf{x}_h, \omega_m - \omega_h\right) \overline{G_0\left(\mathbf{y}_m - \mathbf{y}_h, \mathbf{x}_m - \mathbf{x}_h, \omega_m - \omega_h\right)}$ represents data at position $\mathbf{x}_m - \mathbf{x}_h$ relocated to the image location $\mathbf{y}_m - \mathbf{y}_h$, and the relation $P\left(\mathbf{x}_m + \mathbf{x}_h, \omega_m - \omega_h\right) \overline{G_0\left(\mathbf{y}_m + \mathbf{y}_h, \mathbf{x}_m + \mathbf{x}_h, \omega_m + \omega_h\right)}$ represents data at position $\mathbf{x}_m + \mathbf{x}_h$ relocated to the image location $\mathbf{y}_m + \mathbf{y}_h$.

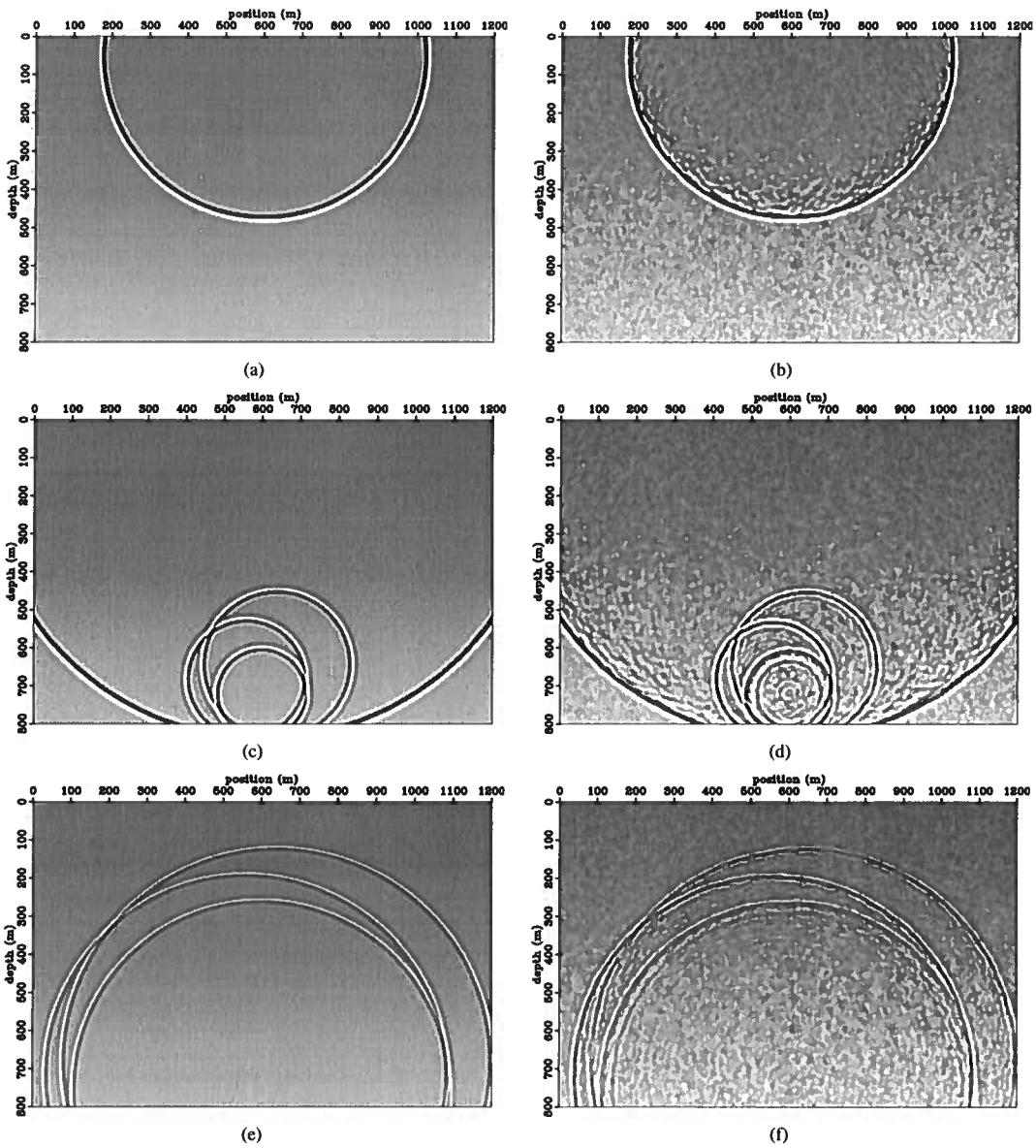

Figure 3. Wavefields simulated in the smooth background velocity v_0, panels (a) and (c) and in the random velocity v, panels (b) and (d).

2.4 Comparison of imaging functionals

At first glance, the imaging functionals (3) and (5) look similar in shape and imaging properties. However, from a practical point of view, the two imaging functionals are fundamentally different:

- Imaging functional (3) achieves statistical stability by cross-correlating and averaging wavefields parametrized function of the location of receivers on the acquisition surface. In this functional, the wavefields subject to cross-correlation are $P(\mathbf{x}_m - \mathbf{x}_h, \omega_m - \omega_h)\overline{G_0(\mathbf{y}_m, \mathbf{x}_m - \mathbf{x}_h, \omega_m - \omega_h)}$ and $P(\mathbf{x}_m + \mathbf{x}_h, \omega_m + \omega_h)\overline{G_0(\mathbf{y}_m, \mathbf{x}_m + \mathbf{x}_h, \omega_m + \omega_h)}$. This operation requires that we reconstruct wavefields at all image locations $\mathbf{y}_m$ for every receiver location on the acquisition surface $\mathbf{x}_m$, for every experiment. This requires to construct solutions of the wave-equation for every trace on the surface acting as an independent source (number of $\mathbf{x}_m$ receivers solutions to the acoustic wave-equation), which is an impractical operation in complex media.

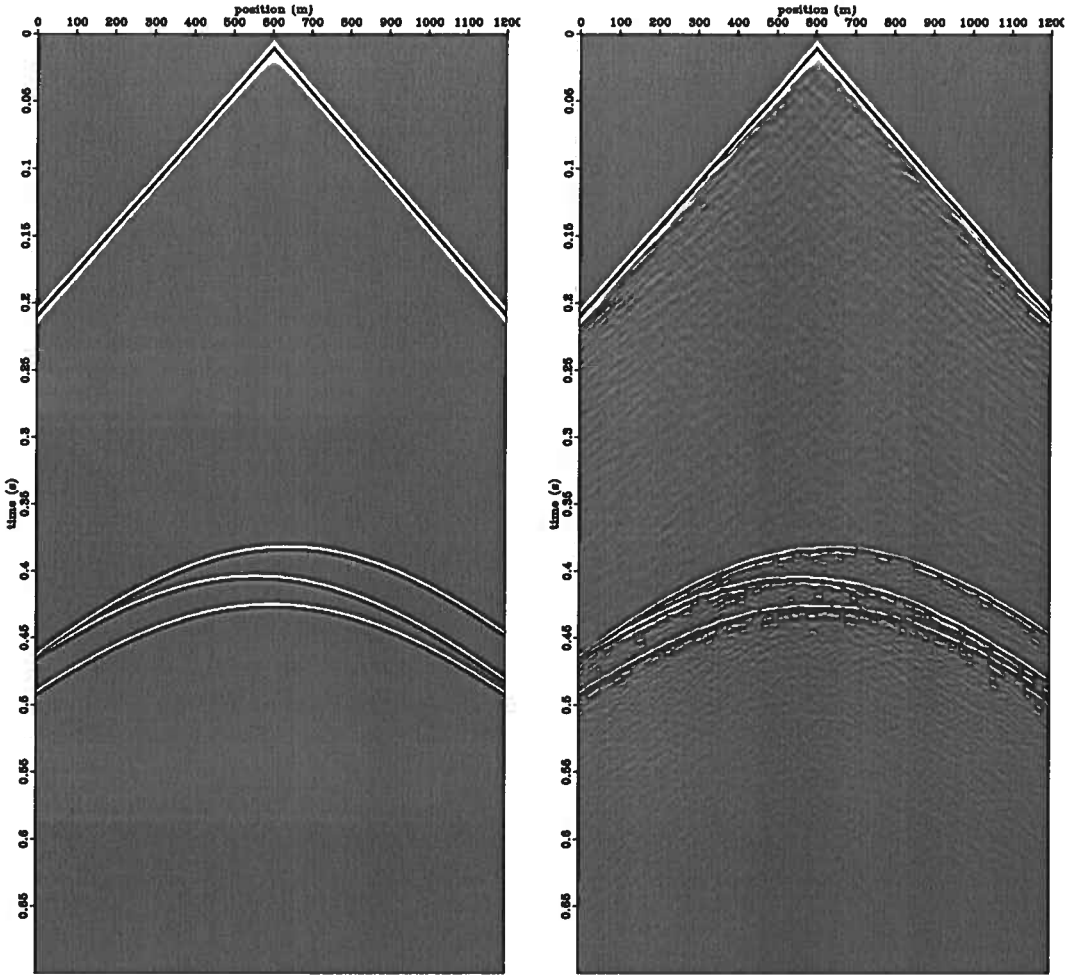

Figure 4. Data recorded for the smooth velocity model, panel (a), and for the model with random velocity variations, panel (b).

• Imaging functional (5) achieves statistical stability by cross-correlating and averaging wavefields parametrized function of the image location. In this functional, the wavefields subject to cross-correlation are $\int_{\mathbf{x}_m} d\mathbf{x}_m\, P(\mathbf{x}_m, \omega_m - \omega_h)\, \overline{G_0(\mathbf{x}_m, \mathbf{y}_m - \mathbf{y}_h, \omega_m - \omega_h)}$ and $\int_{\mathbf{x}_m} d\mathbf{x}_m\, P(\mathbf{x}_m, \omega_m + \omega_h)\, \overline{G_0(\mathbf{x}_m, \mathbf{y}_m + \mathbf{y}_h, \omega_m + \omega_h)}$. This operation requires that we reconstruct wavefields at all image locations $\mathbf{y}_m$ for all receiver locations on the surface $\mathbf{x}_m$, for every experiment. The cost associated with this operation is comparable with the cost of conventional imaging. This requires to construct solutions of the wave-equation for all trace on the surface acting as simultaneous sources (one solution to the acoustic wave-equation), which is an affordable operation in complex media.

3 STATISTICAL STABILITY

The interferometric imaging condition described in the preceding section is used to reduce imaging artifacts by attenuating the incoherent energy corresponding to velocity errors, as illustrated in figures 5(d) and 6(d). The random model used for this example corresponds to the *weak fluctuation regime*, as explained in Appendix A (characteristic wavelength of similar scale with the random fluctuations in the medium and fluctuations with small magnitude).

By statistical instability we mean that images obtained for different realizations of random models with the identical statistics are different. Figures 7(a)-7(d) illustrate data modeled for different realizations of the random model in figures 3(a)-3(f). The general

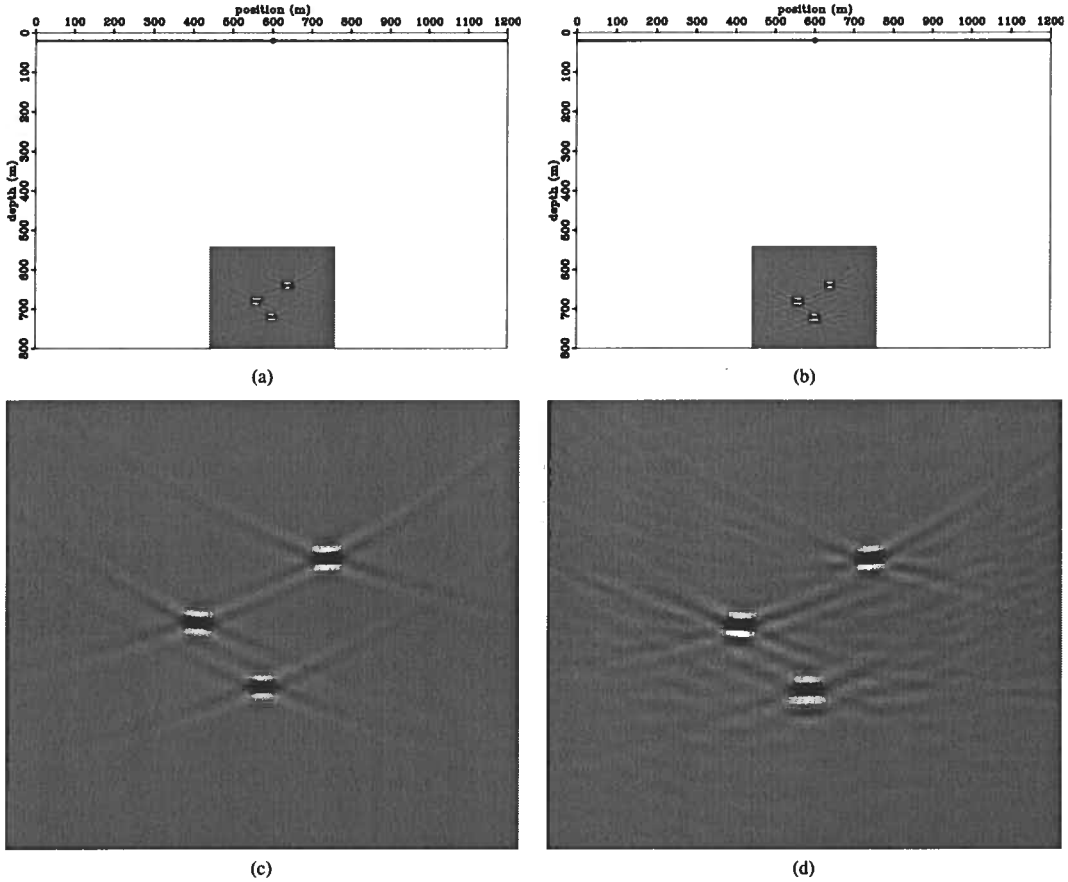

Figure 5. Images produced using the *conventional imaging condition*. Panels (a) and (c) correspond to modeling and imaging in the smooth known velocity model v_0, and panels (b) and (d) correspond to modeling using the random velocity model v and imaging using the smooth velocity model v_0. Panels (c) and (d) depict enlarged versions of the images shown in panels (a) and (b), respectively.

kinematics of the data are the same, but subtle differences exist between the various dataset due to the random model variations. Migration using conventional imaging condition leads to the images in figures 7(e)-7(h) which also show variations from realization to realization. In contrast, figures 7(i)-7(l) show images obtained by the interferometric imaging condition which are more similar to one-another since many of the spurious artifacts have been attenuated.

In typical seismic imaging problems, we cannot ensure that random velocity fluctuations are small (e.g. $\sigma \leq 5\%$). It is desirable that imaging remains statistically stable even in cases when velocity varies with larger magnitude. We investigate the statistical properties of the imaging functional in equation (6) using numeric experiments similar to the one used earlier. We describe the random noise present in the velocity models using the following parameters explained in Appendix A:

- Seismic spatial wavelength $\lambda = 20$ m.
- Wavelet central frequency $\omega = 150$ Hz.
- Background velocity: $v_0 = 3000 + k\,z$ m/s ($k = 1s^{-1}$).
- Random fluctuations parameters: $r_a = 8$, $r_c = 8$, $\alpha = 2$.
- Random noise magnitude σ between 0% and 80%.

This numeric experiment simulates a situation that mixes the theoretical regimes explained in Appendix A: random model fluctuations of comparable scale with the seismic wavelength lead to destruction of the wavefronts, as suggested by the "weak fluctuations" regime; large magnitude of the random noise leads to diffusion of the wavefronts, as suggested by the "diffusion approximation" regime. This combination of parameters could be regarded as a worst-case-scenario from a theoretical standpoint.

Figures 8(a)-8(d) show data sets modeled in models similar to the one in figure 3(b), but where the random noise component

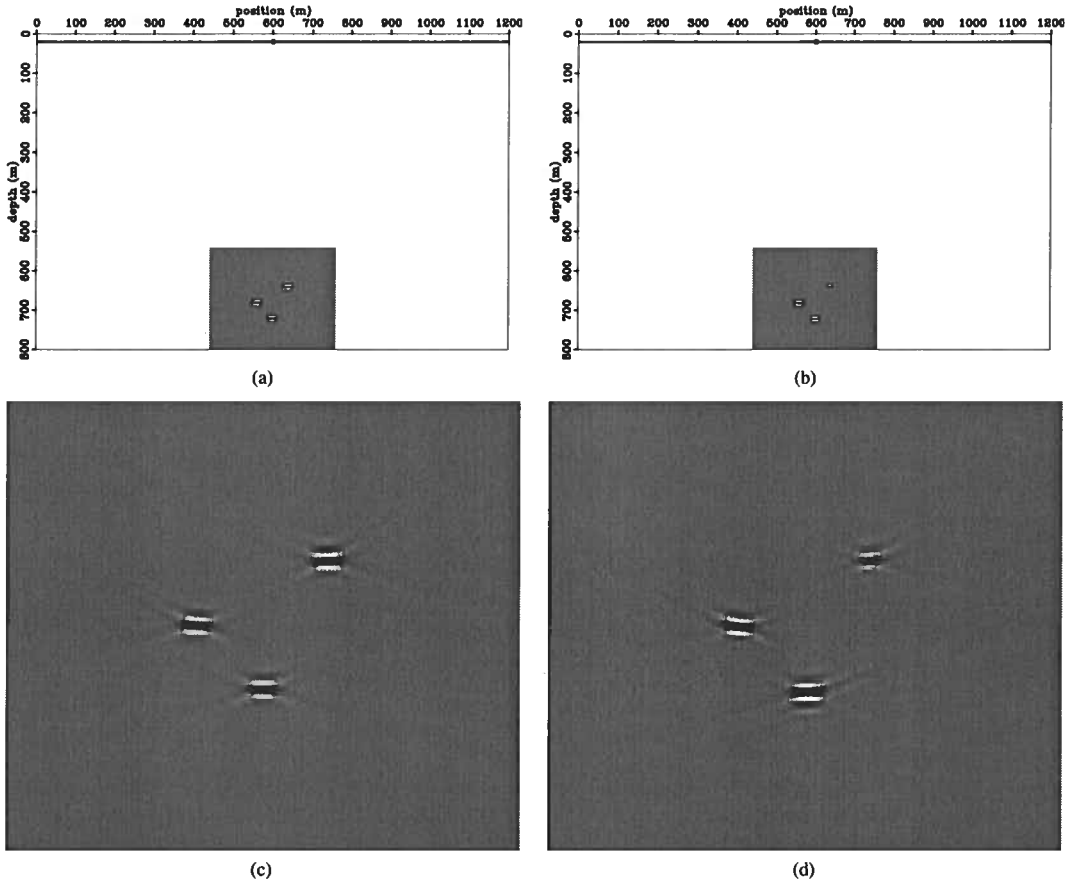

Figure 6. Images produced using the *interferometric imaging condition*. Panels (a) and (c) correspond to modeling and imaging with the smooth and known velocity model v_0, while panels (b) and (d) correspond to modeling using the random velocity model v and imaging using the smooth velocity model v_0. Panels (c) and (d) depict enlarged versions of the images shown in panels (a) and (b), respectively.

of the model is described by $\sigma = 0, 15, 30, 45\%$, respectively. As expected, the wavefronts recorded at the surface are increasingly distorted to the point where some of the later arrival are not even visible in the data.

Migration using conventional imaging condition leads to the images in figures 8(e)-8(h). As expected, the images show stronger artifacts due to the larger defocusing caused by the unknown random fluctuations in the model. However, migration using the interferometric imaging condition leads to the images in figures 8(i)-8(l). Artifacts are significantly reduced and the images are much better focused. While a complete theoretical study of the proposed functional remains to be done, the numerical results confirm its efficiency in complicated imaging regimes. This theoretical analysis falls outside the scope of this paper and remains subject for future investigation.

4 IMAGING EXAMPLES

There are many potential applications for this interferometric imaging functional. The application we concentrate on in this paper refers to imaging complex stratigraphy through a medium characterized by random variation. Accurate imaging in this situation requires velocity models that incorporate all random velocity variations. However, practical migration velocity analysis does not produce models of this level of accuracy, but approximates them with smooth, large-scale fluctuations one order of magnitude larger than that of the typical seismic wavelength. Here, we study the impact of the unknown (random) component of the velocity model on the images and whether interferometric imaging increases the image statistical stability.

For all our examples, we extrapolate wavefields using time-domain finite-differences both for modeling and for migration.

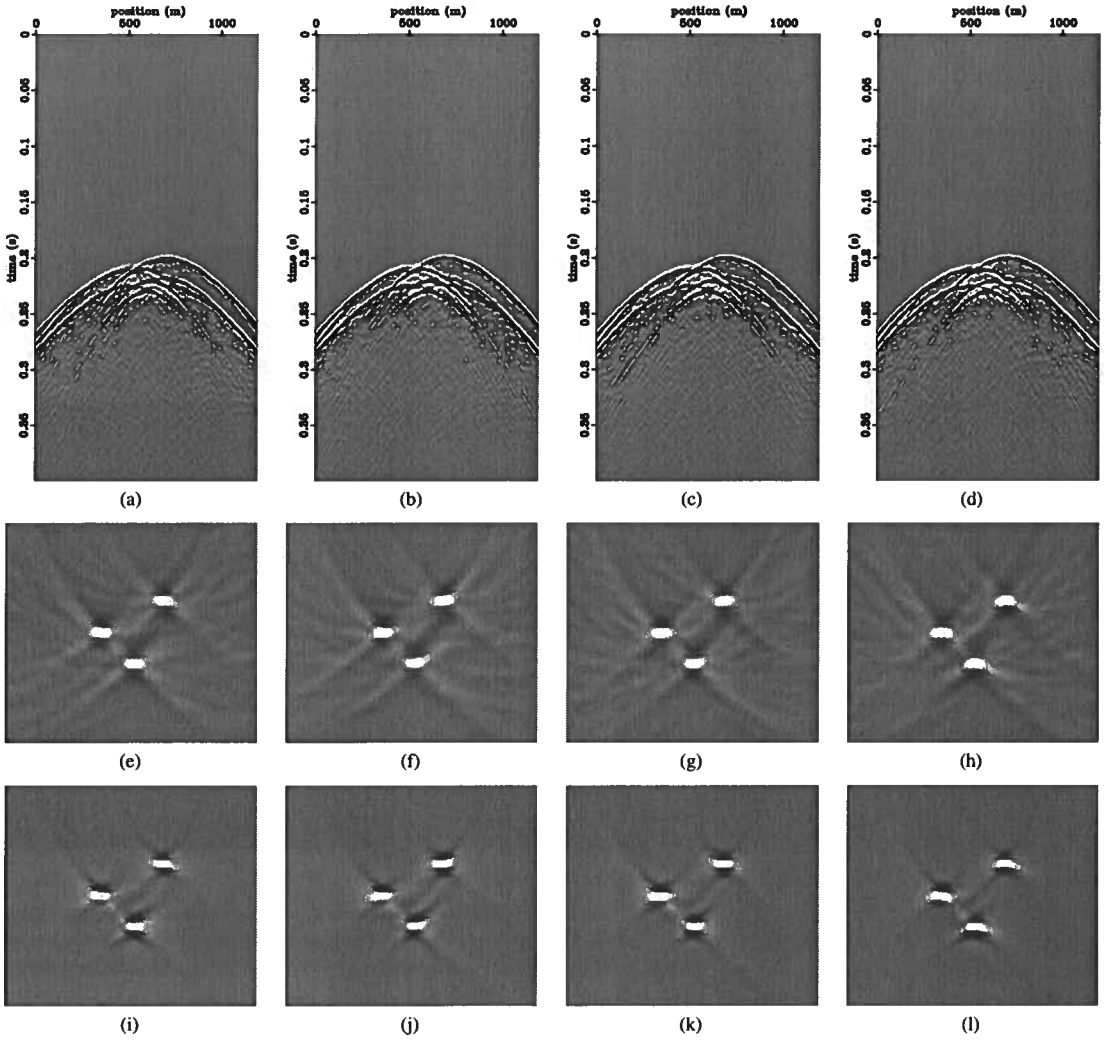

Figure 7. Illustration of statistical stability for the interferometric imaging condition in presence of random model variations. Data modeled with velocity with random variations with magnitude $\sigma = 20\%$, for different realizations of the noise model n. Images obtained by conventional imaging (e)-(h) and images obtained by interferometric imaging (i)-(l).

Thus, we simulate a reverse-time imaging procedure, although the theoretical results derived in this paper apply equally well to other wavefield reconstruction techniques, e.g. downward continuation, Kirchhoff integral methods, etc.

The parameters used in our examples, explained in Appendix A, are:

- seismic spatial wavelength $\lambda = 20$ m,
- wavelet central frequency $\omega = 150$ Hz,
- background velocity: $v_0 = 3000 + k\,z$ m/s ($k = 1s^{-1}$),
- random fluctuations parameters: $r_a = 30$, $r_c = 5$, $\alpha = 2$, and
- random velocity v constructed from the background velocity v_0.

Consider the model depicted in figures 10(a)-10(f). As in the preceding example, the left panels depict the known smooth velocity v_0, and the right panels depict the model with random variations. The imaging target is represented by the oblique lines, figure 9(b), located around $z = 700$ m, which simulate a cross-section of a complex stratigraphic model (e.g. meandering channels).

We model data with random velocity and image using the smooth model. Figures 10(a)-10(f) show wavefield snapshots in the two models for different propagation times, one before the source wavefields interact with the target reflectors and one after

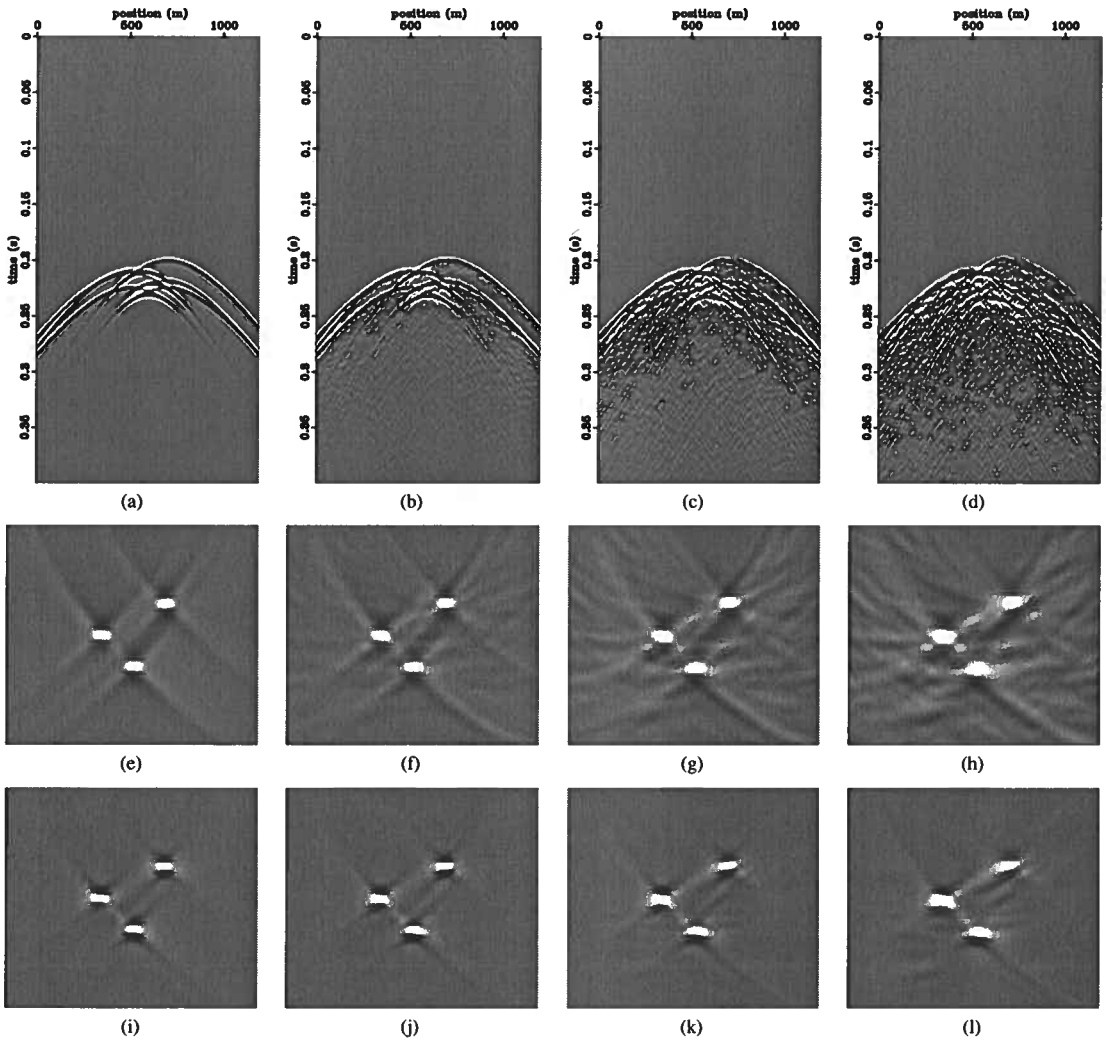

Figure 8. Illustration of interferometric imaging condition robustness in presence of random model variations. Data modeled with velocity with random variations with magnitude $\sigma = 0\%$ (a), $\sigma = 15\%$ (b), $\sigma = 30\%$ (c), and $\sigma = 45\%$ (d). Images obtained by conventional imaging (e)-(h) and images obtained by interferometric imaging (i)-(l).

this interaction. Figures 11(a) and 11(b) show the corresponding recorded data on the acquisition surface located at $z = \lambda$, where λ represents the wavelength of the source pulse.

Migration with conventional imaging condition of the data simulated in the smooth model using the smooth velocity produces the images in figures 12(a)-12(c). The targets are well imaged, although the image also shows artifacts due to truncation of the data on the acquisition surface. In contrast, migration with the conventional imaging condition of the data simulated in the random model using the smooth velocity produces the images in figures 12(b)-12(d). Those images are distorted by the random variations in the model that are not accounted for in the smooth migration velocity. The targets are hard to discern since they overlap with many truncation and defocusing artifacts caused by the inaccurate migration velocity. Finally, figures 13(a)-13(c) show the migrated images for the same situation as the one depicted in figures 12(a)-12(c), except that migration uses the interferometric imaging condition from equation (5). In this situation, since we are using the same model for modeling and migration, the interferometric imaging condition is not expected to change the image much. Interestingly, some of the truncation artifacts are attenuated, but otherwise the images are similar and the targets are easy to identify. Similarly, figures 13(b)-13(d) show the migrated images for the same situation as the one depicted in figures 12(b)-12(d), with migration using the interferometric imaging condition in

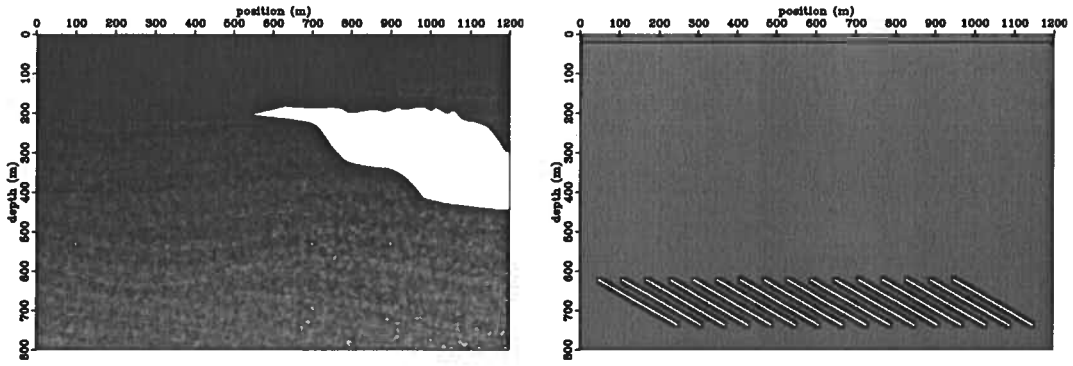

(a) (b)

Figure 9. Random velocity model (a) and imaging target located around $z = 700$ m (b).

equation (5). Many of the artifacts caused by the inaccurate velocity model are suppressed and the imaging targets are more clearly visible and easier to interpret. Furthermore, the general patterns of amplitude variation along the imaged reflectors are similar between figures 12(d) and 13(d). We note that the reflectors are not as well imaged as the ones obtained when the velocity is perfectly known. This is because the interferometric imaging condition described in this paper does not correct kinematic errors due to inaccurate velocity. It only acts on the extrapolated wavefields to reduce wavefield incoherency and add statistical stability to the imaging process. Further extensions to the interferometric imaging condition can improve focusing and enhance the images by correcting wavefields prior to imaging. However, this topic falls outside the scope of this paper and we do not elaborate on it further.

5 DISCUSSION

The interferometric imaging conditions defined by equations (5) or (7) represent extensions of conventional cross-correlation imaging conditions. Statistical stability in presence of model random variations is achieved by averaging in local windows in space and time. The computational cost of interferometric imaging condition is proportional to the number of samples in the image multiplied by the number of cross-correlation lags involved in the local space and time averaging, i.e. the size of the image times the sizes of the decoherence length and time. When the size of the decoherence windows is reduced to zero, the interferometric imaging condition becomes similar to the conventional autocorrelation imaging condition with identical properties and implementation cost.

As indicated earlier, the actual method used for wavefield reconstruction is not relevant for our discussion about this imaging condition. Any type of wavefield extrapolation can be substituted when reconstructing Green's functions in the velocity model without random variation. Thus, this form of imaging condition can be applied equally well to migration by downward continuation using space, wavenumber or mixed space-wavenumber extrapolation, reverse-time migration or Kirchhoff migration.

Areas of application for interferometric imaging include geologic areas with rapid velocity variations caused by stratigraphic features unaccounted for in typical velocity analysis or imaging through highly scattering media, e.g. basalt, anhydrite or inhomogeneous salt.

6 CONCLUSIONS

Conventional seismic imaging conditions based on wavefield cross-correlations are extended to achieve statistical stability for models with rapid, small-scale velocity variations. Random velocity variations on a scale comparable with the seismic wavelength are modeled by correlated Gaussian distributions.

Statistical stability is achieved by local averaging of cross-correlated wavefields at image locations. The proposed interferometric imaging condition is a natural extension of and reduces to the conventional cross-correlation imaging condition when the averaging window is made infinitely small.

The main characteristic of the method is that it operates on extrapolated wavefields at image positions (thus the name *interferometric imaging condition*), in contrast with alternative approaches involving migration of interferograms obtained by local data cross-correlations on the acquisition surface.

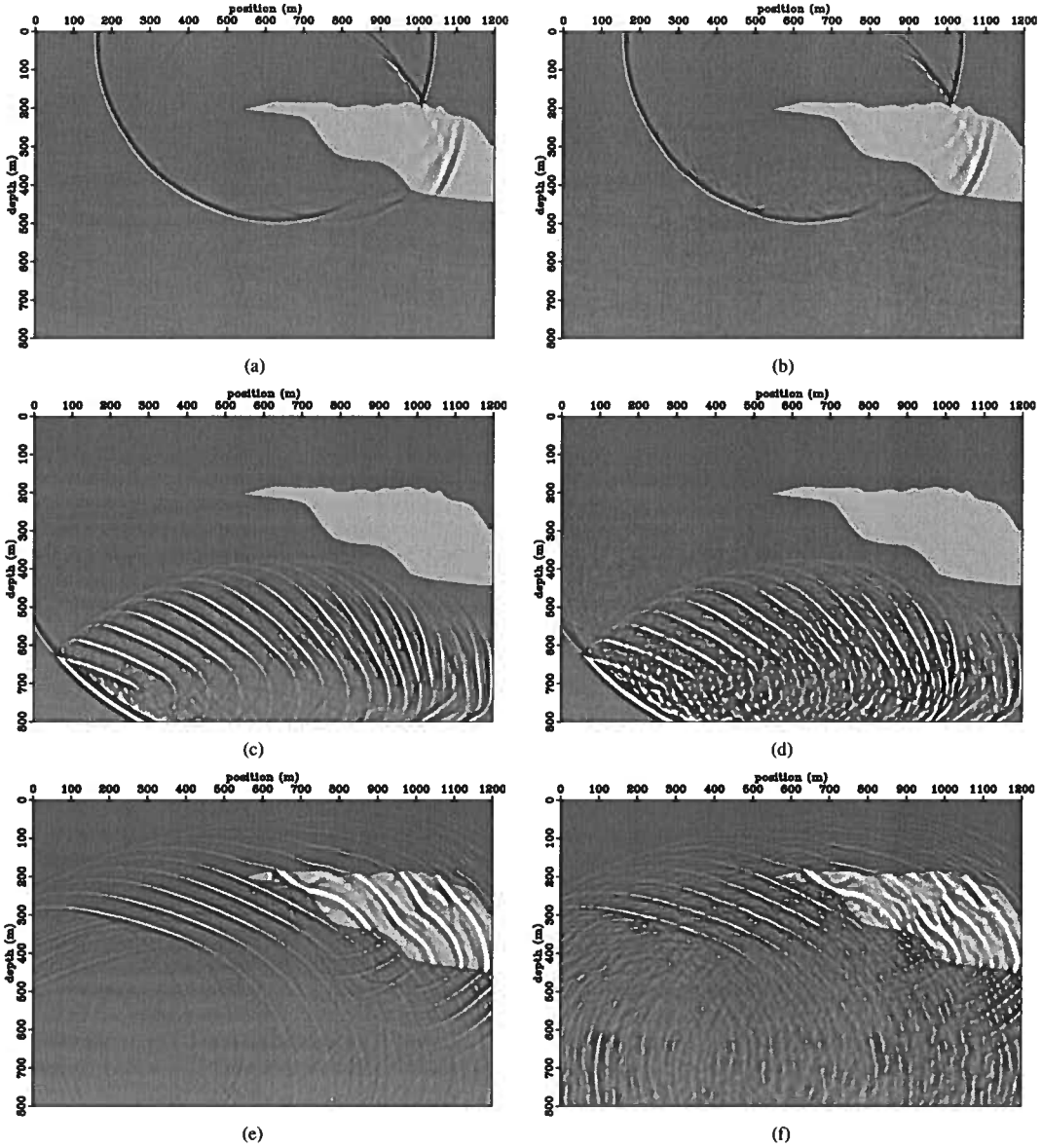

Figure 10. Wavefields simulated in the smooth background velocity v_0, panels (a) and (c) and in the random velocity v, panels (b) and (d).

REFERENCES

Artman, B., 2006, Imaging passive seismic data: Geophysics, **71**, SI117–SI187.

Artman, B., G. Alvarez, and K. Matson, 2007, Image-space surface-related multiple prediction: Geophysics, **72**, S113–S122.

Biondi, B. and W. W. Symes, 2004, Angle-domain common-image gathers for migration velocity analysis by wavefield-continuation imaging: Geophysics, **69**, 1283–1298.

Borcea, L., G. Papanicolaou, and C. Tsogka, 2005, Interferometric array imaging in clutter: Inverse Problems, **21**, 1419–1460.

———, 2006a, Adaptive interferometric imaging in clutter and optimal illumination: Inverse Problems, **22**, 1405–1436.

———, 2006b, Coherent interferometric imaging in clutter: Geopysics, **71**, SI165–SI175.

———, 2006c, Coherent interferometry in finely layered random media: SIAM Journal on Multiscale Modeling and Simulation, **5**, 62–83.

Claerbout, J. F., 1985, Imaging the Earth's interior: Blackwell Scientific Publications.

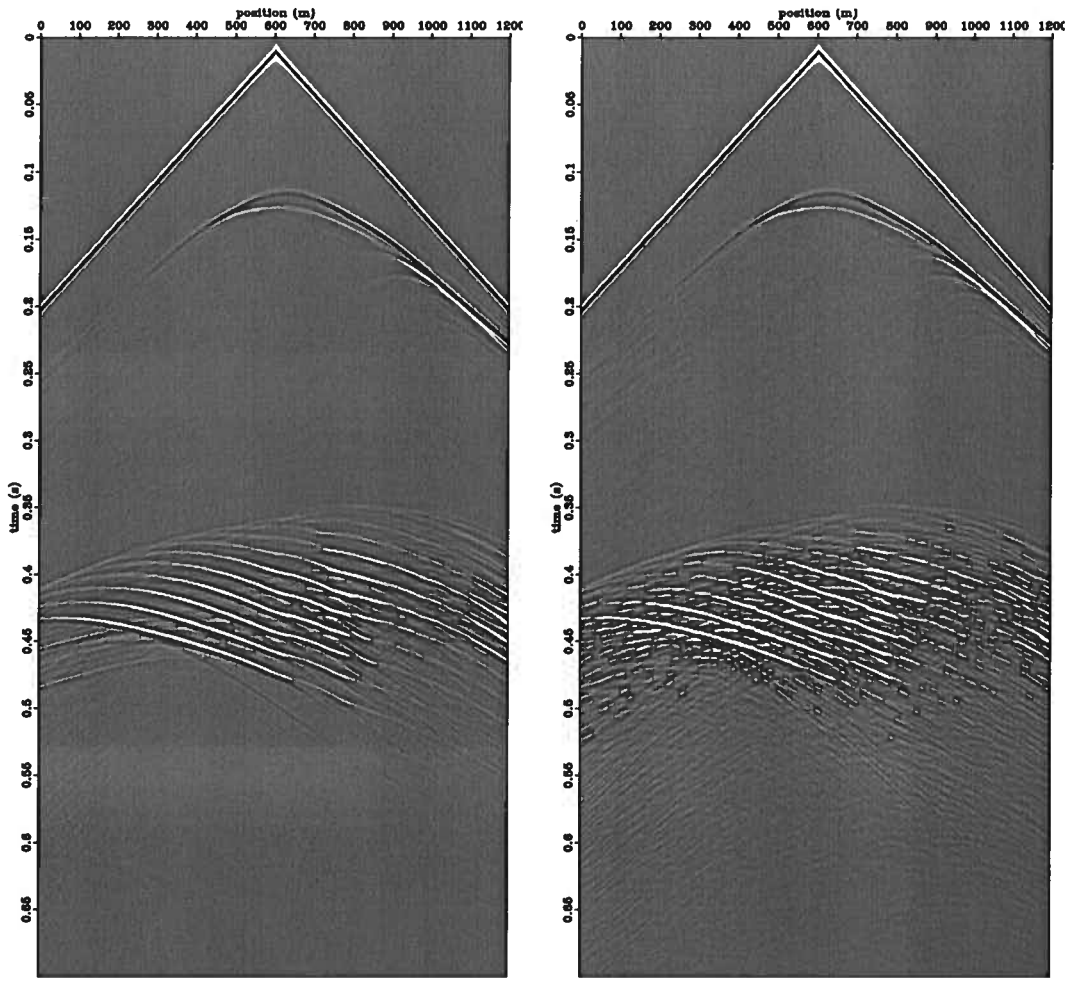

Figure 11. Data recorded for the smooth velocity model, panel (a), and for the model with random velocity variations, panel (b).

Dussaud, E., 2005, Velocity analysis in the presence of uncertainty: Ph.D. Thesis, Rice University.

Fink, M., 1999, Time-reversed acoustics: Scientific American, **281**, 91–97.

Fomel, S., 2004, Theory of 3-D angle gathers in wave-equation imaging, *in* 74th Ann. Internat. Mtg., Soc. of Expl. Geophys.

Fouque, J., J. Garnier, A. Nachbin, and K. Solna, 2005, Time reversal refocusing for point source in randomly layered media: Wave Motion, **42**, 191–288.

Kosloff, D. D. and E. Baysal, 1983, Migration with the full acoustic wave equation: Geophysics, **48**, 677–687.

Papanicolaou, G., L. Ryzhik, and K. Solna, 2004, Statistical stability in time reversal: SIAM J. Appl. Math., **64**, 1133–1155.

Pratt, R. G., 1990, Inverse theory applied to multi-source cross-hole tomography. part 2: Elastic wave-equation method: Geophys. Prosp., **38**, 311–312.

Pratt, R. G. and M. H. Worthington, 1990, Inverse theory applied to multi-source cross-hole tomography. part 1: Acoustic wave-equation method: Geophys. Prosp., **38**, 287–310.

Rickett, J. and P. Sava, 2002, Offset and angle-domain common image-point gathers for shot-profile migration: Geophysics, **67**, 883–889.

Sava, P. and B. Biondi, 2004a, Wave-equation migration velocity analysis - I: Theory: Geophysical Prospecting, **52**, 593–606.

———, 2004b, Wave-equation migration velocity analysis - II: Subsalt imaging examples: Geophysical Prospecting, **52**, 607–623.

Sava, P. and S. Fomel, 2003, Angle-domain common image gathers by wavefield continuation methods: Geophysics, **68**, 1065–1074.

———, 2005, Coordinate-independent angle-gathers for wave equation migration: 75th Ann. Internat. Mtg., Expanded Abstracts, 2052–2055, Soc. of Expl. Geophys.

———, 2006, Time-shift imaging condition in seismic migration: Geophysics, **71**, S209–S217.

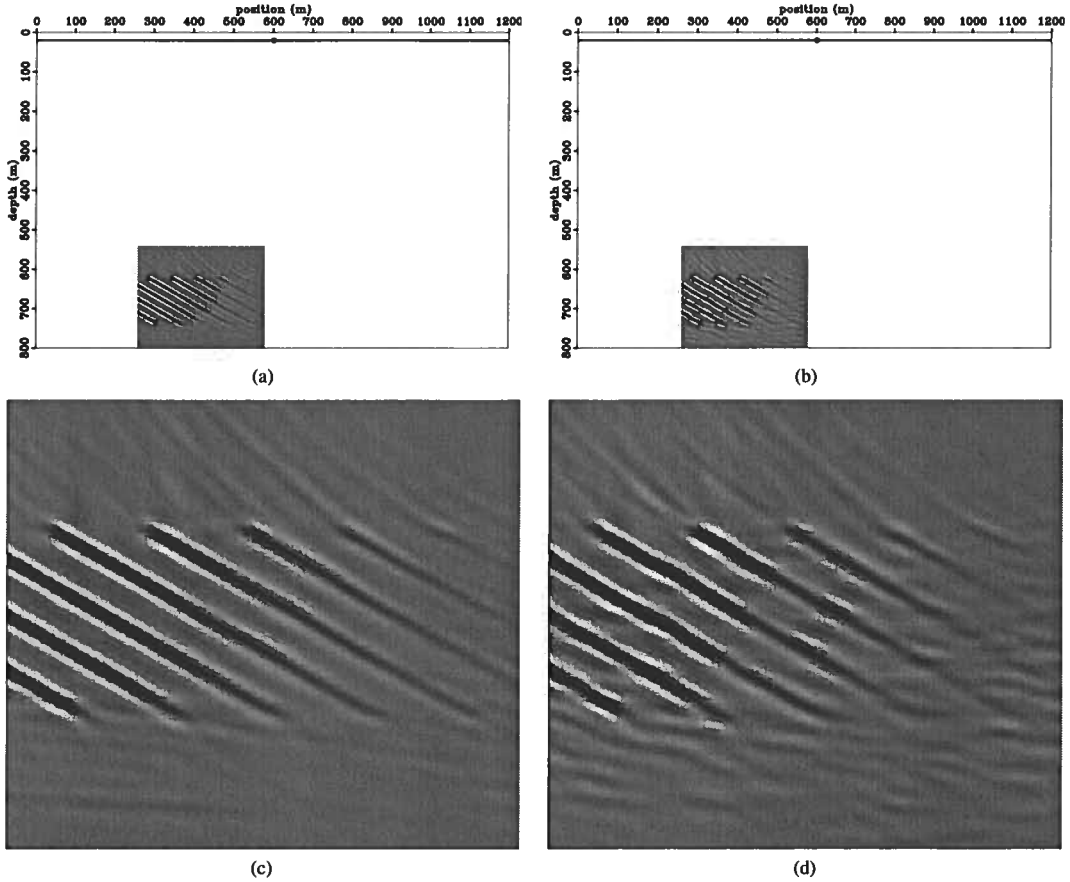

Figure 12. Images produced using the *conventional imaging condition*. Panels (a) and (c) correspond to modeling and imaging in the smooth known velocity model v_0, and panels (b) and (d) correspond to modeling using the random velocity model v and imaging using the smooth velocity model v_0. Panels (c) and (d) depict enlarged versions of the images shown in panels (a) and (b), respectively.

Shen, P., W. W. Symes, S. Morton, and H. Calandra, 2005, Differential semblance velocity analysis via shot profile migration: 2249–2253.
Stolk, C. C. and W. W. Symes, 2004, Kinematic artifacts in prestack depth migration: Geophysics, **69**, 562–575.
Tarantola, A., 1987, Inverse Problem Theory: methods for data fitting and model parameter estimation: Elsevier.
Woodward, M. J., 1992, Wave-equation tomography: Geophysics, **57**, 15–26.

7 APPENDIX A

7.1 Noise model

Consider a medium whose behavior is completely defined by the acoustic velocity, i.e. assume that the density $\rho(x,y,z) = \rho_0$ is constant and the velocity $v(x,y,z)$ fluctuates around a homogenized value $v_0(x,y,z)$ according to the relation

$$\frac{1}{v^2(x,y,z)} = \frac{1+\sigma m(x,y,z)}{v_0^2(x,y,z)}\,, \tag{A-1}$$

where the parameter m characterizes the type of random fluctuations present in the velocity model, and σ denotes their strength.

Consider the covariance orientation vectors

$$\mathbf{a} = (a_x,a_y,a_z)^\top \in \mathbb{R}^3 \tag{A-2}$$

$$\mathbf{b} = (b_x,b_y,b_z)^\top \in \mathbb{R}^3 \tag{A-3}$$

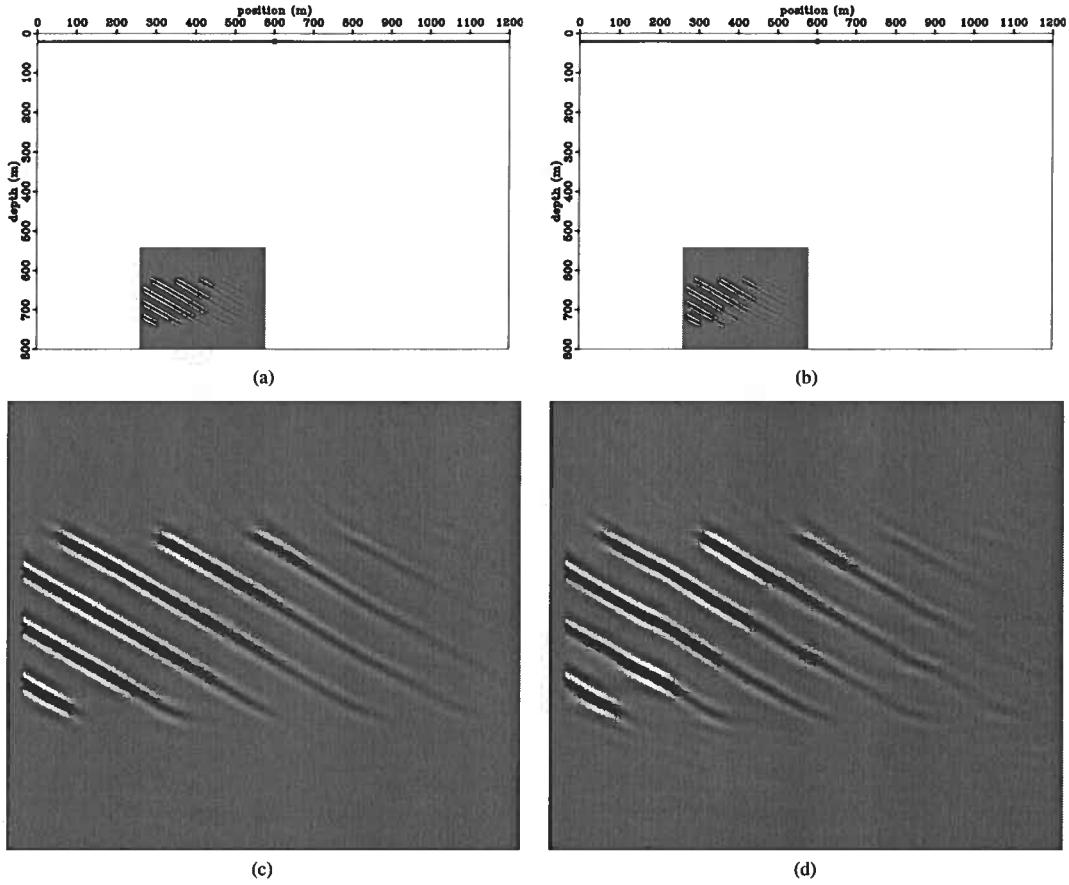

Figure 13. Images produced using the *interferometric imaging condition*. Panels (a) and (c) correspond to modeling and imaging with the smooth and known velocity model v_0, while panels (b) and (d) correspond to modeling using the random velocity model v and imaging using the smooth velocity model v_0. Panels (c) and (d) depict enlarged versions of the images shown in panels (a) and (b), respectively.

$$\mathbf{c} \quad = \quad (c_x, c_y, c_z)^{\mathsf{T}} \in \mathbb{R}^3 \tag{A-4}$$

defining a coordinate system of arbitrary orientation in space. Let $r_a, r_b, r_c > 0$ be the covariance range parameters in the directions of **a**,**b** and **c**, respectively.

We define a covariance function

$$\mathrm{cov}(x,y,z) = \exp\left[-l^{\alpha}(x,y,z)\right] , \tag{A-5}$$

where $\alpha \in [0,2]$ is a distribution shape parameter and

$$l(x,y,z) = \sqrt{\left(\frac{\mathbf{a}\cdot\mathbf{r}}{r_a}\right)^2 + \left(\frac{\mathbf{b}\cdot\mathbf{r}}{r_b}\right)^2 + \left(\frac{\mathbf{c}\cdot\mathbf{r}}{r_c}\right)^2} \tag{A-6}$$

is the distance from a point at coordinates $\mathbf{r} = (x,y,z)$ to the origin in the coordinate system defined by $\{r_a\mathbf{a}, r_b\mathbf{b}, r_c\mathbf{c}\}$.

Given the IID Gaussian noise field $n(x,y,z)$, we obtain the random noise $m(x,y,z)$ according to the relation

$$m(x,y,z) = \mathscr{F}^{-1}\left[\sqrt{\widehat{\mathrm{cov}}\left(k_x,k_y,k_z\right)}\,\hat{n}\left(k_x,k_y,k_z\right)\right] , \tag{A-7}$$

where k_x, k_y, k_z are wavenumbers associated with the spatial coordinates x, y, z, respectively. Here,

$$\widehat{\mathrm{cov}} \quad = \quad \mathscr{F}[\mathrm{cov}] \tag{A-8}$$

$$\hat{n} \quad = \quad \mathscr{F}[n] \tag{A-9}$$

are Fourier transforms of the covariance function cov and the noise n, $\mathscr{F}[\cdot]$ denotes Fourier transform, and $\mathscr{F}^{-1}[\cdot]$ denotes inverse Fourier transform. The parameter α controls the visual pattern of the field, and $\mathbf{a},\mathbf{b},\mathbf{c},r_a,r_b,r_c$ control the size and orientation of a typical random inhomogeneity.

7.2 Wave propagation and scale regimes

Acoustic waves characterized by pressure $p(x,y,z,t)$ propagate according to the second order acoustic wave-equation for constant density

$$\frac{\partial^2 p}{\partial t^2} = v^2\nabla^2 p + F_\lambda(t)\,, \tag{A-10}$$

where $F_\lambda(t)$ is a wavelet of characteristic wavelength λ.

Given the parameters l (size of inhomogeneities), λ (wavelength size), L (propagation distance) and σ (noise strength), we can define several propagation regimes:

- The *weak fluctuations regime* characterized by waves with wavelength of size comparable to that of typical inhomogeneities propagating over a medium with small fluctuations to a distance of many wavelengths. This regime is characterized by negligible back scattering, and the randomness impacts the propagating waves through forward multipathing. The relevant length parameters are related by

$$l \sim \lambda \ll L\,, \tag{A-11}$$

and the noise strength is assumed small

$$\sigma \ll 1\,. \tag{A-12}$$

- The *diffusion approximation regime* characterized by waves with wavelength much larger than that of typical inhomogeneities propagate over a medium with strong fluctuations to a distance of many wavelengths. This regime is characterized by traveling waves that are statistically stable but diffuse with time. Back propagation of such waves in a medium without random fluctuations results in loss of resolution. The relevant length parameters are related by

$$l \ll \lambda \ll L\,, \tag{A-13}$$

and the noise strength is not assumed small

$$\sigma \sim 1\,. \tag{A-14}$$

8 APPENDIX B

8.1 Time-domain implementation

The imaging functional (5) can be implemented in the frequency-domain or in the time-domain. However, the time-domain implementation is not an exact equivalent of the frequency-domain implementation, but an analog implementation, as explained in this appendix.

Consider the imaging functional (5) and restrict the analysis to the space variables $\mathbf{y}_h$:

$$\begin{aligned} I(\mathbf{y}_m) \;=\; & \int_{\omega_m} d\omega_m \int_{|\mathbf{y}_h|\le Y/2} d\mathbf{y}_h \\ & \overline{G_0(\mathbf{x}_s,\mathbf{y}_m-\mathbf{y}_h,\omega_m)} \int_{\mathbf{x}_m} d\mathbf{x}_m\, P(\mathbf{x}_m,\omega_m)\, \overline{G_0(\mathbf{x}_m,\mathbf{y}_m-\mathbf{y}_h,\omega_m)} \\ & \overline{\overline{G_0(\mathbf{x}_s,\mathbf{y}_m-\mathbf{y}_h,\omega_m)} \int_{\mathbf{x}_m} d\mathbf{x}_m\, P(\mathbf{x}_m,\omega_m)\, \overline{G_0(\mathbf{x}_m,\mathbf{y}_m+\mathbf{y}_h,\omega_m)}}\,. \end{aligned} \tag{B-1}$$

Expression (B-1) can be written equivalently as:

$$I(\mathbf{y}_m) = \int_{\omega_m} d\omega_m \int_{|\mathbf{y}_h|\le Y/2} d\mathbf{y}_h\, \overline{U_S(\mathbf{y}_m-\mathbf{y}_h,\omega_m)} U_R(\mathbf{y}_m-\mathbf{y}_h,\omega_m)\, \overline{\overline{U_S(\mathbf{y}_m+\mathbf{y}_h,\omega_m)} U_R(\mathbf{y}_m+\mathbf{y}_h,\omega_m)}\,, \tag{B-2}$$

where $U_S(,)$ represents the source wavefield and $U_R(,)$ represents the receiver wavefield reconstructed at various image locations, $\mathbf{y}_m-\mathbf{y}_h$ or $\mathbf{y}_m+\mathbf{y}_h$.

If we introduce the notation $U(,) = U_S(,)\, U_R(,)$, then we can write equation (B-2) as

$$I(\mathbf{y}_m) = \int_{\omega_m} d\omega_m \int_{|\mathbf{y}_h| \le Y/2} d\mathbf{y}_h\, U(\mathbf{y}_m - \mathbf{y}_h, \omega_m) \overline{U(\mathbf{y}_m + \mathbf{y}_h, \omega_m)}\,, \tag{B-3}$$

where the overline denotes cross-correlation of the wavefields $U(,)$ at coordinates $\mathbf{y}_m - \mathbf{y}_h$ and $\mathbf{y}_m + \mathbf{y}_h$.

The average cross-correlation of $U(\mathbf{y}_m - \mathbf{y}_h, \omega_m)$ and $U(\mathbf{y}_m + \mathbf{y}_h, \omega_m)$ can be written in the time domain as

$$I(\mathbf{y}_m, \tau) = \int_t dt \int_{|\mathbf{y}_h| \le Y/2} d\mathbf{y}_h\, U(\mathbf{y}_m - \mathbf{y}_h, t - \tau) U(\mathbf{y}_m + \mathbf{y}_h, t + \tau)\,, \tag{B-4}$$

therefore, the zero cross-correlation time lag imaging condition in the time domain can be written as

$$I(\mathbf{y}_m) = \int_t dt \int_{|\mathbf{y}_h| \le Y/2} d\mathbf{y}_h\, U(\mathbf{y}_m - \mathbf{y}_h, t) U(\mathbf{y}_m + \mathbf{y}_h, t)\,. \tag{B-5}$$

We can also achieve higher stability by local time averaging in windows of size T:

$$I(\mathbf{y}_m) = \int_t dt \int_{|\tau| \le T/2} d\tau \int_{|\mathbf{y}_h| \le Y/2} d\mathbf{y}_h\, U(\mathbf{y}_m - \mathbf{y}_h, t - \tau) U(\mathbf{y}_m + \mathbf{y}_h, t + \tau)\,. \tag{B-6}$$

Expression equation (**??**) represents an imaging functional for seismic data, since if the windows Y and T reduce to one sample in space and time, the image is formed by the auto-correlation of the extrapolated wavefields. If the the zero-lag of the cross-correlation of the source and receiver wavefields maximizes at an image point, the auto-correlation of this function also maximizes at the same location.

Stereographic imaging condition for wave-equation migration

Paul Sava

Center for Wave Phenomena, Colorado School of Mines, Golden CO 80401, USA

ABSTRACT

Single-scattering imaging consists of two steps: wavefield extrapolation, whose goal is to reconstruct source and receiver wavefields from recorded data, and an imaging, whose goal is to extract from the extrapolated wavefields the locations where reflectors occur. Conventionally, the imaging condition indicates the presence of reflectors when the propagation time of reflections in the source and receiver wavefields match. The main drawback of conventional cross-correlation imaging conditions is that they ignore the local spatial coherence of reflected events and rely purely on their propagation time. This leads to interference (cross-talk) between unrelated events that occur at the same time. Sources of cross-talk include seismic events corresponding to different seismic experiments, seismic events corresponding to different propagation paths, etc. An alternative imaging condition operates on the same extrapolated wavefields, but cross-correlation takes place in a higher-dimensional domain where seismic events have been separated based on their local space-time slope. Events are matched based on two parameters (time and local slope), thus justifying the name "stereographic" for this imaging condition. Several numeric examples demonstrate that stereographic imaging attenuates cross-talk and reduces imaging artifacts compared with conventional imaging.

Key words: imaging, wave-equation, cross-talk

1 INTRODUCTION

Seismic depth imaging in complex environments faces many challenges, mainly related to the large volume of acquired data, processing difficulties due to incomplete wavefield coverage, inaccurate knowledge of the velocity model, etc. Accurate imaging requires that all components be covered with sufficient accuracy and manageable cost, both relative to acquisition and processing.

Conventional depth migration consists of two steps: wavefield extrapolation used to reconstruct the seismic wavefields at all locations in the imaging volume from data recorded at the surface, and imaging used to extract reflectivity information from wavefields extrapolated from the sources and receivers.

Accurate imaging requires accurate implementation of both steps. Recent seismic imaging research places larger emphasis on wavefield extrapolation than on imaging. We can characterize wavefield extrapolation based on the type of numeric solution employed, e.g. differential or integral, or based on the wave-equation solved. Among the existing wavefield extrapolation techniques, we can find numeric solutions to the full acoustic wave-equation, numeric solutions to the one-way wave-equation, etc. Sustained progress in wavefield extrapolation methodology enables accurate imaging of complex geology, e.g. sub-salt.

This paper concentrates on the imaging condition assuming that wavefield extrapolation can be performed by one of the mentioned techniques with sufficient accuracy. In contrast with wavefield extrapolation, the imaging condition used in standard seismic practice has been largely unchanged for several decades. Imaging condition is often implemented as a cross-correlation or deconvolution of source and receiver wavefields extrapolated from the acquisition surface (Claerbout, 1985). The reason for this choice is that conventional cross-correlation imaging is fast and robust, producing good-quality images in fairly complex environments.

Conventional imaging condition operates in a simple way: source and receiver wavefields are probed to determine the locations in space where they match, i.e. where the traveltime of events simulated from the source and back-propagated from the receivers are equal. This is usually achieved by extracting the zero-lag of the temporal cross-correlation between

the two wavefields computed at every location in the imaging volume.

An apparent property of this imaging condition is that it completely ignores the structure of the analyzed seismic wavefields, i.e. the imaging condition does not use the local space-time coherence of the reflected wavefields. This is a striking feature, since analysis of space-time kinematic coherence is one of the most important attributes employed in geophysical analysis of seismic data. This property, however, is ignored in conventional imaging.

The consequence of this is that different seismic events present in the extrapolated wavefields interfere with one-another leading to artifacts in seismic images. This interference, also know as cross-talk, can occur between unrelated events corresponding to multiple seismic experiments, multiple branches of the seismic wavefields, multiple reflections in the subsurface, multiple seismic modes, etc. In all of those cases, it is possible to identify events that occur at the same time, although they describe different propagation paths in the subsurface. As a consequence, such unrelated events appear as real reflections due to the imaging condition.

This paper presents an extension of the conventional imaging condition designed to exploit the local space-time coherence of extrapolated wavefields. Different seismic events are matched not only function of propagation time, but also function of their local coherence attributes, e.g. local slope measured function of position and time. The consequence is that events with different propagation paths are distinguished from one-another, although their propagating time to a given point in the subsurface may be identical.

The paper is structured as follows: conventional imaging is reviewed in the first part, followed by a description of the new imaging condition and by several numeric examples simulating different imaging situations and different levels of model complexity.

2 EXTENDED IMAGING CONDITION

Under the single scattering (Born) assumption, seismic imaging consists of two components:

- The first component is *wavefield extrapolation* which represents a solution to the considered (acoustic) wave-equation with recorded data as boundary condition. We can consider many different numeric solutions to the acoustic wave-equation, which are distinguished, for example, by implementation domain (space-time, frequency-wavenumber, etc.) or type of numeric solution (differential, integral, etc.). Irrespective of numeric implementation, we reconstruct using wavefield extrapolation two wavefields, one extrapolated from the source and one extrapolated from the receiver locations. Those wavefields can be represented as four-dimensional objects function of position in space $\mathbf{x} = (x, y, z)$ and time t:

$$U_S = U_S(\mathbf{x}, t) \tag{1}$$

$$U_R = U_R(\mathbf{x}, t) , \tag{2}$$

where U_S denotes the source wavefield and U_R denotes the receiver wavefield.

- The second component is the *imaging condition* which is designed to extract from the extrapolated wavefields (U_S and U_R) the locations where reflectors occur in the subsurface.

A conventional imaging condition (Claerbout, 1985) exploits the similarities between the source and receiver wavefields. Thus, an image if formed when the zero-lag of the temporal cross-correlation between U_S and U_R maximizes. This imaging condition can be represented mathematically as

$$R(\mathbf{x}) = \int U_S(\mathbf{x}, t)\, U_R(\mathbf{x}, t)\, dt , \tag{3}$$

where R represents the image function of position $\mathbf{x}$.

This conventional imaging condition uses the match between source and receiver wavefields U_S and U_R along the time axis, independently at every location in space. Thus, the conventional imaging condition represents a special case of an extended imaging condition which uses the similarities between the source and receiver wavefields on all 4 dimensions, space $\mathbf{x}$ and time t. More generally, the source and receiver wavefields are coincident (form an image) if the local cross-correlation between the source and receiver wavefields maximizes at zero-lag on all four dimensions. An extended imaging condition (Sava and Fomel, 2005; Sava and Fomel, 2006) can be formulated mathematically as

$$R(\mathbf{x}, 2\mathbf{l}, 2\tau) = \int U_S(\mathbf{x} - \mathbf{l}, t - \tau)\, U_R(\mathbf{x} + \mathbf{l}, t + \tau)\, dt , \tag{4}$$

where $\mathbf{l}$ and τ represent the spatial and temporal cross-correlation lags between the source and receiver wavefields. Other extended imaging conditions (Rickett and Sava, 2002; Biondi and Symes, 2004) represent special cases of the extended imaging condition corresponding to horizontal $\mathbf{l} = (l_x, l_y, 0)$, or vertical $\mathbf{l} = (0, 0, l_z)$ space lags, respectively.

The four-dimensional cross-correlation maximizes at zero lag if the wavefields are correctly reconstructed, i.e. if the extrapolation operator is correct, if the velocity model used for extrapolation is accurate and if the data subject to extrapolation fulfills the single scattering assumption. In this case, we can extract the image by selecting the zero cross-correlation lag from the extended imaging condition (4), which is equivalent with the zero cross-correlation lag from the conventional imaging condition (3).

If the source and receiver wavefields are inaccurately reconstructed, either because we are using an approximate extrapolation operator (e.g. one-way extrapolator with limited angular accuracy), or because the velocity used for extrapolation is inaccurate, the four-dimensional cross-correlation does not maximize at zero lag. In this case, part of the cross-correlation energy is smeared over the space and time lags ($\mathbf{l}$ and τ), therefore extended imaging conditions can be used to evaluate imaging accuracy, for example by decomposition of reflectivity function of scattering angle at every image location (Sava and Fomel, 2003; Biondi and Symes, 2004; Sava and Fomel, 2006). Angle-domain images carry information useful for migration velocity analysis (Biondi and Sava, 1999; Sava and Biondi, 2004a; Sava and Biondi, 2004b; Shen et al., 2005),

or for amplitude analysis (Sava et al., 2001), or for attenuation of multiples (Sava and Guitton, 2005; Artman et al., 2007)

The extended and conventional imaging conditions, represented in equations (3) and (4), represent the focus of this paper. As discussed above, assuming accurate extrapolation (i.e. accurate operator and velocity model), those imaging conditions should produce accurate images at zero cross-correlation lags. However, this conclusion does not always hold true, as illustrated by the simple models depicted in figures 1(a)-1(d) and figures 2(a)-2(d).

Figures 1(a) and 1(b) represent a simple model of constant velocity with a horizontal reflector. Data in this model are simulated from sources triggered simultaneously at coordinates $x = 600, 1000, 1200$ m. Using the standard imaging procedure outlined in the preceding paragraphs, we can reconstruct the source and receiver wavefields, U_S and U_R, and apply the conventional imaging condition equation (3) to obtain the image in figure 1(c). The image shows the horizontal reflector superposed with linear artifacts of comparable strength.

Figures 2(a) and 2(b) represent another simple model of spatially variable velocity with a horizontal reflector. Data in this model are simulated from sources located at coordinate $x = 1000$ m. The negative Gaussian velocity anomaly present in the velocity model creates triplications of the source and receiver wavefields. Using the same standard imaging procedure outlined in the preceding paragraphs, we can reconstruct the source and receiver wavefields, U_S and U_R, and apply the conventional imaging condition equation (3) to obtain the image in figure 2(c). The image shows the horizontal reflector superposed with complex artifacts of comparable strength.

In both cases discussed above, the velocity model is perfectly known and the acoustic wave equation is solved with the same finite-difference operator implemented in the space-time domain. Therefore, the artifacts are caused only by properties of the conventional imaging condition used to produce the migrated image and not by inaccuracies of wavefield extrapolation or of the velocity model.

The cause of artifacts is *cross-talk* between unrelated events present in the source and receiver wavefields, which are not supposed to match, For example, cross-talk can occur between

- wavefields corresponding to multiple sources, as illustrated in the example shown in figures 1(a)-1(b),
- multiple branches of a wavefield corresponding to one source, as illustrate in the example shown in figures 2(a)-2(b),
- events that correspond to multiple reflections in the subsurface, or
- multiple wave modes of an elastic wavefield, for example between PP and PS reflections, etc.

The common cause of cross-talk between unrelated events is that the conventional imaging condition operates by matching the source and receiver wavefield only in time, with no regard for other attributes of the wavefields subject to cross-correlation. If two events occur at the same position in space and at the same time, then the conventional imaging condition produces an event in the image.

For illustration, consider the wavefields shown in figures 3(a)-3(c). Panel (a) depicts the source wavefield U_S, panel (b) depicts the receiver wavefield U_R, and panel (c) depicts the product of the source and receiver wavefields $U_S U_R$ at depth $z = 260$ m in the model depicted in figures 1(a)-1(b). According to the conventional imaging condition, the image at this depth level is formed by summing the product wavefield shown in figure 3(c) over time. Since there is no reflector, no image should be formed at this depth. However, the wavefield product is non-zero, therefore the image at this depth level is non-zero, leading to non-physical events (artifacts).

This simple analysis illustrates the origin of the cross-talk artifacts present in the image. Events in the source and receiver wavefields match in time, although they do not match in slope measured in the $\mathbf{x} - t$ space. This is because the conventional imaging condition considers only one attribute of the analyzed wavefields, time, and ignores other attributes, e.g. spatial coherence of seismic events as measured by their local slope.

3 STEREOGRAPHIC IMAGING CONDITION

One possibility to remove the artifacts caused by the cross-talk between unrelated events in the wavefield is to modify the imaging condition to use more than one attribute to match events in the source and receiver wavefields. For example, we could use the time and slope to match events in the wavefield, thus distinguishing between unrelated events that occur at the same time.

One way of decomposing the source and receiver wavefields function of local slope at every position and time is by local slant-stacks at coordinates $\mathbf{x}$ and t in the four-dimensional source and receiver wavefields. Thus, we can write the total source and receiver wavefields (U_S and U_R) as a sum of the decomposed wavefields (W_S and W_R):

$$U_S(\mathbf{x},t) = \int W_S(\mathbf{x},\mathbf{p},t)\,d\mathbf{p} \tag{5}$$

$$U_R(\mathbf{x},t) = \int W_R(\mathbf{x},\mathbf{p},t)\,d\mathbf{p}\,. \tag{6}$$

Here $\mathbf{p}$ represents the local slope function of position and time (figure 4).

Using the wavefields decomposed function of local slope, W_S and W_R, we can design a stereographic imaging condition which is mathematically represented by an expression like

$$R(\mathbf{x}) = \int\int W_S(\mathbf{x},\mathbf{p},t)\,W_R(\mathbf{x},\mathbf{p},t)\,d\mathbf{p}dt\,. \tag{7}$$

The choice of the word "stereographic" for this imaging condition is analogous to the similar choice made for the velocity estimation method called stereotomography (Billette and Lambare, 1997; Billette et al., 2003) which also employs two parameters (time and slope) to constrain traveltime seismic tomography.

For comparison with the stereographic imaging condition (7), we can reformulate the conventional imaging condition using the wavefield notation (5)-(6) as follows:

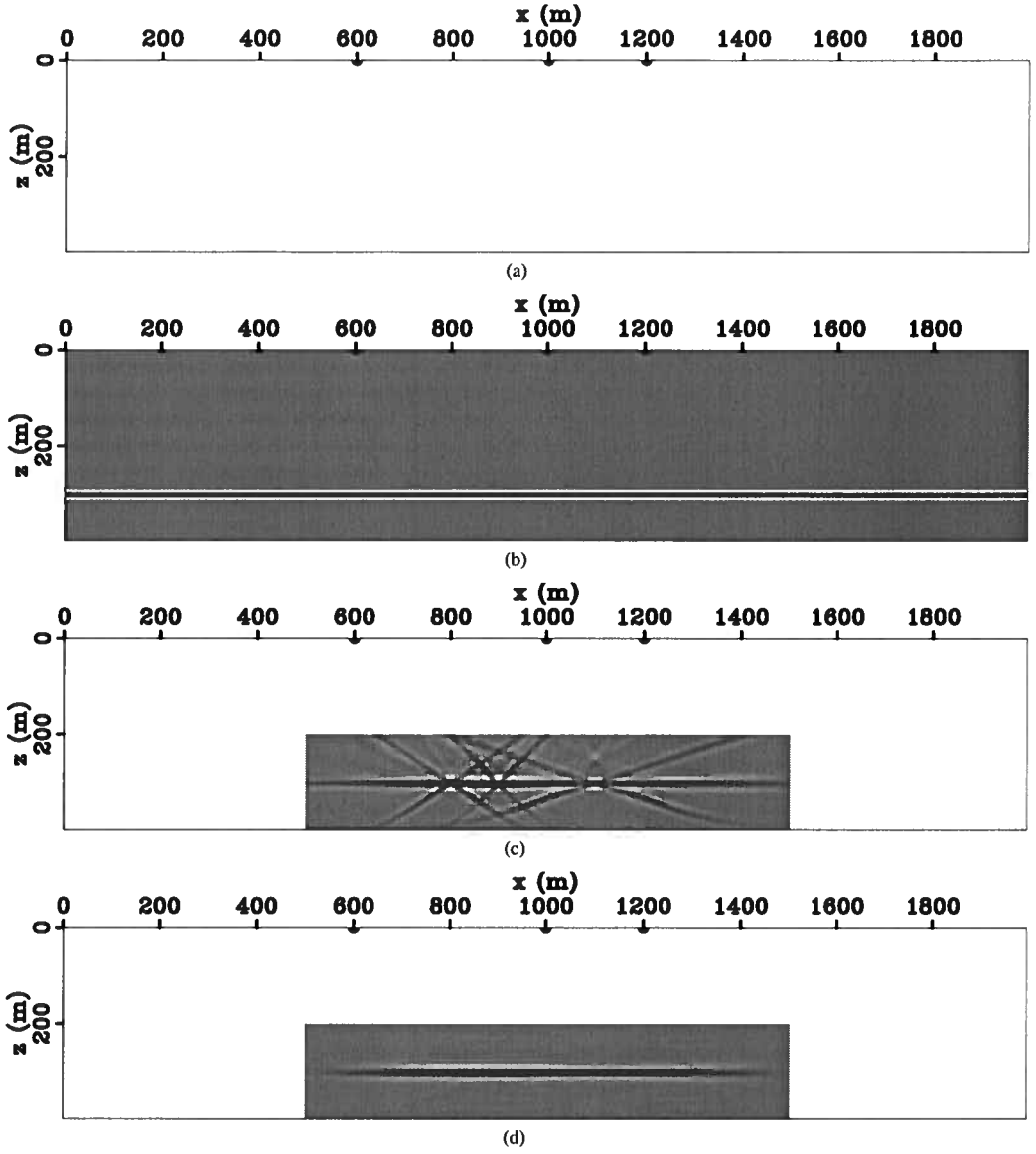

Figure 1. Velocity model (a), reflectivity model (b) and shot locations at $x = 600, 1000, 1200$ m). Image obtained using the conventional imaging condition (c) and the stereographic imaging condition (d).

$$R(\mathbf{x}) = \int \left[\int W_S(\mathbf{x},\mathbf{p},t)\, d\mathbf{p} \right] \left[\int W_R(\mathbf{x},\mathbf{p},t)\, d\mathbf{p} \right] dt \,. \qquad (8)$$

The main difference between imaging conditions (7) and (8) is that in one case we are comparing independent slope components of the wavefields separated from one-another, while in the other case we are comparing a superposition of them, thus not being able to distinguish between waves propagating in different directions. This situation is analogous to that of reflectivity analysis function of scattering angle at image locations, in contrast with reflectivity analysis function of acquisition offset at the surface. In the first case, waves propagating in different directions are separated from one-another, while in the second case all waves are superposed in the data, thus leading to imaging artifacts (Stolk and Symes, 2004).

Figure 1(d) shows the image produced by stereographic imaging of the data generated for the model depicted in figures 1(a)-1(b), and figure 2(d) shows the similar for the model depicted in figures 2(a)-2(b). Images 1(d) and 2(d) use the same source receiver wavefields as images 1(c) and 2(c), re-

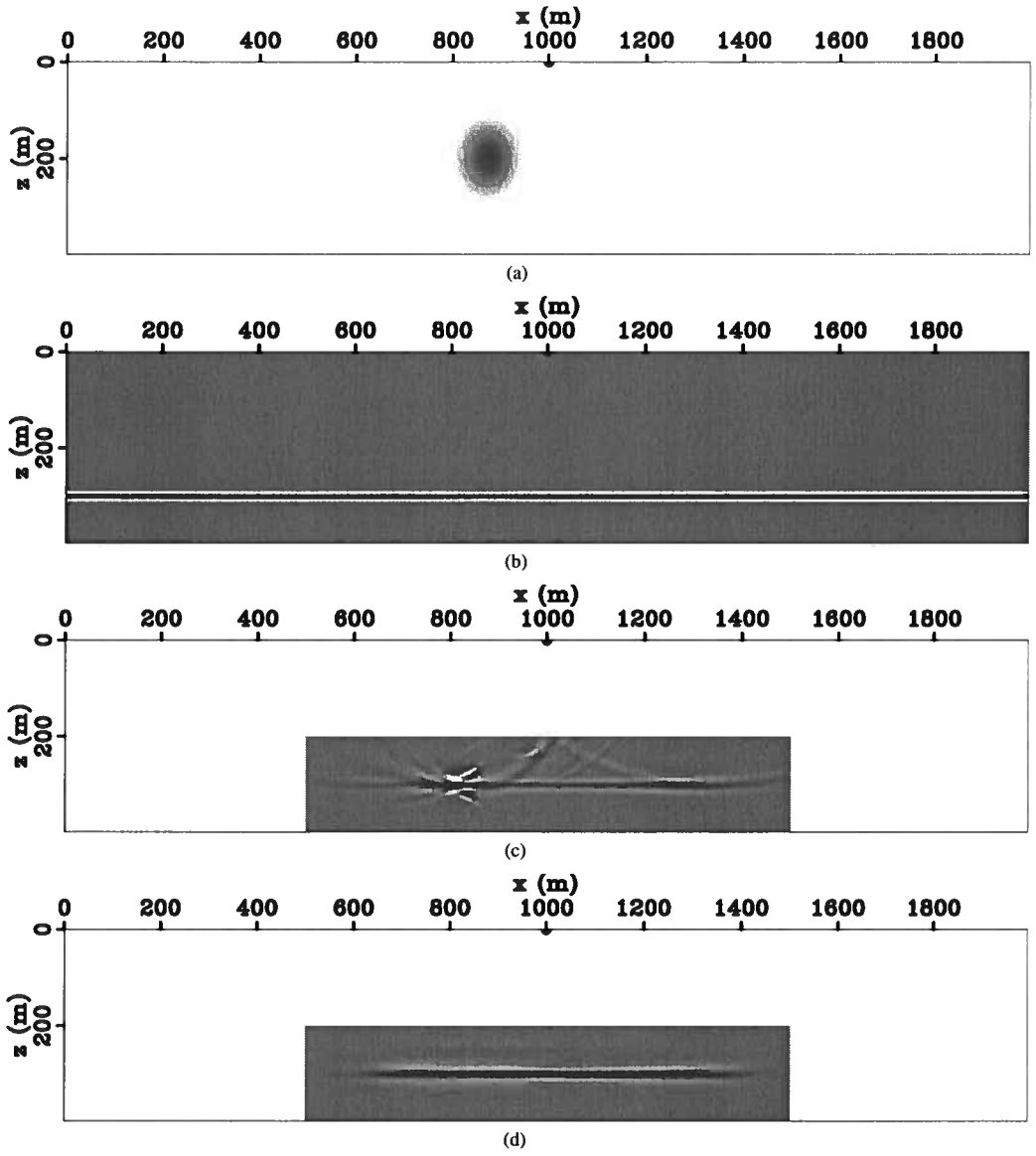

Figure 2. Velocity model (a), reflectivity model (b) and shot location at $x = 1000$ m). Image obtained using the conventional imaging condition (c) and the stereographic imaging condition (d).

spectively. In both cases, the cross-talk artifacts have been eliminated by the stereographic imaging condition.

4 EXAMPLES

The stereographic imaging condition is illustrated with two examples derived from the Sigsbee 2A dataset (Paffenholz et al., 2002).

The first model simulates a simple $v(z)$ velocity function by extracting a vertical profile from the left side of the model and extending it laterally, figure 5(d). Two shots are simulated on this model, figures 5(a)-5(b), and a third shot is synthesized by summing the two shots together, figure 5(c).

Migration with conventional imaging condition of the three shots produces the images in figures 6(a)-6(c). We can notice that the two shots independently illuminate different parts of the model, figures 6(a)-6(b), while the third composite shot illuminates both sides of the image, figure 6(c). As expected, however, the image produced by the composite shot is

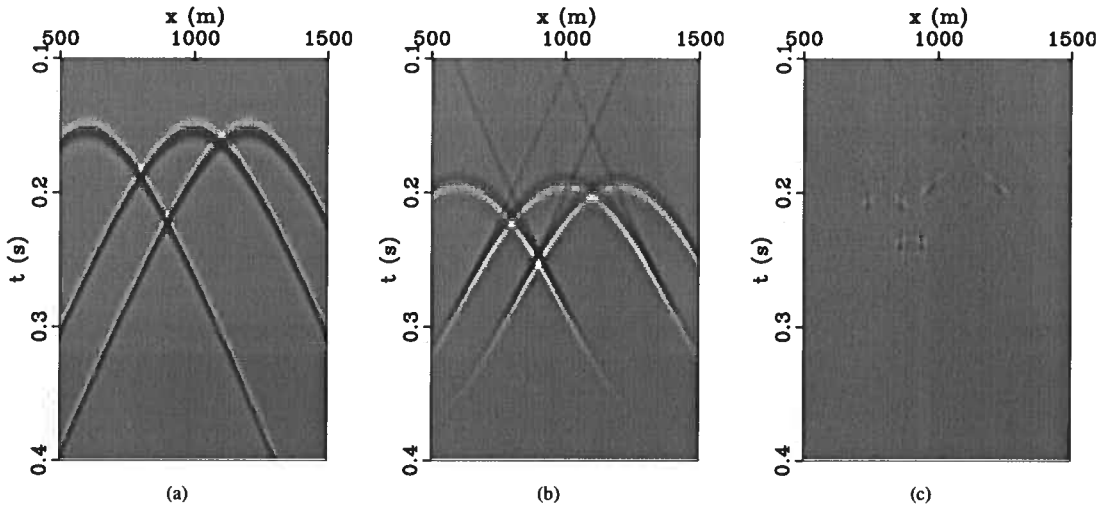

Figure 3. Wavefields at depth $z = 260$ m. Source wavefield U_S (a), receiver wavefield U_R (b) and the products of the two $U_S U_R$ (c).

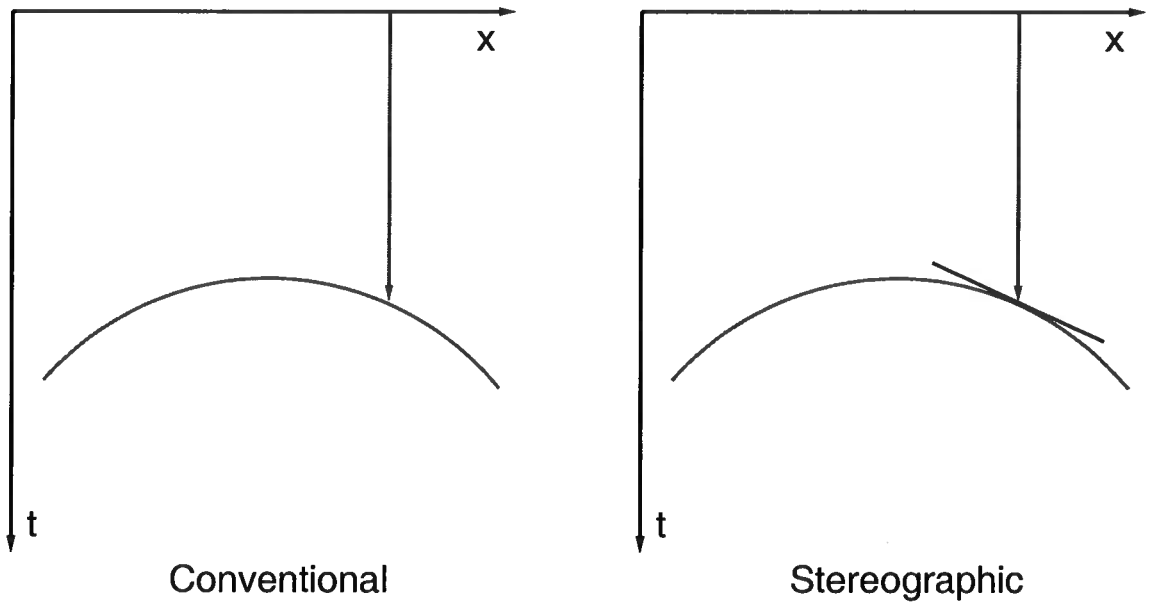

Figure 4. Comparison of parameters used for conventional imaging condition (left) and stereographic imaging condition (right).

populated with strong artifacts due to the cross-talk between the wavefields originating at the two shot locations.

Figure 6(d) shows the image obtained by imaging the composite shot, figure 5(c), using the stereographic imaging condition. The image is free of artifacts and shows reflectors extending over the entire image, as would be expected for illumination from two shots at different locations.

Figures 7(a)-8(d) show a similar example to the one in figures 5(a)-6(d) for a velocity model with lateral variation. In this case, too, the conventional imaging condition produces cross-talk artifacts, figure 8(c), but the stereographic imaging condition produces an artifact-free image, figure 8(d).

The main difference between the two examples presented in this section is that, in the second case, the stereographic imaging condition needs to take into account the local dip of the image. Wavefield spatial coherence can be measured in reflector planes, therefore an analysis similar to the one done in figures 1(a)-1(d) is not appropriate. Since we cannot know the

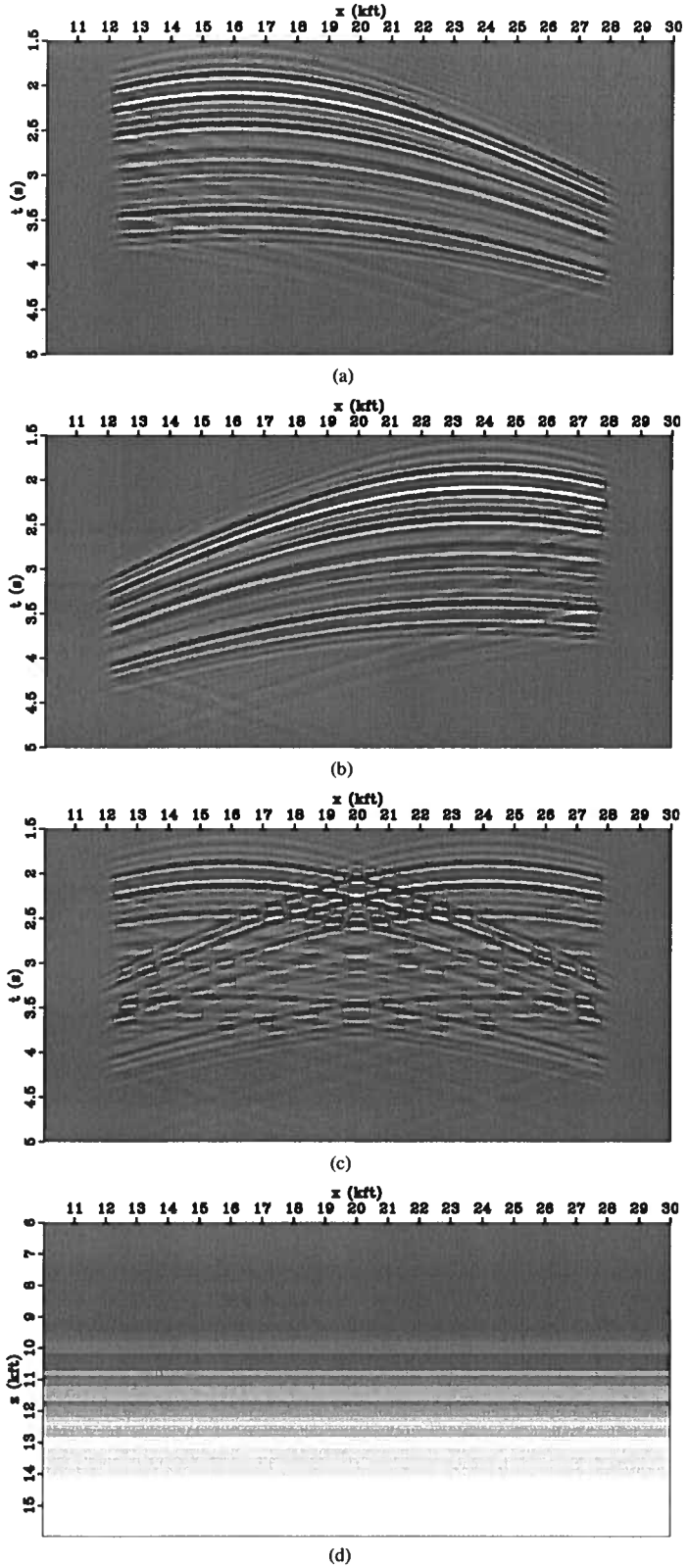

Figure 5. Data corresponding to shots at locations $x = 16$ kft (a), $x = 24$ kft (b), and the sum of data for both shots (c). $v(z)$ model extracted from the Sigsbee 2A model and shot locations at $x = 16, 24$ kft (d).

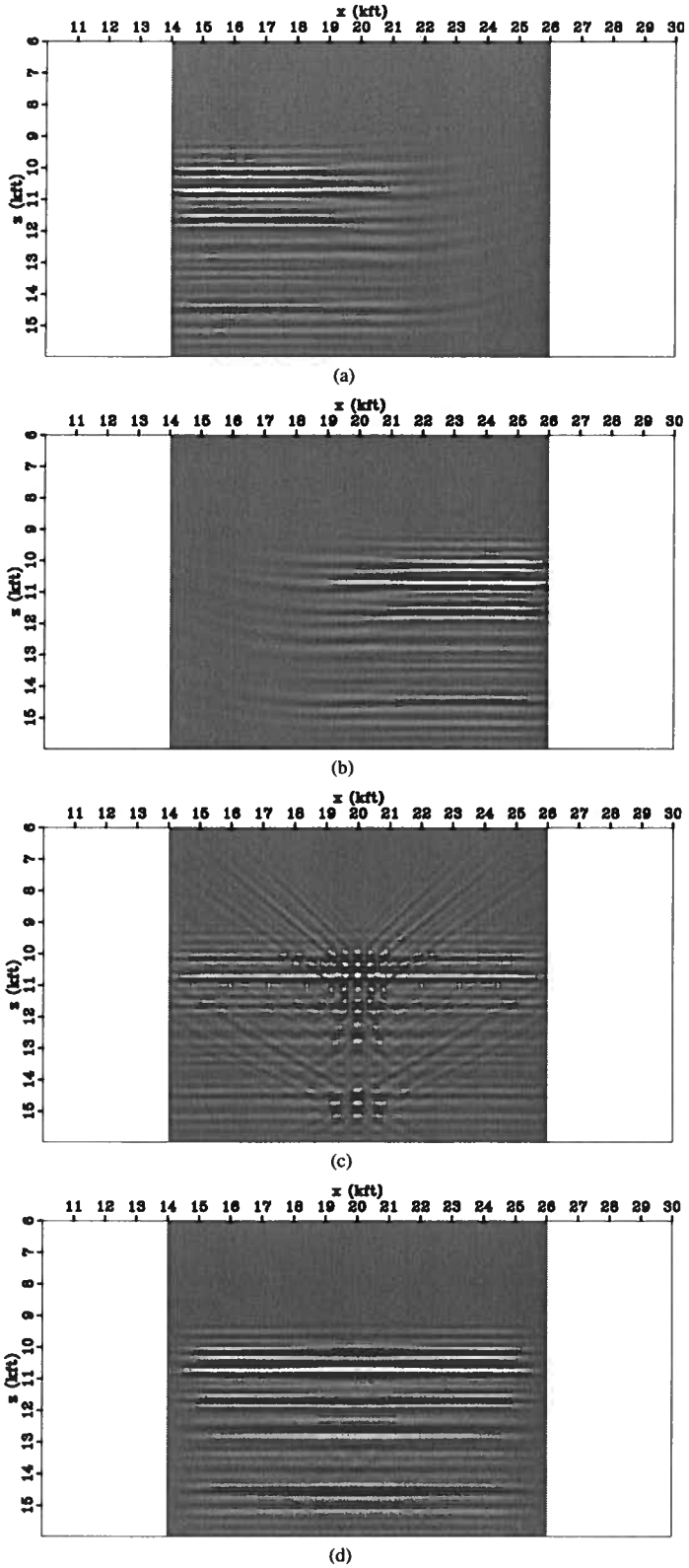

Figure 6. Image obtained by conventional imaging condition for the shots at locations $x = 16$ kft (a), $x = 24$ kft (b) and the sum of data for both shots (c). Image from the sum of the shots located at $x = 16$ kft and $x = 24$ kft obtained using the stereographic imaging condition (d).

reflector dip prior to the application of the imaging condition, we need to loop over a range of possible dip angles and decompose the wavefields locally for all possible combinations.

5 DISCUSSION

The stereographic imaging condition (7) operates by decomposing extrapolated wavefields in local components with space and time coherence at every point in the image. The decomposition method used in this paper involves local slant-stacks computed in the time-domain, prior to imaging. However, slant-stacking is not the only possible decomposition in wavefield components with spatial and temporal coherence. Other possibilities include decompositions with curvelet transforms (Candes and Demanet, 2004; Douma and de Hoop, 2004) or seislet transforms (Fomel, 2006).

The stereographic imaging condition implemented by local slant-stacks requires selection of additional parameters, e.g. size of the slant-stack window, sampling of slant-stack slopes, slant-stack window tapering etc. Those parameters are data dependent and a procedure for selection of their optimal values requires further analysis. In addition, the slant-stack used in this paper are conventional and not particularly high resolution. Future improvements of the stereographic imaging condition include high-resolution slant-stacks which may allow for even better separation of events in the extrapolated wavefields.

The stereographic imaging condition requires local spatial coherence of seismic events. This property holds only for reflection events and does not apply to, for example, diffracted events. This property of stereographic imaging can be seen as positive or negative, depending on the imaging application. In principle, this property can be exploited to tune the imaging condition to specific imaging goals, like separation of specular from non-specular energy.

The implementation cost of stereographic imaging conditions is higher than the cost of conventional imaging conditions, since data are decomposed in a larger domain which is proportional with the size of the source/receiver wavefields used for imaging.

Applications of stereographic imaging include many situations where cross-talk between un-related events hampers imaging accuracy. For example, we can consider imaging with multiple shots, imaging with data contaminated by multiples or converted waves, etc. Despite its higher cost, stereographic imaging might be advantageous when imaging multiple seismic experiments (shots), thus compensating higher computational cost by lower acquisition cost due to the smaller number of field experiments.

6 CONCLUSIONS

Conventional imaging condition based on cross-correlation of extrapolated wavefields does not take into account the local spatial coherence of reflection events. Events are matched purely based on their propagation times, which leads to cross-talk between unrelated events.

The stereographic imaging condition introduced in this paper operates on seismic wavefields that are first decomposed function of their local slope in space and time. Events are matched based on two parameters (time and local slope), which separates unrelated events and eliminates cross-talk. Higher imaging accuracy is achieved at the expense of larger computational cost.

REFERENCES

Artman, B., G. Alvarez, and K. Matson, 2007, Image-space surface-related multiple prediction: Geophysics, **72**, S113–S122.

Billette, F., S. L. Begat, P. Podvin, and G. Lambare, 2003, Practical aspects and applications of 2D sterotomography: Geophysics, **68**, 1008–1021.

Billette, F. and G. Lambare, 1997, Velocity macro model estimation by stereotomography: 59th Mtg., Session:P095.P095, Eur. Assn. Geosci. Eng.

Biondi, B. and P. Sava, 1999, Wave-equation migration velocity analysis: 69th Ann. Internat. Meeting, Expanded Abstracts, 1723–1726, Soc. of Expl. Geophys.

Biondi, B. and W. W. Symes, 2004, Angle-domain common-image gathers for migration velocity analysis by wavefield-continuation imaging: Geophysics, **69**, 1283–1298.

Candes, E. and L. Demanet, 2004, The curvelet representation of wave propagators is optimally sparse, *in* Technical Report, California Institute of Technology.

Claerbout, J. F., 1985, Imaging the Earth's interior: Blackwell Scientific Publications.

Douma, H. and M. de Hoop, 2004, Wave-character preserving prestack map migration using curvelets: 74th Ann. Internat. Mtg., 961–964, Soc. of Expl. Geophys.

Fomel, S., 2006, Towards the seislet transform, *in* 76th Ann. Internat. Mtg., Soc. of Expl. Geophys.

Paffenholz, J., B. McLain, J. Zaske, and P. Keliher, 2002, Subsalt multiple attenuation and imaging: Observations from the Sigsbee2B synthetic dataset: 72nd Ann. Internat. Mtg, 2122–2125, Soc. of Expl. Geophys.

Rickett, J. and P. Sava, 2002, Offset and angle-domain common image-point gathers for shot-profile migration: Geophysics, **67**, 883–889.

Sava, P. and B. Biondi, 2004a, Wave-equation migration velocity analysis - I: Theory: Geophysical Prospecting, **52**, 593–606.

——, 2004b, Wave-equation migration velocity analysis - II: Subsalt imaging examples: Geophysical Prospecting, **52**, 607–623.

Sava, P., B. Biondi, and S. Fomel, 2001, Amplitude-preserved common image gathers by wave-equation migration: 71st Ann. Internat. Mtg., Expanded Abstracts, 296–299, Soc. of Expl. Geophys.

Sava, P. and S. Fomel, 2003, Angle-domain common image gathers by wavefield continuation methods: Geophysics, **68**, 1065–1074.

——, 2005, Coordinate-independent angle-gathers for wave equation migration: 75th Ann. Internat. Mtg., Expanded Abstracts, 2052–2055, Soc. of Expl. Geophys.

——, 2006, Time-shift imaging condition in seismic migration: Geophysics, **71**, S209–S217.

Sava, P. and A. Guitton, 2005, Multiple attenuation in the image space: Geophysics, **70**, V10–V20.

Shen, P., W. W. Symes, S. Morton, and H. Calandra, 2005, Differen-

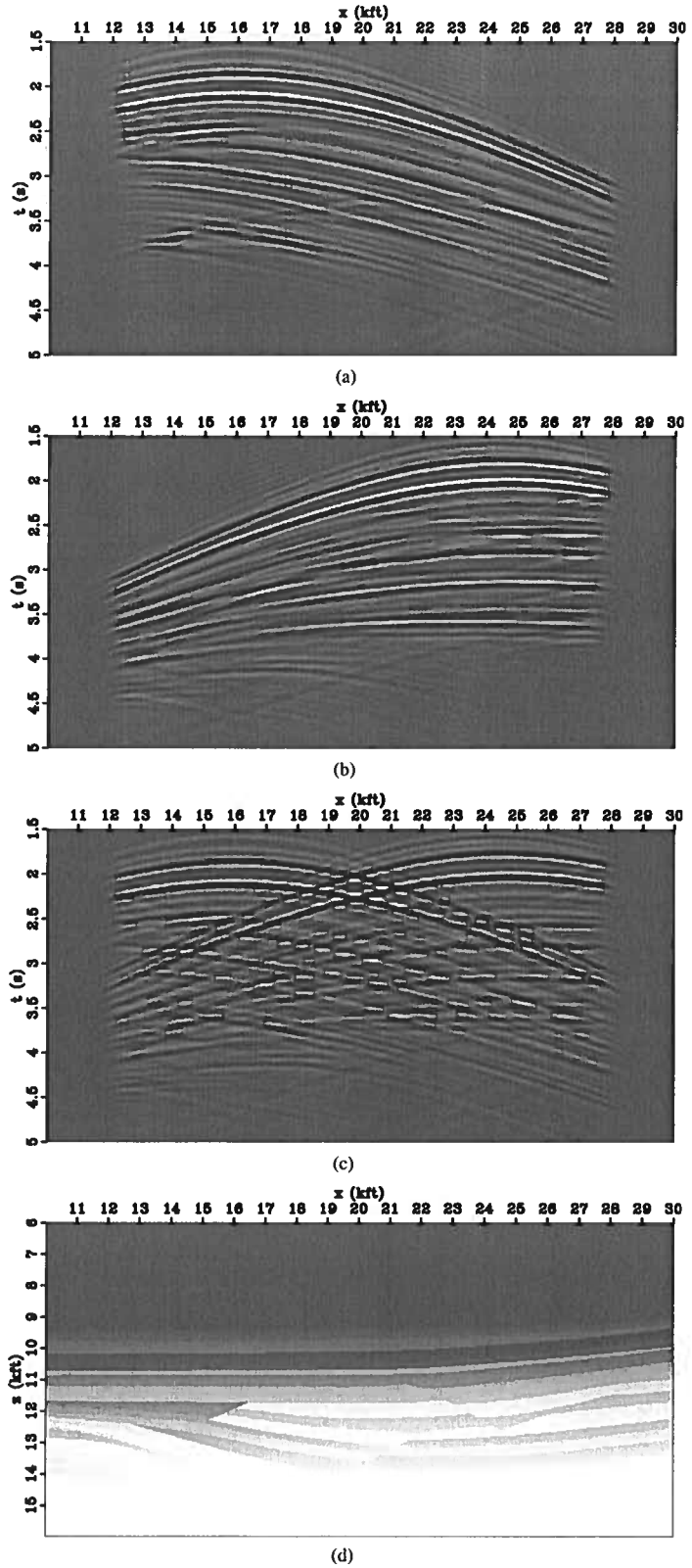

Figure 7. Data corresponding to shots at locations $x = 16$ kft (a), $x = 24$ kft (b), and the sum of data for both shots (c). $v(z)$ model extracted from the Sigsbee 2A model and shot locations at $x = 16, 24$ kft (d).

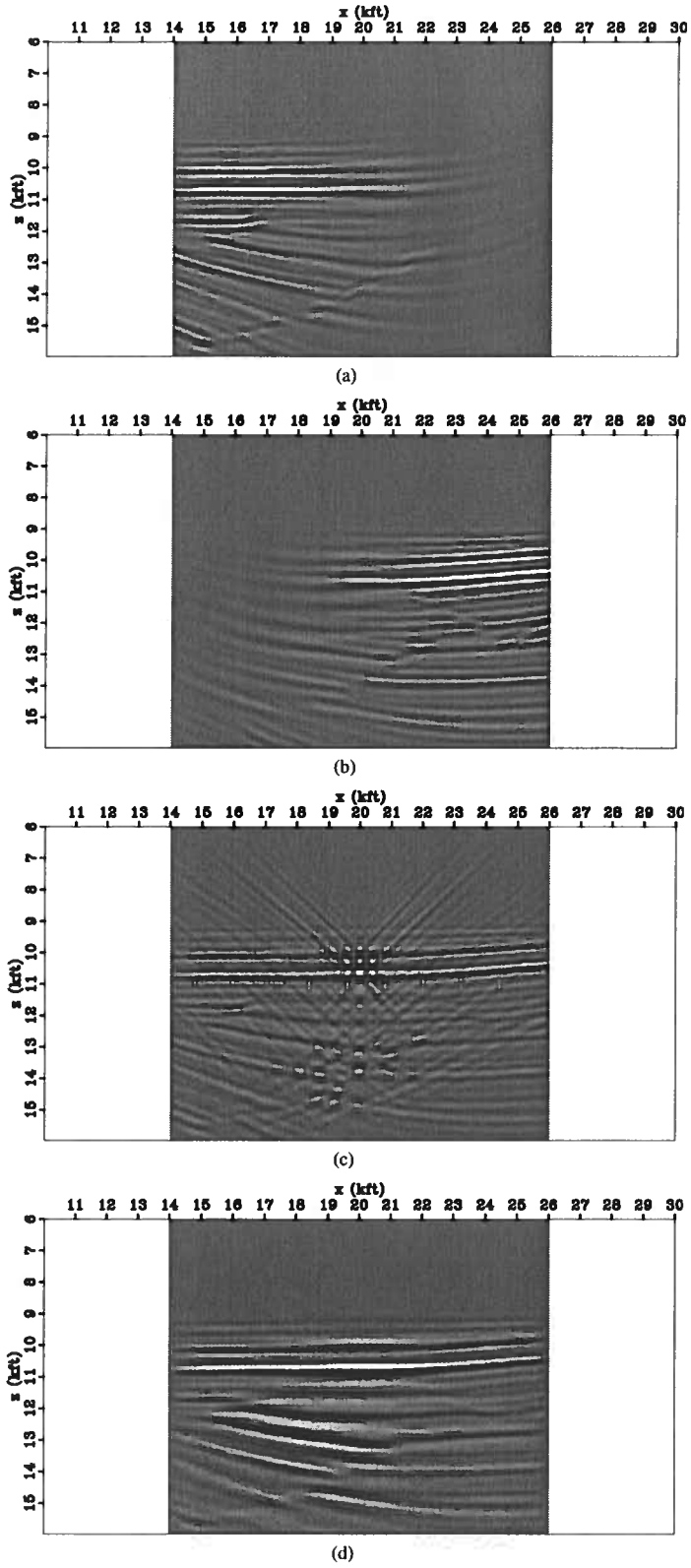

Figure 8. Image obtained by conventional imaging condition for the shots at locations $x = 16$ kft (a), $x = 24$ kft (b) and the sum of data for both shots (c). Image from the sum of the shots located at $x = 16$ kft and $x = 24$ kft obtained using the stereographic imaging condition (d).

tial semblance velocity analysis via shot profile migration: 2249–2253.

Stolk, C. C. and W. W. Symes, 2004, Kinematic artifacts in prestack depth migration: Geophysics, **69**, 562–575.

Migration velocity analysis and imaging for tilted TI media

Laxmidhar Behera[1,2] and Ilya Tsvankin[2]

[1] *National Geophysical Research Institute, Hyderabad 500007, India*

[2] *Colorado School of Mines, Department of Geophysics, Center for Wave Phenomena, Golden, CO 80401-1887, USA.*

ABSTRACT

Tilted transversely isotropic (TTI) formations cause serious imaging distortions in active tectonic areas (e.g., fold-and-thrust belts) and in subsalt exploration. Here, we introduce a methodology for P-wave prestack depth imaging in TTI media that properly accounts for the tilt of the symmetry axis as well as for spatial velocity variations.

For purposes of migration velocity analysis (MVA), the model is divided into blocks with constant values of the anisotropy parameters ϵ and δ and linearly varying symmetry-direction velocity V_{P0} controlled by the vertical (k_z) and lateral (k_x) gradients. Since estimation of tilt from P-wave data is generally unstable, the symmetry axis is kept orthogonal to the reflectors in all trial velocity models. It is also assumed that the velocity V_{P0} is either known at the top of each block or remains continuous in the vertical direction. The MVA algorithm estimates the velocity gradients k_z and k_x and the anisotropy parameters ϵ and δ in the layer-stripping mode using a generalized version of the method introduced by Sarkar and Tsvankin for factorized VTI media.

Synthetic tests for several TTI models typical in exploration (a syncline, uptilted shale layers near a salt dome, and a bending shale layer) confirm that if the symmetry-axis direction is fixed, the parameters k_z, k_x, ϵ, and δ can be resolved from reflection data. It should be emphasized that estimation of ϵ (with known V_{P0}) in TTI media requires using nonhyperbolic moveout for long offsets reaching at least twice the reflector depth. We also demonstrate that application of VTI processing algorithms to data from TTI media may lead to significant image distortions and errors in parameter estimation, even when tilt is moderate (e.g., 20-30°). The ability of our MVA algorithm to separate the anisotropy parameters from the velocity gradients can be also used in lithology discrimination and geologic interpretation of seismic data in complex areas.

Key words: transverse isotropy, velocity analysis, tilted symmetry axis, prestack migration, depth imaging, P-waves

1 INTRODUCTION

Transverse isotropy with a tilted symmetry axis (TTI) is a model of ten used to describe dipping shale layers in active tectonic areas such as the Canadian Foothills and near salt bodies (e.g., Vestrum et al., 1999; Tsvankin, 2005). TTI symmetry can also be created by systems of parallel dipping fractures embedded in otherwise isotropic rock (Dewangan and Tsvankin, 2006a, 2006b). Serious distortions caused by TTI layers in conventional (isotropic) seismic imaging are well documented in the literature (e.g., Isaac and Lawton, 1999; Vestrum et al., 1999). To properly image targets overlaid by TTI formations, migration algorithms have to be able to handle the tilt of the symmetry axis, which often varies laterally (Vestrum et al., 1999; Kumar et al., 2004). Since

the influence of tilt creates ambiguity in parameter estimation, a major problem in seismic processing for TTI media is accurate velocity analysis and model building.

P-wave kinematic signatures for tilted transverse isotropy can be described by the symmetry-direction velocity V_{P0}, Thomsen (1986) parameters ϵ and δ, and two angles responsible for the orientation of the symmetry axis. In 2D models treated here, the symmetry direction is described by the angle ν (tilt) with the vertical. Estimation of this parameter set even for a single horizontal or dipping TTI layer generally requires combining P-wave data with mode-converted PS-waves (Dewangan and Tsvankin, 2006a; 2006b). Inversion of P-wave reflection traveltimes alone for the TTI parameters is generally nonunique, unless NMO ellipses from reflectors with two different dips are available (Grechka and Tsvankin, 2000).

For TTI shale layers, the symmetry axis is usually orthogonal to the layer boundaries, which helps to reduce the number of independent parameters and make velocity analysis more stable. If the dip ϕ of the reflector is equal to the tilt ν, the dip-line P-wave normal-moveout (NMO) velocity in a homogeneous TTI layer is described by the isotropic cosine-of-dip dependence (Tsvankin, 1995; 1997):

$$V_{\rm nmo}(\phi) = \frac{V_{\rm nmo}(0)}{\cos\phi} = \frac{V_{\rm nmo}(0)}{\sqrt{1 - p^2 V_{P0}^2}}, \qquad (1)$$

where $p = \sin\phi/V_{P0}$ is the ray parameter of the zero-offset ray; note that p can be determined from time slopes on the zero-offset or stacked section. In some cases (e.g., for a bending layer), it may be possible to directly estimate the zero-dip NMO velocity given by

$$V_{\rm nmo}(0) = V_{P0}\sqrt{1+2\delta}\,. \qquad (2)$$

Then equation 1 can be used to find the vertical velocity V_{P0}, which can be substituted into equation 2 to obtain δ. Still, the parameter ϵ even in this simple model remains unconstrained by the P-wave NMO velocity from the bottom of the layer. Grechka et al. (2001) demonstrate on physical-modeling data that for relatively simple models it may be possible to estimate ϵ using the NMO velocities for reflections from deeper interfaces.

Additional information about the anisotropy parameters is provided by nonhyperbolic moveout. If the symmetry axis is orthogonal to the bottom of a TTI layer, the P-wave quartic moveout coefficient on the dip line of the reflector is proportional to the anellipticity parameter $\eta \equiv (\epsilon-\delta)/(1+2\delta)$ (Pech et al., 2003). Therefore, if δ has been found by inverting NMO velocities, nonhyperbolic moveout can be used to constrain ϵ.

These parameter-estimation issues have serious implications for migration velocity analysis (MVA) in TTI media discussed here. An efficient MVA method for TI media with a vertical symmetry axis (VTI) media was introduced by Sarkar and Tsvankin (2004) who divided the model into factorized VTI blocks. A medium is called factorized if all ratios of the stiffness elements c_{ij} are constant, which implies that the anisotropy parameters are constant as well. The reference velocity (in our case, V_{P0}) in factorized models represents an arbitrary function of the spatial coordinates (Červený, 1989). Factorized transverse isotropy with a linear velocity function $V_{P0}(x,z)$ is the simplest model that accounts for both anisotropy and heterogeneity.

Since anisotropy parameters are usually obtained with a relatively low spatial resolution, neglecting their variation within factorized blocks does not impair the quality of the velocity model. Sarkar and Tsvankin (2003, 2004, 2006) demonstrate on synthetic and field data that if the velocity V_{P0} is known at a single point in each factorized block, the MVA algorithm accurately estimates the parameters ϵ and δ, as well as the vertical (k_z) and lateral (k_x) gradients of V_{P0}. It should be emphasized that stable recovery of the parameter ϵ (or η) requires using either long-spread data (with the maximum offset-to-depth ratio of at least two) or dipping events.

Here, we extend the MVA algorithm of Sarkar and Tsvankin (2004) to tilted transversely isotropic media with the symmetry axis confined to the vertical incidence plane. The model is divided into TTI blocks with constant values of ϵ and δ and a linearly varying symmetry-direction velocity V_{P0}. These blocks, however, are not strictly factorized because the symmetry axis is kept orthogonal to reflectors, which may have arbitrary shape. As a result, the symmetry-axis direction and, therefore, the ratios of the stiffnesses c_{ij} may vary within each block. (Note that the stiffness ratios remain constant in the rotated coordinate system tied to the symmetry axis.)

We begin by introducing the methodology of Kirchhoff prestack depth migration and migration velocity analysis for TTI media. In particular, we describe the modifications needed to account for tilt in ray tracing and MVA-based parameter estimation. Then the method is tested on several typical TTI models that include dipping anisotropic layers. The velocity-analysis and imaging results are compared with those obtained by VTI algorithms to illustrate the need to account for tilt in anisotropic imaging. We also study the influence of spreadlength on the errors in the medium parameters and show that parameter ϵ cannot be constrained without including residual moveout for large (reaching at least two) offset-to-depth ratios.

2 METHODOLOGY

The migration velocity analysis algorithm of Sarkar and Tsvankin (2004), designed for piecewise-factorized VTI media, includes the same two main steps as conventional MVA in isotropic media (e.g., Liu and Bleistein, 1995). The first step is Kirchhoff depth migration with a trial velocity model that creates an image of the subsurface.

After picking reflectors on the migrated section, semblance scanning is used to evaluate the residual moveout of reflection events on image gathers (often called "common image gathers" in offset domain). The second step is a linearized parameter update designed to minimize the residual moveout after the next application of migration. The two steps are iterated until events in image gathers are sufficiently flat.

In order to estimate the vertical gradient of V_{P0}, Sarkar and Tsvankin (2004) use two reflectors located at different depths in each factorized block. Also, to constrain the parameter η (and, therefore, ϵ), the residual moveout in image gathers is described by the following nonhyperbolic equation:

$$z_M^2(h) = z_M^2(0) + r_1 h^2 + r_2 \frac{h^4}{h^2 + z_M^2(0)}, \qquad (3)$$

where z_M is the migrated depth and h is the half-offset. The parameters r_1 and r_2, which quantify the magnitude of residual moveout, are estimated by a 2D semblance scan.

To make the modeling and migration algorithms of Sarkar and Tsvankin (2004) suitable for a medium composed of TTI blocks or layers, we used ray-tracing software that can handle an arbitrary tilt of the symmetry axis (Seismic Unix codes "unif2aniso" and "sukdsyn2d"; see Alkhalifah, 1995). The model is assumed to be 2D, with the vertical incidence plane containing the symmetry axis and, therefore, the reflector normals. At the parameter-estimation step, we keep the symmetry axis orthogonal to the reflectors picked on the trial image and update the parameters ϵ and δ and the gradients k_z and k_x of the symmetry-direction velocity V_{P0} (ϵ, δ, k_z and k_x are constant within each block). As in the VTI case, the velocity V_{P0} either has to be known at one point in each factorized block or assumed to be continuous in the vertical direction. The MVA is applied in a layer-stripping mode starting at the top of the model, with at least two reflectors at different depths analyzed for each factorized block.

For TTI media with a positive vertical gradient in V_{P0}, reflections from steeply dipping interfaces often arrive at the surface as *turning* rays (Tsvankin, 1997; 2005). Hence, our algorithm properly accounts for turning-ray reflections in the computation of the traveltime field used by the migration operator.

3 TESTS ON SYNTHETIC DATA

Here, we generate synthetic seismograms and test our MVA/imaging algorithm on three common geological models that often include TTI layers: a syncline, a salt dome flanked by uptilted shale layers, and a bending shale layer. To conform to our model assumptions, the symmetry axis is kept orthogonal to the bottom of the TTI layers.

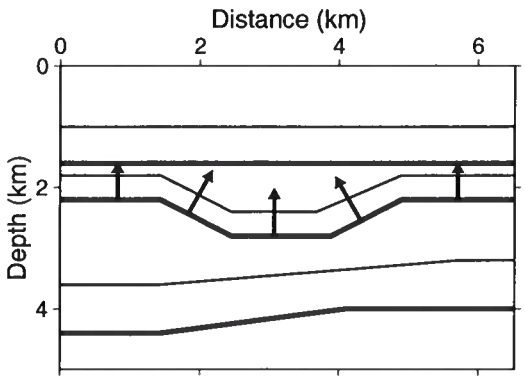

Figure 1. Model with a TTI syncline sandwiched between two isotropic layers. The bold lines mark the layer boundaries; the additional reflectors used in MVA are shown by the thinner lines. The parameters of the TTI layer are $V_{P0} = 2.3$ km/s, $k_z = 0.6\ s^{-1}$, $k_x = 0.1\ s^{-1}$, $\epsilon = 0.1$, and $\delta = -0.1$ ($\eta = 0.25$). The symmetry axis (marked by the arrows) is orthogonal to the layer's bottom; the dips are 30°. The top layer has $V_{P0} = 1.5$ km/s, $k_z = 1.0\ s^{-1}$, $k_x = \epsilon = \delta = 0$; for the bottom layer, $V_{P0} = 2.7$ km/s, $k_z = 0.3\ s^{-1}$, and $k_x = \epsilon = \delta = 0$. The velocity V_{P0} is specified at the top of each layer at the 1 km coordinate.

3.1 Syncline model

The first model includes a TTI syncline with dips of 30° sandwiched between two isotropic media (Figure 1). The isotropic layers are vertically heterogeneous but have no lateral velocity gradient, while the TTI layer is both vertically and laterally heterogeneous. As required by the MVA algorithm, each layer contains two reflecting interfaces, with every second reflector representing the boundary between layers. Synthetic data generated by anisotropic ray tracing (see above) consist of 260 shot gathers with shot and receiver intervals of 25 m and 40 traces per gather.

The section obtained after anisotropic prestack depth migration using the ray-tracing algorithm mentioned above with the true model parameters for all layers is shown in Figure 2a. The influence of the tilt of the symmetry axis in the TTI layer is taken into account during the computation of the traveltime table by anisotropic ray tracing. Then the same traveltime table is used for Kirchhoff prestack depth migration. As expected, all reflectors are well focused and accurately positioned, and all image gathers in Figure 2b are perfectly flat.

3.1.1 TTI velocity analysis and migration

We applied our MVA algorithm for TTI media to 10 image gathers located at horizontal coordinates ranging from 1.5 km to 5.0 km (Figure 3). Since it is essential to

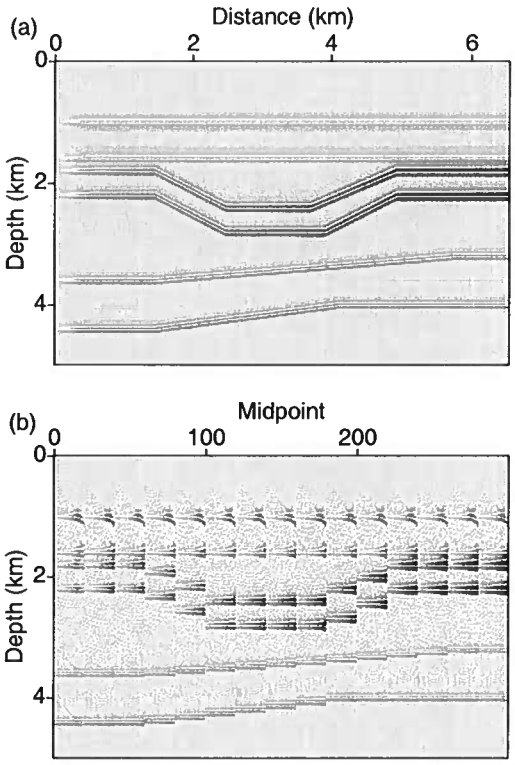

Figure 2. (a) True image of the model from Figure 1 obtained by anisotropic prestack depth migration with the correct medium parameters. (b) The corresponding image gathers in the offset domain at 0.4 km intervals (displayed with the corresponding midpoints along the x-axis) for each reflector.

use nonhyperbolic moveout in parameter estimation for TTI media (see the introduction), the maximum offset-to-depth ratio for the bottom of the TTI layer is close to two. The medium parameters are estimated in the layer-stripping fashion starting at the surface.

The initial velocity model used in the first iteration of MVA is homogeneous and isotropic. For the first (top) layer, the velocity V_{P0} is assumed to be known at a single surface location [$V_{P0}(x = 1$ km, $z = 0) = 1500$ m/s]. This assumption is needed only if this layer is treated as anisotropic. We also assign the correct value to the symmetry-direction velocity V_{P0} at the top of the second and third layers. As discussed above, the symmetry axis in the second layer is kept orthogonal to the layer's bottom.

The inverted parameters are close to the true values in all three layers, and the migrated image (Figure 3a) is practically indistinguishable from the benchmark section in Figure 2. According to the analysis in the introduction, the NMO velocities from the horizontal and dipping reflectors in the TTI layer constrain the parameters V_{P0} and δ (see equations 1 and 2). Although this result is obtained for a homogeneous TTI medium, it should remain valid for our heterogeneous model because we estimate the velocity gradients by using image gathers at different depths and lateral positions. Also, we make the parameter estimation more stable by assuming that the velocity V_{P0} is known at the top of the layer. To resolve ϵ, it is necessary to use nonhyperbolic moveout on long spreads, which is controlled by the anellipticity parameter $\eta \approx \epsilon - \delta$. Evidently, the relatively large offset-to-depth ratios (up to two) we used in MVA are sufficient to provide a tight constraint on ϵ. The influence of spreadlength on the stability of parameter estimation is analyzed in more detail below.

We also computed the error bars for each parameter by setting the standard deviation in the picked migrated depths on selected image gathers to $\pm$ 5 m. The picking errors are then substituted in the inversion operator to find the corresponding standard deviations of the model parameters (Sarkar and Tsvankin, 2004). This procedure yields relatively small errors of up to ± 0.02 in all estimated velocity gradients and anisotropy parameters.

The improvements achieved by the MVA algorithm in reducing the residual moveout in image gathers is illustrated in Figures 3b-d. After six iterations of MVA using the first two reflectors, image gathers of events in the first layer are flat, but there is substantial residual moveout in the two deeper layers (Figure 3c). Upon completion of the parameter estimation for all three layers, image gathers are flat throughout the model (Figure 3d).

3.1.2 Sensitivity to spreadlength

To quantify the dependence of errors in the medium parameters on the maximum offset-to-depth ratio, we repeated MVA for the TTI syncline model with a range of spreadlengths. As before, the errors were computed by the algorithm of Sarkar and Tsvankin (2004) for a ± 5 m picking error in migrated depths. The increase in the offset-to-depth ratio (computed for the midpoint of the dipping reflectors) makes estimation of all parameters much more stable (Figure 4). The parameters k_z, k_x, and δ are constrained by NMO velocity, which can be measured on conventional-length spreads close to the reflector depth. For that reason, the error curves for k_z, k_x, and δ show a similar trend and flatten out for offset-to-depth ratios between unity and 1.5.

In contrast, the error in the parameter ϵ continues to decrease until the maximum offset reaches two times the reflector depth, which is in good agreement with the analytic results discussed above. Indeed, ϵ in our model is determined from the quartic moveout coefficient (i.e., from nonhyperbolic moveout), which is poorly resolved if the maximum offset-to-depth ratio is smaller than two (Tsvankin, 2005). Thus, the results in Figure 4 suggest that for stable estimation of all relevant parameters of

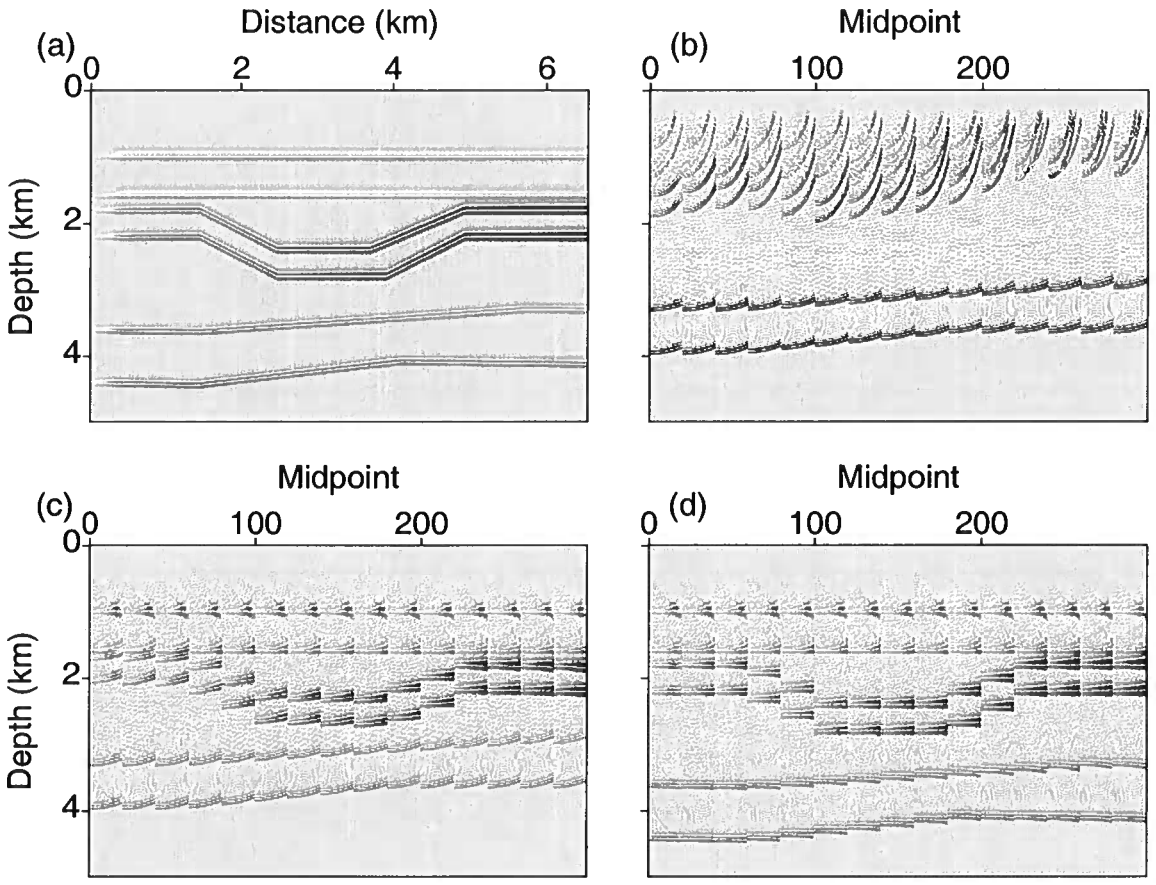

Figure 3. (a) Final image of the syncline model obtained after MVA and prestack depth migration for TTI media. The estimated parameters of the first (subsurface) layer are $k_z = 0.99\ s^{-1}$ and $k_x = \epsilon = \delta = 0$. For the second layer, $k_z = 0.59\ s^{-1}$, $k_x = 0.09\ s^{-1}$, $\epsilon = 0.09$, and $\delta = -0.11$. For the third layer, $k_z = 0.29\ s^{-1}$ and $k_x = \epsilon = \delta = 0$. The error for each parameter varies from ± 0.01 to ± 0.02, if the depth picking error is assumed to be ± 5 m. Image gathers obtained (b) with the initial model parameters before MVA; (c) after six iterations of MVA for the first two layers; (d) after MVA for all three layers.

TTI media, it is highly desirable to employ offsets twice as large (or more) as the reflector depth.

3.1.3 Influence of noise

To assess the stability of our MVA and migration algorithms, we added random uncorrelated Gaussian noise to the synthetic data set for the model from Figure 1. The signal-to-noise ratio (S/N), measured as the ratio of the peak signal amplitude to the root-mean-square (rms) amplitude of the background noise, is close to two; the frequency bands of the signal and noise are identical (Figure 5a). The semblance maxima for most events in the presence of noise become less focused (Figure 5b), which enhances the tradeoff between the moveout parameters r_1 and r_2 in equation 3 (Tsvankin, 2005). However, since any pair of values (r_1, r_2) within the innermost semblance contour provides nearly the same variance of migrated depths, this tradeoff does not hamper the convergence of the MVA algorithm.

On the whole, despite the low S/N ratio, random noise does not significantly distort the MVA results (only the error in ϵ is non-negligible). Although the imaged reflectors are not as well focused as those on the noise-free section, they are clearly visible and correctly positioned (Figure 5c).

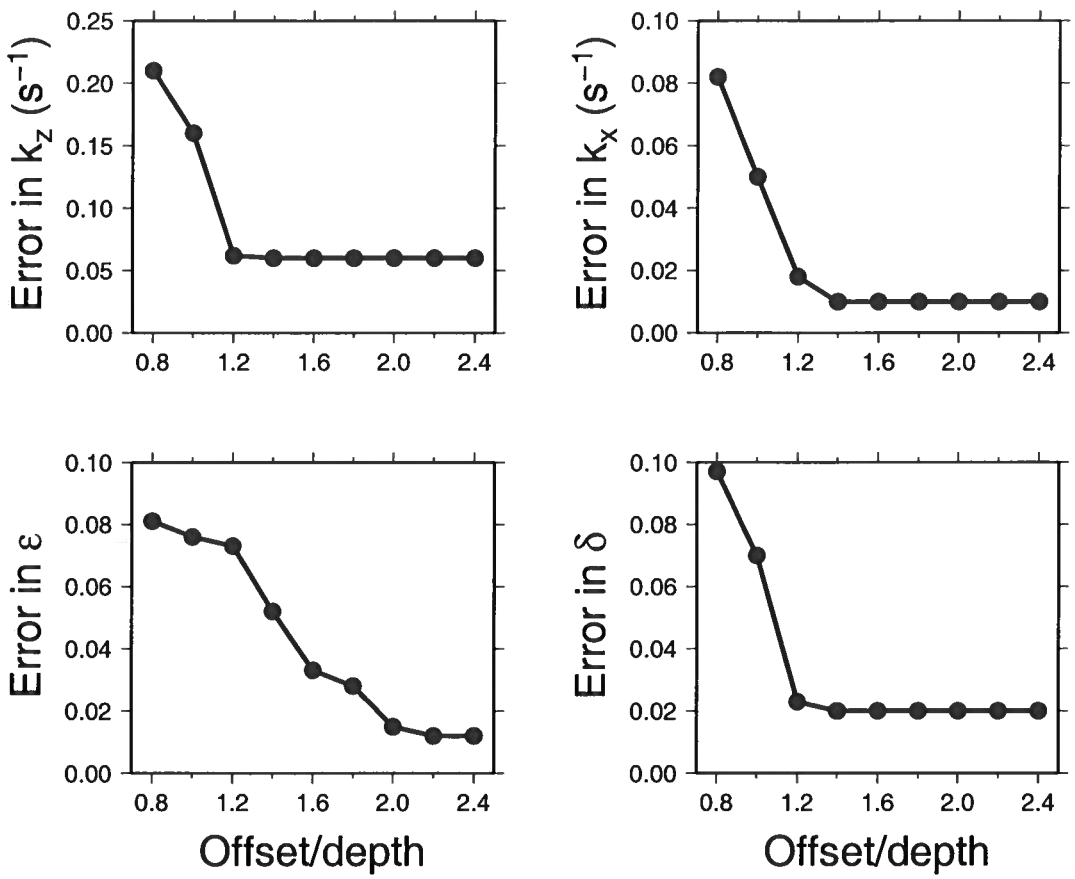

Figure 4. Influence of the maximum offset-to-depth ratio on the absolute errors in the parameters k_z, k_x, ϵ, and δ. The errors are estimated from the MVA results for the left part of the syncline model in Figure 1.

3.1.4 Errors of VTI-based processing

Since most anisotropic imaging algorithms used in industry are designed for VTI media, it is important to evaluate the influence of the tilted symmetry axis on the quality of the migrated image. The section in Figure 6 is obtained by setting the tilt in the syncline to zero, which makes the second layer VTI. Although the velocity model includes the correct values of ϵ and δ, the dipping reflectors in the TTI layer are strongly misfocused and somewhat shifted spatially. The image gathers for these dipping interfaces exhibit significant residual moveout (Figure 6b), which indicates that the velocity field is highly inaccurate.

To emulate a complete VTI processing sequence applied to this model, we repeated migration velocity analysis, but without allowance for a tilted symmetry axis (i.e., the MVA code treated the second layer as VTI). After several iterations of parameter updating, the image gathers are largely flattened, and the image quality is only marginally inferior to that achieved for the true model (Figure 7). The parameters k_z, ϵ, and δ of the second layer, however, are distorted. These errors are introduced by the MVA algorithm, which has to flatten image gathers in the TTI layer with the incorrect tilt of the symmetry axis. It is interesting to note that despite the distortions in ϵ and δ, the best-fit VTI model has an accurate value of the anellipticity parameter η.

The ability of the VTI-based algorithm to compensate for the influence of tilt decreases for a larger relative thickness of the TTI syncline (Figure 8). Because of the more significant contribution of the interval traveltime in the TTI layer, the dipping reflectors in Figure 8 are misfocused and shifted in the vertical direction. Such artifacts generated by VTI imaging can serve as an indication that the medium immediately above the distorted reflectors may have a tilted symmetry axis. The quality of the image produced by VTI processing also decreases for strongly anisotropic TTI models and larger magnitudes of the parameters ϵ, δ, and η.

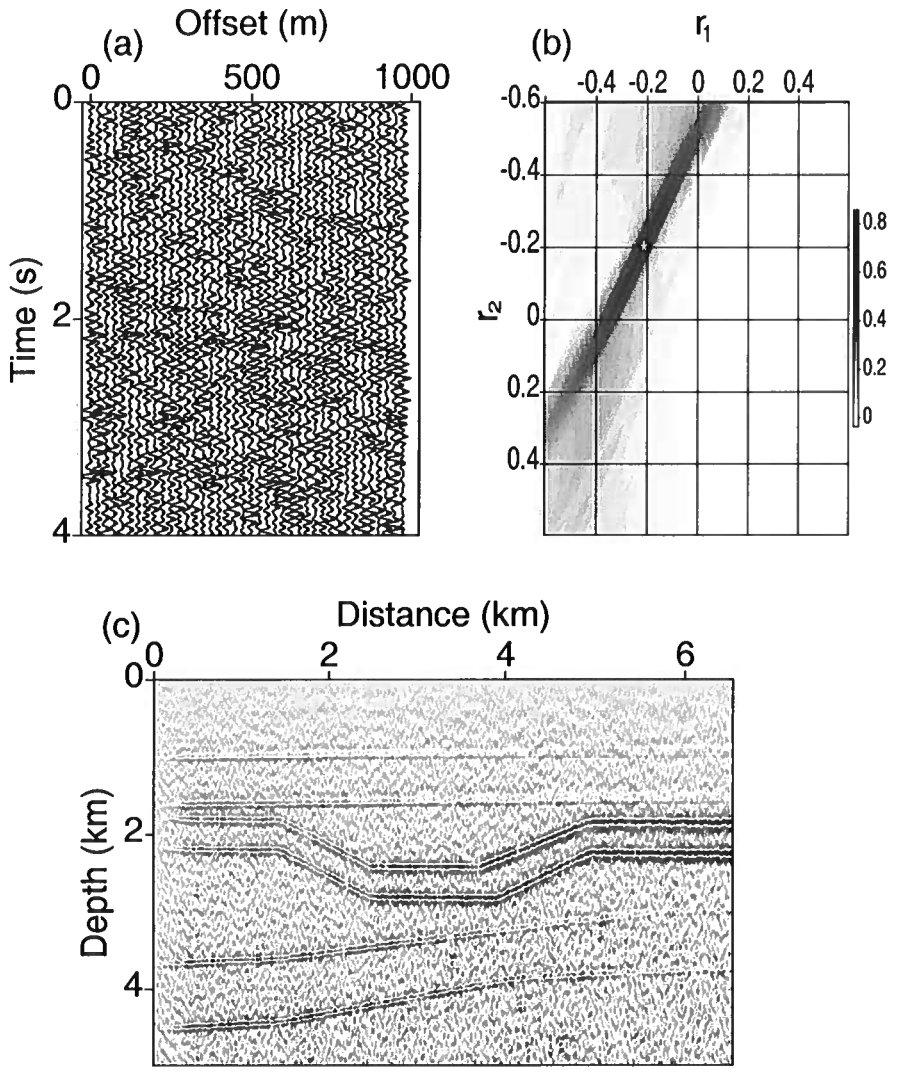

Figure 5. Influence of Gaussian noise on MVA and migration for the model from Figure 1. (a) One of the noise-contaminated shot gathers (the lateral coordinate is close to 2 km). (b) The semblance scan for the bottom of the TTI layer (the lateral coordinate is 1.9 km) computed as a function of the moveout coefficients r_1 and r_2 (equation 3). The maximum semblance is marked by the star. (c) The image obtained for the noise-contaminated data set. The estimated parameters of the first layer are $k_z = 1.06\ s^{-1}$, $k_x = 0.01\ s^{-1}$, $\epsilon = -0.01$, and $\delta = 0$. For the second layer, $k_z = 0.56\ s^{-1}$, $k_x = 0.11\ s^{-1}$, $\epsilon = 0.14$, and $\delta = -0.08$. For the third layer, $k_z = 0.35\ s^{-1}$, $k_x = 0.01\ s^{-1}$, $\epsilon = 0.02$, and $\delta = -0.02$. The errors for each parameter vary from ± 0.03 to ± 0.05 under the assumption that the picking error for the noisy data is ± 20 m.

3.2 Salt-dome model

The next test is performed for a simplified salt model, which can be considered typical for subsalt exploration plays. The model includes an isotropic salt dome with steep flanks overlaid by a TI shale formation. The symmetry axis in the shale is vertical directly above the dome and tilted (orthogonal to the bedding) in the dipping layers on both sides of the salt body (Figure 9). TTI migration, applied in the same way as for the syncline model using the correct medium parameters, produces a sharp, accurate image (Figure 10a) with flat image gathers even at the steep flanks of the salt (Figure 10b).

3.2.1 Processing using TTI and VTI models

When tilt is properly taken into account by the MVA algorithm, both the dipping reflectors and the salt dome

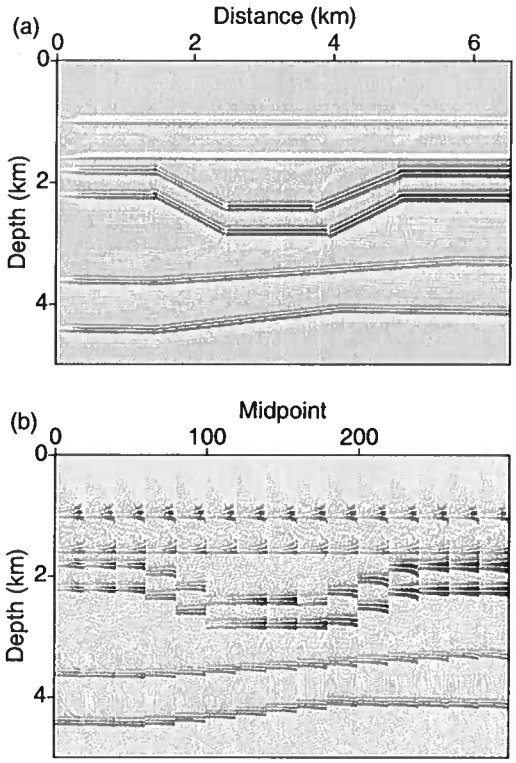

Figure 6. (a) Image of the model from Figure 1 obtained without taking the symmetry-axis tilt in the second layer into account; the rest of the model parameters are correct. (b) The corresponding image gathers.

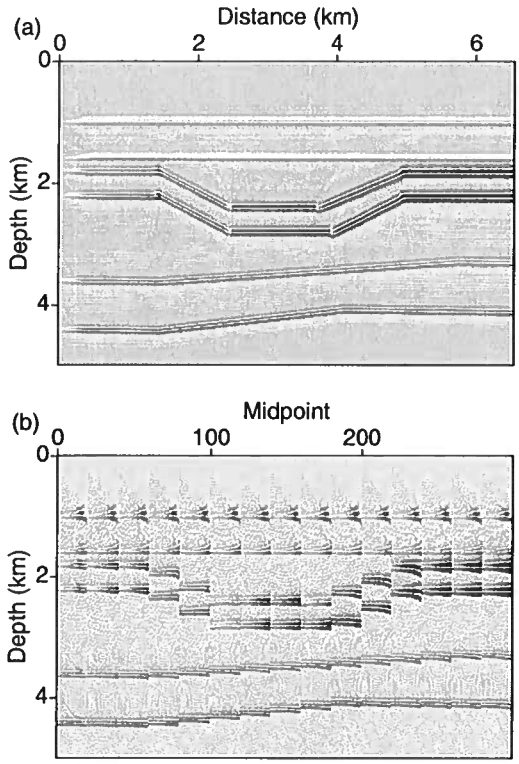

Figure 7. (a) Image of the model from Figure 1 obtained after applying MVA under the assumption that the second layer is VTI. The estimated parameters of the second layer used in the migration are $k_z = 0.53\ s^{-1}$, $k_x = 0.12\ s^{-1}$, $\epsilon = 0.15$, and $\delta = -0.06$ ($\eta = 0.24$). (b) The corresponding image gathers.

are well focused and properly positioned (Figure 11). As before, the parameters are estimated in the layer-stripping mode using the correct values of the velocity V_{P0} at the top of each layer. For purposes of MVA, the shale formation was divided into two blocks along the vertical axis of the salt dome. Errors in both anisotropy parameters and velocity gradients are relatively small, although ϵ is not as well constrained as δ. The larger error in ϵ is expected because, as discussed above, this parameter does not influence NMO velocity and is constrained only by nonhyperbolic moveout on long spreads.

Figure 12 shows the processing results obtained for a velocity model that does not include tilt and treats the shale as VTI (the parameters ϵ, δ, k_z, and k_x are correct). The substantial residual moveout in the image gathers for the dipping reflectors and pronounced image distortions indicate that the influence of tilt for this model is more significant than that for the syncline model discussed above.

Similar to the previous example, the VTI imaging result can be improved by deriving the best-fit VTI model from migration velocity analysis (Figure 13). Al-

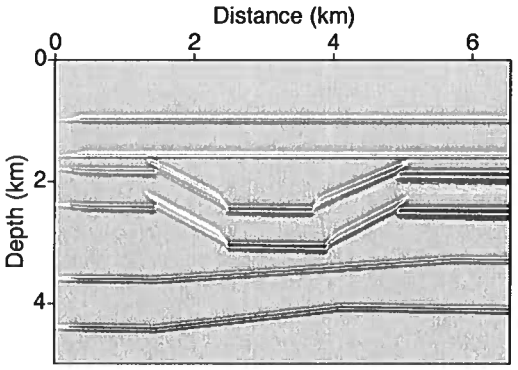

Figure 8. Same as Figure 7a (i.e., the image obtained for the best-fit VTI model), but the thickness of the TTI layer from Figure 1 is increased by 200 m. The estimated parameters are $k_z = 0.52\ s^{-1}$, $k_x = 0.12\ s^{-1}$, $\epsilon = 0.13$, and $\delta = -0.08$ ($\eta = 0.26$).

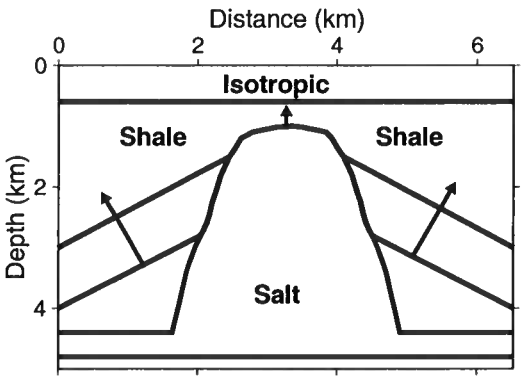

Figure 9. Simplified salt model that includes a salt dome overlaid by a TI shale formation. The symmetry axis in the shale (marked by the arrows) is vertical on top of the salt and orthogonal to the bedding in the uptilted layers, which are dipping at 30°. The parameters of the shale are $V_{P0} = 2.6$ km/s, $k_z = 0.6\ s^{-1}$, $k_x = 0.2\ s^{-1}$, $\epsilon = 0.3$, and $\delta = 0.15$. The subsurface horizontal layer is isotropic with $V_{P0} = 1.5$ km/s, $k_z = 1.0\ s^{-1}$, and $k_x = \epsilon = \delta = 0$; for the salt dome, $V_{P0} = 4.5$ km/s, $k_z = k_x = 0.1\ s^{-1}$, $\epsilon = \delta = 0$.

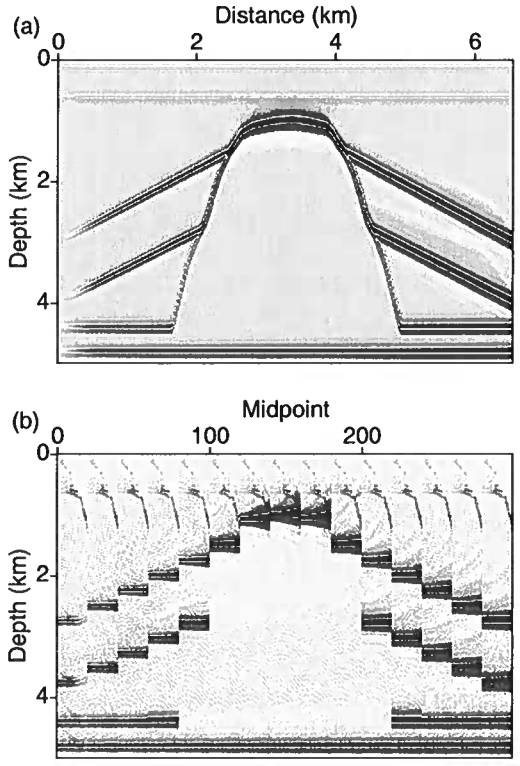

Figure 10. (a) True image of the model from Figure 9 obtained by anisotropic prestack depth migration with the correct parameters. (b) The corresponding image gathers.

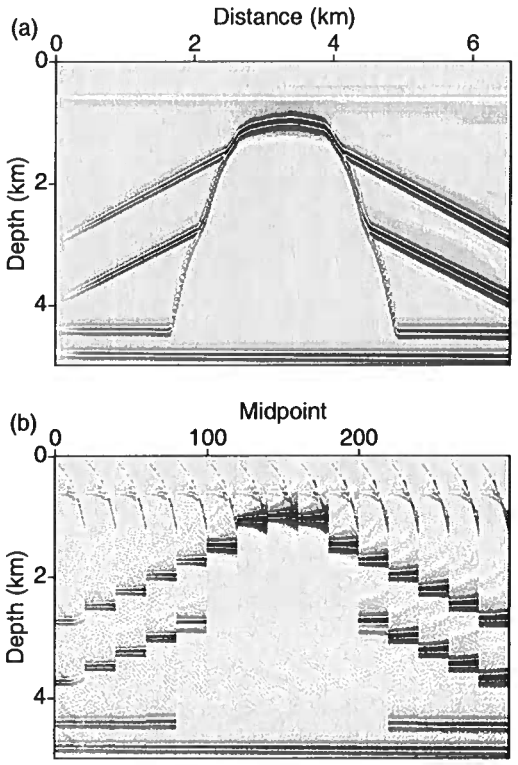

Figure 11. (a) Final image of the salt model obtained after MVA and prestack depth migration for TTI media. The estimated parameters of the first subsurface layer are $k_z = 0.97\ s^{-1}$ and $k_x = \epsilon = \delta = 0$. For the shale layer to the left of the salt, $k_z = 0.58\ s^{-1}$, $k_x = 0.19\ s^{-1}$, $\epsilon = 0.34$, and $\delta = 0.14$. To the right of the salt, $k_z = 0.59\ s^{-1}$, $k_x = 0.18\ s^{-1}$, $\epsilon = 0.32$, and $\delta = 0.15$. For the salt, $k_z = 0.09\ s^{-1}$, $k_x = 0.1\ s^{-1}$, and $\epsilon = \delta = 0$. The parameters of the left and right blocks below the shale layer on either side of salt dome are $k_z = 0.11, 0.10\ s^{-1}$, $k_x = 0.09, 0.12\ s^{-1}$, $\epsilon = \delta \approx 0.0$ respectively. The error for each parameter varies from ± 0.01 to ± 0.03, if the depth picking error is assumed to be ± 5 m. (b) The corresponding image gathers.

though the reflectors inside and below the shale formation are better focused than those in Figure 12, the flanks of the salt body are somewhat shifted laterally and look blurry (Figure 13a). Also, the image gathers, especially those near the salt, are not completely flattened (Figure 13b). Note that the improved image of the dipping reflectors in Figure 13a is achieved by distorting the parameter δ and, to a lesser extent, the velocity gradients in the shale. Clearly, ignoring the tilt of the symmetry axis in dipping TI layers in the overburden may cause serious problems in imaging salt bodies and, therefore, subsalt reservoirs.

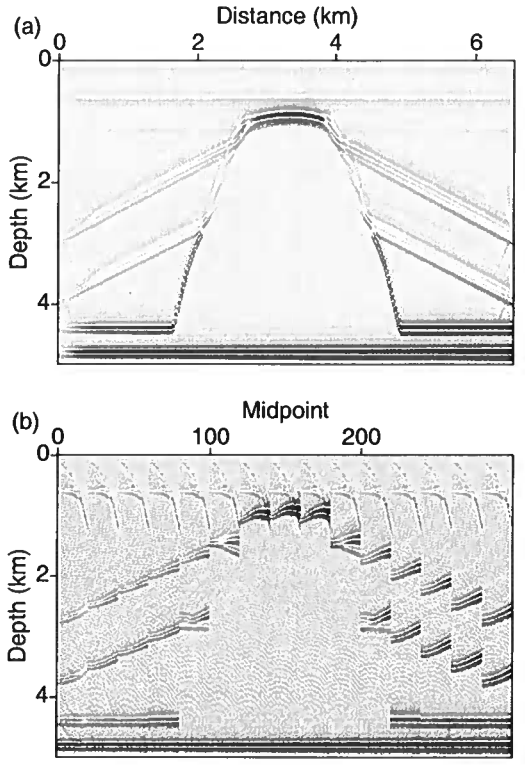

Figure 12. (a) Image of the model from Figure 9 obtained without taking the symmetry-axis tilt into account; the rest of the model parameters are correct. (b) The corresponding image gathers.

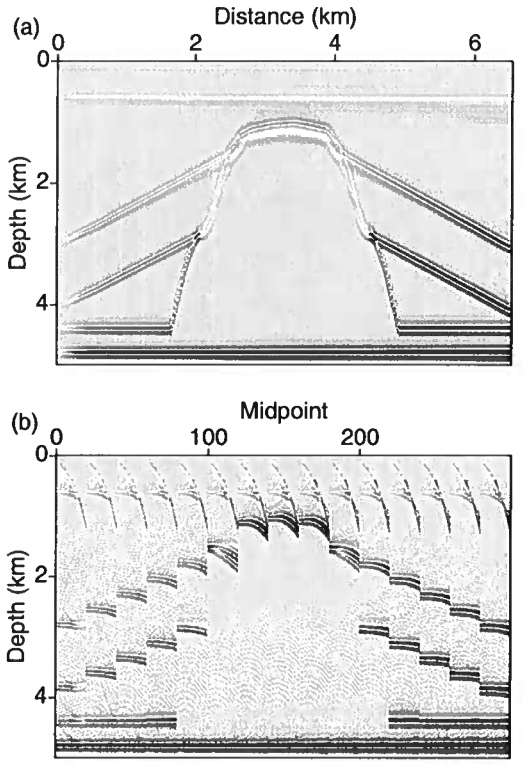

Figure 13. (a) Image of the model from Figure 9 obtained after applying MVA under the assumption that the shale formation is VTI. The estimated parameters for the shale layer to the left of the salt are $k_z = 0.62\ s^{-1}$, $k_x = 0.17\ s^{-1}$, $\epsilon = 0.32$, and $\delta = 0.12$. To the right of the salt, $k_z = 0.62\ s^{-1}$, $k_x = 0.18\ s^{-1}$, $\epsilon = 0.30$, and $\delta = 0.11$. (b) The corresponding image gathers.

3.3 Bending-layer model

Complex tectonic processes in fold-and-thrust belts, such as the Canadian Rocky Mountain Foothills, sometimes produce bending shale layers with variable dip. Here, we process synthetic data generated for a TTI thrust sheet (Figure 14) fashioned after the physical model of Leslie and Lawton (1996). This physical-modeling data set was used by Grechka et al. (2001) for anisotropic parameter estimation. The algorithm of Grechka et al. (2001), however, operates only with NMO velocities measured on conventional spreads and relies on several simplifying assumptions about the model.

The benchmark image computed for the true model is shown in Figure 15a. Apart from relatively low amplitudes of steeply dipping interfaces due to insufficient aperture, the reflectors are well focused and positioned, and all image gathers in Figure 15b are flat. To apply the MVA algorithm, we divided the thrust sheet into four blocks with different dips and carried out the parameter estimation separately for each block. As was the case for the previous two models, the TTI algorithm yields not only accurate parameter estimates, but also a high-quality image (Figure 16). If the medium parameters (except for the tilt) are assumed to be the same in the blocks with different dips, there is no need to specify the symmetry-direction velocity V_{P0} in the TTI layer.

When MVA does not take tilt into account, all boundaries in the thrust sheet are poorly focused, with noticeable artifacts at the points where the interfaces change dip (Figure 17a). It is interesting that the errors in the medium parameters produced by the VTI algorithm are relatively minor. Apparently, image gathers for the thrust sheet (Figure 17b) could not be flattened by distorting the anisotropy parameters or velocity gradients, as long as the symmetry axis is vertical.

4 DISCUSSION AND CONCLUSIONS

The combination of tilted transverse isotropy and structural complexity in many important exploration plays makes it imperative to apply advanced migration velocity analysis (MVA) methods and prestack depth imaging. Here, we presented an MVA methodology for P-

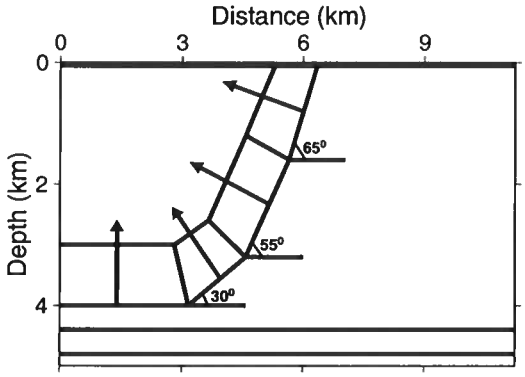

Figure 14. TTI thrust sheet with variable dip for different blocks (0°, 30°, 55°, and 65°) and the symmetry axis (marked by the arrows) orthogonal to the boundaries. Except for the symmetry-axis direction, the parameters of all TTI blocks are the same: $V_{P0} = 2.3$ km/s, $k_z = 0.6\ s^{-1}$, $k_x = 0.1\ s^{-1}$, $\epsilon = 0.1$, and $\delta = -0.1$. The subsurface layer is thin (60 m) and has $V_{P0} = 1.5$ km/s, $k_z = 1.0\ s^{-1}$, and $k_x = \epsilon = \delta = 0$ (i.e., it represents the weathering layer); the velocity V_{P0} across the bottom of the layer is continuous. The medium around the TTI sheet is isotropic with $k_z = 1.0\ s^{-1}$, and $k_x = \epsilon = \delta = 0$. The horizontal layer at the bottom of the model has $V_{P0} = 3.5$ km/s, $k_z = 0.3\ s^{-1}$, and $k_x = \epsilon = \delta = 0$.

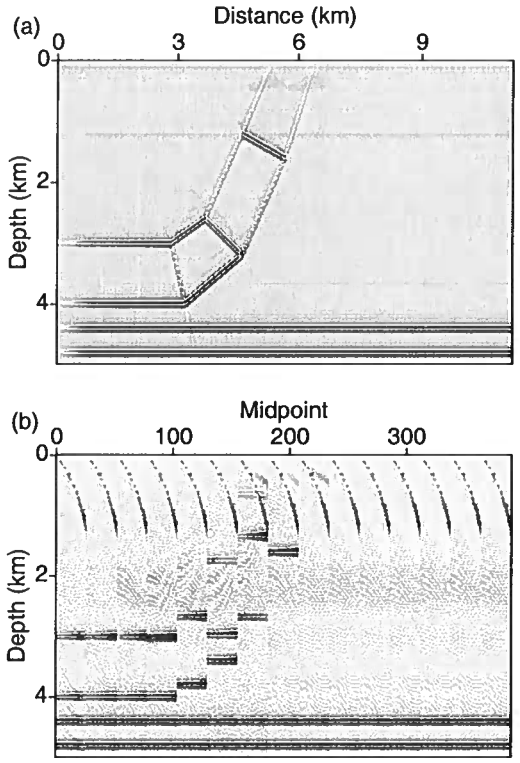

Figure 15. (a) True image of the model from Figure 14 obtained by anisotropic prestack depth migration with the correct parameters. (b) The corresponding image gathers.

waves in heterogeneous TTI media based on dividing the model into "quasi-factorized" blocks. The anisotropy parameters ϵ and δ in each block are constant, while the symmetry-direction velocity V_{P0} represents a linear function of the spatial coordinates and is described by the vertical gradient k_z and lateral gradient k_x. To reduce the uncertainty in parameter estimation, the symmetry axis in each block or layer is taken to be orthogonal to the reflector at the bottom of the block. Since reflectors may have arbitrary shape, the symmetry-axis orientation generally varies in space, which means that blocks are not fully factorized. (In factorized TI media, the symmetry-axis direction is fixed.)

Our algorithm represents an extension to TTI media of the MVA methodology developed by Sarkar and Tsvankin for vertical transverse isotropy. MVA is combined with Kirchhoff prestack depth migration based on anisotropic ray tracing for heterogeneous TI media with arbitrary tilt. Parameter estimation is performed in the layer-stripping mode starting at the surface, with the symmetry-direction velocity V_{P0} either specified at a single point in each block or assumed to be continuous in the vertical direction. To estimate the vertical gradient k_z, we use image gathers for at least two reflectors at different depths within each block.

If the velocity V_{P0} is known, the parameter δ in TTI media with the symmetry axis orthogonal to the reflector can be constrained using the NMO velocities for either horizontal or dipping events. In contrast to VTI media, where the parameters η and ϵ (with known V_{P0}) for some models can be found from dip-dependent NMO velocity, estimation of these parameters in TTI media generally requires using nonhyperbolic moveout. In our MVA algorithm, the residual moveout in long-spread image gathers is evaluated using the two-parameter nonhyperbolic equation described by Sarkar and Tsvankin. We found that sufficiently stable estimation of the parameter ϵ in TTI media with a fixed symmetry-axis orientation can be achieved if the offset-to-depth ratio reaches at least two.

The MVA and migration algorithms were tested on several typical TTI models including a syncline, a salt dome with dipping TTI layers on both sides, and a bending TTI layer (thrust sheet). For all three models we were able to accurately reconstruct the velocity gradients k_z and k_x throughout the medium and the anisotropy parameters ϵ and δ in the TTI blocks. The migrated sections computed with the estimated velocity model are practically indistinguishable from the true images, with good focusing and positioning of reflectors beneath the TTI formations.

To assess the influence of tilt on image quality, we

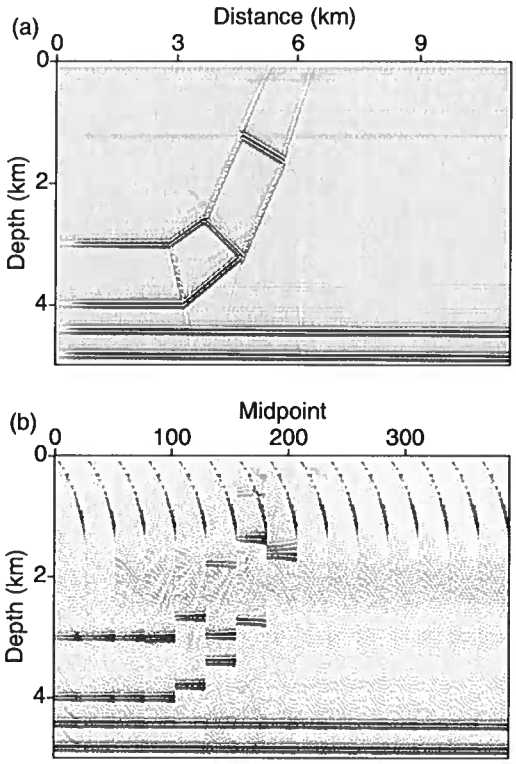

Figure 16. (a) Final image of the thrust model obtained after MVA and prestack depth migration for TTI media. The parameters were estimated for each block of the thrust sheet (i.e., for each dip) separately. For the horizontal TTI block (dip=0°), $k_z = 0.62\ s^{-1}$, $k_x = 0.11\ s^{-1}$, $\epsilon = 0.11$, and $\delta = -0.09$; for the 30° dip, $k_z = 0.59\ s^{-1}$, $k_x = 0.12\ s^{-1}$, $\epsilon = 0.09$, and $\delta = -0.11$; for the 55° dip, $k_z = 0.58\ s^{-1}$, $k_x = 0.09\ s^{-1}$, $\epsilon = 0.11$, and $\delta = -0.08$; for the 65° dip, $k_z = 0.62\ s^{-1}$, $k_x = 0.12\ s^{-1}$, $\epsilon = 0.09$, and $\delta = -0.1$. For the horizontal layer beneath the TTI sheet, $k_z = 0.29\ s^{-1}$, $k_x = \epsilon = 0$, and $\delta = 0.01$. The error for each parameter varies from ± 0.01 to ± 0.03, if the depth picking error is assumed to be ± 5 m. (b) The corresponding image gathers.

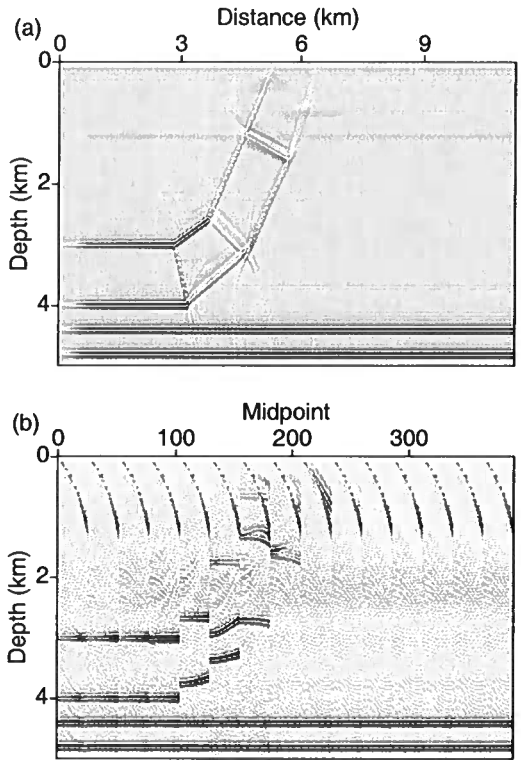

Figure 17. (a) Image of the model from Figure 14 obtained after applying MVA under the assumption that the thrust sheet is VTI. The parameters of the horizontal block (dip=0°) are $k_z = 0.59\ s^{-1}$, $k_x = 0.09\ s^{-1}$, $\epsilon = 0.09$, and $\delta = -0.11$; for the 30° dip, $k_z = 0.62\ s^{-1}$, $k_x = 0.11\ s^{-1}$, $\epsilon = 0.11$, and $\delta = -0.09$; for the 55° dip, $k_z = 0.61\ s^{-1}$, $k_x = 0.1\ s^{-1}$, $\epsilon = 0.13$, and $\delta = -0.12$; and for the 65° dip, $k_z = 0.63\ s^{-1}$, $k_x = 0.13\ s^{-1}$, $\epsilon = 0.11$, and $\delta = -0.08$. (b) The corresponding image gathers.

migrated the data with the VTI model (i.e., with zero tilt) that has the correct values of V_{P0}, k_z, k_x, ϵ and δ. Although the tilt in our first two models (the syncline and salt dome) is moderate (30°), setting it to zero results in significant misfocusing and mispositioning of reflectors. The inaccuracy of the VTI velocity field also manifests itself through substantial residual moveout in image gathers.

In order to emulate a complete VTI processing sequence applied to TTI media, we per formed MVA without allowance for a tilted symmetry axis to obtain the "best-fit" VTI model. The MVA algorithm can achieve partial flattening of image gathers with the incorrect tilt, but at the expense of distorting the medium parameters, especially ϵ and δ (although the value of η remains accurate). Such artificial adjustments in ϵ and δ improve image quality, although migrated sections typically are inferior to those generated with the TTI model. Also, the ability of the VTI-based algorithm to compensate for the influence of tilt decreases for more complicated models and TTI layers with relatively large thickness or strong anisotropy.

On the whole, the MVA methodology introduced here provides a practical tool for building TTI velocity models with minimal *a priori* information. Combined with prestack depth migration, this MVA algorithm can be efficiently used to image targets beneath TTI formations in structurally complex environments.

5 ACKNOWLEDGMENTS

We are grateful to the A(nisotropy)-Team of the Center for Wave Phenomena (CWP), Colorado School of

Mines (CSM), and other colleagues at CWP for fruitful discussions. L. B. thanks the Department of Science and Technology (DST), Govt. of India, for awarding him BOYSCAST Fellowship and V. P. Dimri, Director of the National Geophysical Research Institute (NGRI), Council of Scientific and Industrial Research (CSIR), for granting him permission to pursue postdoctoral research in CWP. This work was partially supported by the Consortium Project on Seismic Inverse Methods for Complex Structures at CWP.

REFERENCES

Alkhalifah, T., 1995, Efficient synthetic-seismogram generation in transversely isotropic, inhomogeneous media: Geophysics, **60**, 1139–1150.

Červený, V., 1989, Ray tracing in factorized anisotropic inhomogeneous media: Geophysical Journal International, **99**, 91–100.

Dewangan, P., and I. Tsvankin, 2006a, Modeling and inversion of PS-wave moveout asymmetry for tilted TI media: Part 1 – Horizontal TTI layer: Geophysics, **71**, D107–D121.

Dewangan, P., and I. Tsvankin, 2006b, Modeling and inversion of PS-wave moveout asymmetry for tilted TI media: Part 2 – Dipping TTI layer: Geophysics, **71**, D123–D134.

Grechka, V., and I. Tsvankin, 2000, Inversion of azimuthally dependent NMO velocity in transversely isotropic media with a tilted axis of symmetry: Geophysics, **65**, 232–246.

Grechka, V., A. Pech, I. Tsvankin, and B. Han, 2001, Velocity analysis for tilted transversely isotropic media: A physical modeling example: Geophysics, **66**, 904–910.

Isaac, J. H., and D. C. Lawton, 1999, Image mispositioning due to dipping TI media: A physical modeling study: Geophysics, **64**, 1230–1238.

Kumar, D., M. K. Sen, and R. J. Ferguson, 2004, Traveltime calculation and prestack depth migration in tilted transversely isotropic media: Geophysics, **69**, 37–44.

Leslie, J. M., and D. C. Lawton, 1996, Structural imaging below dipping anisotropic layers: Predictions from seismic modeling: 66th Annual International Meeting, SEG, Expanded Abstracts, 719–722.

Liu, Z., and N. Bleistein, 1995, Migration velocity analysis: Theory and an iterative algorithm: Geophysics, **60**, 142–153.

Pech, A., I. Tsvankin, and V. Grechka, 2003, Quartic moveout coefficient: 3D description and application to tilted TI media: Geophysics, **68**, 1600–1610.

Sarkar, D., and I. Tsvankin, 2003, Analysis of image gathers in factorized VTI media: Geophysics, **68**, 2016–2025.

Sarkar, D., and I. Tsvankin, 2004, Migration velocity analysis in factorized VTI media: Geophysics, **69**, 708–718.

Sarkar, D., and I. Tsvankin, 2006, Anisotropic migration velocity analysis: Application to a data set from West Africa: Geophysical Prospecting, **54**, 575–587.

Thomsen, L., 1986, Weak elastic anisotropy: Geophysics, **51**, 1954–1966.

Tsvankin, I., 1995, Normal moveout from dipping reflectors in anisotropic media: Geophysics, **60**, 268–284.

Tsvankin, I., 1997, Moveout analysis for transversely isotropic media with a tilted symmetry axis: Geophysical Prospecting, **45**, 479–512.

Tsvankin, I., 2005, Seismic signatures and analysis of reflection data in anisotropic media, 2nd ed.: Elsevier Science Publ. Co., Inc.

Vestrum, R., D. C. Lawton, and R. Schmid, 1999, Imaging structures below dipping TI media: Geophysics, **64**, 1239–1246.

Advanced non-invasive geophysical monitoring techniques

Roel Snieder[1], Susan Hubbard[2], Matthew Haney[3], Gerald Bawden, Paul Hatchell, André Revil & DOE Geophysical Monitoring Working Group[4]

[1] *Center for Wave Phenomena and Department of Geophysics, Colorado School of Mines, Golden CO 80401*
[2] *Earth Science Division, Lawrence Berkeley National Laboratory, Berkeley, CA 94720*
[3] *Geophysics Department, Sandia National Laboratories, Albuquerque NM 87185-0750*
[4] *DOE Geophysical Monitoring working group: R. Calvert, A. Curtis, M. Fehler, P. Gerstoft, B. Hornby, M. Landrø, D. Lesmes, K. Mehta, M. Mooney, C. Pacheco, S. Prejean, H. Sato, J. Schuster, K. Wapenaar, M. Wilt*

ABSTRACT

Geophysical methods can be used to create images of the Earth's interior that constitute snapshots at the moment of data acquisition. In many applications, it is important to measure the temporal change in the subsurface, because the change is associated with deformation, fluid flow, temperature changes, or changes in material properties. We present an overview how noninvasive geophysical methods can be used for this purpose. We focus on monitoring mechanical properties, fluid transport, and biogeochemical processes, and present case studies that illustrate the use of geophysical method for detecting time-lapse changes in associated properties. The examples include: measuring uplift of the Earth's surface, compaction near a producing hydrocarbon reservoir, the seismic detection of stress changes, monitoring buildings, the detection of fluid flow along a fault zone, electrical monitoring of fluid infiltration and redox potential, and electrical and seismic monitoring of microbially mediated processes. An overlying research question in geophysical monitoring concerns the use of these time-lapse changes, notably the assesment of uncertainty, the combination of disparate data, and the interface with those who make decisions based on time-lapse information.

Key words: time-lapse, monitoring, deformation, fluid flow, biogeochemical processes

1 INTRODUCTION

Monitoring structures and processes in the subsurface is of increasing importance. The focus of the petroleum industry has shifted from exploration to monitoring production. When tackling environmental problems, especially those associated with contaminant remediation, it is essential to monitor the processes in the subsurface. Monitoring is routinly performed to assess water resources quality and quantity. An important component in climate change studies is to monitor environmental parameters. Monitoring can be achieved most easily if it can be carried out in-situ by direct sampling of the properties of interest. However, for the earth's subsurface this is often not feasible because of technical or economic limitations. Moreover, in-situ measurements often have a much smaller support scale than the volume of interest, and the presence of measurement devices used for in-situ measurements may disturb the properties that one seeks to measure. For these reasons non-invasive monitoring techniques are increasingly important.

In this work we present recent developments in the field of non-invasive geophyiscal monitoring of the subsurface. Although incomplete, this overview aims to describe ongoing work in research areas of increasing complexity. In section 2, we discuss monitoring of me-

chanical properties of the earth, presenting an example of monitoring the deformation of the earth's surface. In principle, this is a simple, non-invasive, monitoring problem, but the required accuracy makes it a challenging problem. Monitoring the mechanical properties of the subsurface can be achieved with seismic waves. Recent research has shown that one can carry out seismic imaging with random noise, rather than controlled seismic sources as the source. This offers the opportunity to continuously monitor the subsurface using ambient noise. The next level of complexity is to monitor fluid flow in the subsurface. In section 3 we show evidence of a fluid pulse that propagates along a fault zone, as inferred from seismic data, and give an example of monitoring infiltration processes using the self-potential. Another challenge is that of monitoring biogeochemical processes remotely. We treat this problem in section 4, and show an example how the redox potential in the subsurface can be inferred from measurements of the self-potential. We also show an example of a controlled laboratory experiment wherein chemical changes caused by microbial activity can be monitored with seismic fields and with induced polarization measurements.

Together, these case studies highlight the potential that geophysical methods hold for monitoring mechanical, fluid, and biogeochemical processes. Although much of this reseach is in an early stage of development, the advances illustrated by these case studies suggest that further research is warrented.

2 MONITORING MECHANICAL PROPERTIES

2.1 Monitoring vertical ground motion

The simplest way to monitor changes in the subsurface is to detect deformation of the earth's free surface. Although conceptually straightforward, this is technically challenging because in many applications to be useful the deformation must be measured with an accuracy smaller than a centimeter. Geodetic techniques are the tool of choice. Recent developments in the use of the Global Positioning System (GPS) (Dixon 1991; Enge and Misra 1999) and Interferometric Synthetic Aperture Radar (InSAR) (Massonnet and Feigl 1998, Bamler and Hartl 1998, Bürgmann et al. 2000) make it possible to measure the deformation of the earth's surface with such an accuracy.

InSAR relies on coherent reflections of a radar beam from a satellite to the earth's surface and back. The phase difference of these reflections recorded during subsequent passes of the satellite can be used to create a map of the deformation of the earth's surface in the direction of the reflecting radar beam (Massonnet and Feigl 1998, Bamler and Hartl 1998, Bürgmann et al. 2000). The phase difference between the backscattered waves measured in the two passes of the satellite is based on an interferometric technique that quantifies to which degree the two waves are on phase or out of phase for each pixel on the ground surface. The used pixel size usually is 30 meters. Adding an integer number of cycles to one of the waves does not change the interference of these two waves. The phase difference can thus be measured only modulo 2π, where deformation corresponding to a phase difference greater than 2π is shown in color images of the deformation as a repeat in the color pallet. The magnitude of the surface deformations measured in one fringe (a phase difference between 0 to 2π) is governed by the satellite radar wavelength (European Space Agency ERS1, ERS2, and ENVISAT and the Canadian Space RADARSAT-1 and RADARSAT2 all use 5.6 cm C-band) and is calculated by dividing the wavelength in half to account for the two-way travel path of the radar pulse. Therefore, if the land surface subsidence by 85 mm it would be seen as three repeating color cycles of 28.3 mm in the interferogram.

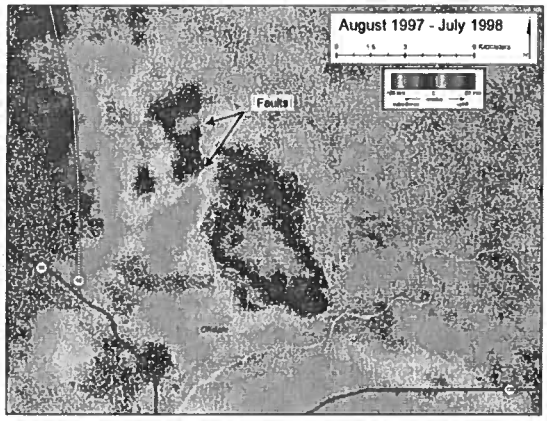

Figure 1. InSAR observed subsidence north of Bakersfield California associated with hydrocarbon extraction between August 1997 and July 1998. The color-scale gives the phase-wrapped vertical displacement with one cycle of color corresponding to 28.3 mm.

An example of the vertical ground deformation measured with InSAR, in Figure 1, shows the observed subsidence north of Bakersfield, California, associated with hydrocarbon extraction between August 1997 and July 1998. The figure shows two distinct regions of subsidence. The northwest region subsides about 3 cm, and the southeastern region has an overall pattern with 3 cm of subsidence over an area about 5 km wide with as much as 5 cm of subsidence in two localized features on the western margin of the subsidence trough. The northwestern region of subsidence is limited by faults on both the eastern and southern margins. Since the faults delimit the subsidence associated with the hydrocarbon extraction, this implies that these faults likely act as barriers for the fluid flow. In this example, InSAR mea-

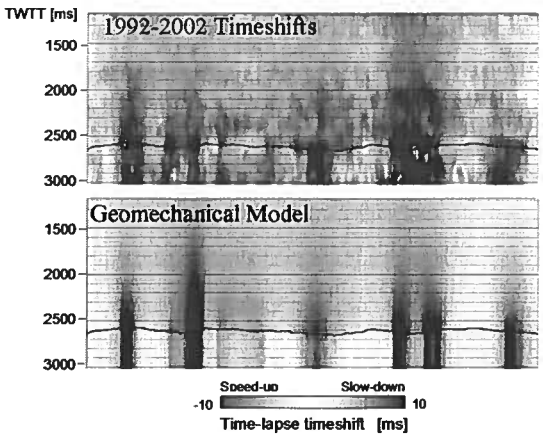

Figure 2. Top panel: the change in the two-way travel time over a chalk reservoir in Norway as obtained from stacked seismic data. Bottom panel: the change in the travel computed from a geomechanical model of the reservoir and its surroundings using equation (3) with the value $R = 5$.

surements can thus be used to make inferences about the fluid flow in the subsurface, and the sealing properties of faults. InSAR has been used to monitor co-seismic and tectonic deformation (Massonnet and Feigl 1998), to monitor the deformation associated with the extraction of water or hydrocarbons (Bawden et al. 2001), and to monitor the heaving of the surface caused by cyclic steam injection in the recovery of heavy oil (Stancliffe and van der Kooij 2001).

2.2 Monitoring compaction

It is also important to monitor the deformation within the earth. The compaction of hydrocarbon reservoirs during production leads to mechanical changes in the subsurface in the vicinity of the reservoir. The regions above and below a reservoir usually are in a state of an extension in order to accommodate the compaction in the reservoir. This leads to detectable changes in the P-wave velocity above and below the reservoir that can be retrieved by a comparison of the reflections in time-lapse seismic data.

The top panel of Figure 2 shows the change in arrival time of reflected waves in a North Sea Chalk Reservoir obtained from a comparison of time-lapse stacked field data. The top of the reservoir is marked with the solid line in that figure. Note that the change in the arrival time is not confined to the reservoir (two-way travel time larger than 2600 ms) and that waves reflected above the reservoir are slowed down appreciably.

The change in the arrival time caused by the extension arises from two factors. First, an extension of the subsurface produces a longer path length from the surface down to a reflector and back. For a vertically propagating wave, this geometric factor changes a depth interval dz into $(1 + \varepsilon_{zz})\, dz$. Using that the travel time is related to the seismic velocity v by $t = \int v^{-1} dz$, this gives the following geometric contribution to the travel time change δt:

$$\delta t_{geometric} = \int \frac{\varepsilon_{zz}}{v} dz \,. \tag{1}$$

The strain also introduces changes in the material properties, and the relative velocity change due to the strain is given by $\delta v/v = -R\varepsilon_{zz}$. The proportionality constant R depends on the rock properties. For a variety of different rocks, this dimensionless constant has values usually between 1 and 5 (Hatchell and Bourne 2005). The associated travel time is given by

$$\delta t_{properties} = \int R \frac{\varepsilon_{zz}}{v} dz \,, \tag{2}$$

This travel time change could have been expressed in the stress-change rather than the strain, but the corresponding value for R then would be much more variable for different rock types. Combining these expressions gives

$$\delta t = \int (1 + R) \frac{\varepsilon_{zz}}{v} dz \,. \tag{3}$$

For the North Sea Chalk reservoir, the travel-time change computed using equation (3) and a geomechanical model of this reservoir is shown in the bottom panel of Figure 2. Note that the travel-time change measured from stacked seismic data (top panel) agrees well with the travel time change computed from a geomechanical model (bottom panel). Such a comparison can be used to validate geomechanical models of the subsurface (Hatchell and Bourne 2005), especially when in addition to changes in the travel time, changes in reflection strength are also taken into account (Tura et al. 2005).

2.3 Seismic interferometry

Interferometry is a sensitive method for detecting minute changes by using waves that bounce repeatedly within the medium that is probed (Lauterborn et al. 1995). This principle is widely used in optics and now also finds application for monitoring purposes in the geosciences. *Coda wave interferometry* uses the sensitivity of waves that have bounced repeatedly in the medium thus enabling monitoring of minute changes in the medium (Snieder et al. 2002, Snieder 2004a, Snieder 2006b). This technique has been used to monitor volcanoes (Ratdomopurbo and Poupinet 1995, Grêt et al. 2005, Pandolfi et al. 2006, Wegler et al. 2006) and fault-zone properties (Poupinet et al. 1984), for the the detection of velocity changes related to earhthquakes (Nishimura et al. 2000, Nishimura et al. 2005) or secular changes in tectonic stress (Furumoto et al. 2001),

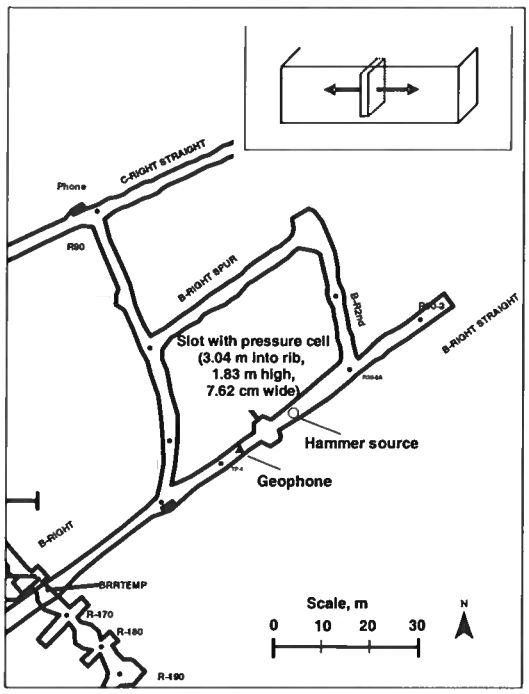

Figure 3. Geometry of the experiment in the Edgar Mine. Geophone and hammer source locations are labeled in the plan. The pressure cell in the slot is indicated by the small line between geophone and source location. The inset (top right) sketches the pressure cell installed in the pillar.

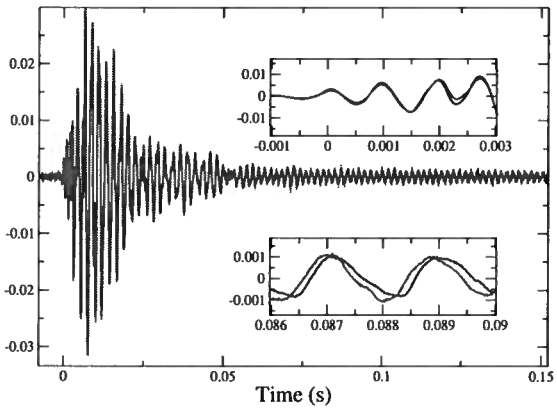

Figure 4. Waveforms measured at 4.14 MPa of pressure (blue) applied by the jack (blue) and measured at a pressure from the jack of 12.41 MPa (red). The upper panel shows the waveforms in the early time window and the lower panel those in a later window.

and for the detection of changes in materials using ultrasound (Roberts et al. 1992, Grêt et al. 2006a).

We illustrate the principle of coda wave interferometry with a controlled experiment wherein the stress in a mine pillar was changed using a hydraulic jack (Grêt et al. 2006b). The experiment was carried out in the Edgar Mine in Idaho Springs, Colorado, an experimental mine owned by the Colorado School of Mines. The geometry of experiment is shown in Figure 3. The mine pillar shown in this figure is surrounded by tunnels that are about 3-m high. The stress-state in the pillar is changed by jacks that load two plates with a surface area of about 1 m^2 placed in a slit cut into the pillar (inset in Figure 3). Seismic waves generated with a hammer source are recorded on a accelerometer mounted on the tunnel wall; see Figure 3. The waveforms for two pressure-states of the jack are shown in Figure 4: the waves recorded for a pressure applied by the jack of 4.14 MPA are shown in blue, while the red line shows the waves recorded for a pressure of 12.41 MPa.

The early arriving waves are shown in the panel in the top-right. These first-arriving waves are so repeatable that based on these first arrivals it is impossible to make any statements about the change in the seismic velocity associated with the change in stress. The panel in the bottom right shows a portion of the later-arriving waves. These later-arriving waves show a clear change in the phase with changing pressure. This phase change can be quantified using a time-shifted cross-correlation and used to estimate the change in seismic velocity (Snieder 2006b). Several non-overlapping time windows provide independent estimates of the velocity change that can be used as a consistency check on the employed method and can also be used to estimate the uncertainty in the estimated change in the velocity (Snieder et al. 2002, Grêt et al. 2006a). For a change in pressure from 0 MPa to 8 MPa, the estimated velocity change is 0.25% with an uncertainty of 0.02% (Grêt et al. 2006b). The high sensitivity of this technique is due to the sampling of the region where the stress is changed by the later-arriving waves that bounce back and forth repeatedly within the mine pillar.

Another active area of research in seismic interferometry is the extraction of the response of a system from the measurement of incoherent signals in the system. By cross-correlating, or deconvolving, noise recorded at two receivers, it is possible to retrieve the impulse response associated with the wave propagation between these receivers. (In mathematical jargon, the response of the system to an impulsive loading is referred to as the *Green's function.*) Derivations of this principle have been presented based on normal modes (Lobkis and Weaver 2001), on representation theorems (Wapenaar 2004, Weaver and Lobkis 2004, Wapenaar et al. 2005), on time-reversal invariance (Derode et al. 2003a, Derode et al. 2003b), and on the principle of stationary phase (Snieder 2004b, Roux et al. 2005b, Snieder

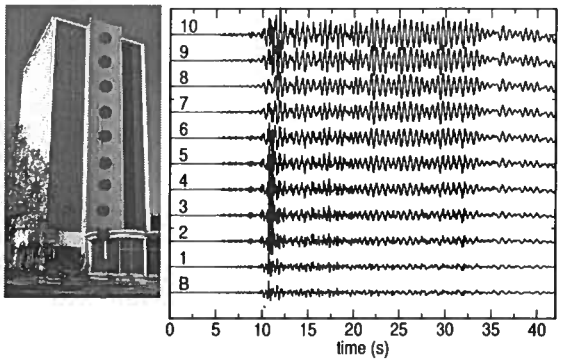

Figure 5. The Robert A. Millikan Library in Pasadena (left panel) and locations of the accelerometers (red circles). Right panel: the North-South component of the acceleration recorded at the west side of the building after the Yorba Linda earthquake of 03 Sep 2002 (ML=4.8, Time: 02:08:51 PDT, 33.917N 117.776W Depth 3.9km).

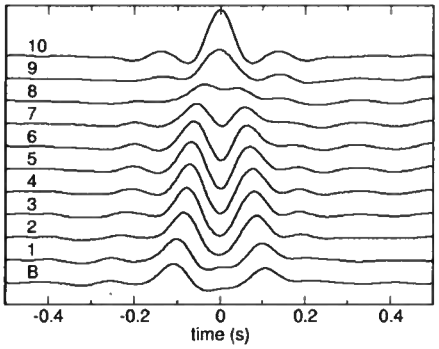

Figure 6. The waveforms of Figure 5 after deconvolution with the waves recorded at the top floor.

et al. 2006b). This technique has found applications in ultrasound (Weaver and Lobkis 2001, Malcolm et al. 2004, Larose et al. 2006), crustal seismology (Campillo and Paul 2003, Shapiro et al. 2005, Roux et al. 2005a, Sabra et al. 2005), exploration seismology (Calvert et al. 2004, Bakulin and Calvert 2004), structural engineering (Snieder and Şafak 2006, Snieder et al. 2006a) , and numerical modeling (van Manen et al. 2005). Snieder (2006a) showed theoretically that the Green's function for the diffusion equation can be extracted by correlating pressure fluctuations recorded at different locations within reservoir. This makes it possible to retrieve the impulse response for fluid transport from ambient pressure fluctuations.

As an example, we show in Figure 5 the horizontal motion recorded in the basement and the 10 floors of the Robert A. Millikan library of Caltech (Pasadena) after the Yorba Linda earthquake of 03 Sep 2002 (ML=4.8, Time: 02:08:51 PDT, 33.917N 117.776W Depth 3.9km). The excitation of the building by the earthquake is incoherent. The waveforms of Figure 5 are the result of a combination of (i) the incoherent excitation, (ii) the mechanical properties of the building, and (iii) the coupling of the building with the subsurface. In order to unravel these different physical factors, Snieder and Şafak (2006) deconvolved the motion at different levels with respect to the motion at a target level. The motion at all levels, after deconvolution with the motion at the 10th floor is shown in Figure 6. In contrast to the incoherent waveforms of Figure 5, the deconvolved waves are simple: they consist of one upgoing wave and one downgoing wave. These upgoing and downgoing waves can be used to estimate the shear velocity and attenuation in the Millikan library. This method can also be applied to sensors placed in the subsurface. Mehta et al. (2006) extract coherent P- and S-waves, as well as P to S converted waves, propagating along a borehole from incoherent waveforms. Snieder and Şafak (2006) show that the deconvolved waveforms depend neither on the specific excitation on the building, nor on the coupling of the building to the subsurface (with the associated radiation loss). In fact, in seismic interferometry one can even create coherent wave states of the system under different boundary conditions than those of the physical system in which the waves are recorded (Snieder et al. 2006a).

The advantages of seismic interferometry in the geosciences are twofold. First, the receiver whose signal is used as a reference for the deconvolution, plays the role of a (virtual) source. This means that it is possible to diagnose the subsurface as if there were subsurface sources, although in reality only receivers are present in the subsurface. Second, since this technique is based on recordings of incoherent waves, it can be used to continuously monitor the subsurface using continuous noise recordings. One can combine this method with coda wave interferometry for continuous monitoring using ambient noise. This has been used to monitor daily variations in the seismic velocity associated with rainfall (Sens-Schönfelder and Wegler 2006) and with stress-changes caused by an earthquake (Wegler and Sens-Schönfelder 2006). For the Millikan library, for example, one can use subsequent earthquakes to monitor temporal changes in the building. This technique can be extended to other structures (e.g., drilling rigs, bridges, aircraft) and is of particular interest for detecting changes in structures caused by traumatic events such as explosions, hurricanes, fire, and earthquakes.

2.4 Challenges and future Directions in Monitoring Mechanical Properties

While the measurement of mechanical properties, such as seismic velocity, is fairly well-developed, the connection of these mechanical properties with micostructure is often unclear. An example is seismic anisotropy. The theory of seismic wave propagation in anisotropic media is advanced (Tsvankin 2001), but the relation between temporal changes in seismic anisotropy and associated microstructure (such rock formation, deformation, and fluid migration) is not nearly as well established.

Seismic attenuation is another physical property that can be measured, but whose connection with local material properties is often not clear. Because of the dependence of seismic attenuation on the presence of fluids, this quantity might be useful for diagnosing fluids in the subsurface. Attenuation can be attributed both to intrinsic attenuation and to scattering attenuation. (Intrinsic attenuation is the transfer of mechanical energy of wave propagation to other forms of energy, such as heat or squirt-flow, while scattering attenuation is the conversion of energy of a propagating wave to energy of scattered waves.) The separation of these different mechanisms of attenuation needs further research, as well as does the relation between instrinsic attenuation and properties of fluid-filled porous media (Pride et al. 2003).

Seismic interferometry has much potential for passively monitoring the mechanical properties of the subsurface and of structures such as buildings, bridges, pipelines, and drilling rigs. For these structures the detection of incipient change is of special importance because it could lead to remediation of damage that is about to develop. This technique can also be important for assessing damage to structures caused by traumatic events such as hurricances or explosions. One hurdle in the application of new monitoring techniques is that legislation often is slow to take advantage of new technological developments.

Real-time diagnostics would be useful in a number of applications for monitoring the subsurface, which include monitoring reservoirs, remediation, and monitoring in civil engineering projects and construction. The development and utilization of permanent sensors can play an important role in permanent monitoring.

Temporal variations caused by natural sources can offer new ways to diagnose the subsurface. For example, the imprint of ocean tides on pore pressure has been measured in reservoirs (Furnes et al. 1991, Smit and Sayers 2005), and changes in P-wave velocity associated with the solid earth tides have been measured as well (Yamamura et al. 2003). Micro-seismic events have been observed during the passage of Rayleigh waves excited by large earthquakes (Miyazawa and Mori 2006). The earth response to these variations might carry important information about the mechanical properties and microstructure of rocks and their interaction with fluids.

3 MONITORING FLUID TRANSPORT

Geophysicists often exploit the sensitivity of their recorded signals to the presence of fluids in order to address questions concerning subsurface fluid distributions. For instance, exploration seismologists invoke the Gassmann equation to interpret if reflected waveforms bear the imprint of fluid saturation. The Gassmann equation relates the elastic properties of a porous medium to the properties of the rock matrix and those of the pore fluid (Gassmann 1951, Wang 2000). Similarly, since pore pressures modify seismic velocities, reflection tomography can be used to predict pore pressures (Sayers et al. 2002). Though much is known about the fluid sensitivity of geophysical signals, the interaction of rocks and fluids continues to be an active research area. Current topics in rock/fluid properties are widening the scope of geophysical knowledge by studying fluid effects on poorly-understood rock types, such as carbonates, fault gouge, and marine sediments containing gas hydrates (Chand and Minshull 2003). In addition, longstanding questions persist concerning the precise role of fluids in seismic wave attenuation (Pride et al. 2003).

With periodic time-lapse or even continuous monitoring techniques becoming more widespread, characteristic fluid signatures can be further exploited to study dynamic flow processes and mechanisms of fluid transport. Applications of these techniques with societal impact include the long-term sequestration (storage) of CO_2 in subsurface traps, delineation of the water table, and detection of fluid transport near radioactive-waste depositories (Long and Ewing 2004). Whether the cause of subsurface fluid flow is natural or induced, advanced monitoring techniques provide a more complete picture of various flow phenomena, such as pore pressure fronts, microseismicity, the interactions of fluids and fractures, flow-related interface phenomena, fluid migration, and pathways for flow in the presence of multiple fluid phases.

Fluid transport in the subsurface can arise from natural processes such as tides, earthquakes, and fluid migration. Several recent studies utilize monitoring techniques to reveal the dynamics of these events. Teanby et al. (2004) report temporal variations in seismic anisotropy caused by fluctuations of the stress field in response to ocean tides. A monitoring technique proposed by Silver et al. (2004) exploits this phenomenon to calibrate stress sensitivity of transmitted waves. Unusual earthquakes in the Long Valley Caldera, as observed by Hill et al. (2003), are attributed to fluid migration of magma or hydrothermal brine. These earthquakes are enriched in low frequencies and have non double-couple source radiation patterns. Hill et al. (2003) make the case that understanding the earthquake source in these instances is a necessary part of effectively alerting the public to impending volcanic eruption. Crampin et al. (2003) observe water-level fluctuations in wells close to the Húsavík-Flately Fault in

Iceland, where the water level is continuously monitored during times of increased seismicity. The theory of anisotropic poroelasticity is able to accurately explain these changes. Similar earthquake-related water-level fluctuations are described by Roeloffs et al. (2003).

Use of time-lapse radar and electrical tomographic methods for monitoring infiltration pathways and moisture variations in the near-subsurface is now fairly well developed (e.g., Hubbard et al. 1997, Binley et al. 2002, Alumbaugh et al. 2002, Kowalsky et al. 2004). Monitoring techniques have been applied to problems concerning flow induced by reservoir production, pumping, and drilling operations (Calvert 2005). For instance, absolute gravity measurements have been acquired in both petroleum and groundwater applications (Brown et al. 2002, Cogbill et al. 2005). In the case of groundwater, Cogbill et al. (2005) have observed positive changes in absolute gravity in a region surrounding a water well that are believed to be associated with nearby aquifer recharge. In contrast, no gravity changes were recorded in the immediate vicinity of wells being pumped even though significant changes in the surface elevation had occurred, as measured by GPS. The lack of a gravity signal during a time of surface deformation can be used to constrain models for how the fracture system has been modified by the pumping of water. As an example of a petroleum application of absolute gravity, Brown et al. (2002) have observed a clear and widespread change in absolute gravity and have mapped it to indicate where pumped saline water has replaced oil at Prudhoe Bay.

Landrø and Stronen (2003) have demonstrated that when more than two time-lapse surveys are available, waterfronts in a reservoir can be tracked in differenced 4D seismic images. They showed the use of CO_2 as a tracer to aid structural interpretation. The CO_2 in this case was not injected for the specific purpose of sequestration or enhanced oil recovery - it was simply used to highlight the permeable pathways in the reservoir. Such information can prove invaluable for planning drilling programs to optimally produce reservoirs. Time-lapse seismic techniques continue to be improved for the monitoring of CO_2 sequestration. At the West Pearl Queen field, a DOE test site for CO_2 sequestration, Benson and Davis (2005) have reported on the detection of injected CO_2 from two high-quality, highly-repeatable seismic surveys. Below, we review two examples of the novel use of geophyiscal data for monitoring fluid transport.

3.1 Detection of a fluid pulse migrating along a fault zone

Recently, Haney et al. (2005) investigated the mechanism of strong fault-plane reflections from a growth fault at the South Eugene Island field in the Gulf of Mexico. Fault-plane reflections, unlike reflections from sedimentary layers, might not be primarily associated with lithological differences. Since faults often act as either fluid seals or conduits (Hooper 1991), strong pore-pressure differences in and around faults can give rise to fault-plane reflectivity (Haney et al. 2006). By examining two seismic images, one from 1985 and another from 1992, Haney et al. (2005) observed that an area of strong fault-plane reflectivity associated with a fault known as the B-fault appeared to move 1 km along the fault-plane in the up-dip direction. This up-dip movement is depicted in the two reflectivity maps of Figure 7.

Fluid movement up the fault-plane is particularly noteworthy at South Eugene Island since several lines of evidence exist suggesting that natural fluid migration is presently occurring in the mini-basin petroleum system (Anderson et al. 1991, Anderson et al. 1994, Losh et al. 1999, Whelan et al. 2001, Revil and Cathles 2002, Haney et al. 2005). The pulsing of fluid up a permeable fault zone is also consistent with a nonlinear permeability model first introduced by Rice (1992) and later proposed by Revil and Cathles (2002) to be directly applicable at South Eugene Island. In this model, the fluid pulse is a pore-pressure shock wave that moves along the fault with velocity that is predicted from theory. Miller et al. (2004) use the same shock-wave model to explain the migration of fluid-related earthquake hypocenters along an active fault in Italy. The existence of these pore-pressure shock waves is due to the deformation of the porous media pore-pressure variations. The existence of the shock-wave thus provides direct evidence of a coupling between the fluid flow and deformation of the host rock (Minkoff et al. 2004).

3.2 Direct measurement of fluid flow with the self-potential

Through combined numerical, laboratory, and field experiments, Suski et al. (2006) have made significant progress toward showing how to successfully monitor the water table using self-potential (SP) methods. Self-potential signals originate from a variety of mechanisms, including electro-kinetic (the so-called *streaming potential*) and electro-redox effects (which are discussed in a section 4.1 of this work) (Nyquist and Corry 2002). Electro-kinetic effects (Revil and Linde 2006) are the same phenomena responsible for coupling seismic and electromagnetic fields in the field of electroseismics (Pride and Morgan 1991).

Shown in Figure 8 are details of the infiltration experiment conducted by Suski et al. (2006). The experiment is based on the idea that groundwater flow in soil produces a self-potential signal that can be measured at the surface. Hence, the self-potential method detects and maps out the effects of dynamic flow. The upper left panel of Figure 8 is a map view of the field layout used by Suski et al. (2006) consisting of 18 piezometers and 41 ($Pb/PbCL_2$) non-polarizable electrodes. To monitor the changes in the piezometric surface caused by fluid infiltration, the ditch, shown in the upper left

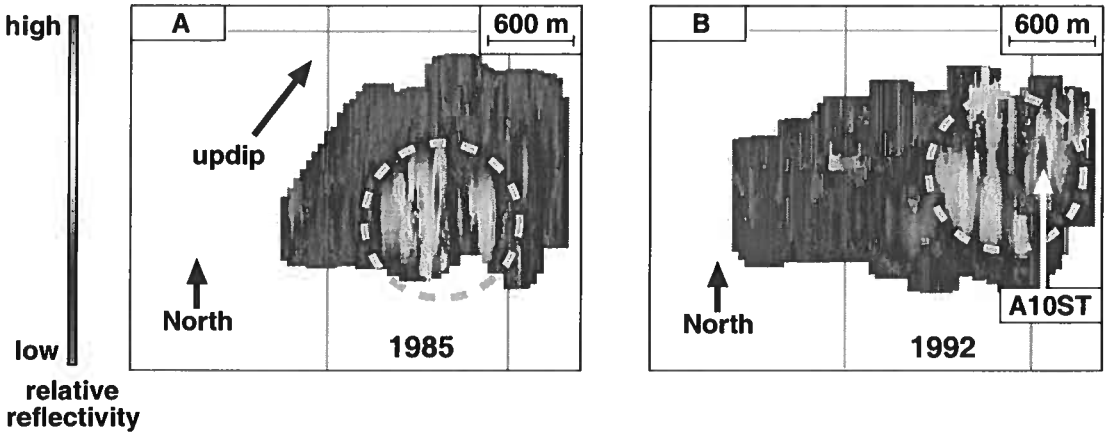

Figure 7. Evidence of fluid transport along a fault in the Gulf of Mexico inferred from seismic images constructed from seismic data recorded in 1985 and 1992. (A) Map view of fault-plane reflectivity from a growth fault known as the B-fault in 1985. The area of highest fault-plane reflectivity is circled in gold. (B) Map view of the B-fault reflectivity, as in (A), but from 1992. The data extend over a slightly larger area than in (A); however, the spatial perspective is identical. The area of highest reflectivity, circled in gold, is shifted roughly 1 km NE in the updip direction relative to its location in 1985, as is expected for a fluid pulse ascending the B-fault (Revil and Cathles 2002). This movement is represented by the arrow in (A). Also shown is the location of the A10ST well intersection, where exceptionally high fluid pressures were encountered while drilling into the B-fault zone in 1993, a year after the 1992 seismic survey (Losh et al. 1999).

panel of Figure 8, is filled with water. The filling of the ditch comprises the short time-duration Phase I of the infiltration experiment pictured in the upper right panel of Figure 8. The other two phases cover the episodes of constant water level in the ditch (Phase II) and relaxation, or drainage, of the head (Phase III). The data plotted in the upper right panel of Figure 8 include the water level in the ditch, the depth to the piezometric surface measured at several piezometers, and the corresponding self-potential signal measured at the electrodes. The trend of the self-potential signal correlates well with the latter two phases of fluid infiltration.

The lower panel in Figure 8 compares the measured self-potential signals to changes in piezometric head. The self-potential signal depends more or less linearly on the piezometric level, with a slope of -5.5 $\pm$ 0.9 mV/m. From soil samples taken at the test site, Suski et al. (2006) independently find in the laboratory that the slope can be between -4.0 mV/m and -5.9 mV/m, depending on the type of fluid saturating the pore space of the soil. Finally, the solid line in the lower panel in Figure 8 is the result of a finite-difference numerical model (Titov et al. 2005). The agreement with the field data shows that the hydrological and self-potential properties of the subsurface are modeled well. With these results, Suski et al. (2006) demonstrate the ability of the self-potential method to non-invasively monitor groundwater flow. An important property of these self-potential measurements for the purposes of continuous monitoring is that they are inexpensive to acquire (Nyquist and Corry 2002) in contrast to 3D seismic data acquisition. In addition, the self-potential method is applicable to the problem of monitoring of CO_2 injection (Moore et al. 2004).

3.3 Challenges in monitoring fluid flow

Many challenges lie ahead for the advanced monitoring of fluid transport. The sensitivity of advanced monitoring techniques aiming to track fluid transport must be maximized with respect to fluid saturation, pressure, and flow. Crampin (2003) argues that certain techniques (e.g., shear-wave splitting) inherently are extremely sensitive because they probe a critical system (e.g., cracks and fractures). In geophysics, the concept of criticality is often invoked when describing the stress state of fault systems in the crust (Zoback and Townend 2000). Extreme sensitivity and criticality are linked to nonlin-

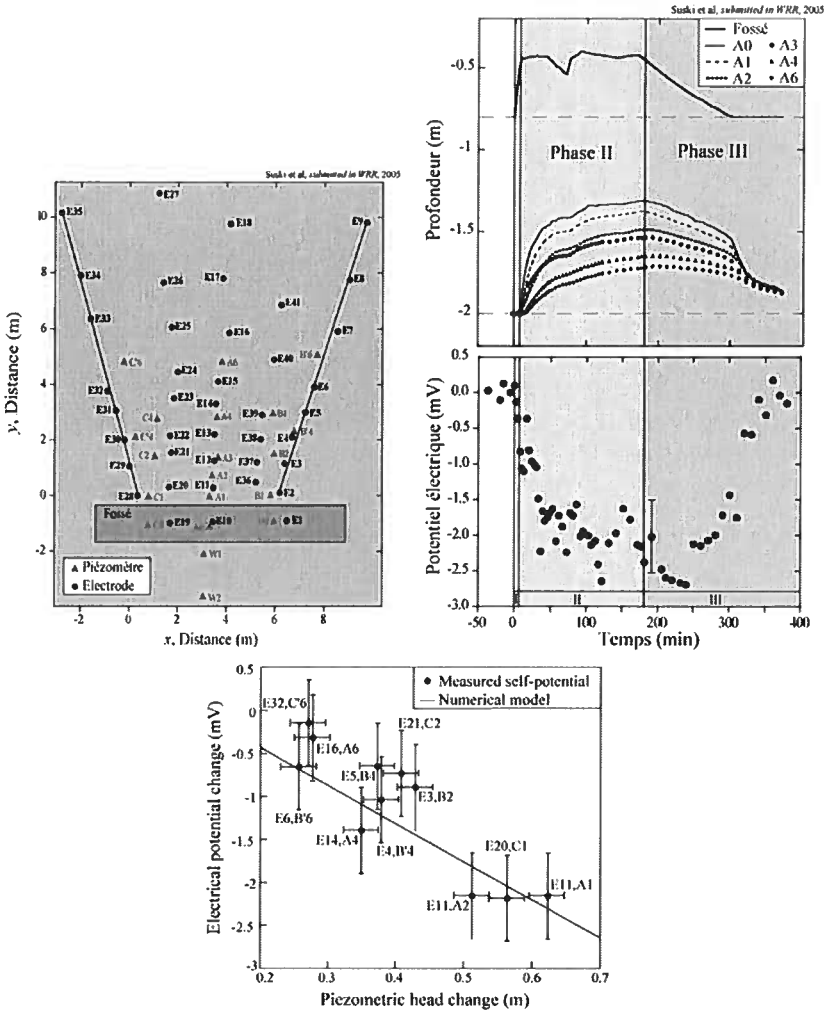

Figure 8. Experimental setup and results of a fluid infiltration test by Suski et al. (2006). The upper left panel shows an array of 18 piezometers and 41 non-polarizable electrodes arranged in and around a rectangular ditch (blue). The soil at the site is comprised of clay and silt with porosity that varies between 0.2 and 0.3. The upper right panel shows three quantities: the water level in the ditch (thick solid line), depths to the piezometric surface (thin solid, dotted, and dashed lines), and self-potential signals (black filled circles). The measurements capture three different stages of infiltration: (I) beginning of infiltration, (II) maintenance of constant head in the ditch, and (III) relaxation of the head. The lower panel is a comparison between measured self-potential signals versus the isometric head change (solid points with error bars) and the results of a finite difference numerical model (solid line).

earity, and nonlinear rock moduli have recently been implicated by Gomberg and Johnson (2005) as a cause of dynamic triggering - a phenomenon in which microearthquakes are initiated on critically-stressed faults by passing seismic waves from earthquakes over 1000 km away (Freed 2005). The dynamic strains in these cases are on the order of only a few microstrains (10^{-6}) (Gomberg and Johnson 2005). In addition to criticality, enhanced sensitivity can also be achieved with methods based on monitoring seismic waves by exploiting the multiply-scattered coda (e.g., coda wave interferometry, as discussed in section 2.3). Perhaps the most daunting challenge is that in order to move in the future from periodic time-lapse measurements to continuous monitoring, the methods used for monitoring cannot be costly. It is worth emphasizing again that the self-potential method employed by Suski et al. (2006) is relatively inexpensive. In contrast, the method of using

injected CO_2 as a structural tracer to find permeable pathways, although promising, is currently vastly more expensive.

Advanced monitoring plays a prime role in the growing field of CO_2 sequestration. To make sequestration successful, it is necessary to determine whether the injected CO_2 is sequestered or is leaking to the surface. Leakage to the surface can occur via fracture systems and fault zones, or simply through the casing of injection wells. Finally, it remains a challenge to fully understand the hydraulic properties of a field area. The method described by Shapiro et al. (2002), which uses microseismicity triggering fronts to measure the (possibly anisotropic) permeability tensor, is one way to achieve this goal through advanced monitoring. Other examples, which focus on the development of approaches to jointly invert time-lapse tomographic radar data and hydrological data (such as wellbore measurements or tracer tests) have illustrated the utility of geophysical methods for providing high resolution estimates of hydrualic conduductivity (e.g., Kowalsky et al. 2005).

4 MONITORING BIOGEOCHEMICAL PROCESSES

Successful management of subsurface systems often requires information about biogeochemical properties and processes, such as the type and concentration of pore fluids or sediment geochemistry, redox zonation, and the transformation of and interactions between species as a system is being manipulated. In addition to using geophyiscal methods to track fluid distribution as was described in the previous section, there is also a need to track the onset and characteristics of geochemical changes that occur in response to fluid introduction or replacement. For example, the potential of using geophysical techniques to monitor CO_2 distribution associated with petroleum and sequestration applications was previously discussed. In addition to the fluid migration, introduction of the CO_2 can cause dissolution of minerals or can mobilize trace metals (e.g., Kharaka et al. 2006). A current challenge is to use geophysical methods to monitor these geochemical changes. Although many studies have focused on investigating the geophysical signatures of pore fluid substitutions associated with infiltrating soil water, hydrocarbon extraction, or saltwater intrusion, few studies have explored the impact of other types of (bio)geochemical alterations on the effective geophysical signature.

Recent investigations have explored the use of different types of geophysical methods for monitoring biogeochemical changes, some of which are microbially mediated. Several studies have revealed anomalously higher electrcal conductivity signatures associated with hydrocarbon contaminated sites, which has been attributed to altered fluid chemistry associated with biological degradation (e.g., Atekwana et al. 2005). Abdel Aal et al. (2004) explored the effects of microbial processes on electrolytic and interfacial electrical properties Ntarlagiannis et al. (2005b) explored how induced polarization measurements changed as a function of microbial cell concentration and grain surface coating. The use of self-potential methods to map large-scale variations in redox conditions was described by Naudet et al. (2004). Chen et al. (2004) illustrated how Ground Penetrating Radar (GPR) amplitudes could be used to estimate sediment geochemistry. Williams et al. (2005) and Ntarlagiannis et al. (2005a) describe seismic and Induced Polarization (Fink et al. 1990) responses to biomineralization under controlled column conditions. The results from these and other recent studies highlight the potential that geophysical methods have for monitoring complex biogeochemical processes, which is a prerequisite for successful management of subsurface problems or resources. Two of these studies are briefly described below.

4.1 Characterization of Redox Potential

The observed distribution of redox processes is an important factor in the design of remedial strategies for contaminated groundwater systems. Redox potential, or Eh, indicates the tendency for oxidation-reduction reactions to occur. A series of redox gradients often is established adjacent to contaminant plumes (e.g., Loveley et al. 1994). Understanding redox zonation is a particularly important factor in designing an optimal remediation approach. Under equilibrium conditions, insitu measurements of redox potential can be obtained through well-bore measurements, although disturbance and contamination associcated with drilling often corrupt these measurements. The distribution of the kinetic redox processes can also be deduced by observing patterns of electron acceptor consumption, final product production, and concentrations of dissolved hydrogen based on measurements retrieved from well-bores. However, many studies suggest that inference of redox processes using such approaches is not straightforward.

A recent study assessed redox potentials associated with a landfill contaminant plume using the self-potential technique (Naudet et al. 2004). Self-potential signals measure the potential difference between a fixed reference non polarizable electrode and a roving electrode using a high input impedance voltmeter. In near-surface systems, the self-potential response depends on the groundwater flow (electro-kinetic contribution) and redox conditions (electro-redox contribution). Naudet et al. (2004) used the variation in hydraulic head measurements in an aquifer near a landfill to estimate the electro-kinetic contribution (Figures. 9a and 9b), which was subsequently removed from the effective self-potential signal. The residual self-potential signal correlated well with redox potential measurements collected in well-bores, and was used to provide spatially exten-

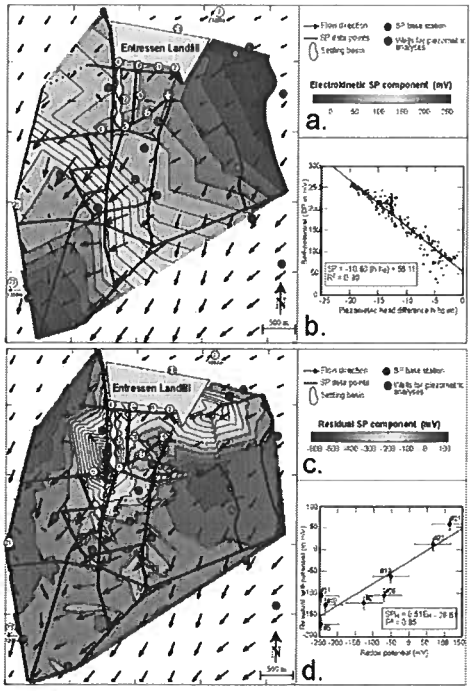

Figure 9. The streaming potential component of the self-potential signals is calibrated outside the contaminant plume by plotting the kriged self-potential signals and the hydraulic heads. The arrows provide the direction of ground water flow and are proportional to the hydraulic head gradient (b). The streaming potential component is then estimated everywhere using the kriged hydraulic heads (a). The residual self-potential signals are obtained by removing the streaming potential component from the measured self-potential signals (c). This residual self-potential map is proportional to the redox potentials measured in the aquifer in a set of piezometers (d).

sive estimates of redox potential (Figure 9c and 9d). This study illustrates the value of an inexpensive geophysical technique to provide information about redox potential over field-relevant spatial scales and in a non invasive manner. Such information can be used to design remediation treatments or to choose the locations of monitoring wells.

4.2 Monitoring biogeochemical dynamics using seismic and induced polarization methods

Remediation treatments may induce dynamic transformations in biogeochemical and hydrological properties in the subsurface. Potential alterations due to remediation treatments include, for example, dissolution and precipitation of minerals, surface complexation, gas evolution, changes in soil water and oxygen levels, sorption, attachment/detachment, oxidation and reduction, biofilm generation, and changes in permeability and porosity. Although understanding and ultimately manipulating these transformations is critical for sustainable in-situ remediation, developing such an understanding is hindered by our inability to observe biogeochemical dynamics in-situ over a spatial scale relevant for investigating the macroscopic behavior of a system, in the presence of natural heterogeneity.

Recent research has explored the use of time-lapse seismic and induced polarization methods for detecting the evolution of gasses, biofilms, and precipitates associated with processes that commonly occur during biostimulation, such as during denitrification and sulfate reduction. Biostimulation involves the addition of carbon sources, nutrients, and electron acceptors or donors into the subsurface to increase, or 'stimulate' the activity and growth of naturally occuring microorganisms. Once stimulated, these organisms can mediate processes that benifially change the toxicity and mobility of contaminants (Office of Biological and Environmental Research of the Department of Energy 2003). Williams et al. (2005) conducted laboratory biostimulation experiments under saturated flow conditions to monitor the biogeochemical, hydrological, and geophysical responses associated with sulfate reduction using a suite of columns having vertically distributed samplers and geophysical sensors (Figure 10a). This study indicated how microbe-mediated zinc and iron sulfides, which developed along grain surfaces within the pore space, were attached to microbial cells (Figure 10b). The acoustic amplitude and induced polarization signatures were altered as the nanocrystals formed, attached to the migrating microbes, and eventually aggregated (Figure 10c and 10d). These results illustrate the potential that geophysical methods have for elucidating important biogeochemical processes over space and time, such as those that often accompany bioremediation of metal-contaminated aquifers.

4.3 Challenges and Future Directions in Monitoring Biogeochemical Processes

Advances in monitoring changes in biogeochemical properties have to date primarily been applied to environmental problems, where there is a significant interest in manipulating biogeochemical processes to render contaminants less mobile or less toxic. However, these approaches could also be used to assist in petroleum reservoir investigations, such as to monitor reservoir stimulation or well-bore completion procedures. For example, a new chemical injection treatment has recently been developed to increase sand consolidation and cementation in the near vicinity of the borehole, thereby significantly decreasing sand production (Kotlar et al. 2005), and injection of bacterial suspensions following water flooding has been explored as a technique to enhance

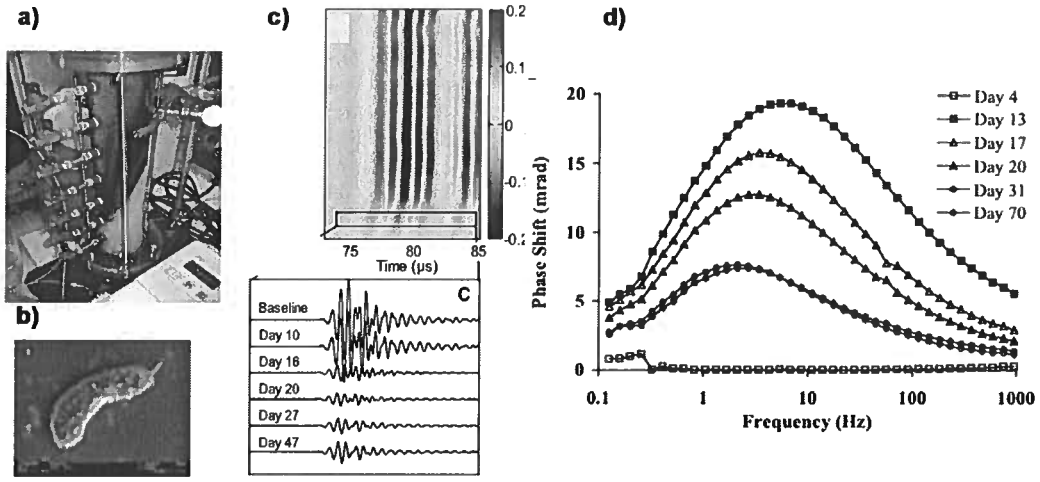

Figure 10. (a) Example experimental column illustrating how measurements are collected down the length of the column and the presence of a developed sulfide precipitation front associated with sulfate reduction. (b) TEM image illustrating the mineralized encrustation on the experimental microbe due to the formation of sulfide precipitates (scale approximately 1 μm), Changes in (c) seismic amplitude and (d) induced polarization response associated with the initiation and aggregation of sulfide precipitates. Modified from Williams et al. (2005).

oil recovery, which has been shown to increase the recovery factor by 3-5% (Crecente et al. 2005). In these cases, time-lapse 3D VSP surveys, where waves excited by sources on the earth's surface are recorded by sensors in a borehole, could likely provide valuable information about the spatial distribution of the treated zones, and the the quality and distribution of the cementation.

Quantitative geochemical characterization using geophysical methods poses several challenges. Perhaps greatest among these are the challenges associated with scaling, non-uniqueness, and data fusion. Scale matching issues are significant because many of the biogeochemical properties or processes occur at microscopic scales that are much smaller than the smallest scale resolved by the geophysical measurement. Non-uniqueness of the geophysical responses is a problem because geophysical signatures often respond to hydrogeological as well as geochemical heterogeneity. Additionally, as a system is treated (for example, during environmental remediation), multiple biogeochemical transformations often occur simultaneously over the support scale of the geophysial measurement (e.g., Hubbard et al. 2006), and modified biogeochemical properties can in turn alter hydrological properties (such as pore clogging associated with gas or precipitate development), thereby further modifying the geophysical response. Together, these complex and coupled transformations hinder the ability to uniquely interpret system transformations given a particular geophysical response. Understanding the full capacity of geophysical methods for characterization geochemical properties and processes is

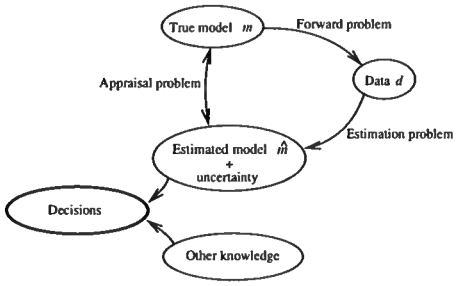

Figure 11. Different elements in creating an interface between geophysical measurements and decision-making.

expected to improve through increased laboratory and field experimental efforts, development of rock physics relationships and estimation approaches, and through comparisons of geophysically obtained geochemical parameter estimates with numerical modeling predictions of geochemical transformations.

5 DISCUSSION AND FUTURE CHALLENGES

Although much progress has been made in non-invasive monitoring, there are several open research questions. Some of these research questions are related to technical aspects of a specific monitoring techniques. Other research questions are common to many different as-

pects of non-invasive monitoring. We introduce these over-riding research questions using Figure 11.

In a physical experiment data are collected. These data are determined by the true earth model through the physics of the *forward problem* (geomechanical, hydrological, biogeochemical). From the data one can estimate an earth model, or in the case of monitoring, changes in the the earth model. Because the data are limited, contaminated with noise, and often sampled at disparate scales, these model estimates differ from the true model. Quantifying these differences and associated uncertianty is the *appraisal problem.* In practical implementations of monitoring techniques, measuring the changes in geophysical attributes or even estimating the change in subsurface properties using the geophysical data is not sufficient. Instead, these data must be integrated with other information to ascertain the impact that the estimated changes have on how a system should be managed or treated to solve problems of scientific, economic, or other societal relevance.

Figure 11 illustrates several research challenges in optimally using non-invasive monitoring. The forward problem, that gives the data for a given model often is sometimes well-known, as in the case of InSAR where the change in the phase of the radar waves is connected by well-known physics to the deformation of the earth's surface. In other applications, the forward problem is not well known. Examples include the relation between compaction and seismic velocity (section 2.2, or between various geophysical attributes and biogeochemical properties (section 4),

Data collection is changing because of new developents of instrumention and the capability to handle increasingly larger continuous data streams. Cheap microinstrumentation, such as *smart dust* (Kahn et al. 2000) as well as Micro Electro Mechanical Systems, or MEMS (Gibson et al. 2005) make it possible to carry out measurements at an unprecedented scale. This has led to the concept of the *instrumented oilfield* (Tura and Cambois 2001). Research challenges in this area include the transmission of information of large amounts of subsurface instruments to the surface, and handling the data streams of large networks of sensors that operate continuously.

The estimation of uncertainty is a long-standing problem in model estimation, and the same holds for monitoring techniques. For linear inverse problem, the assessment of uncertainty is well-developed (e.g., Tarantola 1987, Parker 1994, Aster et al. 2004). The application to current large-scale estimation problem is still problematic (e.g., how does one visualize a correlation matrix for 10^6 parameters?). For nonlinear estimation problems, there is no general theory to estimate the uncertainty (Snieder 1998). In this case, numerical techniques are presently the only available tool (e.g., Mosegaard and Tarantola 1995, Sambridge 1998, Sambridge et al. 2006), but the computational cost for many problems is prohibitive.

In many practical problems, different kinds of data are collected. Combining these disparate data streams is a challenge. Data fusion, where different data are combined, and data assimilation, where new data are used to update existing models for the subsurface, still are challenging issues when it concerns the implementation in practical monitoring problems.

As indicated in figure 11, decisions are often based on the outcome of monitoring experiments and other knowledge. The integration of these different pieces of information is often achieved by the expertise of the decision-makers and their advisers. There is a lack of techniques to integrate the a-priori knowledge of the problem effectively in the mathematical formulation, and numerical implementation, of the estimation problem. For example, model parameterization and estimation of uncertainty are often more driven by mathematical and/or numerical considerations, than by the geological reality of the subsurface. Geologically realistic information is often difficult to glean from experts due to standard, human cognitive biases (Baddeley et al. 2004), and real-world knowledge is often difficult to parameterize. Nevertheless, it is critical that such information is introduced correctly as it directly affects not only model estimates but their associated uncertainties. Consequently, research into methods to include reliable information in monitoring-type problems has begun in a variety of fields (e.g., Thore et al. 2002, Wood and Curtis, 2004).

The interface with the decision-makes is often not optimal. The outcome of the monitoring experiment as a change in the model parameters plus its uncertainty, is often not in the form that is useful for the decision-maker. Knopman (2006) described the importance of scientists engaging with decision-makers during the research stage, rather than first focusing on understanding or predicting processes and subsequently informing decision makers after completion of the research. He suggests that with early inclusion, scientific experiments and decision-making tools can be designed that optimally guide the choices about the level of complexity that is needed to guide decisions about large environmental problems, such as climate change, nuclear waste storage, or sustainable water management. Another problem in using monitoring techniques effectively is the gap in the time-scale with which the decision-maker needs results, and the time-scale on which a monitoring experiment can be carried out. In this context it is also important that monitoring techniques can be carried out economically, because this allows the monitoring to be carried out more frequently.

Much progress has been made in non-invasive geophysical monitoring of the subsurface, but as shown here, there are numerous open research questions. Resolving these research questions is crucial for optimally

exploiting our technological capabilities for monitoring the subsurface.

Acknowledgments: We thank Ken Larner and Raymond Jeanloz for their comments. This work resulted from the workshop "Advanced non-invasive monitoring techniques" that was financially supported by the office of Basic Energy Science of the Department of Energy. We are grateful for their financial support, and by the support and advice of David Lesmes, Nick Woodward, and Sophia Kitts.

Note: This paper has been submitted to the Annual Review of Earth and Planetary Sciences.

REFERENCES

G.Z. Abdel Aal, E. Atekwana, Slater L.D., and E.A. Atckwana. Effects of microbial processes on electrolytic and interfacial electrical properties of unconsolidated sediments. *Geophys. Res. Lett.*, 31:L12505, doi: 10.1029/2004GL020030, 2004.

D. Alumbaugh, R.P. Chang, L. Paprocki, J. Brainard, R.J. Glass, and C.A. Rautman. Estimating moisture contents in the vadose zone using cross-borehole ground penetrating radar: a study of accuracy and repeatability. *Water Resources Res.*, page 1309, 2002.

R. N. Anderson, P. Flemings, S. Losh, J. Austin, and R. Woodhams. Gulf of Mexico growth fault drilled, seen as oil, gas migration pathway. *Oil & Gas Journal*, 92:97–103, 1994.

R. N. Anderson, W. He, M. A. Hobart, C. R. Wilkinson, and H. R. Roice. Active fluid flow in the Eugene Island area, offshore Louisiana. *The Leading Edge*, 10:12–17, 1991.

R. Aster, B. Borchers, and C.H. Thurber. *Parameter Estimation and Inverse Problems*. Academic Press, San Diego, 2004.

E.A. Atekwana, E. Atekwana, F.D. Legall, and R.V. Krishnamurthy. Biodegredation and mineral weathering controls on bulk electrical conductivity in a shallow hydrocarbon contaminated aquifer. *J. of Contaminant Hydrology*, 80:149–167, 2005.

M. Baddeley, A. Curtis, and R. Wood. An introduction to prior information derived from probabilistic judgements: elicitation of knowledge, cognitive bias and herding. In Wood R. and A. Curtis, editors, *Geological Prior Information*, number 239 in Geol. Soc. Lond. Special Publication, pages 15–27. 2004.

A. Bakulin and R. Calvert. Virtual source: new method for imaging and 4D below complex overburden. *Expanded abstracts of the 2004 SEG-meeting*, pages 2477–2480, 2004.

R. Bamler and P. Hartl. Synthetic aperture radar interferometry. *Inverse Problems*, 14:R1–R54, 1998.

G.W. Bawden, W. Thatcher, R.S. Stein, K.W. Hudnut, and G. Peltzer. Tectonic contraction across Los Angeles after removal of groundwater pumping effects. *Nature*, 412:812–815, 2001.

R. D. Benson and T. L. Davis. CO_2 Sequestration in a Depleted Oil Reservoir - West Pearl Queen Field. In *67th EAGE Conference and Exhibition*, page P137, 2005.

A. Binley, G. Cassiani, R. Middleton, and P. Winship. Vadose zone model parameterisation using cross-borehole radar and resistivity imaging. *J. Hydrology*, 267:147–159, 2002.

J. Brown, F. Klopping, D. van Westrum, T. Niebauer, R. Bilson, J. Brady, J. Ferguson, T. Chen, and J. Siebert. Preliminary absolute gravity survey results from water injection monitoring program at Prudhoe Bay. In *72nd Ann. Internat. Mtg., Society of Exploration Geophysicists, Expanded Abstracts*, pages 791–793, 2002.

R. Bürgmann, P.A. Rosen, and E.J. Fielding. Synthetic aperture radar interferometry to measure earth's surface topography and its deformation. volume 28 of *Ann. Rev. Earth Planet. Sci.*, pages 169–209. 2000.

R. Calvert. *Insights and methods of 4D reservoir monitoring and characterization*, volume 8 of *Distinguished instructor series*. Society of Exploration Geohysicists, Tulsa, OK, 2005.

R.W. Calvert, A. Bakulin, and T.C. Joners. Virtual sources, a new way to remove overburden problems. *Expanded abstracts of the 2004 EAEG-meeting*, 2004.

M. Campillo and A. Paul. Long-range correlations in the diffuse seismic coda. *Science*, 299:547–549, 2003.

S. Chand and Minshull. T. A. Seismic constraints on the effects of gas hydrate on sediment physical properties and fluid flow: a review. *Geofluids*, 3:275–289, 2003.

J. Chen, S. Hubbard, Y. Rubin, E. Murray, C. andRoden, and E. Majer. Geochemical characterization using geophysical data and Markov Chain Monte Carlo methods: A case study at the South Oyste bacterial transport site in Virginia. *Water Resources Res.*, pages W12412, doi: 1029/2003WR002883, 2004.

A. Cogbill, F. Ferguson, and E. Keating. Use of Absolute Gravity Measurements to Monitor Groundwater in the Española Basin, New Mexico. In *EOS Trans., AGU, 86(18), Jt. Assem. Suppl.*, Abstract GP23A–03, 2005.

S. Crampin. The new geophysics: Shear-wave splitting provides a window into the crack-critical rock mass. *The Leading Edge*, 22:536–549, 2003.

S. Crampin, S. Chastin, and Y. Guo. Shear-wave splitting in a critical crust: III - preliminary report of multi-variable measurements in active tectonics. *J. of Appl. Geophys.*, 54:265–277, 2003.

C. Crecente, K. Rasmussen, O. Torsaeter, A. Strom, and E. Kowalewski. An experimental study of microbial improved oil recovery by using Rhodococcus SP. 094. *Soc. of Core Analysts*, pages CA2005–45, 2005.

A. Derode, E. Larose, M. Campillo, and M. Fink. How to estimate the Green's function for a heterogeneous medium between two passive sensors? Application to acoustic waves. *Appl. Phys. Lett.*, 83:3054–3056, 2003a.

A. Derode, E. Larose, M. Tanter, J. de Rosny, A. Tourin, M. Campillo, and M. Fink. Recovering the Green's function from far-field correlations in an open scattering medium. *J. Acoust. Soc. Am.*, 113:2973–2976, 2003b.

T.H. Dixon. An introduction to the Global Positioning System and some geological applications. *Rev. of Geophys.*, 29:249–276, 1991.

P. Enge and P. Misra. Special issue on global positioning system. *Proc. IEEE*, 87:3–15, 1999.

J.B. Fink, B.K. Sternberg, E.O. McAlister, W.G. Wieduwilt, and S.H. Ward, editors. *Induced polarization, applications and case histories*. Number 4 in Investigations in

geophysics. Society of Exploration Geophysicitst, Tulsa, OK, 1990.

A.M. Freed. Earthquake triggering by static, dynamic, and postseismic stress transfer. In R. Jeanloz, A.L. Albee, and K.C. Burke, editors, *Ann. Rev. Earth Planet. Sci.*, volume 33, pages 335–367. 2005.

G.K. Furnes, O.B. Kvamme, and O. Nygaard. Tidal response on the reservoir pressure at the Gulfaks oil field. *Pure Appl. Geoph.*, 135:425–445, 1991.

M. Furumoto, Y. Ichimori, N. Hayashi, and Y. Hiramutsu. Seismic wave velocity changes and stress build-up in the crust of the Kanto-Tokai region. *Geophys. Res. Lett.*, 28:3737–3730, 2001.

F. Gassmann. Über die Elastizität poroser Medien. *Vierteljahrsschrift der Naturforschenden Gesellschaft in Zürich*, 96:1–23, 1951.

J. Gibson, R. Burnett, S. Ronen, and H. Watt. MEMS sensors: Some issues for consideration. *The Leading Edge*, 24:786–790, 2005.

J. Gomberg and P. Johnson. Dynamic triggering of earthquakes. *Nature*, 437:830, 2005.

A. Grêt, R. Snieder, R.C. Aster, and P.R. Kyle. Monitoring rapid temporal changes in a volcano with coda wave interferometry. *Geophys. Res. Lett.*, 32:L06304, 10.1029/2004GL021143, 2005.

A. Grêt, R. Snieder, and J. Scales. Time-lapse monitoring of rock properties with coda wave interferometry. *J. Geophys. Res.*, 111:B03305, doi:10.1029/2004JB003354, 2006a.

A. Grêt, R. Snieder and U. Özbay. Monitoring in-situ stress changes in a mining environment with coda wave interferometry. *Geophys. J. Int., in press*, 2006b.

M. Haney, R. Snieder, J.P. Ampuero, and R. Hofmann. Spectral element modelling of fault-plane reflections arising from fluid presssure distributions. *submitted to Geophys. J. Int.*, 2006.

M. Haney, R. Snieder, J. Sheiman, and S. Losh. A moving fluid pulse in a fault zone. *Nature*, 437:46, 2005.

P. Hatchell and S. Bourne. Rocks under stain: Strain-induced time-lapse time shifts are observed for depleting reservoirs. *The Leading Edge*, 24:1222–1225, 2005.

D. P. Hill, J. O. Langbein, and S. Prejean. Relations between seismicity and deformation during unrest in Long Valley Caldera, California, from 1995 through 1999. *J. of Volcanology and Geothermal Res.*, 127:175–193, 2003.

E. C. D. Hooper. Fluid migration along growth faults in compacting sediments. *J. of Pet. Geology*, 14:161–180, 1991.

S. Hubbard, J. Chen, Y. Fang, K. Williams, S. Mukhopadhyay, E. Sonnenthal, K. McFarlane, N. Linde, and T. Scheibe. Improved parameterization of hydrological models and reduction of geophysical monitoring data ambiguity through joint use of geophysical and numerical modeling methods. In *Extended proceedings, CWMR XVI-Computational Methods in Water Resources*, 2006.

S.S. Hubbard, J.E. Peterson Jr, E.L. Majer, P.T. Zawislanski, K.H. Williams, J. Roberts, and F. Wobber. Estimation of permeable pathways and water content using tomographic radar data. *The Leading Edge*, 16:1623–1630, 1997.

J.M. Kahn, R.H. Katz, and K.S.J. Pister. Emerging challenges: Mobile networking for "smart dust". *J. of Comm. and Networks*, 2:188–196, 2000.

Y.K. Kharaka, R.D. Cole, S.D. Hovorka, W.D. Gunter, K.G. Knauss, and B.M. Freifeld. Gas-water-rock interactions in Frio formation following co_2 injection: Implications for the storage of greenhouse gases in sedimentary basins. *Geology*, 34(7):577–580, doi:10.1130/G22357.1, 2006.

D.S. Knopman. Success matters: recasting the relationship among geophysical, biological, and behavioral scientists to support decision making on major environmental challenges. *Water Resources Res.*, 42:W03S09, doi: 10.1029/2005WR004333, 2006.

H.K. Kotlar, F. Haavind, M. Springer, S.S. Bekkelund, and O. Torsaeter. A new concept of chemical sand consolidation: From idea and laboratory qualification to field application. *SPE*, page 95723, 2005.

M.B. Kowalsky, S. Finsterle, J. Peterson, S. Hubbard, Y. Rubin, E. Majer, A. Ward, and G. Gee. Estimation of field-scale soil hydraulic and dielectric parameters through joint inversion of GPR and hydrological data. *Water Resources Res.*, 41:doi: 10.1029/2005WR004237, 2005.

M.B. Kowalsky, S. Finsterle, and Y. Rubin. Estimating flow parameter distributions using ground-penetrating radar and hydrological measurements during transient flow in the vadose zone. *Adv. in Water Res.*, 27(6):583–599, 2004.

M. Landrø and L. K. Stronen. 4d study of fluid effects on seismic data in the Gullfaks Field, North Sea. *Geofluids*, 3:233–244, 2003.

E. Larose, G. Montaldo, A. Derode, and M. Campillo. Passive imaging of localized reflectors and interfaces in open media. *Appl. Phys. Lett.*, 88:104103, 2006.

W. Lauterborn, T. Kurz, and M. Wiesenfeldt. *Coherent Optics, Fundamentals and Applications*. Springer-Verlag, Berlin, 1995.

O.I. Lobkis and R.L. Weaver. On the emergence of the Green's function in the correlations of a diffuse field. *J. Acoust. Soc. Am.*, 110:3011–3017, 2001.

J.N.S. Long and R.C. Ewing. Yucca Mountain: Earth-science issues at a geological repository for high-level nuclear waste. In R. Jeanloz, editor, *Ann. Rev. Earth Planet. Sci.*, volume 32, pages 363–401, 2004.

S. Losh, L. Eglinton, M. Schoell, and J. Wood. Vertical and lateral fluid flow related to a large growth fault. *AAPG Bulletin*, 83:244–276, 1999.

D.R. Loveley, F.H. Chapelle, and J.C. Woodward. Use of dissolved H_2 concentrations to determine distribution of microbially catalyzed redox reactions in anoxic groundwater. *Env. Science and Techn.*, 21:1210–1255, 1994.

Miyazawa M. and J. Mori. Evidence suggesting fluid flow beneath Japan due to periodic seismic triggering from the 2004 Sumatra-Andaman earthquake. *Geophys. Res. Lett.*, 33:L05303, doi:10.1029/2005GL025087, 2006.

A. Malcolm, J. Scales, and B.A. van Tiggelen. Extracting the Green's function from diffuse, equipartitioned waves. *Phys. Rev. E*, 70:015601, 2004.

D. Massonnet and K.L. Feigl. Radar interferometry and its application to changes in the earth's surface. *Rev. Geophys.*, 36:441–500, 1998.

K. Mehta, R. Snieder, and V. Graizer. Extraction of near-surface properties for lossy layered medium using propagator matrix. *Submitted to Geophys. J. Int.*, 2006.

S. A. Miller, C. Collettini, L. Chiaraluce, M. Cocco, M. Barchi, and B. J. P. Kaus. Aftershocks driven by a high-pressure CO_2 source at depth. *Nature*, 427:724–727,

2004.

S. E. Minkoff, C. M. Stone, S. Bryant, and M. Peszynska. Coupled geomechanics and flow simulation for time-lapse seismic modeling. *Geophysics*, 69:200–211, 2004.

J. R. Moore, S. D. Glaser, H. F. Morrison, and G. M. Hoversten. The streaming potential of liquid carbon dioxide in Berea sandstone. *Geophys. Res. Lett.*, 31:L17610, 2004.

K. Mosegaard and A. Tarantola. Monte Carlo sampling of solutions to inverse problems. *J. Geophys. Res.*, 100:12431–12447, 1995.

V. Naudet, A. Revil, E. Rizzo, J.-Y. Bottero, and P. Bégassat. Groundwater redox conditions and conductivity in a contaminant plume from geoelectrical investigations, hydrology and earth system. *Hydrology and Earth System Sciences*, 8(1):8–22, 2004.

T. Nishimura, S. Tanaka, H. Yamamoto, T. Sano, M. Sato, H. Nakahara, N. Uchida, S. Hori, and H. Sato. Temporal changes in seismic velocity of the crust around Iwate volcano, Japan as inferred from analyses of repeated active seismic experiment data from 1998 to 2003. *Earth Planets Space*, 57:491–505, 2005.

T. Nishimura, N. Uchida, H. Sato, M. Ohtake, S. Tanaka, and H. Hamaguchi. Temporal changes of the crustal structure associated with the M6.1 earthquake on September 3, 1998, and the volcanic activity of Mount Iwate, Japan. *Geophys. Res. Lett.*, 27:269–272, 2000.

D. Ntarlagiannis, K.H. Williams, Slater L., and S. Hubbard. The low frequency response to microbial induced sulfide precipitation. *J. Geophys. Res.*, 110:G02009, 10.1029/2005JG000024, 2005.

J. E. Nyquist and C. E. Corry. Self-potential: The ugly duckling of environmental geophysics. *The Leading Edge*, 21:446–451, 2002.

Office of Biological and Environmental Research of the Department of Energy. *Bioremediation of metals and radionuclides.* 2003.

D. Pandolfi, C.J. Bean, and G. Saccorotti. Coda wave interferometric detection of seismic velocity changes associated with the 1999 M=3.6 event at Mt. Vesuvius. *Geophys. Res. Lett.*, 33:L06306, doi:10.1029/2005GL025355, 2006.

R.L. Parker. *Geophysical Inverse Theory.* Princeton Univ. Press, Princeton NJ, 1994.

G. Poupinet, W.L. Ellsworth, and J. Fréchet. Monitoring velocity variations in the crust using earthquake doublets: an application to the Calaveras Fault, California. *J. Geophys. Res.*, 89:5719–5731, 1984.

S. R. Pride, J. M. Harris, D. L. Johnson, A. Mateeva, K. T. Nihei, R. L. Nowack, J. W. Rector, H. Spetzler, R. Wu, T. Yamomoto, J. G. Berryman, and M. Fehler. Permeability dependence of seismic amplitudes. *The Leading Edge*, 22:518–525, 2003.

S. R. Pride and F. D. Morgan. Electrokinetic dissipation induced by seismic waves. *Geophysics*, 56:914–925, 1991.

A. Ratdomopurbo and G. Poupinet. Monitoring a temporal change of seismic velocity in a volcano: Application to the 1992 eruption of Mt. Merapi (Indonesia). *Geophys. Res. Lett.*, 22:775–778, 1995.

A. Revil and L. M. Cathles. Fluid transport by solitary waves along growing faults: A field example from the South Eugene Island Basin, Gulf of Mexico. *Earth and Planet. Sci. Lett.*, 202:321–335, 2002.

A. Revil and N. Linde. Chemico-electromechanical coupling in microporous media. *J. of Colloid and Interface Sci., in press*, 2006.

J. R. Rice. Fault stress states, pore pressure distributions, and the weakness of the San Andreas fault. In B. Evans and T.-F. Wong, editors, *Fault Mechanics and Transport Properties of Rocks*, pages 475–503. Academic Press, San Diego, 1992.

P.M. Roberts, W. Scott Phillips, and M.C. Fehler. Development of the active doublet method for measuring small velocity and attenuation changes in solids. *J. Acoust. Soc. Am.*, 91:3291–3302, 1992.

E. Roeloffs, M. Sneed, D. L. Galloway, M. L. Sorey, C. D. Farrar, J. F. Howie, and J. Hughs. Water level changes induced by local and distant earthquakes at Long Valley Caldera, California. *J. of Volc. and Geoth. Res.*, 127:175–193, 2003.

P. Roux, K.G. Sabra, P. Gerstoft, and W.A. Kuperman. P-waves from cross correlation of seismic noise. *Geophys. Res. Lett.*, 32:L19303, doi: 10.1029/2005GL023803, 2005a.

P. Roux, K.G. Sabra, W.A. Kuperman, and A. Roux. Ambient noise cross correlation in free space: Theoretical approach. *J. Acoust. Soc. Am.*, 117:79–84, 2005b.

K.G. Sabra, P. Gerstoft, P. Roux, W.A. Kuperman, and M.C. Fehler. Extracting time-domain Green's function estimates from ambient seismic noise. *Geophys. Res. Lett.*, 32:L03310, doi: 10.1029/2004GL021862, 2005.

M. Sambridge. Exploring mutidimensional landsapes without a map. *Inverse Problems*, 14:427–440, 1998.

M. Sambridge, C. Beghein, F. Simons, and R. Snieder. How do we understand and visualize uncertainty? *The Leading Edge*, 25:542–546, 2006.

C. M. Sayers, M. J. Woodward, and R. C. Bartman. Seismic pore pressure prediction using reflection tomography and 4-C seismic data. *The Leading Edge*, 21:188–192, 2002.

C. Sens-Schönfelder and U. Wegler. Passive image interferometry snd seasonal variations at Merapi volcano, Indonesia. *Submitted to Geophys. Res. Lett.*, 2006.

N.M. Shapiro, M. Campillo, L. Stehly, and M.H. Ritzwoller. High-resolution surface-wave tomography from ambient seismic noise. *Science*, 307:1615–1618, 2005.

S. A. Shapiro, E. Rothert, V. Rath, and J. Rindschwentner. Characterization of fluid transport properties of reservoirs using induced seismicity. *Geophysics*, 67:212–220, 2002.

P. G. Silver, F. Niu, T. M. Daley, and E. L. Majer. Developing a Methodology for Measuring Stress Transients at Seismogenic Depths. In *EOS Trans., AGU, 85(47), Fall Meet. Suppl.*, pages Abstract S13E–01, 2004.

D. Smit and C.M. Sayers. Can tidal-driven pressure changes reveal reservoir properties for use in 4D monitoring? *World oil*, pages 37–43, March 2005.

R. Snieder. The role of nonlinearity in inverse problems. *Inverse Problems*, 14:387–404, 1998.

R. Snieder. Coda wave interferometry. In *2004 McGraw-Hill yearbook of science & technology*, pages 54–56. McGraw-Hill, New York, 2004a.

R. Snieder. Extracting the Green's function from the correlation of coda waves: A derivation based on stationary phase. *Phys. Rev. E*, 69:046610, 2004b.

R. Snieder. Retrieving the Green's function of the diffusion equation from the response to a random forcing. *Submitted to Phys. Rev. E*, 2006a.

R. Snieder. The theory of coda wave interferometry. *Pure and Appl. Geophys.*, 163:455–473, 2006b.

R. Snieder and E. Şafak. Extracting the building response using seismic interferometry; theory and application to the Millikan library in Pasadena, California. *Bull. Seismol. Soc. Am.*, 96:586–598, 2006.

R. Snieder, A. Grêt, H. Douma, and J. Scales. Coda wave interferometry for estimating nonlinear behavior in seismic velocity. *Science*, 295:2253–2255, 2002.

R. Snieder, J. Sheiman, and R. Calvert. Equivalence of the virtual source method and wavefield deconvolution in seismic interferometry. *Phys. Rev. E*, 73:066620, 2006a.

R. Snieder, K. Wapenaar, and K. Larner. Spurious multiples in seismic interferometry of primaries. *Geophysics, in press*, 2006b.

R.P.W. Stancliffe and W.A. van der Kooij. The use of satellite-based radar interferometry to monitor production activity at the Cold Lake heavy oil field, Alberta, Canada. *AAPG Bulletin*, 85:781–793, 2001.

B. Suski, A. Revil, A. Boleve, K. Titov, P. Konosavsky, M. Voltz, C. Dages, and O. Huttel. Monitoring of an Infiltration Experiment Using the Self-Potential Method. *submitted to Water Resources Res.*, 2006.

A. Tarantola. *Inverse Problem Theory.* Elsevier, Amsterdam, 1987.

N. Teanby, J.-M. Kendall, R. H. Jones, and O. Barkved. Stress-induced temporal variations in seismic anisotropy observed in microseismic data. *Geophys. J. Int.*, 156:459–466, 2004.

P. Thore, A. Shtuka, M. Lecour, T. Ait-Ettajer, and R. Cognot. Structural uncertainties: Determination, management, and applications. *Geophysics*, 67:840–852, 2002.

K. Titov, A. Revil, P. Konosavsky, S. Straface, and S. Troisi. Numerical modelling of self-potential signals associated with a pumping test experiment. *Geophys. J. Int.*, 162:641–650, 2005.

I. Tsvankin. *Seismic signatures and analysis of reflection data in anisotropic media.* Pergamon, 2001.

A. Tura, T. Barker, P. Cattermole, C. Collins, J. Davis, P. Hatchell, K. Koster, P. Schutjens, and P. Wills. Monitoring primary depletion reservoirs using amplitudes and time shifts from high-repeat seismic surveys. *The Leading Edge*, 24:1214–1221, 2005.

A. Tura and G. Cambois. Instrumented oil fields, an introduction to this special section. *The Leading Edge*, 20(6):613, 2001.

D.J. van Manen, J.O.A. Robertson, and A. Curtis. Modelling of wave propagation in inhomogeneous media. *Phys. Rev. Lett.*, 94:164301, 2005.

H.F. Wang. *Theory of linear poroelasticity, with applications to geomechanics and hydrogeology.* Princeton Univ. Press, Princeton, 2000.

K. Wapenaar. Retrieving the elastodynamic Green's function of an arbitrary inhomogeneous medium by cross correlation. *Phys. Rev. Lett.*, 93:254301, 2004.

K. Wapenaar, J. Fokkema, and R. Snieder. Retrieving the Green's function by cross-correlation: a comparison of approaches. *J. Acoust. Soc. Am.*, 118:2783–2786, 2005.

R.L. Weaver and O.I. Lobkis. Ultrasonics without a source: Thermal fluctuation correlations and MHz frequencies. *Phys. Rev. Lett.*, 87:134301, 2001.

R.L. Weaver and O.I. Lobkis. Diffuse fields in open systems and the emergence of the Green's function. *J. Acoust. Soc. Am.*, 116:2731–2734, 2004.

U. Wegler, B.-G. Lühr, R. Snieder, and A. Ratdomopurbo. Increase of shear velocity before the 1998 eruption of Merapi volcano Indonesia. *Geophys. Res. Lett.*, 33:L09303, doi:10.1029/2006GL025928, 2006.

U. Wegler and C. Sens-Schönfelder. Fault zone monitoring with passive image interferometry. *Submitted to Geophys. J. Int.*, 2006.

J. K. Whelan, L. Eglinton, M. C. Kennicutt, II, and Y. Qian. Short-time-scale (year) variations of petroleum fluids from the U. S. Gulf Coast. *Geochim. Cosmochim. Acta*, 65:3529–3555, 2001.

K.H. Williams, D. Ntarlagiannis, L.D. Slater, A. Dohnalkova, Hubbard S.S., and J.F. Banfield. Geophysical imaging of stimulated microbial biomineralization. *Environ. Sci. Technol.*, 39(19):7592–7600; DOI: 10.1021/es0504035, 2005.

R. Wood and A. Curtis. Geological prior information, and its applications to solving geoscientific problems. In Wood R. and A. Curtis, editors, *Geological Prior Information*, number 239 in Geol. Soc. Lond. Special Publication, pages 1–14. 2004.

K. Yamamura, O. Sano, H. Utada, Y. Takei, S. Nakao, and Y. Fukao. Long-term observations of in situ seismic velocity and attenuation. *J. Geophys. Res.*, 108(B6):doi:10.1029/2002JB002005, 2003.

M. D. Zoback and J. Townend. How faulting keeps the crust strong. *Geology*, 28:399–402, 2000.

CWP-565

Theory of traveltime shifts around compacting reservoirs: 3D solutions for heterogeneous anisotropic media

Rodrigo Felício Fuck[1], Andrey Bakulin[2], and Ilya Tsvankin[1]

[1] *Center for Wave Phenomena and Department of Geophysics, Colorado School of Mines, Golden, CO 80401*
[2] *Shell International, Bellaire Technology Center, Houston, TX 77001*

ABSTRACT

Time-lapse traveltime shifts of reflection events recorded above hydrocarbon reservoirs can be used to monitor production-related compaction and pore-pressure changes. Existing methodology, however, is limited to zero-offset rays and cannot be applied to traveltime shifts measured on prestack seismic data. Here, we give an analytic 3D description of stress-related traveltime shifts for rays propagating along arbitrary trajectories in heterogeneous anisotropic media.

The nonlinear theory of elasticity helps to express the velocity changes in and around the reservoir through the excess stresses associated with reservoir compaction. Since this stress-induced velocity field is both heterogeneous and anisotropic, it should be studied using prestack traveltimes or amplitudes. Then we obtain the traveltime shifts by first-order perturbation of traveltimes that accounts not only for the velocity changes, but also for 3D deformation of reflectors. The resulting closed-form expression can be efficiently used for numerical modeling of traveltime shifts and, ultimately, for reconstructing the stress distribution around compacting reservoirs.

The analytic results are applied to a 2D model that includes a compacting rectangular resevoir embedded in an initially homogeneous and isotropic medium. The computed velocity changes around the reservoir are primarily caused by deviatoric stresses and produce an anisotropic medium with substantial values of the Thomsen parameters ϵ and δ and variable orientation of the symmetry axis. The offset dependence of the traveltime shifts should play a crucial role in estimating the anisotropy parameters and the compaction-related deviatoric stress components.

Key words: traveltime shifts, time-lapse seismic, stress-induced anisotropy, reservoir compaction

1 INTRODUCTION

Traveltime shifts (differences), measured between two or more time-lapse seismic reflection surveys, have become an important tool for reservoir characterization. Traveltime shifts can help to map compaction throughout a reservoir and, therefore, optimize infill drilling and production by identifying compartments and pressure cells inside the producing units. Hydrocarbon production induces pore-pressure changes and compaction inside the reservoir, which causes accumulation of excess stress throughout the section. The excess stress modifies the elastic properties of the rocks in and around the reservoir, and the corresponding velocity changes can be estimated using reflection traveltimes recorded in time-lapse surveys.

The stress dependence of traveltime shifts is well understood for vertically propagating waves and horizontal layers (i.e., for zero-offset data). Traveltime shifts estimated on stacked seismic data above horizontally layered media have been successfully used to delineate compartments in reservoirs, e.g., (Landrø and Stammeijer, 2004), (Hatchell and Bourne, 2005). However, the existing theory breaks down in the presence of dip and for prestack data (i.e., for non-zero offsets). Traveltimes shifts for prestack data were analyzed by (Røste et al., 2006), but their theory is restricted to horizontally layered isotropic media.

Here we provide an analytic 3D description of traveltime shifts around a compacting reservoir embedded in a heterogeneous, layered, anisotropic medium. Taking heterogeneity and anisotropy into account is necessary for an adequate physical description of traveltime shifts. Indeed, the excess stress field created by compaction is anisotropic (in general, it is triaxial) and heterogeneous because the magnitude of stress depends on reservoir geometry and varies spatially around the reservoir.

Our description of traveltimes shifts in and around a compacting reservoir involves two steps. First, we express the velocity changes through the excess stress and strain fields created by compaction. Then, we use first-order perturbations of traveltimes to obtain the traveltime shifts as a linear function of the velocity.

To relate excess stress and strain to velocity changes we use the nonlinear theory of elasticity, e.g. (Toupin and Bernstein, 1961) and (Thurston and Brugger, 1964). This theory has three main advantages over the traditional approaches to model stress-sensitivity of velocity fields. It is more general because it does not rely on a specific micromechanical model to describe stress sensitivity, like other approaches based on stiffening of grain contacts or the closing or opening of specific micro-cracks distributions (Shapiro and Kaselow, 2005). In addition, the nonlinear elasticity approach yields the full tensor of the deformed medium, which allows computation of traveltimes and other signatures for generally anisotropic media. Lastly, all possible mechanisms of stress sensitivity are absorbed by a small number of nonlinear coefficients.

Also, the nonlinear theory has already been successfully applied to measure stress-induced anisotropy and the stress-sensitivity tensor in sandstones and shales. Examples include ultrasonic velocity measurements on rock samples (Johnson and Rasolofosaon, 1996; Sarkar et al., 2003; Prioul et al., 2004) and in-situ stress estimation in boreholes (Winkler et al., 1998; Sinha and Plona, 2001).

The main complication in using nonlinear theory is that measurements of the nonlinear elastic coefficients (components of a sixth-order tensor) for sedimentary rocks are rare, with most existing results obtained for crystals and man-made materials. This is an inherent limitation of our approach, but we expect more measurements to be available in the near future. Nevertheless, the results by (Prioul et al., 2004) indicate that detailed knowledge of the sixth-order tensor is not critical, and for most applications in exploration and reservoir geophysics this tensor can be assumed to be isotropic.

In the next sections we explain our approach in more detail. First, we describe the variational problem related to the first-order perturbation of traveltimes. Then we link the time perturbations with nonlinear elasticity to develop an equation for traveltime shifts, in terms of the excess stresses and volumetric strains caused by reservoir compaction.

2 P-WAVE TRAVELTIME SHIFTS FROM FIRST PRINCIPLES

Assuming that reservoir compaction produces only small changes in the traveltimes of seismic waves propagating through the medium, such shifts can be expressed through small perturbations of the model parameters. These perturbations include those of the elastic moduli and of the geometry of the reflectors. Indeed, the deformation caused by compaction changes the relative positions of the reflectors in the medium, while the extra stress alters the elastic properties.

First-order traveltime perturbations can be obtained by taking into account both types of variations. To describe these perturbations, we apply Hamilton's principle of least action to traveltimes computed for rays traced in an unperturbed background medium. For simplicity, we consider this background medium to be isotropic and concentrate on P-waves. Then traveltime shifts δt are described by the following equation, which is well known in classical mechanics, e.g., (Lanczos, 1986):

$$\delta t = \mathbf{p} \cdot \delta \mathbf{x} \Big|_{\tau_1}^{\tau_2} - \int_{\tau_1}^{\tau_2} \Delta \mathcal{H} \, \mathrm{d}\tau \,, \tag{1}$$

where $\mathbf{p}$ is the slowness vector of the reference ray traced in the background medium, $\delta \mathbf{x}$ is the first-order variation of the position vector of the reference ray in 3D Cartesian coordinates, $\Delta \mathcal{H}$ is the corresponding variation of the system's Hamiltonian and τ is the integration parameter along the reference ray. The Hamiltonian $\mathcal{H}$ of the system is the scaled Eikonal equation, in which the integration parameter τ represents the traveltime along the reference ray, e.g., (Červený, 2001):

$$\mathcal{H}(\mathbf{x}, \mathbf{p}) = \frac{1}{2} \left[V^2(\mathbf{x}, \mathbf{p}) \, p_k \, p_k - 1 \right] = 0 \,, \tag{2}$$

where $V(\mathbf{x}, \mathbf{p})$ is the phase velocity; summation over repeated indices is implied throughout the paper.

Equation 1 provides important insights into the nature of the traveltime shifts caused by reservoir compaction. First, in the linear approximation the contributions of the geometric and the velocity changes to traveltimes are independent. Second, the changes of

the ray trajectory (i.e., geometric changes) contained in the term $\mathbf{p}\cdot\delta\mathbf{x}$ do not contribute to first-order traveltime perturbations, unless they occur at the endpoints. Third, the influence of the velocity changes is represented by the perturbed Hamiltonian $\Delta\mathcal{H}$, which should be integrated along the reference ray.

2.1 Traveltime shifts in layered media

Equation 1 helps to account for 3D deformation of reflectors in a layered medium in a straightforward way. Following (Farra and Le Bégat, 1995), we transform every point where the unperturbed ray crosses an interface or reflects from it (i.e.,"scattering points") into a new endpoint. Then equation 1 is applied sequentially to all N scattering points (excluding the source and receiver points) along the ray:

$$\delta t = \delta t^e + \sum_i^N \delta t^i - \int_{\tau_1}^{\tau_2} \Delta\mathcal{H} d\tau\,, \tag{3}$$

where

$$\delta t^e = \mathbf{p}\cdot\delta\mathbf{x}\Big|_{\tau_1}^{\tau_2}, \quad \delta t^i = (\grave{\mathbf{p}} - \acute{\mathbf{p}})\cdot\delta\mathbf{x}\,, \tag{4}$$

where δt^i is the contribution of the change of the interface position, which is proportional to the difference between the slowness vectors of the reference ray on both sides of the interface.

According to Snell's law, the projection of the slowness vector onto the interface is conserved. Therefore, the only component of vector $(\grave{\mathbf{p}} - \acute{\mathbf{p}})$ that contributes to the traveltime shifts is the one orthogonal to the interfaces. If the interfaces are horizontal, then the traveltime shifts depend on the vertical components of the vector $(\grave{\mathbf{p}} - \acute{\mathbf{p}})$. The unit normal vector at the reflection/transmission point $\mathbf{x}$ is given by the gradient of the unperturbed interface $f(\mathbf{x}) = 0$:

$$\mathbf{N}(\mathbf{x}) = \frac{\nabla f(\mathbf{x})}{|\nabla f(\mathbf{x})|}\,. \tag{5}$$

To find the component of the vector $(\grave{\mathbf{p}} - \acute{\mathbf{p}})$ in the direction of the normal $\mathbf{N}(\mathbf{x})$ to an interface we use the projection operator $\mathbf{A}(\mathbf{x})$, e.g., (Scales et al., 2001):

$$\mathbf{A} = \frac{\mathbf{N}\mathbf{N}^{\mathsf{T}}}{\mathbf{N}^{\mathsf{T}}\mathbf{N}}\,. \tag{6}$$

Applying equation 6 to each term $(\grave{\mathbf{p}} - \acute{\mathbf{p}})\cdot\delta\mathbf{x}$ in equation 3 gives

$$(\grave{p}_i - \acute{p}_i)\,\delta x_i = A_{ij}\,(\grave{p}_j - \acute{p}_j)\,\delta x_i\,. \tag{7}$$

2.2 Traveltime shifts in heterogeneous anisotropic media

As discussed above, reservoir compaction causes the velocity field around the reservoir to become both heterogeneous and anisotropic. The generality of equation 1 is very useful because it involves no assumptions regarding the heterogeneity or anisotropy of the Hamiltonian $\mathcal{H}$ or of its perturbation $\Delta\mathcal{H}$. Indeed, this is a property that is often exploited to construct ray-tracing systems for heterogeneous, arbitrarily anisotropic media, e.g., (Jech and Pšenčík, 1989; Chapman and Pratt, 1992; Červený, 2001). Because the first-order variation of the slowness vector $\mathbf{p}$ is already accounted for in equation 1, it follows from equation 2 that $\Delta\mathcal{H} = \Delta V/V$. The velocity perturbation ΔV is found by perturbing the Christoffel equation, which leads to the following equation obtained for P-waves under the assumption that reference rays are traced in an isotropic medium (Červený, 2001):

$$\Delta\mathcal{H} = \frac{1}{2}\frac{\Delta a_{ijkl}(\mathbf{x})\,n_i n_j n_k n_l}{V^2(\mathbf{x})}\,, \tag{8}$$

where Δa_{ijkl} are the perturbations of the density-normalized stiffness coefficients, and n_i are the components of the unit slowness vector.

3 RELATING EXTRA STRESSES TO VELOCITY CHANGES

Equations 3 and 8 provide the basis for deriving an equation describing the traveltime shifts inside and around compacting reservoirs. The next step is to express the elements Δa_{ijkl} in terms of the strains and excess stresses caused by reservoir compaction. As discussed in the introduction, we use the nonlinear theory of elasticity to describe the stress sensitivity of the stiffness coefficients. The two main assumptions used below are that the stress-sensitivity tensor is isotropic and that the stress-induced anisotropy is weak.

3.1 Nonlinear elasticity

According to (Prioul et al., 2004), the effective stiffness coefficients c_{ijkl} of a deformed elastic medium can be written in terms of the stiffnesses before deformation (c°_{ijkl}) and the deformation-induced stress (ΔS_{ij}) and strain (Δe_{ij}) changes:

$$\begin{aligned} c_{ijkl} =& \Delta S_{ik}\delta_{jl} + c^{\circ}_{ijkl} + c_{ijklmn}\Delta e_{mn} \\ &+ c^{\circ}_{ijpl}\Delta e_{kp} + c^{\circ}_{ipkl}\Delta e_{jp}\,, \end{aligned} \tag{9}$$

where δ_{ij} is Kronecker's symbol and c_{ijklmn} is a sixth-order tensor, which has no more than 56 independent elements (Hearmon, 1953)*. We reduce this number to

*The main assumption behind equation 9 is that deformation is small and reversible. Then the strain energy is described by a Taylor series expansion with nonlinear terms, where the fourth-order c_{ijkl} tensor represents the Taylor series second-order term, while the sixth-order tensor c_{ijklmn} is the series third-order term. The qualifier "nonlinear" of the elasticity theory comes from inclusion of the c_{ijklmn} tensor (obtained as Taylor series coefficients for the strain energy function) into Hooke's law (Thurston and Brugger, 1964).

three by assuming that this tensor is isotropic, as suggested by the laboratory results of (Prioul et al., 2004).

For a typical range of the stiffnesses of rocks and of the pore-pressure changes related to reservoir compaction, equation 9 can be further simplified by dropping relatively small terms. As pointed out by (Prioul et al., 2004),

$$\Delta S_{ij} \approx c^{\circ}_{ijkl}\Delta e_{ij} \ll c_{ijklmn}\Delta e_{mn} \ll c^{\circ}_{ijkl}\,, \tag{10}$$

which allows us to neglect the terms involving the stress change ($\Delta S_{ik}\delta_{jl}$ and $c^{\circ}_{ijkl}\Delta e_{ij}$). Alternatively, using a linear Taylor series expansion, the stiffness tensor $\mathbf{C}$ of the deformed medium can be written as

$$\mathbf{C} = \mathbf{C}^{\circ} + \frac{\partial \mathbf{C}^{\circ}}{\partial e_{mn}}\Delta e_{mn}\,, \tag{11}$$

where $\mathbf{C}^{\circ}$ is the reference tensor, c°_{ijkl}. Comparison with equation 9 shows that the term $\frac{\partial \mathbf{C}^{\circ}}{\partial e_{mn}}$ coincides with the tensor c_{ijklmn}. Hence, this tensor is a measure of the sensitivity of the stiffnesses c_{ijkl} to the deformation Δe_{ij}.

By ignoring changes in the medium density ρ, we can obtain the density-normalized stiffnesses Δa_{ijkl} needed in equation 8:

$$\Delta a_{ijkl} = \rho^{-1}\frac{\partial c^{\circ}_{ijkl}}{\partial e_{mn}}\Delta e_{mn} = \rho^{-1}c_{ijklmn}\Delta e_{mn}\,. \tag{12}$$

Evaluation of the term $c_{ijklmn}\Delta e_{mn}$ using matrix-vector computations and the resulting stiffness perturbations are discussed in Appendix A. Since we are working with a first-order approximation, we follow (Sarkar et al., 2003) and use linear Hooke's law to relate Δ_{eij} to ΔS_{ij}, thus

$$\Delta a_{ijkl} = \rho^{-1}c_{ijklmn}\left(c^{\circ}_{mnpq}\right)^{-1}\Delta S_{pq} \tag{13}$$

3.2 Traveltime shifts due to compaction

A concise expression for traveltime shifts can be derived by substituting equation 13 into equation 8 for the perturbation of the Hamiltonian:

$$\Delta\mathcal{H} = \frac{1}{2}\frac{B}{V^2(\mathbf{x})}\,, \tag{14}$$

with

$$B = \Delta a_{ijkl}\, n_i n_j n_k n_l\,.$$

A detailed derivation of the term B as a function of the excess stress and strain can be found in Appendix B. The final form of the perturbation of the Hamiltonian $\Delta\mathcal{H}$ is found by substituting B from equation B10 into equation 14:

$$\Delta\mathcal{H} = \frac{1}{2}\left[B_1\Delta e_{kk} + B_2\left(\mathbf{n}^{\mathsf{T}}\Delta\sigma\,\mathbf{n}\right)\right]\,, \tag{15}$$

$$B_1 = \frac{1}{3C^{\circ}_{33}}\left(C_{111}+2C_{112}\right)\,; \quad B_2 = 2\frac{C_{155}}{C^{\circ}_{33}C^{\circ}_{44}}\,. \tag{16}$$

Where, Δe_{kk} is the trace of the strain tensor and $\Delta\sigma$ is the tensor of deviatoric stress. The constants C_{111}, C_{112} and C_{155} are elements of the isotropic sixth-order tensor c_{ijklmn} written in Voigt notation, while C°_{33} and C°_{44} are the elastic stiffnesses of the background isotropic medium. Note that all terms in equation 15 are dimensionless, which is indicated by equation 3. The traveltime shifts given by equation 3 can then be rewritten as

$$\delta t = \underbrace{\delta t^{e} + \sum_{i=1}^{N}\delta t^{i}}_{geom.} \underbrace{- \frac{1}{2}\int_{\tau_1}^{\tau_2} B_1\Delta e_{kk} + B_2\left(\mathbf{n}^{\mathsf{T}}\Delta\sigma\,\mathbf{n}\right)\mathrm{d}\tau}_{vel.}\,. \tag{17}$$

Typically, the main contribution to δt is made by the velocity changes (the last term in equation 17). Indeed for the geometric changes to produce a traveltime shift of at least 1 ms, an unlikely set of conditions have to take place: the displacements should be on the order of meters; the slowness contrasts cannot be smaller than 10^{-2} s/km throughout the model, and summation should include from 10 to 100 scattering points. In most typical cases, however, the displacements throughout the section are on the order of centimeters, while there is little room to increase the number of reflection/transmission points without decreasing the slowness contrasts.

As shown in equation 17, the traveltime shifts associated to velocity changes are an arithmetic average between isotropic ($B_1\Delta e_{kk}$) and anisotropic ($B_2\,\mathbf{n}^{\mathsf{T}}\Delta\sigma\,\mathbf{n}$) contributions along the raypath. According to our sign convention, negative strains denote contraction, while positive strains denote extension. Likewise, negative stresses imply compression, while positive stresses imply expansion. This means that the coefficient C_{155} and the combination $C_{111}+2C_{112}$ should be negative. Then, according to equations 15–17, compression or contraction lead to increase in velocity, which results in negative traveltime shifts. In contrast, extension causes velocity decrease and positive traveltime shifts.

To clarify how equation 17 generalizes existing results, we reduce it to the equation for zero-offset data from

(Hatchell and Bourne, 2005). For two-way traveltimes shifts their equation reads,

$$\delta t = 2\int_0^Z (1+R)\,\frac{\Delta e_{zz}}{V(\mathbf{x})}\,\mathrm{d}z\,, \tag{18}$$

where integration is carried out from the surface (z=0) to the reflector depth (z=Z); $V(\mathbf{x})$ is the velocity of the isotropic reference medium and $R\Delta e_{zz} = -\Delta V(\mathbf{x})/V(\mathbf{x})$. Without loss of generality, we consider a zero-offset ray going from the surface to a horizontal reflector, without any other interfaces in between. Dividing the ray into the downgoing and the upgoing

segments, we can write equation 17 as

$$\begin{aligned}\delta t =& \delta t^e + \delta t^i - \int_{\tau_1}^{\tau_2} \frac{\Delta V}{V}\,\mathrm{d}\tau\,,\\ \delta t =& p_3\delta z\Big|_{\tau_1}^{\tau_r} - p_3\delta z\Big|_{\tau_r}^{\tau_2} - \int_{\tau_1}^{\tau_2} \frac{\Delta V}{V}\,\mathrm{d}\tau\,,\\ \delta t =& \int_{\tau_1}^{\tau_r} \frac{d\,(p_3\delta z)}{d\tau}\mathrm{d}\tau - \int_{\tau_r}^{\tau_2} \frac{d\,(p_3\delta z)}{d\tau}\mathrm{d}\tau - \int_{\tau_1}^{\tau_2} \frac{\Delta V}{V}\,\mathrm{d}\tau\,.\end{aligned} \tag{19}$$

Making the substitution $d\tau = dz/V$, we get

$$\delta t = \int_0^Z \frac{d\,(Vp_3\delta z)}{V dz}\mathrm{d}z - \int_Z^0 \frac{d\,(Vp_3\delta z)}{V dz}\mathrm{d}z - 2\int_0^Z \frac{\Delta V}{V^2}\,\mathrm{d}z\,, \tag{20}$$

and observing that $p_3 = 1/V$ and $\Delta e_{zz} \equiv d\delta z/dz$, we can simplify equation 20 to obtain

$$\delta t = 2\int_0^Z \left(\Delta e_{zz} - \frac{\Delta V}{V}\right)\frac{\mathrm{d}z}{V}\,, \tag{21}$$

thus recovering equation 18. Because of equation 17 we note that the Ratio R from equation 18 can be written as the average of two other ratios:

$$\delta t = 2\int_0^Z \left[1 + \frac{1}{2}\,(R_1 + R_2)\right]\frac{\Delta e_{zz}}{V(\mathbf{x})}\,\mathrm{d}z\,,$$

where,

$$\Delta e_{zz}R_1 = -B_1\Delta e_{kk}\,; \quad \Delta e_{zz}R_2 = -B_2\Delta\sigma_{33}\,. \tag{22}$$

4 NUMERICAL TESTS

In this section we use equation 17 to model the influence of both reflector deformation and velocity changes on traveltime shifts. First, we apply equation 17 to obtain the traveltime shifts caused by movement of reflectors in a simple horizontally layered medium. Then we compute and discuss the spatial distribution of traveltime shifts in shot gathers for a 2D model of a compacting reservoir.

4.1 Reflector deformation in a layered medium

We consider a ray that travels from the surface to the bottom of the model comprised of two horizontal isotropic layers. The layers are assumed to have been deformed uniaxially in the z-direction such that the thickness of layer 1 was increased by δz_1 and of layer 2 by δz_2 (Figure 1).

To study the influence of geometric changes only, the velocities in the layers (v_1 and v_2) remain constant after the deformation. Therefore, the exact one-way traveltime after the deformation from the top to the bottom of the model can be written as

$$t = \frac{z_1 + \delta z_1}{v_1\cos\theta_1} + \frac{z_2 + \delta z_2}{v_2\cos\theta_2}\,, \tag{23}$$

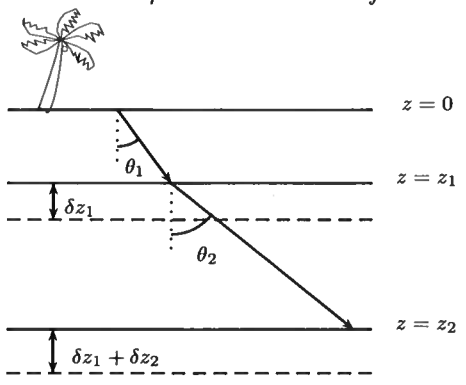

Figure 1. Model of two horizontal layers above a compacting reservoir. The compaction increases the thickness of the layer 1 by δz_1 and of layer 2 by δz_2. The velocities remain constant after the deformation.

where θ_1 and θ_2 are the angles between the ray and the vertical in the first and second layers, respectively. Hence, the exact traveltime difference due to the deformation is

$$\Delta t_{ex} = \frac{\delta z_1}{v_1\cos\theta_1} + \frac{\delta z_2}{v_2\cos\theta_2} \tag{24}$$

Expressing Δt_{ex} in equation 23 in terms of the vertical components of the slowness vector (q_i) and the propagation angle θ_i ($i = 1, 2$), we find:

$$\Delta t_{ex} = \delta z_1\, q_1\left(1 + \tan^2\theta_1\right) + \delta z_2\, q_2\left(1 + \tan^2\theta_2\right)\,. \tag{25}$$

Applying equation 3 to the same model yields an approximation (Δt_{pert}) for Δt_{ex}:

$$\begin{aligned}\Delta t_{pert} =& (q_1 - q_2)\,\delta z_1 + (\delta z_1 + \delta z_2)\,q_2\,,\\ \Delta t_{pert} =& \delta z_1\, q_1 + \delta z_2\, q_2\,.\end{aligned} \tag{26}$$

For propagation angles of up to 30° equations 25 and 26 give similar results because the $\tan^2\theta$ term is much smaller than unity. In particular, for zero-offset rays the result is exact.

4.2 Traveltime shifts due to velocity changes

To illustrate the distribution of traveltime shifts in prestack data, we applied equation 17 to a 2D model composed of a rectangular reservoir embedded in a homogeneous isotropic halfspace (Figure 2). In such a model, traveltime shifts are due solely to velocity changes, because there are no interfaces. The pore-pressure change was confined to the reservoir, and the resulting excess stress, strain and displacement were computed using analytic expressions adapted from (Hu, 1989). The strain was confined to the incidence plane $[x, z]$, with no deformation on the y-direction ($e_{12} = e_{22} = e_{23} = 0$).

Table 1 lists the model parameters. The values of the Biot-Willis coefficient (α) and the zero-frequency

Table 1. Model parameters used to generate Figures 3–8. These values correspond to the sample of Berea sandstone studied by (Sarkar et al., 2003).

Model parameters		
V_P = 2.3 km/s	V_P/V_S=1.58	ρ=2.14 g/cc
c_{111}=-13904 GPa	c_{155}=-3609 GPa	
α=0.85	s=0.9	

scaling coefficient (s) were chosen arbitrarily. The Biot-Willis coefficient is a measure of how well "pore-pressure counteracts confining pressure to produce volumetric strain" (Wang, 2000) and ranges between the rock porosity and unity. The closer α is to unity, the more excess stress is generated by reducing the pore pressure inside the reservoir. To model the static deformation generated by pore-pressure changes, we need zero-frequency stiffness coefficients, which were not available. For well-consolidated rocks with low porosity, as the sandstone used in our numerical modeling, the zero-frequency P-wave velocity generally is about 10% lower than that measured for frequencies typical for seismic data, while V_P/V_S ratio remains about the same (Yale and Jamieson, 1994)[†]. Therefore, we scaled the P-wave velocity provided by (Sarkar et al., 2003) by $s = 0.9$. Since both strain and displacement are proportional to V_P^{-2}, the deformation around the reservoir increases for a lower scaling factor s.

Figure 3 shows the spatial distribution of the deviatoric stress and volumetric strain generated by the pore-pressure drop inside the reservoir. We also computed Thomsen parameters ϵ and δ ($\epsilon = \delta$ in our model) and the rotation of the symmetry plane around the y-axis in the plane $[x, z]$ (Figure 4). The δ values in and near the reservoir reach 0.1, which indicates that the stress-induced anisotropy is non-negligible even for the relatively small pressure drop $\Delta P = -10$ MPa used in the test. The similarity between δ and the normal deviatoric stress components ($\Delta\sigma_{11}$ and $\Delta\sigma_{33}$) is explained by the fact that to first-order (Sarkar et al., 2003)

$$\delta = \frac{C_{155}}{C_{33}^{\circ} C_{44}^{\circ}} (\Delta\sigma_{11} - \Delta\sigma_{33}) . \qquad (27)$$

Because the stress-sensitivity tensor and the background medium are isotropic, the stress-induced anisotropy is elliptical ($\epsilon = \delta$). For the plane strain problem treated here, the stress tensor is triaxial, so that the medium symmetry becomes orthorhombic. Close to the reservoir corners, accumulation of the shear stress $\Delta\sigma_{13}$ causes rotation of the symmetry planes, changing the symmetry to tilted orthorhombic[‡]. In particular, at the reservoir corners the tilt of the symmetry planes is maximum, reaching 45° in absolute value.

Figures 5 and 6 show the spatial distribution of the traveltime shifts for four shot locations at the top of the model. Figure 5 helps to compare the contributions to the traveltime shifts of the deviatoric stress and volumetric changes (see equation 15). Clearly, for the homogeneous background model used in the test, the traveltime shifts are caused primarily by the deviatoric stresses, which make the medium anisotropic.

The influence of moving the shot position with respect to the center of the reservoir on the total traveltime shifts is illustrated in Figure 6. Because the deviatoric stress changes are symmetric with respect to the reservoir, so are the traveltime shifts for shot 1, both in offset and depth. As the shot moves away from the center of the reservoir, this symmetry no longer exists. The traveltime shifts for shots 2, 3 and 4 increase at longer offsets and are confined to the reservoir and the medium below it.

The traveltime shifts depend on the interplay between the spatial distribution of the extra deviatoric stress $\Delta\sigma_{ij}$ and the angle of incidence θ. We used shots 1 and 3 from Figure 6 to compare the contributions of different components of the deviatoric stress to the traveltime shifts for a range of offsets. As expected from equation 17, the vertical stress changes contribute mostly to the traveltime shifts at near offsets (i.e., for small θ), while the horizontal stresses dominate at far offsets (i.e., for larger θ). Due to the $\sin 2\theta$ dependence in equation 17, the contribution of the shear stress $\Delta\sigma_{13}$ increases up to offsets corresponding to $\theta = 45°$, and then decreases.

5 DISCUSSION AND CONCLUSIONS

The results of this work are based on three major assumptions. The first of them is that the traveltime shifts can be obtained using the first-order ray theory. Although we did not verify the accuracy of this assumption here, it can be expected to give accurate results for compaction-related shifts, which are relatively small. In addition, we note that first-order ray theory assumption should also work well for converted and pure shear waves, making extension of our expressions straightforward for these types of waves as well.

Second, we used an isotropic sixth-order tensor to describe the influence of stress on the stiffness coefficients. While this assumption limits the stress-induced anisotropic model to the special case of tilted or-

[†]For unconsolidated rocks with high porosity this difference can be as high as 70%.

[‡]the medium symmetry can be verified by setting $e_{22} = e_{12} = e_{23} = 0$ in equations A10–A27.

thorhombic symmetry[§], it also reduces the number of parameters and helps to derive closed-form expressions for the traveltime shifts.

Third, we assumed deformation to be purely elastic, which is not always appropriate for reservoir compaction, since it may involve plastic deformation. We believe, however, that the physical insight provided by our relatively simple equations justifies the elastic assumption. Also, the experimental studies discussed above confirm that this assumption is sufficient to describe a wide range of deformation processes observed in various geological settings.

The main result of our analytic developments is equation 17, which generalizes the expressions for zero-offset traveltime shifts of (Landrø and Stammeijer, 2004) and (Hatchell and Bourne, 2005), and those for non-zero offsets traveltime shifts in isotropic media of (Røste et al., 2006). The simple structure of equation 17 helped us to gain valuable insights into the behavior of the offset-dependent traveltime shifts in and around a compacting reservoir.

Traveltime shifts are caused by two independent first-order phenomena: geometric and velocity changes. Analysis of equation 17 indicates that the geometric contributions to the traveltime shifts are likely to be at least an order of magnitude smaller than the contributions of the velocity changes.

According to equation 17, the traveltime shifts due to the velocity changes could be further split into two components, one of which is related to volumetric changes and the other to deviatoric stresses. The volumetric changes may be caused by hydrostatic stress variations inside the reservoir and by surface subsidence. The deviatoric stress term is related to nonhydrostatic stress changes and controls the resulting anisotropy of the deformed elastic medium. Equations 16 and 17 also reveal the role of the different components of the stress-sensitivity tensor. In particular, the combination $C_{111} + 2C_{112}$ is responsible for the hydrostatic P-wave velocity changes, while in agreement with the observation of (Sarkar et al., 2003) C_{155} governs the magnitude of the stress-induced velocity anisotropy.

Although our numerical results are obtained for a simple 2D model, they illustrate several important properties of the stress-induced traveltime shifts related to the velocity changes in and around the reservoir. For instance, they help to better understand the complex spatial distribution of the traveltime shifts caused by the interplay between the propagation direction and the spatial variation of excess stress or strain. Finally, the numerical results demonstrate that compaction-related traveltime shifts should be primarily associated with stress-induced anisotropy.

[§]In each of the symmetry planes, the stress-induced anisotropy is elliptical.

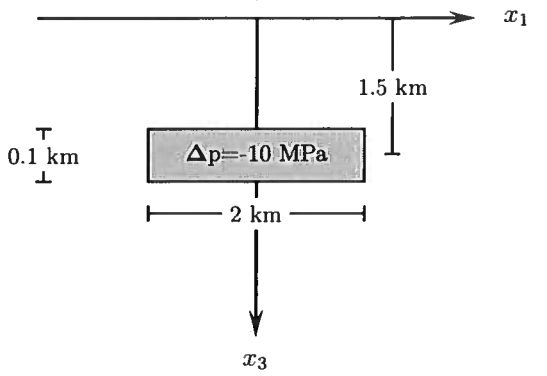

Figure 2. 2D model of a rectangular reservoir embedded in an isotropic homogeneous medium. The parameters not shown on the plot are listed in Table 1.

6 ACKNOWLEDGMENTS

We are grateful to members of the A(nisotropy)-Team of the Center for Wave Phenomena (CWP) at Colorado School of Mines (CSM) for helpful discussions. This work was supported by the Consortium Project on Seismic Inverse Methods for Complex Structures at CWP and by the Chemical Sciences, Geosciences and Biosciences Division, Office of Basic Energy Sciences, U.S. Department of Energy.

REFERENCES

Červený, V., 2001, Seismic ray theory: Cambridge University Press.

Chapman, C. H. and R. G. Pratt, 1992, Traveltime tomography in anisotropic media — I. Theory: Geophysical Journal International, **109**, 1–19.

Farra, V. and S. Le Bégat, 1995, Sensitivity of qP-wave traveltime and polarization vectors to heterogeneity, anisotropy and interfaces: Geophysical Journal International, **121**, 371–384.

Hatchell, P. and S. Bourne, 2005, Rocks under strain: strain-induced time-lapse time-shifts are observed for depleting reservoirs: The Leading Edge, **24**, 1222–1225.

Hearmon, R. F. S., 1953, Third-order elastic coefficients: Acta Crystallographica, **6**, 331–340.

Hu, S. M., 1989, Stress from a parallelepipedic thermal inclusion in a semispace: Journal of Applied Physics, **66**, 2741–2743.

Jech, J. and I. Pšenčík, 1989, First-order perturbation method for anisotropic media: Geophysical Journal International, **99**, 369–379.

Johnson, P. A. and P. N. J. Rasolofosaon, 1996, Nonlinear elasticity and stress-induced anisotropy in rock: Journal of Geophysical Research, **101**, 3113–3124.

Lanczos, C., 1986, Variational principles of mechanics: Dover Publications Inc., 4th edition.

Landrø, M. and J. Stammeijer, 2004, Quantitative estimation of compaction and velocity changes using 4D impedance and traveltime changes: Geophysics, **69**, 949–957.

Prioul, R., A. Bakulin, and V. Bakulin, 2004, Nonlinear rock

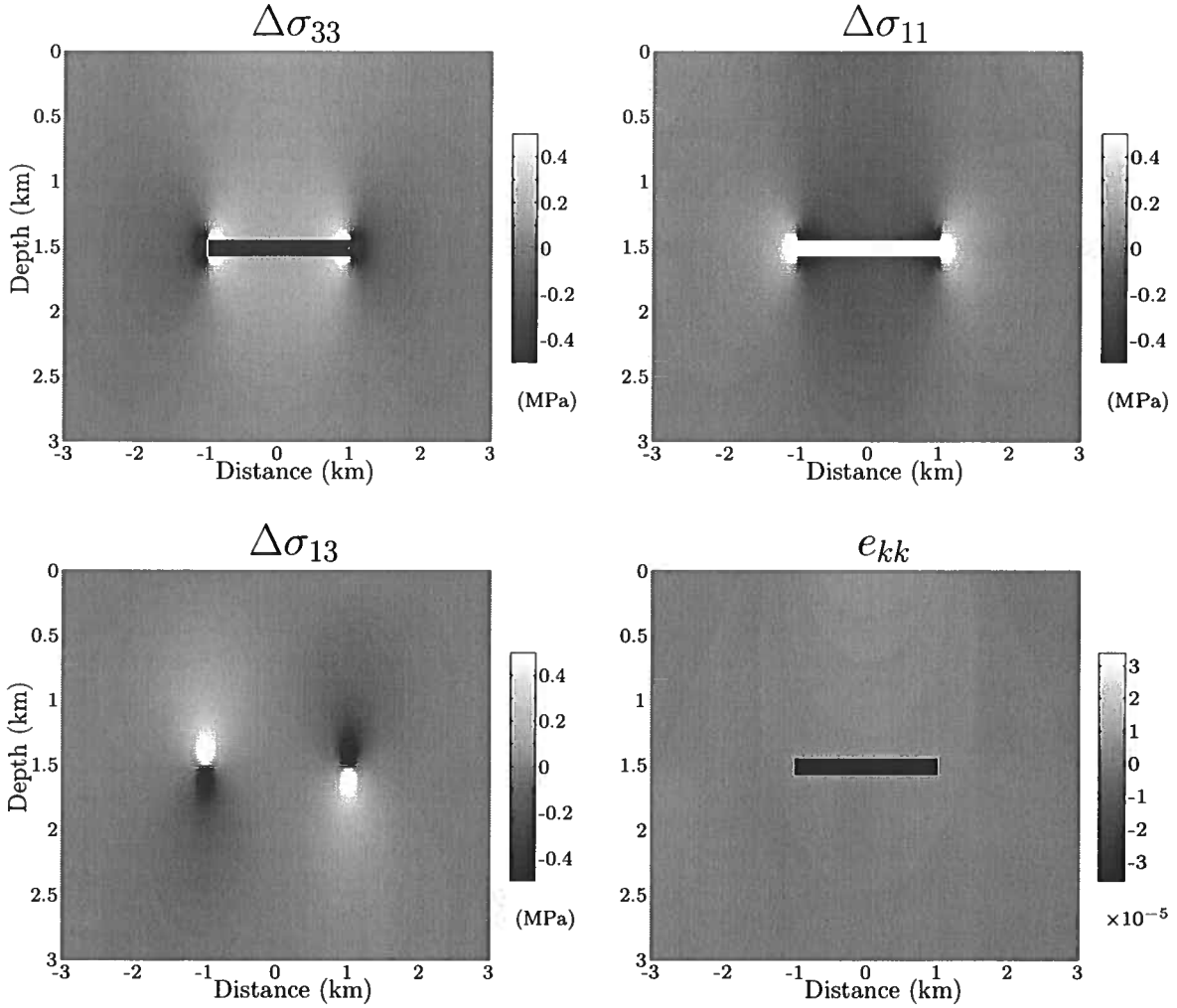

Figure 3. Stress changes caused by reservoir compaction, for the model from Table 1 and Figure 2. The top row shows changes in vertical ($\Delta\sigma_{33}$) and horizontal ($\Delta\sigma_{11}$) normal deviatoric stresses. The shear deviatoric stress ($\Delta\sigma_{13}$) and the trace of the strain tensor Δe_{kk} are shown on the second row. Negative values imply compression; for strain, negative values imply contraction (shortening). Outside the reservoir, $\Delta\sigma_{11} \approx -\Delta\sigma_{33}$.

physics model for estimation of 3d subsurface stress in anisotropic formations: theory and laboratory verification: Geophysics, **69**, 415–425.

Røste, T., A. Stovas, and M. Landrø, 2006, Estimation of layer thickness and velocity changes using 4Dprestack seismic data: Geophysics, **71**, S219–S234.

Sarkar, D., A. Bakulin, and R. L. Kranz, 2003, Anisotropic inversion of seismic data for stressed media: theory and a physical modeling study on Berea sandstone: Geophysics, **68**, 690–704.

Scales, J., M. L. Smith, and S. Treitel, 2001, Introductory geophysical inverse theory: Samizdat Press, http://samizdat.mines.edu.

Shapiro, S. A. and A. Kaselow, 2005, Porosity and elastic anisotropy of rocks under tectonic stress and pore-pressure changes: Geophysics, **70**, N27–N38.

Sinha, B. K. and T. J. Plona, 2001, Wave propagation in rocks with elastic-plastic deformations: Geophysics, **66**, 772–785.

Thurston, R. N. and K. Brugger, 1964, Third-order elastic constants and the velocity of small amplitude elastic waves in homogeneously stressed media: Physical Review, **133**, A1604 – A1610.

Toupin, R. A. and B. Bernstein, 1961, Sound waves in deformed perfectly elastic materials. acoustoelastic effect: Journal of the Acoustical Society of America, **33**, 216–225.

Wang, H. F., 2000, Theory of linear poroelasticity with applications to geomechanics and hydrogeology: Princeton University Press.

Winkler, K. W., B. K. Sinha, and T. J. Plona, 1998, Effects of borehole stress concentrations on dipole anisotropy measurements: Geophysics, **63**, 11–17.

Yale, D. P. and W. H. Jamieson, Jr., 1994, Static and dy-

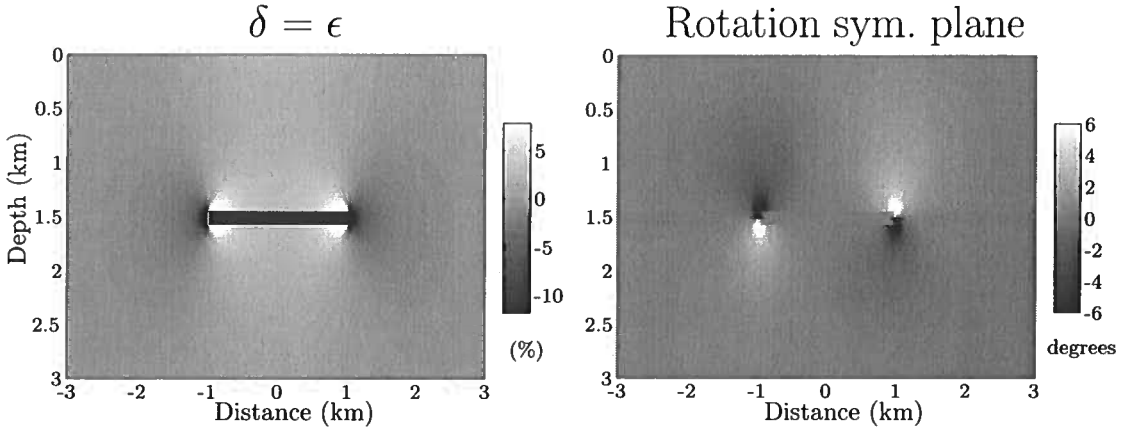

Figure 4. Owing to reservoir compaction the medium becomes heterogeneous and anisotropic. The right panel shows the anisotropy parameter $\delta = \epsilon$, while the left panel shows the direction of the symmetry plane in relation to Cartesian coordinates. Positive means clockwise rotation of the symmetry plane, while negative values mean counterclockwise rotation.

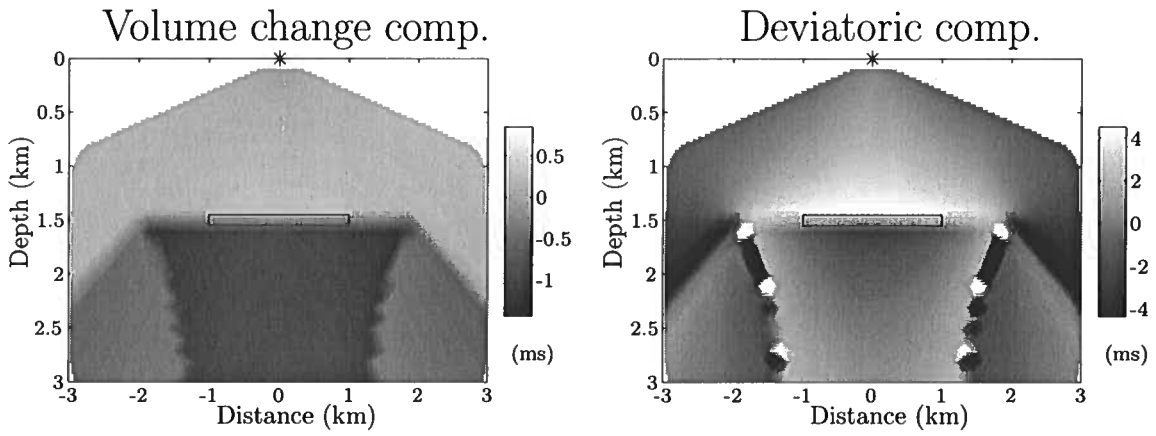

Figure 5. Traveltime shifts for the model from Table 1. The left panel shows the shifts caused by the volumetric changes; the right panel shows the contribution from the deviatoric stress changes. The shifts plotted at each (x, z) point would be recorded at the receiver $(x, 0)$ for a ray reflected from an imaginary horizontal interface at depth z. The shot locations are indicated by the asterisks, and the boundaries of the reservoir are marked by solid black rectangle.

namic mechanical properties of carbonates, *in* Nelson, P. P. and S. E. Laubach, eds., Rock Mechanics Models and Measurements challenges from Industry. Proceedings of the 1st North American Rock Mechanics Symposium, 463–471. Balkema.

APPENDIX A: THE ELEMENTS OF THE MATRIX $\Delta C_{\alpha\beta}$

Here we give a brief derivation of the 21 elastic constants obtained from the equation, $\Delta c_{ijkl} = c_{ijklmn}\Delta e_{mn}$. To simplify the summation over repeated indices we take advantage of the following symmetries of the tensor c_{ijklmn}, e.g., (Thurston and Brugger, 1964):

$$c_{ijklmn} = c_{mnijkl} = c_{klmnij} = c_{lkjinm} \quad \text{etc..} \tag{A1}$$

These symmetries make it possible to use Voigt notation, which reduces the numer of independent elements from 729 to 216. These elements are distributed in $6 \times 6 \times 6$ cubes, and the summation is accomplished by multiplying each cube face by the 6×1 vector formed by the element Δe_{ij} of the excess strain tensor:

$$\Delta C_{\alpha\beta} = C_{\alpha\beta\gamma}\,\Delta e_{\gamma} \tag{A2}$$

where

$$\begin{aligned}
\Delta e_{\gamma} &= (\ \Delta e_{11} \quad \Delta e_{22} \quad \Delta e_{33} \mid 2\Delta e_{23} \quad 2\Delta e_{13} \quad 2\Delta e_{12}\ )^{\mathsf{T}}, \\
\Delta e_{\gamma} &= (\ \Delta e_{1} \quad \Delta e_{2} \quad \Delta e_{3} \mid \Delta e_{4} \quad \Delta e_{5} \quad \Delta e_{6}\ )^{\mathsf{T}}, \\
\Delta e_{\gamma} &= (\Delta e_{N} \quad \Delta e_{T})^{\mathsf{T}}
\end{aligned} \tag{A3}$$

The Greek indices run from 1 to 6 and the summation convention is implied. Application of equation A2 is greatly simplified, if the $C_{\alpha\beta\gamma}$ cubes are formed by

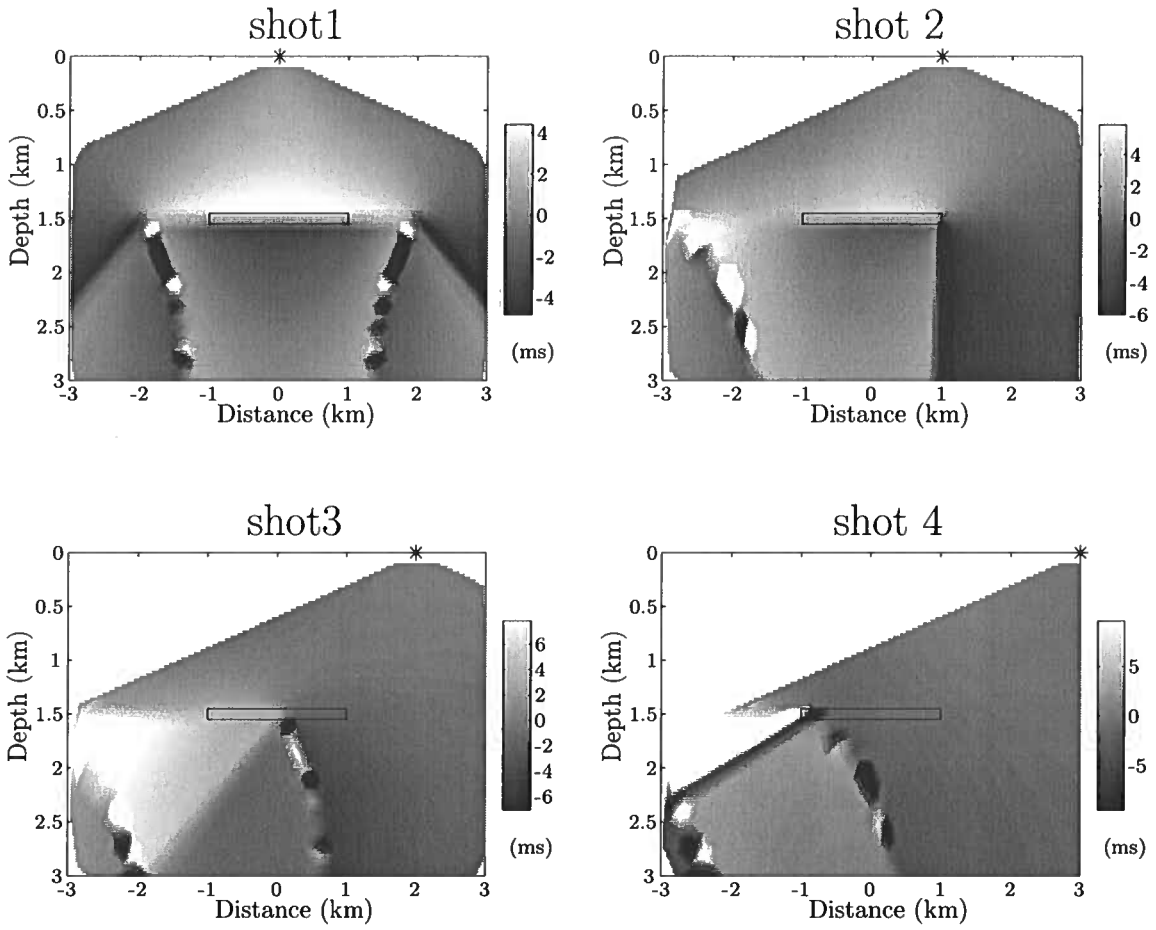

Figure 6. Traveltime shifts for four different shot locations (marked by the asterisks).

isotropic tensors because then the tensor includes only three linearly independent elements. In fact, the cubes for isotropic media are represented by four 3×3 matrices, and three of them are sparse. Skipping some intermediate results, here we give only the final expression for $\Delta C_{\alpha\beta}$:

$$\Delta C_{\alpha\beta} = \begin{pmatrix} (\mathcal{A}\Delta e_N)^{\mathsf{T}} & (\mathcal{B}\Delta e_T)^{\mathsf{T}} \\ (P_1\mathcal{A}P_1\Delta e_N)^{\mathsf{T}} & (P_1\mathcal{B}P_1\Delta e_T)^{\mathsf{T}} \\ (P_2\mathcal{A}P_2\Delta e_N)^{\mathsf{T}} & (P_2\mathcal{B}P_2\Delta e_T)^{\mathsf{T}} \\ (\mathcal{C}\Delta e_T)^{\mathsf{T}} & (\mathcal{C}^{\mathsf{T}}\Delta e_N + \mathcal{D}\Delta e_T)^{\mathsf{T}} \\ (P_1\mathcal{C}P_1\Delta e_T)^{\mathsf{T}} & (P_1\mathcal{C}^{\mathsf{T}}P_1\Delta e_N + P_1\mathcal{D}P_1\Delta e_T)^{\mathsf{T}} \\ (P_2\mathcal{C}P_2\Delta e_T)^{\mathsf{T}} & (P_2\mathcal{C}^{\mathsf{T}}P_2\Delta e_N + P_2\mathcal{D}P_2\Delta e_T)^{\mathsf{T}} \end{pmatrix} \tag{A4}$$

where P_1 and P_2 are permutation matrices used to interchange columns and vectors of the matrices $\mathcal{A}$, $\mathcal{B}$, $\mathcal{C}$ and $\mathcal{D}$:

$$P_1 = \begin{pmatrix} 0 & 1 & 0 \\ 1 & 0 & 0 \\ 0 & 0 & 1 \end{pmatrix}; \quad P_2 = \begin{pmatrix} 0 & 0 & 1 \\ 0 & 1 & 0 \\ 1 & 0 & 0 \end{pmatrix} \tag{A5}$$

$$\mathcal{A} = \begin{pmatrix} c_{111} & c_{112} & c_{112} \\ c_{112} & c_{112} & c_{123} \\ c_{112} & c_{123} & c_{112} \end{pmatrix} \tag{A6}$$

$$\mathcal{B} = \begin{pmatrix} c_{144} & 0 & 0 \\ 0 & c_{155} & 0 \\ 0 & 0 & c_{155} \end{pmatrix} \tag{A7}$$

$$\mathcal{C} = \begin{pmatrix} c_{144} & 0 & 0 \\ c_{155} & 0 & 0 \\ c_{155} & 0 & 0 \end{pmatrix} \tag{A8}$$

$$\mathcal{D} = \begin{pmatrix} 0 & 0 & 0 \\ 0 & 0 & c_{456} \\ 0 & c_{456} & 0 \end{pmatrix} \tag{A9}$$

After carrying out the matrix-vector multiplications in equation A4, we arrived at the following expressions for each of the 18 linearly independent elements of the matrix $\Delta C_{\alpha\beta}$

$$\Delta C_{11} = C_{111}\Delta e_1 + C_{112}(\Delta e_2 + \Delta e_3); \tag{A10}$$

$$\Delta C_{22} = C_{111}\Delta e_2 + C_{112}(\Delta e_1 + \Delta e_3); \tag{A11}$$

$$\Delta C_{33} = C_{111}\Delta e_3 + C_{112}(\Delta e_1 + \Delta e_2); \tag{A12}$$

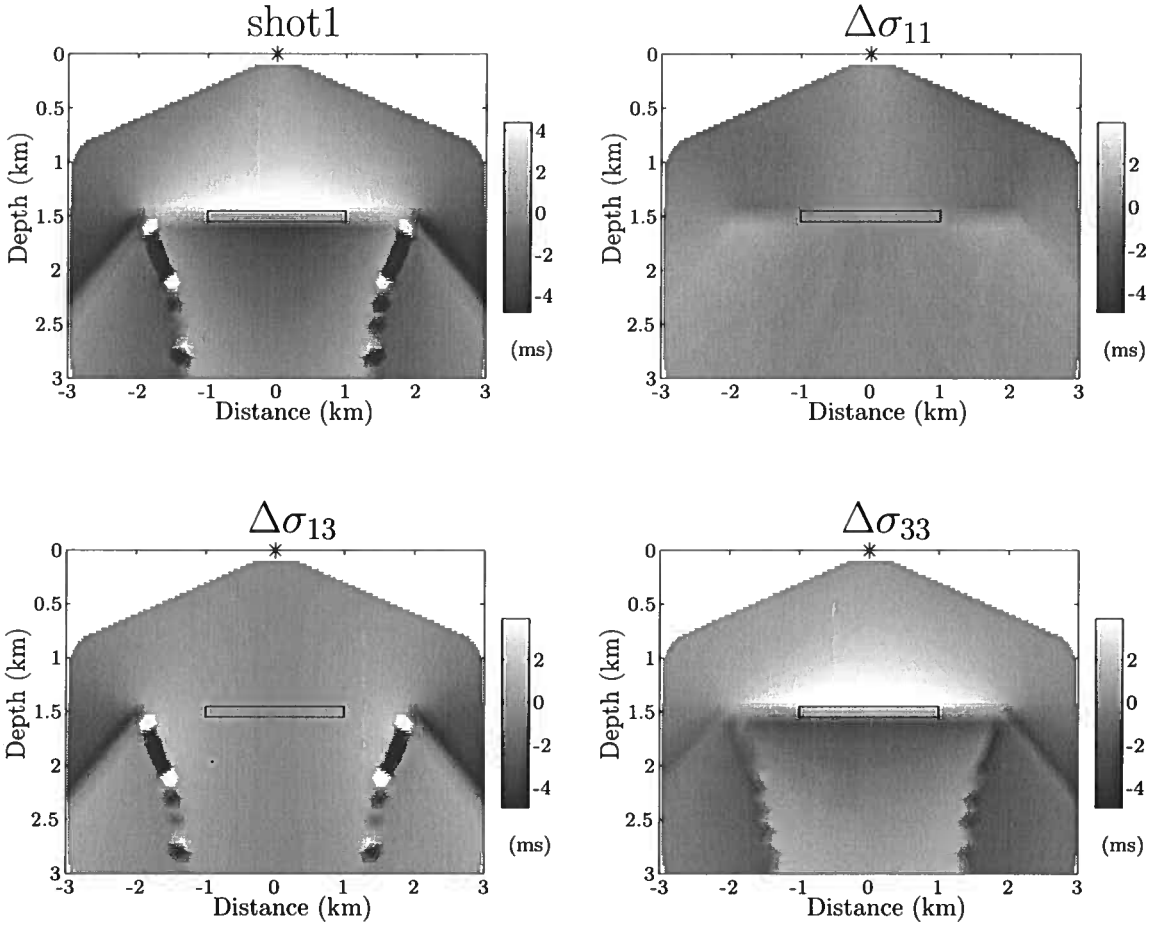

Figure 7. Comparison between the contributions of the three deviatoric stress components to the traveltime shifts. The shot (asterisk) is directly above the center of the reservoir.

$$\Delta C_{44} = C_{144}\Delta e_1 + C_{155}(\Delta e_2 + \Delta e_3); \quad \text{(A13)}$$
$$\Delta C_{55} = C_{144}\Delta e_2 + C_{155}(\Delta e_1 + \Delta e_3); \quad \text{(A14)}$$
$$\Delta C_{66} = C_{144}\Delta e_3 + C_{155}(\Delta e_1 + \Delta e_2); \quad \text{(A15)}$$

$$\Delta C_{12} = C_{123}\Delta e_3 + C_{112}(\Delta e_1 + \Delta e_2); \quad \text{(A16)}$$
$$\Delta C_{13} = C_{123}\Delta e_2 + C_{112}(\Delta e_1 + \Delta e_3); \quad \text{(A17)}$$
$$\Delta C_{23} = C_{123}\Delta e_1 + C_{112}(\Delta e_2 + \Delta e_3); \quad \text{(A18)}$$

$$\Delta C_{14} = C_{144}\Delta e_4; \quad \text{(A19)}$$
$$\Delta C_{15} = \Delta C_{35} = C_{155}\Delta e_5; \quad \text{(A20)}$$
$$\Delta C_{16} = \Delta C_{26} = C_{155}\Delta e_6; \quad \text{(A21)}$$
$$\Delta C_{24} = \Delta C_{34} = C_{155}\Delta e_4; \quad \text{(A22)}$$
$$\Delta C_{25} = C_{144}\Delta e_5; \quad \text{(A23)}$$
$$\Delta C_{36} = C_{144}\Delta e_6; \quad \text{(A24)}$$

$$\Delta C_{45} = C_{456}\Delta e_6; \quad \text{(A25)}$$
$$\Delta C_{46} = C_{456}\Delta e_5; \quad \text{(A26)}$$
$$\Delta C_{56} = C_{456}\Delta e_4; \quad \text{(A27)}$$

Only three elements $C_{\alpha\beta\gamma}$ appearing in equations A10–A27 are linearly-independent, as is implied by the definition of the isotropic sixth-order elastic tensor. According to (Thurston and Brugger, 1964), all $C_{\alpha\beta\gamma}$ elements can be expressed through linear combinations of three Lamé-type parameters ν_i:

$$C_{111} = \nu_1 + 6\nu_2 + 8\nu_3\,, \quad \text{(A28)}$$
$$C_{112} = \nu_1 + 2\nu_2\,, \quad \text{(A29)}$$
$$C_{123} = \nu_1\,, \quad \text{(A30)}$$
$$C_{144} = \nu_2\,, \quad \text{(A31)}$$
$$C_{155} = \nu_2 + 2\nu_3\,, \quad \text{(A32)}$$
$$C_{456} = \nu_3\,. \quad \text{(A33)}$$

APPENDIX B: PERTURBATION TERM B OF THE HAMILTONIAN

Here, we express $B = \Delta a_{ijkl} n_i n_j n_k n_l$ through the volumetric strain and the deviatoric stress tensor. To

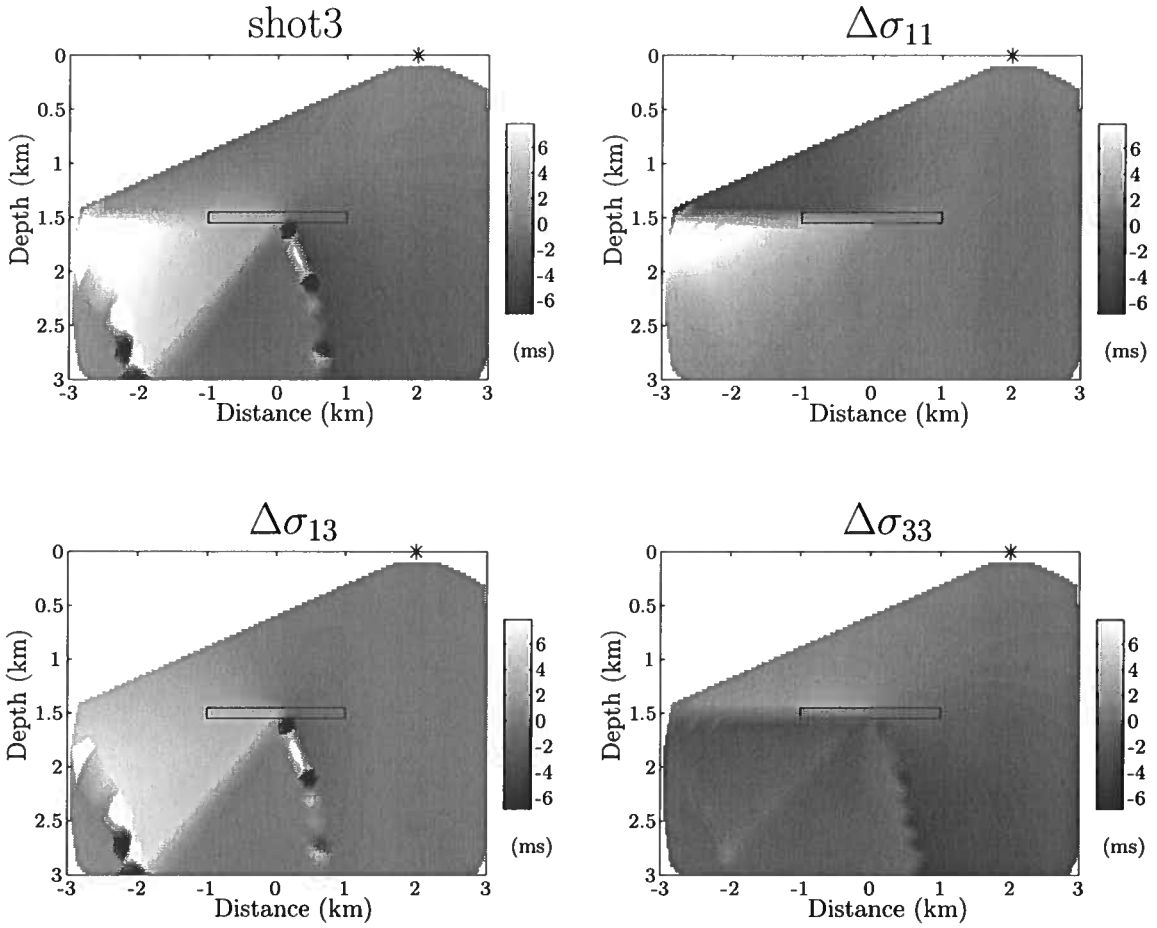

Figure 8. Comparison between the contributions of the three deviatoric stress components to traveltime shifts for shot 3 (asterisk) from Figure 6.

simplify the summations needed to obtain B, we employ matrix-vector multiplications using Voigt notation. Then B becomes the following function of the 6×6 matrix ΔC given in equations A10–A27:

$$B = \rho^{-1}\mathbf{n}^{\mathsf{T}}\mathbf{L}^{\mathsf{T}}\Delta\mathbf{C}\,\mathbf{L}\,\mathbf{n}, \tag{B1}$$

where

$$\mathbf{L}^{\mathsf{T}} = \begin{pmatrix} n_1 & 0 & 0 & 0 & n_3 & n_2 \\ 0 & n_2 & 0 & n_3 & 0 & n_1 \\ 0 & 0 & n_3 & n_2 & n_1 & 0 \end{pmatrix}, \tag{B2}$$

and the unit slowness vector $\mathbf{n}$ is expressed through the incidence anlge θ and the azimuthal angle ϕ:

$$\mathbf{n} = \begin{pmatrix} \sin\theta\cos\phi \\ \sin\theta\sin\phi \\ \cos\theta \end{pmatrix}. \tag{B3}$$

Carrying out the multiplications in equation B1 and using linear Hooke's law to express excess strain Δe_{ij} through excess stress ΔS_{ij}, we find B as:

$$\rho B = \frac{(C_{111} - 2gC_{155})}{3K}\Delta S_{kk} + 2g\frac{C_{155}}{C^{\circ}_{33}}\left(\mathbf{n}^{\mathsf{T}}\Delta\mathbf{S}\,\mathbf{n}\right), \tag{B4}$$

where

$$g \equiv \frac{C^{\circ}_{33}}{C^{\circ}_{44}} \quad \text{and} \quad K \equiv C^{\circ}_{33} - \frac{4}{3}C^{\circ}_{44}. \tag{B5}$$

Hence, B can be separated into two terms, one of which is multiplied by the trace of the extra stress tensor, ΔS_{kk}, and the other by the expectation value of ΔS_{ij} for a certain direction $\mathbf{n}$. Further simplifications can be achieved by separating the excess stress tensor into the hydrostatic and deviatoric parts.

$$\Delta\mathbf{S} = \frac{\Delta S_{kk}}{3} + \Delta\sigma = -\Delta P\mathbf{I} + \Delta\sigma, \tag{B6}$$

where ΔP is the change in pressure, $\Delta\sigma$ is the deviatoric stress tensor and $\mathbf{I}$ is the 3×3 identity matrix. Therefore

$$\mathbf{n}^{\mathsf{T}}\Delta\mathbf{S}\,\mathbf{n} = -\Delta P + \mathbf{n}^{\mathsf{T}}\Delta\sigma\,\mathbf{n}, \tag{B7}$$

since $\mathbf{n}^{\mathsf{T}}\mathbf{n} = 1$. Substitution of equations B6 and B7 into equation B4, followed by simplifications using the definitions for g and K (equations B5) allow us to find B in the form

$$\rho B = [8C_{155} - 3C_{111}]\frac{\Delta P}{3K} + 2g\frac{C_{155}}{C^{\circ}_{33}}\left(\mathbf{n}^{\mathsf{T}}\Delta\sigma\mathbf{n}\right). \quad \text{(B8)}$$

As already mentioned, the isotropic sixth-order tensor is completely defined by only three linearly-independent coefficients, so

$$\rho B = -\frac{1}{3}\left(C_{111} + 2C_{112}\right)\frac{\Delta P}{K} + 2g\frac{A_{155}}{A^{\circ}_{33}}\left(\mathbf{n}^{\mathsf{T}}\Delta\sigma\mathbf{n}\right).$$

Taking into account that

$$\Delta e_{kk} = -\frac{\Delta P}{K}, \quad \text{(B9)}$$

we finally obtain

$$B = \rho^{-1}\left\{\frac{1}{3}\left(C_{111} + 2C_{112}\right)e_{kk} + 2\frac{C_{155}}{C^{\circ}_{44}}\left(\mathbf{n}^{\mathsf{T}}\Delta\sigma\mathbf{n}\right)\right\}. \quad \text{(B10)}$$

A method for estimating apparent displacement vectors from time-lapse seismic images

Dave Hale
Center for Wave Phenomena, Colorado School of Mines, Golden CO 80401, USA

ABSTRACT
Reliable estimates of vertical, inline and crossline components of apparent displacements in time-lapse seismic images are difficult to obtain for two reasons. First, features in 3-D seismic images tend to be locally planar, and components of displacement within the planes of such features are poorly resolved. Second, searching directly for peaks in 3-D cross-correlations is less robust, more complicated, and computationally more costly than searching for peaks of 1-D cross-correlations.
We estimate all three components of displacement with a process designed to mitigate these two problems. We address the first problem by computing for each image sample a local phase-correlation instead of a local cross-correlation. We address the second problem with a cyclic sequence of searches for peaks of correlations computed for lags constrained to one of the three axes of our images.

Key words: time-lapse seismic image processing

1 INTRODUCTION

Tiny displacements we observe in 3-D time-lapse seismic images are vectors, with three - vertical, inline, and crossline - components. These *apparent displacements* can be caused by reservoir compaction and are especially sensitive to related changes in strains and seismic wave velocities above reservoirs.

By "tiny", we mean displacements that may be only a fraction of a sampling interval. Figures 1–4 show an example from time-lapse seismic imaging of a high-pressure high-temperature reservoir in the North Sea. Here we estimated vertical apparent displacements roughly equal to the time sampling interval of 4 ms. In the inline and crossline directions, we estimated horizontal apparent displacements of approximately 5 m, which is much less than the 25 m inline and crossline sampling intervals.

Though small, the most significant inline and crossline displacements appear to be correlated with the geometry of the target reservoir. The point of intersection of the three orthogonal slices in each of Figures 1–4 lies just beneath that reservoir.

Apparent vertical (time) displacements like those shown in Figure 2 tend to be downward (positive), even when physical reservoir boundaries are displaced upwards. This difference between physical and apparent vertical displacements has been observed and explained by Hatchell and Bourne (2005).

Apparent horizontal displacements are less well understood, although these too have been measured here and by others (e.g., Hall, 2006). Figures 3 and 4 show apparent displacements that are generally smaller in the inline direction than in the crossline direction.

Figure 4 implies that, near the reservoir, 3-D seismic images are pulling apart in the crossline direction as fluids are extracted. This apparent horizontal stretching is the opposite of the compaction that we might expect if we interpreted such displacements as physical movements of reservoir rocks. However, the apparent stretching we observe here is reasonable if we consider the effect of a mild low-velocity lens above the reservoir induced by compaction. If not accounted for in seismic migration (as it was not here), such a change in seismic velocity could explain these apparent crossline displacements.

Such speculation notwithstanding, our understanding of apparent vector displacements today remains incomplete and beyond the scope of this paper. Our goal

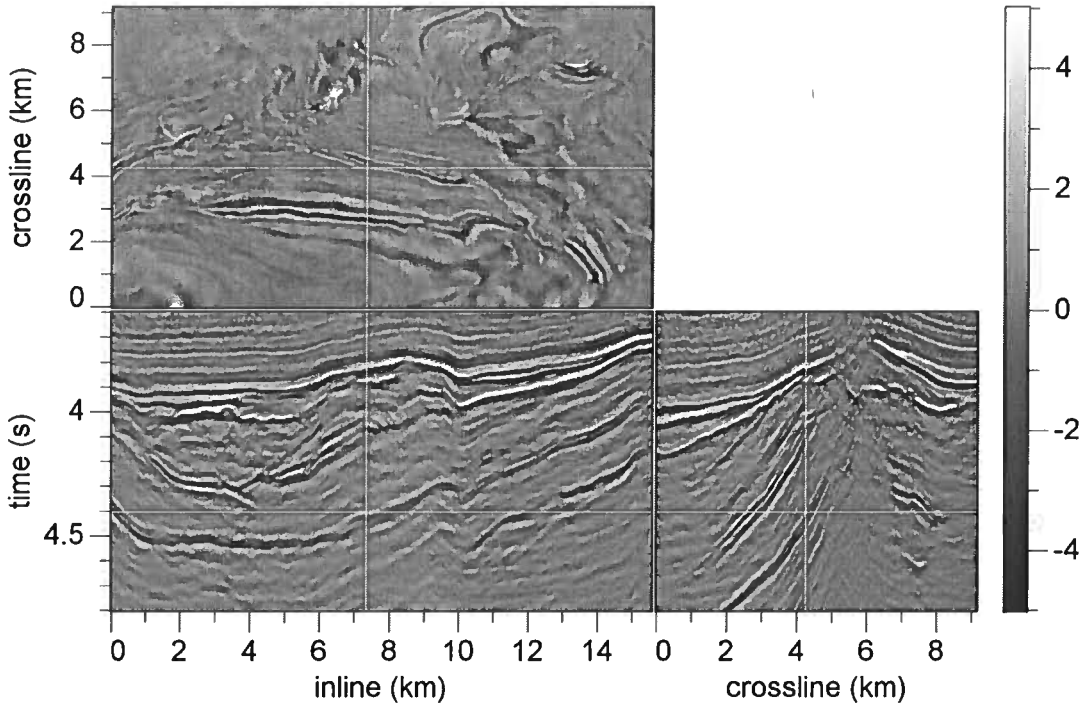

Figure 1. Three orthogonal slices of a 3-D seismic image recorded in 2002. A second image (not shown) was recorded in 2004. Crosshairs in each slice show the locations of the other two slices.

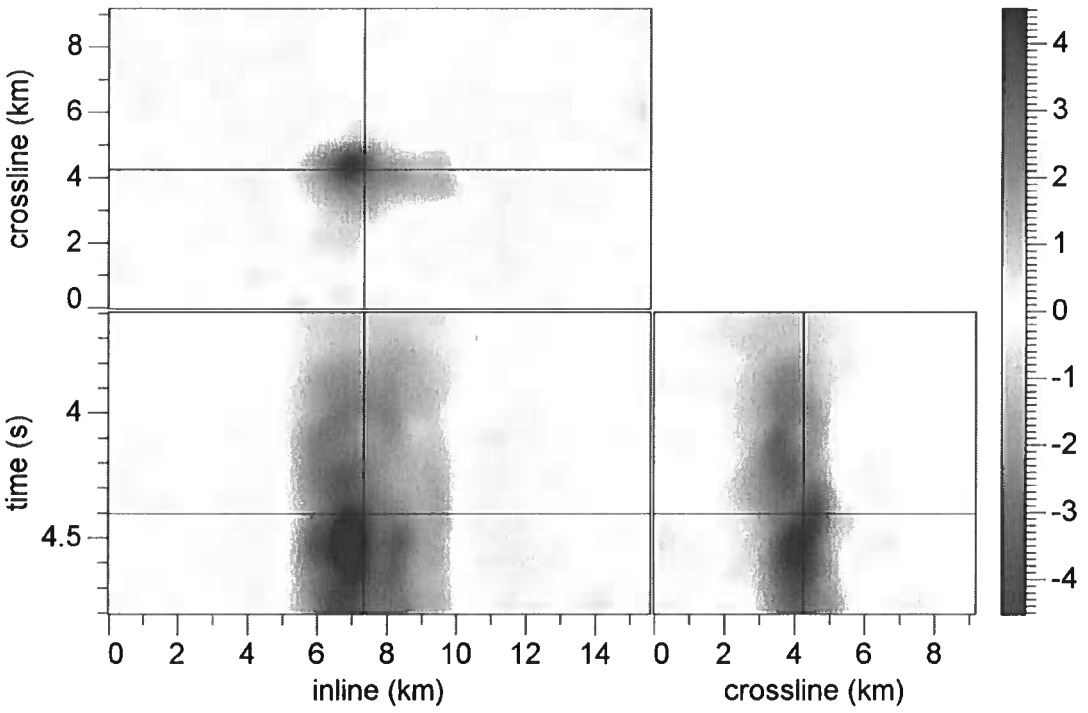

Figure 2. Vertical components of apparent displacement measured in ms.

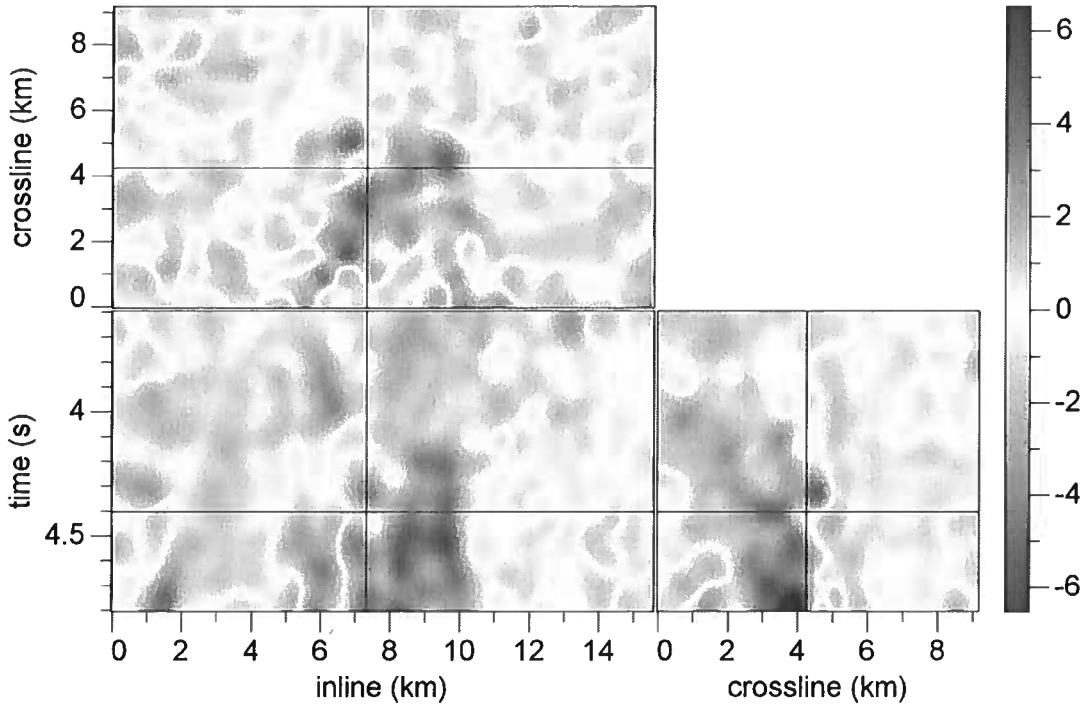

Figure 3. Inline components of apparent displacement measured in m.

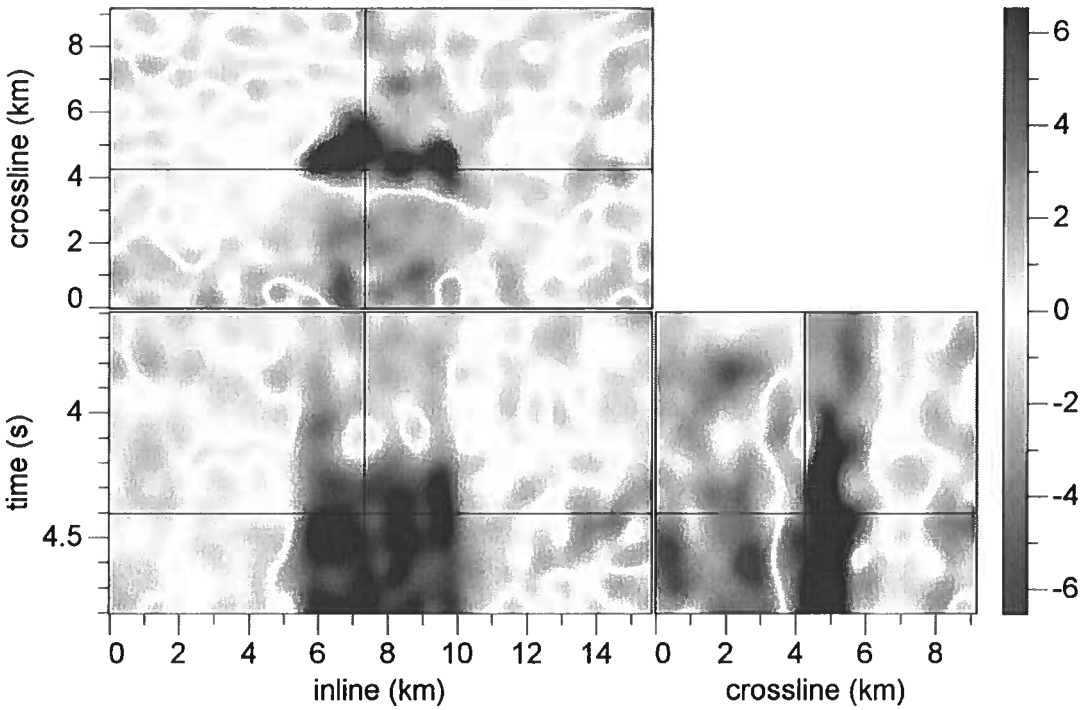

Figure 4. Crossline components of apparent displacement measured in m.

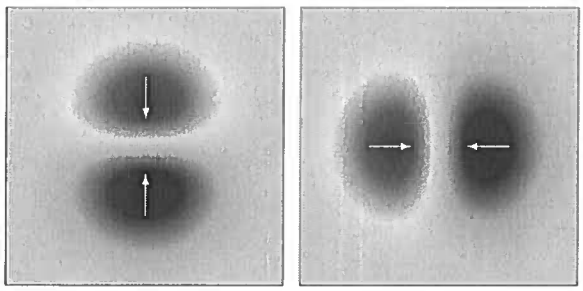

(a) (b)

Figure 5. Vertical (a) and horizontal (b) components of a synthetic vector displacement field representing compaction of an image towards its center. Dark red denotes three samples of vertical displacement (a) downward or (b) toward the right. Dark blue denotes three samples of vertical displacement (a) upward or (b) toward the left.

here is to describe the process by which we obtained these estimates of apparent vector displacements from time-lapse seismic images.

Estimation of all three components of displacements is difficult. One difficulty is that displacements of image features are poorly resolved in directions parallel to those features. Therefore, in seismic images where features are often more or less horizontal, we tend to estimate only the vertical component of displacement, because only that component is well resolved.

A second difficulty is that some processing techniques used to estimate only a single vertical component of displacement do not extend easily to estimation of all three components. For example, estimating the locations of peaks of cross-correlations of images is straightforward when those correlations are functions of only vertical lag. A simple quadratic interpolation of correlation values near a peak may suffice. An extension of this processing to finding peaks in correlations that are a function of two or three components of lag is more complicated and less robust, partly because of the resolution problem described above.

Finally, estimation of three components of displacement requires more computation, and the increase in cost can be significant when estimating a complete field of displacement vectors for every sample in 3-D images.

In this paper we illustrate these difficulties and describe a process that addresses them.

2 LOCAL CROSS-CORRELATIONS

Consider first only the two components of displacement shown in Figure 5. The displacement vectors in this example correspond to compaction or squeezing of an image towards its center.

2.1 Displacements between images

Using the synthetic displacement vector field shown in Figure 5, we can warp one seismic image to obtain another. Specifically, let sampled functions $f[j_1,j_2]$ and $g[j_1,j_2]$ denote two images related by

$$f[j_1,j_2] = g\big(j_1 + u_1[j_1,j_2],\ j_2 + u_2[j_1,j_2]\big), \tag{1}$$

where $u_1[j_1,j_2]$ and $u_2[j_1,j_2]$ represent the vertical and horizontal components of the vector displacement field $\mathbf{u}[j_1,j_2]$.

Throughout this paper we adopt the convention that $f[j_1,j_2]$ (with square brackets) is an image obtained by uniformly sampling a continuous function $f(x_1,x_2)$ (with parentheses) for integer pixel indices j_1 and j_2. We also assume that $f(x_1,x_2)$ is bandlimited and that $f[j_1,j_2]$ is not aliased, so that sinc interpolation can reconstruct the continuous function $f(x_1,x_2)$ with any required precision.

Because components of displacement u_1 and u_2 need not be integer values, the warping operation described by equation 1 implies interpolation of the sampled image $g[j_1,j_2]$ to compute $f[j_1,j_2]$.

Assume that we have two images f and g related by the synthetic displacement vector field of Figure 5. Can we recover the known displacement vectors $\mathbf{u}$ from the images?

2.2 Local cross-correlations

Figure 6 illustrates an attempt to estimate the displacement vector field $\mathbf{u}$ displayed in Figure 5 from two images f and g. The images are displayed in Figures 6a and 6b and at this scale appear to be identical, because maximum displacements are less than three samples in both vertical and horizontal directions.

To estimate displacement vectors $\mathbf{u}$, we search for locations of peaks of local cross-correlations. We define local cross-correlation of two images f and g by

$$c_{fg}[k_1,k_2;l_1,l_2] \equiv \sum_{j_1,j_2} f[j_1,j_2]\ g[j_1+l_1,j_2+l_2] \times w[k_1-j_1,k_2-j_2], \tag{2}$$

where $w[k_1,k_2]$ is a 2-D Gaussian window defined by

$$w[k_1,k_2] \equiv \mathrm{e}^{-(k_1^2+k_2^2)/2\sigma^2} \tag{3}$$

for a specified radius σ. (In the example of Figure 6, we used $\sigma = 12$ samples.) Summation indices j_1 and j_2 are limited by finite image bounds.

Equation 2 implies that for each pair of lag indices $[l_1,l_2]$ we compute a local cross-correlation value for every image sample indexed by $[k_1,k_2]$. In other words, we compute a correlation image c_{fg} as large as f and g for each $[l_1,l_2]$. When we do this for many lags, the resulting $c_{fg}[k_1,k_2;l_1,l_2]$ could consume large amounts of storage. However, when estimating displacements, we

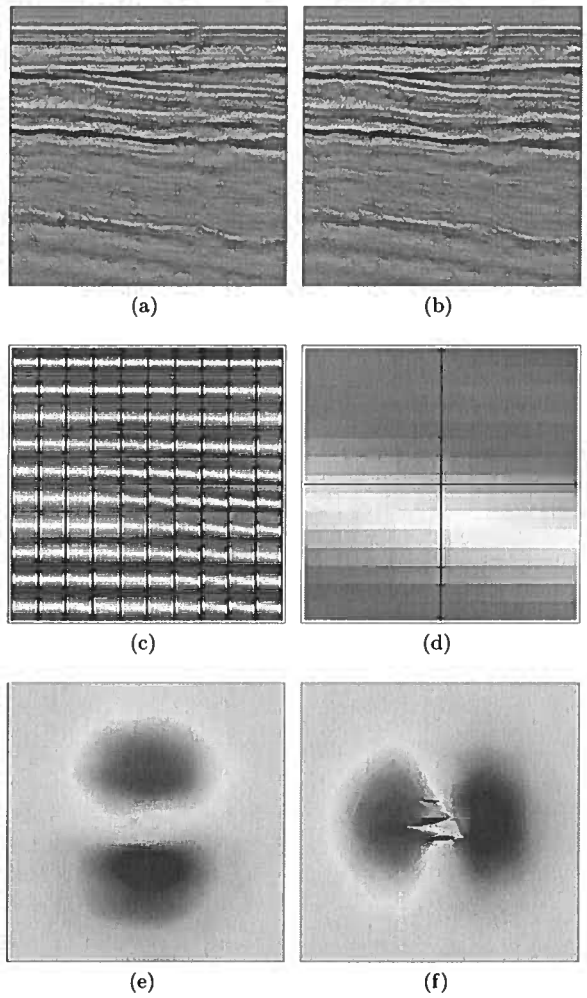

Figure 6. Estimates of displacement vectors from two 315 × 315-pixel images. The two images f (a) and g (b) are related by equation 1 for the displacements shown in Figure 5. The subset (c) of normalized local 2-D cross-correlations corresponds to the upper-left quadrant of these images, where displacements are downward and rightward. The downward shift is especially visible in one of these cross-correlations (d) shown in detail. A straightforward search for peaks of such cross-correlations yields estimates of both vertical (e) and horizontal (f) components of displacements.

need to store for each image sample only those correlation values required to locate correlation peaks.

The Gaussian window w makes the cross-correlations *local*. For any lag $[l_1, l_2]$, equation 2 represents convolution of this Gaussian window with a lagged image product $f[j_1, j_2]\ g[j_1 + l_1, j_2 + l_2]$. We perform this Gaussian filtering efficiently using recursive implementations (Deriche, 1992; van Vliet et al., 1998; Hale, 2006) with computational cost that is independent of the window radius σ.

Local windows can make cross-correlations sensitive to local amplitude variations. As we vary the lag $[l_1, l_2]$ in equation 2, high-amplitude events in g may slide in and out of the local Gaussian window, creating spurious correlation peaks that are inconsistent with true displacements.

2.3 Normalized local cross-correlations

To avoid this problem, the cross-correlation values displayed in Figures 6c and 6d have been normalized. Shown here are values of

$$\begin{aligned} c[k_1, k_2; l_1, l_2] \quad \equiv \quad & c_{fg}[k_1, k_2; l_1, l_2] \\ & \times \frac{1}{\sqrt{c_{ff}[k_1, k_2; 0, 0]}} \\ & \times \frac{1}{\sqrt{c_{gg}[k_1 + l_1, k_2 + l_2; 0, 0]}}. \end{aligned} \tag{4}$$

We compute the normalization factors $1/\sqrt{c_{ff}}$ and $1/\sqrt{c_{gg}}$ using special cases of equation 2:

$$c_{ff}[k_1, k_2; 0, 0] \equiv \sum_{j_1, j_2} f^2[j_1, j_2]\ w[k_1 - j_1, k_2 - j_2]$$

and

$$c_{gg}[k_1, k_2; 0, 0] \equiv \sum_{j_1, j_2} g^2[j_1, j_2]\ w[k_1 - j_1, k_2 - j_2].$$

These scale factors can be computed once and reused for all lags $[l_1, l_2]$. With these definitions (and by the Cauchy-Schwarz inequality), *normalized* local cross-correlations have the property $|c| \leq 1$.

Figure 6c shows a small subset of the 2-D normalized local cross-correlations computed for the upper-left quadrant of the two images in 6a and 6b; Figure 6d shows just one of these cross-correlations. We compute cross-correlations like these for every image sample. Each cross-correlation is local in the sense that it depends on samples within a 2-D Gaussian window of radius $\sigma = 12$ samples. As the window slides across the images, the local cross-correlations vary as in Figure 6c.

Figures 6c and 6d indicate a displacement of cross-correlation peaks vertically downward, which is consistent with the upper-left quadrant of Figure 5a. Horizontal (rightward) displacements of those peaks are more difficult to see. Displacements perpendicular to image features are more well resolved than those parallel to those features.

2.4 Quadratic interpolation

By simply searching over all sampled lags in Figure 6d, we can easily find the integer indices $[l_1, l_2]$ of the lag with highest correlation value. We might then fit some function to that value and others nearby to resolve the correlation peak location with sub-pixel precision.

A common choice for the fitting function is a

quadratic polynomial. For example, in one dimension, this quadratic function has the form

$$c(u) = a_0 + a_1 u + a_2 u^2.$$

We can choose the three coefficients a_0, a_1 and a_2 so that this polynomial interpolates exactly three sampled correlation values $c[l-1]$, $c[l]$ and $c[l+1]$. If a lag l is found such that $c[l]$ is not less than the other two correlation values and is greater than at least one of them, then the quadratic polynomial has a peak at

$$u = l + \frac{c[l-1] - c[l+1]}{2c[l-1] + 2c[l+1] - 4c[l]}. \quad (5)$$

It is both easy to prove and sensible that $|u-l| \leq \frac{1}{2}$. The correlation peak found by quadratic fit lies within half a sample of the largest correlation value found by scanning integer lags l. A scan of sampled correlation values provides a rough integer estimate of displacement; quadratic interpolation simply refines that estimate.

Other fitting functions are possible. In particular, a sinc function is most accurate for interpolating bandlimited sampled signals. But sinc interpolation does not provide a simple closed-form expression like equation 5 for the peak location. Therefore, quadratic interpolation is often used to find peaks.

Though small for bandlimited signals, the error in quadratic interpolation is biased in both peak amplitude and location. In addition to this error, two more problems arise with quadratic interpolation in higher dimensions.

2.5 Quadratic 2-D and 3-D interpolation

One problem is that the number of coefficients in a quadratic polynomial in higher dimensions does not equal the number of samples in any symmetric neighborhood nearest a sampled maximum correlation value. For example, in two dimensions the bi-quadratic polynomial has six coefficients:

$$c(u_1, u_2) = a_0 + a_1 u_1 + a_2 u_2 + a_3 u_1^2 + a_4 u_1 u_2 + a_5 u_2^2.$$

This number exceeds the number of correlation values in a five-sample neighborhood consisting of the values $c[l_1, l_2]$, $c[l_1 \pm 1, l_2]$, and $c[l_1, l_2 \pm 1]$; it is less than the number in a nine-sample neighborhood obtained by also including $c[l_1 \pm 1, l_2 \pm 1]$. To resolve this inconsistency, a bi-quadratic may be least-squares fit to the nine correlation values in the nine-sample neighborhood, but this fitted function does not generally interpolate any of the sampled correlation values within that neighborhood.

Likewise, in three dimensions a tri-quadratic polynomial has 10 coefficients, but symmetric neighborhoods of correlation values nearest a sampled maximum have either 7 (too few), 19 or 27 (too many) values. Quadratic polynomials in dimensions greater than one are either under- or over-constrained by cross-correlation values sampled at integer lags.

A second problem is that a peak location found by least-squares quadratic fit in two (or higher) dimensions need not lie within half a pixel of the integer lag indices $[l_1, l_2]$ corresponding to the maximum sampled correlation value. Indeed, for sampled correlations like those shown in Figures 6c and 6d, a least-squares-fit bi-quadratic may have a saddle point instead of a peak.

In other words, in two (or higher) dimensions, a peak may not exist for the least-squares quadratic fit to nine (or more) correlation values nearest to a sampled maximum value. And even when a quadratic peak does exist, it may be far away from the integer lag indices $[l_1, l_2]$ corresponding to the sampled maximum.

Such cases are pathological but not exceptional. We have observed them often while fitting bi-quadratic polynomials to the nine sampled values nearest the maximum value in correlations like those shown in Figures 6c and 6d.

These problems account for the most significant errors in the estimated components u_1 and u_2 of displacement vectors shown in Figures 6e and 6f. In this example errors are most significant for the horizontal component u_2, because the locations of correlation peaks in Figures 6c and 6d are least well resolved in that direction.

Discontinuities in apparent displacement vectors like those shown in Figure 6f are unreasonable, for they imply infinite apparent strain.

One way to eliminate or at least reduce such discontinuities is to seek displacements that maximize a weighted combination of image correlation and displacement smoothness. As discussed and implemented by Hall (2006), this approach implies a tradeoff. We must choose relative weights for correlation and smoothness. Rickett et al. (2006) discuss a similar correlation and smoothing tradeoff in estimating only vertical (time) shifts. These authors highlight the importance of not smoothing too much.

We describe a different approach below. We improve the accuracy of estimated displacements with a process that includes improved image processing and a more robust method for finding correlation peaks. With this process we obtain more accurate and thereby more continuous estimates of displacements without explicitly smoothing them.

3 LOCAL PHASE-CORRELATION

The first step in our process is to improve the spatial resolution of cross-correlations in directions parallel to features in seismic images. We do this by applying spatially-varying multi-dimensional prediction error filters to both images before cross-correlating them. The prediction error filters whiten the spectra of our images in all spatial dimensions.

Figures 7 illustrate the effect that this spectral whitening step has on our estimates of apparent displacements. After whitening, cross-correlation peaks are

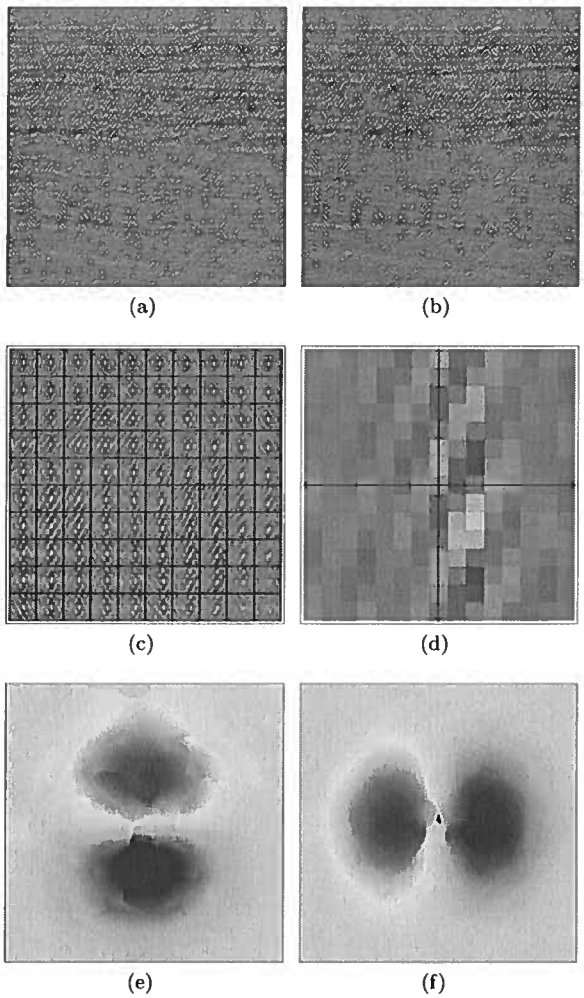

Figure 7. Images (a) and (b) after whitening with local prediction error filters. Peaks of local phase-correlations in (c) and (d) are well resolved in both vertical and horizontal directions. Estimates of vertical and horizontal components of displacement in (e) and (f) are more reliable than those without whitening. Visible patterns of errors and discontinuities in these estimates are caused by fitting 2-D quadratic functions to sampled correlation values nearest the peaks.

well resolved in both vertical and horizontal directions. In Figures 7c and 7d we see horizontal displacements of those peaks that are not apparent in Figures 6c and 6d.

3.1 Phase-correlation with Fourier transforms

Cross-correlation of whitened images is equivalent to phase-correlation, a process that is widely used in the context of image registration (Kuglin and Hines, 1975).

Phase-correlations are usually computed using Fourier transforms. Let F and G denote the Fourier transforms of images f and g, respectively. Then the cross-correlation $c = f \star g$ has Fourier transform $C = F^*G$. Assume temporarily that f and g are related by a constant displacement vector shift $\mathbf{u}$ such that

$$f(x_1, x_2) = g(x_1 + u_1, x_2 + u_2).$$

Then

$$F(k_1, k_2) = G(k_1, k_2)e^{ik_1u_1 + ik_2u_2}$$

and

$$C(k_1, k_2) = |F(k_1, k_2)||G(k_1, k_2)|e^{-ik_1u_1 - ik_2u_2}.$$

In phase-correlation we divide by the amplitude factors to obtain

$$P(k_1, k_2) \equiv \frac{F^*(k_1, k_2)}{|F(k_1, k_2)|} \frac{G(k_1, k_2)}{|G(k_1, k_2)|} = e^{-ik_1u_1 - ik_2u_2}.$$

These divisions in the frequency domain whiten the amplitude spectra of our images f and g. After this division the inverse-Fourier transform of $P(k_1, k_2)$ is a shifted delta function

$$p(x_1, x_2) = \delta(x_1 - u_1, x_2 - u_2).$$

Note that the peak at (u_1, u_2) of the phase-correlation delta function p is equally well-resolved in all directions.

In practice both p and P are sampled functions and we compute the latter with fast Fourier transforms. One method for then estimating the components of constant displacement u_1 and u_2 is to fit by least-squares a plane to the sampled phase of $P(k_1, k_2)$, perhaps restricting the fit to those frequencies (k_1, k_2) for which signal-to-noise ratios are high. The fitting parameters are the unknown components u_1 and u_2. More sophisticated frequency-domain methods are described by Hoge (2003) and by Balsi and Foroosh (2006).

In our discussion of phase-correlations above we temporarily assumed that the components of displacement u_1 and u_2 are constants. When displacements vary spatially, Fourier-transform methods applied to local windows are costly, especially when estimating apparent displacement vectors for every image sample. To estimate a dense spatially varying vector field of apparent displacements, we need an alternative space-domain method.

3.2 Local prediction error filtering

Our alternative is to apply local prediction error filters to the images f and g before computing local cross-correlations. These filters approximately whiten the amplitude spectra of the images, much like frequency-domain division by $|F|$ and $|G|$ in phase-correlation. The difference is that the prediction error filters are local; we compute and apply a different filter for every image sample.

For a sampled image f, the simplest 2-D prediction error filter that could possibly work computes prediction

errors

$$e[j_1,j_2;k_1,k_2] \equiv f[j_1,j_2] \\ -a_1[k_1,k_2]f[j_1-1,j_2] \\ -a_2[k_1,k_2]f[j_1,j_2-1],$$

where the coefficients $a_1[k_1,k_2]$ and $a_2[k_1,k_2]$ are found by minimizing a sum of squared prediction errors:

$$E[k_1,k_2] \equiv \sum_{j_1,j_2} e^2[j_1,j_2;k_1,k_2]\ w[k_1-j_1,k_2-j_2].$$

Again, the Gaussian window w localizes our computation of the prediction coefficents a_1 and a_2. For each image sample indexed by $[k_1,k_2]$, we minimize this sum by setting both $\partial E/\partial a_1$ and $\partial E/\partial a_2$ to zero, which leads to the following system of equations:

$$\begin{bmatrix} R_{11} & R_{12} \\ R_{12} & R_{22} \end{bmatrix} \begin{bmatrix} a_1 \\ a_2 \end{bmatrix} = \begin{bmatrix} r_1 \\ r_2 \end{bmatrix}, \tag{6}$$

where

$$\begin{aligned} R_{11} &= \sum_{j_1,j_2} f^2[j_1-1,j_2]\ w[k_1-j_1,k_2-j_2] \\ &= \sum_{j_1,j_2} f^2[j_1,j_2]\ w[k_1-1-j_1,k_2-j_2] \\ &= C_{ff}(k_1-1,k_2;0,0), \end{aligned}$$

and likewise

$$R_{12} = C_{ff}(k_1-1,k_2;1,-1),$$

$$R_{22} = C_{ff}(k_1,k_2-1;0,0),$$

$$r_1 = C_{ff}(k_1,k_2;-1,0), \text{ and}$$

$$r_2 = C_{ff}(k_1,k_2;0,-1).$$

We use equation 2 to compute the auto-correlation values $C_{ff}(k_1,k_2;l_1,l_2)$. The 2×2 matrix in equations 6 is symmetric and positive-definite (for non-constant f), as it is a Gaussian-weighted sum of outer products:

$$\begin{bmatrix} f[j_1-1,j_2] \\ f[j_1,j_2-1] \end{bmatrix} \begin{bmatrix} f[j_1-1,j_2]\ f[j_1,j_2-1] \end{bmatrix}.$$

Therefore, this matrix is never singular and a solution $[a_1\ a_2]$ always exists.

In the 3-D example of Figures 1–4, we computed three prediction coefficients a_1, a_2, and a_3 in a straightforward extension of equations 6. We again used a 3-D Gaussian window with radius $\sigma = 12$ samples.

It is important that we evaluate the auto-correlation values in equation 6 at the correct sample indices. For example, the value $R_{11} = C_{ff}[k_1-1,k_2;0,0]$ that we need to compute $a_1[k_1,k_2]$ and $a_2[k_1,k_2]$ typically does not equal the value $C_{ff}[k_1,k_2;0,0]$. If the latter value is used, then the system of equations 6 may not be positive-definite and solutions may not exist.

By computing and applying prediction error filters for every sample of the images shown in Figures 6a and 6b, we obtain the images shown in Figures 7a and 7b. Although our local prediction error filters are simple, with only two coefficients, the normalized local cross-correlations shown in Figures 7c and 7d have peaks that are more well-resolved than those in Figures 6c and 6d.

Unfortunately, resolution of the correlation peaks in Figures 7c and 7d is now too high. A quadratic function is inadequate for interpolation of broadband signals such as the sampled correlation function shown in Figure 7d. Errors in quadratic fitting are responsible for the discontinuities and patterns visible in the estimated components of displacement displayed in Figures 7e and 7f.

3.3 Bandlimited local phase-correlations

To reduce errors in quadratic fitting, we apply a 2-D low-pass smoothing filter to our images after spectral whitening. This filter has an isotropic Gaussian impulse response, like the 2-D window w that we use for local cross-correlations, but with a smaller radius $\sigma = 1$ sample.

Figures 8 show the result of smoothing after whitening for our test images. Like those in Figures 7c and 7d, the correlation peaks in Figures 8c and 8d remain well-resolved and more isotropic than those in Figures 6c and 6d, while smooth enough to reduce artifacts caused by errors in quadratic fitting.

In addition to improving the accuracy of quadratic fitting, low-pass filtering has another benefit. Prediction error filtering tends to enhance high-frequency noise. Where this noise is not repeatable in time-lapse experiments, it will degrade estimates of displacements. Gaussian smoothing after prediction error filtering attenuates the higher frequencies.

Smoothing after prediction error filtering is common practice in seismic data processing. For example, spiking deconvolution, a form of prediction error filtering, is often followed by low-pass filtering of seismograms. We use the same processing here, but with multi-dimensional prediction error filters computed and applied seamlessly for each image sample.

3.4 Remaining problems

In all of the examples of Figures 6, 7, and 8, we computed cross-correlation values for multiple integer lags $[l_1,l_2]$, and then fit 2-D quadratic functions to correlation peaks.

Recall that the fitted quadratic function need not exactly interpolate any of the 9 samples nearest to the sampled maximum correlation value, because the bi-quadratic function has only six coefficients. Also recall that this misfit may be greater in 3-D, as we fit 27 sampled correlation values with only 10 tri-quadratic coefficients. Errors in quadratic fitting have been reduced but not eliminated in the example of Figures 8.

Another problem is the amount of memory needed

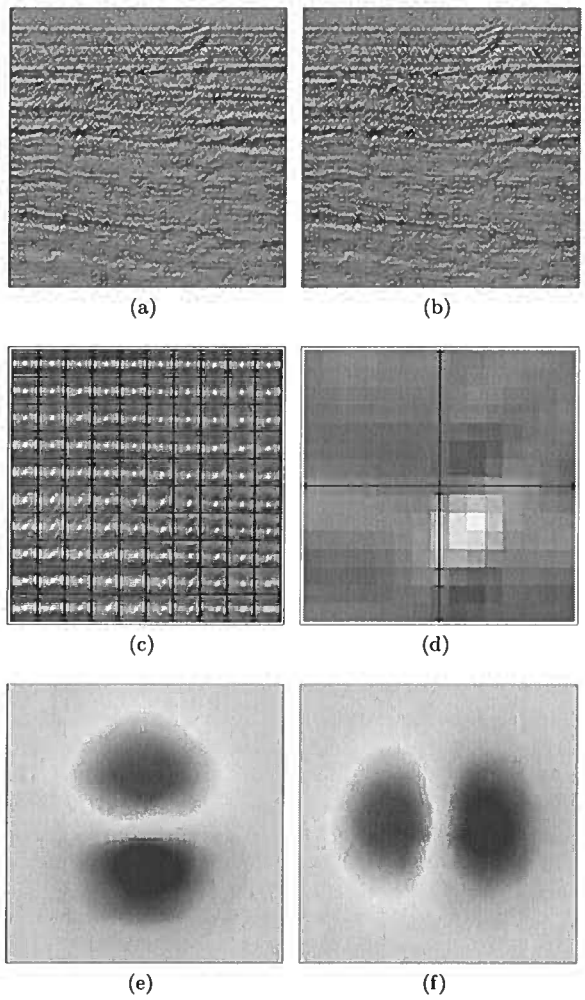

Figure 8. Images (a) and (b) after whitening with local prediction error filters and smoothing with a 2-D Gaussian filter. Smoothing attenuates high-frequency noise that is amplified by whitening, and facilitates location of the peaks of each of the phase-correlations shown in (c) and (d). Estimates of vertical and horizontal components of displacement in (e) and (f) are more accurate than those without smoothing in Figures 7e and 7f.

to hold all of the correlation values required for fitting. Recall that we compute for each lag $[l_1, l_2]$ an entire image of cross-correlation values $C_{fg}[k_1, k_2; l_1, l_2]$. As suggested by equation 2, this computation enables us to implement Gaussian windowing with efficient recursive filters.

As we iterate over lags, we must update for each image sample indexed by $[k_1, k_2]$ the lag $[l_1, l_2]$ for which a maximum sampled correlation value is found. For each sample, if the current correlation value exceeds the maximum value found so far, we update that maximum value and record the lag. After this first iteration over lags, the total number of correlation values computed is the product of the number of image samples times the number of lags.

This product can be a large number, especially for 3-D local correlations of 3-D images. Assuming that we do not store all of the correlation values computed in the first iteration, we must then recompute in a second iteration the sampled correlation values for lags nearest the lag with the maximum value. As we recompute those correlation values, we must update and store the coefficients of the quadratic polynomials required to locate correlation peaks. For 2-D images, 6 coefficients are required; for 3-D images, 10 coefficients.

Compared to memory required for other types of 3-D image processing, storage for 10 3-D volumes of coefficients is large but not prohibitive. And this factor of 10 is typically much less than the number of lags $[l_1, l_2, l_3]$ scanned in the search for correlation peaks. We need not store the correlation values for all lags scanned.

Nevertheless, as described in the following section, we can significantly reduce both the memory required and the number of correlation values computed, while eliminating any errors due to quadratic fitting.

4 CYCLIC SEARCH

Following the whitening-and-smoothing step describe above, the second step in our process is a cyclic sequence of correlations and shifts along each of the axes of our images.

4.1 Correlate-and-shift

We begin by cross-correlating two images in the vertical direction and finding the locations of peaks of those correlations. The peak locations that we find for each image sample correspond to one component of the displacement vectors that we wish to estimate.

We then shift one of the images using high-fidelity sinc interpolation to compensate for our estimated vertical components of displacements. This interpolation aligns the two images by applying spatially varying vertical shifts to one of them.

After compensating for vertical displacements, alignment is incomplete where horizontal components of displacement are non-zero. We therefore repeat this correlation and shifting to estimate and compensate for those horizontal components. After correlating and shifting for each image axis, we repeat the entire sequence of vertical and horizontal correlations and shifts until all shifts are negligible.

Figures 9 show estimated components of displacement for a four-cycle sequence of correlations and shifts. In each cycle we correlate and shift in both vertical and horizontal directions.

As we cross-correlate for one component of lag, say,

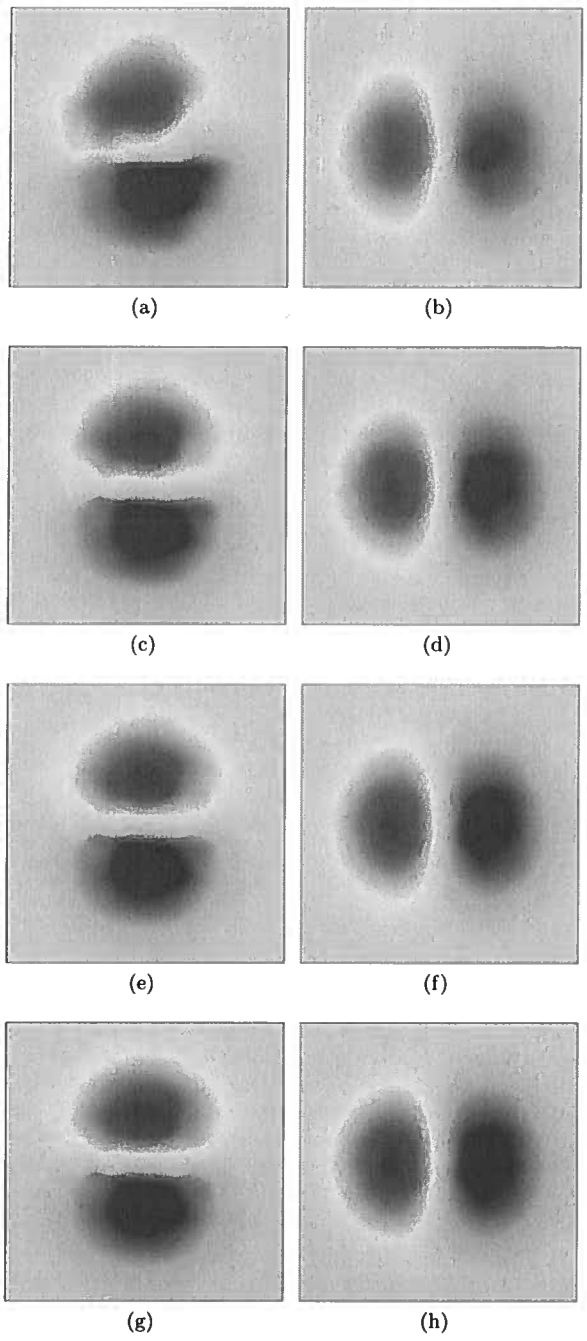

Figure 9. Four cycles of sequential estimation of two components of displacement for the images in Figures 8a and 8b. We first estimate vertical components of displacement (a). After shifting the image in Figure 8b vertically to compensate for these displacements, we estimate and compensate for horizontal components (b). Repeating this process, we obtain second (c and d), third (e and f) and fourth (g and h) estimates of displacements. Compare these final estimates with the known displacements in Figures 5.

l_1, the other components of lag are zero. In other words, we compute only the central column of normalized local cross-correlation functions like that displayed in Figure 8d. The images and the Gaussian correlation windows remain multi-dimensional; we use equation 2 just as before. But we restrict our computation of cross-correlation values to lags for which $l_2 = 0$.

In the example of Figure 8d, the maximum correlation value for $[l_1, l_2 = 0]$ occurs for lag $l_1 = 3$. So we would use quadratic interpolation of the sampled correlation values $c[2,0]$, $c[3,0]$, and $c[4,0]$ with equation 5 to estimate the location of the correlation peak (somewhere between lags $l_1 = 2$ and $l_1 = 3$) with sub-pixel precision.

As we iterate over lags l_1, we need only keep the most recent three cross-correlation values for each image sample. These values correspond to lags $l_1 - 1$, l_1, and $l_1 + 1$. When the correlation value for the middle lag l_1 exceeds the values for the other two lags, we use equation 5 and quadratic interpolation to interpolate a correlation peak value. If that peak value exceeds the maximum peak value found so far, we update the maximum and the displacement u_1 at which the maximum occurs.

The resulting estimates of displacement shown in Figures 9g and 9h are the most accurate of all such estimates shown in this paper. Compare these estimates with the known displacements in Figures 5.

4.2 Why cyclic search is better

Several features make this cyclic sequence of correlations and shifts attractive.

First, because only three (not six or ten) correlation images are required to interpolate peaks, a cyclic sequence of one-dimensional searchs for correlation peaks requires less memory than the direct multi-dimensional search used for Figures 6, 7, and 8.

Second, each 1-D quadratic interpolation we perform to locate peaks is guaranteed to find a peak value within one-half sample of the integer lag at which the maximum sampled correlation value occurs. Recall that no such guarantee exists for bi-quadratic and tri-quadratic fitting of 2-D and 3-D correlation values; the best-fitting quadratic polynomial may be a saddle with no peak at all. In this aspect 1-D quadratic interpolation is more robust.

Third, the cyclic sequence eliminates errors due to quadratic interpolation, because those errors go to zero as the shifts converge to zero. In each correlate-and-shift cycle, we compute shifts with quadratic interpolation, but we apply these shifts using sinc interpolation. (Sinc interpolation is commonly used in seismic data processing to apply one-dimensional shifts that vary with time and space. An example is normal-moveout correction.) Therefore, errors in quadratic interpolation do not accumulate and are gradually eliminated.

Finally, in a cyclic search for correlation peaks, we may compute fewer correlation values than in an exhaustive search over all possible lags $[l_1, l_2]$ (or, in 3-D, $[l_1, l_2, l_3]$) displayed in Figure 8d. In each correlate-and-shift step of cyclic search, we compute only one column or one row of cross-correlation values marked by blue axes in Figure 8d.

Computational cost is proportional to the number of correlate-and-shift cycles required to align the two images, that is, for shifts to become negligible. When displacements are small, convergence requires few iterations. And as shifts decrease in later iterations, cost can be reduced by limiting the range of lags for which we compute correlation values.

Our cyclic search resembles iterative Gauss-Seidel solution of large sparse systems of linear equations, in which one iteratively solves one of many equations for one variable while holding constant the other variables. Cyclic search is also a well-known algorithm for optimization of functions of several variables. In that sense here we use cyclic search to maximize cross-correlation functions computed for every image sample.

In the 3-D example of Figures 1–4, we used two cycles of vertical-crossline-inline shifts. The shifts in the second cycle were large enough to be worth applying, but not so much as to warrant a third cycle.

4.3 Displacements from a sequence of shifts

As our cyclic search converges, the two images become well aligned, and the shifts tend toward zero. How do we estimate displacements from the shifts that we compute and apply in each iteration of cyclic search?

Estimated components of displacements should not be simple sums of shifts computed and applied in each cycle.

To understand how to compute displacements from a sequence of shifts, consider equation 1 for some unknown components of displacement u_1 and u_2. Then suppose that we have initial estimates $u_1^{(0)}$ and $u_2^{(0)}$ (which may be zero) for these components and a corresponding shifted image

$$h_0[j_1, j_2] = g\big(j_1 + u_1^{(0)}[j_1, j_2],\ j_2 + u_2^{(0)}[j_1, j_2]\big).$$

Cross-correlating images f and h_0 for lags $[l_1, l_2 = 0]$, we estimate shifts s_1 that best align these two images vertically. We then use sinc interpolation to compute

$$h_1[j_1, j_2] = h_0\big(j_1 + s_1[j_1, j_2],\ j_2\big)$$

Cross-correlating images f and h_1 for lags $[l_1 = 0, l_2]$, we estimate horizontal shifts s_2, which we again apply with sinc interpolation to obtain

$$h_2[j_1, j_2] = h_1\big(j_1,\ j_2 + s_2[j_1, j_2]\big).$$

Now suppose that this one cycle of two shifts has aligned the two images, that our cyclic search has converged such that $f[j_1, j_2] = h_2[j_1, j_2]$. How do we compute the components of displacements u_1 and u_2?

Combining equations in the sequence above,

$$\begin{aligned} h_2[j_1, j_2] &= h_1\big(j_1,\ j_2 + s_2[j_1, j_2]\big) \\ &= h_0\big(j_1 + s_1(j_1,\ j_2 + s_2[j_1, j_2]),\ j_2 + s_2[j_1, j_2]\big) \\ &= g\big(j_1 + u_1[j_1, j_2],\ j_2 + u_2[j_1, j_2]\big), \end{aligned}$$

where the components of displacements u_1 and u_2 are

$$u_1[j_1, j_2] = s_1\big(j_1,\ j_2 + s_2[j_1, j_2]\big) + u_1^{(0)}\big(j_1 + s_1(j_1,\ j_2 + s_2[j_1, j_2]),\ j_2 + s_2[j_1, j_2]\big)$$

and

$$u_2[j_1, j_2] = s_2[j_1, j_2] + u_2^{(0)}\big(j_1 + s_1(j_1,\ j_2 + s_2[j_1, j_2]),\ j_2 + s_2[j_1, j_2]\big).$$

It would be awkward and inefficient to compute displacements in this way, only after our cyclic correlate-and-shift sequence has converged. Instead we compute

$$u_1^{(1)}[j_1, j_2] = u_1^{(0)}\big(j_1 + s_1[j_1, j_2],\ j_2\big) + s_1[j_1, j_2]$$

$$u_2^{(1)}[j_1, j_2] = u_2^{(0)}\big(j_1 + s_1[j_1, j_2],\ j_2\big),$$

and then

$$u_1^{(2)}[j_1, j_2] = u_1^{(1)}\big(j_1,\ j_2 + s_2[j_1, j_2]\big)$$

$$u_2^{(2)}[j_1, j_2] = u_2^{(1)}\big(j_1,\ j_2 + s_2[j_1, j_2]\big) + s_2[j_1, j_2].$$

And because this single cycle of sequential shifts has converged,

$$u_1[j_1, j_2] = u_1^{(2)}[j_1, j_2]$$

$$u_2[j_1, j_2] = u_2^{(2)}[j_1, j_2].$$

More generally, in the mth iteration of cyclic search, we estimate shifts s_m from local cross-correlations of images f and h_{m-1}. If m is odd, we then compute

$$h_m[j_1, j_2] = h_{m-1}\big(j_1 + s_m[j_1, j_2], j_2\big)$$

$$u_1^{(m)}[j_1, j_2] = u_1^{(m-1)}\big(j_1 + s_m[j_1, j_2], j_2\big) + s_m[j_1, j_2]$$

$$u_2^{(m)}[j_1, j_2] = u_2^{(m-1)}\big(j_1 + s_m[j_1, j_2], j_2\big);$$

otherwise, if m is even, we compute

$$h_m[j_1, j_2] = h_{m-1}\big(j_1, j_2 + s_m[j_1, j_2]\big)$$

$$u_1^{(m)}[j_1, j_2] = u_1^{(m-1)}\big(j_1, j_2 + s_m[j_1, j_2]\big)$$

$$u_2^{(m)}[j_1, j_2] = u_2^{(m-1)}\big(j_1, j_2 + s_m[j_1, j_2]\big) + s_m[j_1, j_2].$$

We repeat this cyclic sequence of correlations and shifts until s_m is negligible.

The least obvious result of this analysis is this: in the mth iteration of cyclic search we should use the computed shifts s_m to interpolate not only the image h_{m-1}, but both estimated components of displacement

$u_1^{(m-1)}$ and $u_2^{(m-1)}$ as well, *before* adding those shifts to either $u_1^{(m-1)}$ or $u_2^{(m-1)}$.

In this way we iteratively computed the two components of displacement shown in Figures 9. We used a straightforward generalization of this cyclic sequence to estimate the three components of displacement shown in Figures 2–4.

The significance of interpolating displacements before accumulating shifts depends on the spatial variability of the displacements. Where displacements are constant, this interpolation is unnecessary. Where displacements vary, as in the examples shown in this paper, omitting their interpolation would yield biased errors. Whether small or large, these errors can be eliminated by the sequence of computations described above.

5 CONCLUSION

Our process for estimating apparent displacements from time-lapse seismic images consists of two steps: (1) spectral whitening and Gaussian low-pass filtering followed by (2) a cyclic sequence of local correlations and shifts.

This process exploits readily available tools for image processing. We use efficient recursive filters to achieve seamlessly overlapping Gaussian windows in our computation of local cross-correlations and for isotropic low-pass filtering. We use local cross-correlations to estimate displacements and to compute multi-dimensional local prediction error filters

The combination of cross-correlation after spectral whitening with prediction error filters approximates phase-correlation, a well-known tool used for image registration. Our adaptation of this tool enables a local phase-correlation function to be computed efficiently for every image sample.

The cyclic sequence of correlations and shifts is a natural extension of today's common estimation of vertical apparent displacements from time-lapse seismic images. Indeed, we typically begin by correlating and shifting in the vertical direction, because that direction is likely to yield the largest shifts. We then apply repeatedly the same simple, accurate and robust process commonly used today for the vertical dimension to all three spatial dimensions of 3-D images.

The one parameter that must be chosen with care in our process is the radius σ of the Gaussian windows. Computational cost is independent of this radius, but the accuracy and resolution with which we can measure apparent displacements depends on it. Local correlations become less reliable as windows become smaller. Our ability to resolve changes in these correlations decreases as windows become larger.

In all of the examples shown in this paper, we have used $\sigma = 12$ samples. If we assume that a Gaussian is effectively zero for radii greater than 3σ, then each of the 3-D correlation windows used for the example shown in Figures 1–4 contains almost 200,000 samples. This number implies extensive averaging, and accounts in part for the smoothness in our estimated displacements.

Large windows do not however guarantee smooth displacements. For example, in Figure 6 estimated horizontal components of apparent displacement are discontinuous, implying infinite apparent strain. Where others (e.g., Rickett et al., 2005; Hall, 2006) have imposed smoothness constraints on estimated apparent displacements (in addition to using local windows for correlations) we have instead refined our processing to address the sources of these discontinuities.

While there is no guarantee that this improved processing will ensure sufficient accuracy or resolution, there is also no reason why this same processing could not be used in conjunction with the additional smoothness constraints developed by others.

ACKNOWLEDGMENT

Thanks to Shell U.K. Limited and the Shearwater partnership (Shell, BP, and ExxonMobil) for providing access to their time-lapse seismic images and permission to publish results derived from them.

REFERENCES

Balci, M., and H. Foroosh, 2006, Subpixel estimation of shifts directly in the Fourier domain: IEEE Transactions on Image Processing, **15**, 1965–1972.

Deriche, R., 1992, Recursively implementing the Gaussian and its derivatives: Proceedings of the 2nd International Conference on Image Processing, Singapore, 263–267.

Hale, D., 2006, Recursive Gaussian filters: CWP Report 546.

Hall, S., 2006, A methodology for 7D warping and deformation monitoring using time-lapse seismic data: Geophysics, **71**, O21–O31.

Hatchell, P. and S. Bourne, 2005, Measuring reservoir compaction using time-lapse timeshifts 75th Annual International Meeting, SEG, Expanded Abstracts, 2500–2504.

Hoge, W. S., 2003, A subspace identification extension to the phase correlation method: IEEE Transactions on Medical Imaging, **22**, 277–280.

Kuglin, C. D., and D. C. Hines, 1975, The phase correlation image alignment method: IEEE Proceedings of the International Conference on Cybernetics and Society, 163–165.

Rickett, J.E., L. Duranti, T. Hudson, and N. Hodgson, 2006, Compaction and 4-D time strain at the Genesis Field: 76th Annual International Meeting, SEG, Expanded Abstracts, 3215–3219.

van Vliet, L., Young, I., and Verbeek, P. 1998, Recursive Gaussian derivative filters: Proceedings of the International Conference on Pattern Recognition, Brisbane, 509–514.

CWP-567

Local dip filtering with directional Laplacians

Dave Hale

Center for Wave Phenomena, Colorado School of Mines, Golden CO 80401, USA

ABSTRACT

Local dip filters attenuate or enhance features with a specified dip that may vary for each image sample. Because these multi-dimensional filters change with each sample, they should have a small number of coefficients that can be computed efficiently from local dips. They should handle features that are vertical as well as horizontal. They should have efficient and stable inverses that facilitate the design and application of more discriminate notch filters. Local dip filters constructed from approximations to directional Laplacians have these properties and are easily implemented in any number of dimensions.

Key words: seismic image processing

1 INTRODUCTION

In seismic imaging of the earth's subsurface, we often describe the orientations of locally planar features by dip angles θ and, for 3-D images, azimuthal angles ϕ. Dip filters attenuate or enhance planar features based on their dips and azimuths, and *local dip filters* are those that can adapt locally to sample-to-sample changes in those parameters.

Orientations of locally planar features may also be described by reflection slopes. Fomel (2002) describes a method for implementing *plane-wave destruction filters* with numerous applications, including estimation of local slopes σ. Most of the applications described by Fomel are for images that have not been migrated, for which the vertical axis is time, and for which slopes are limited by seismic wave velocities.

After migration, slopes of features in seismic images may be infinite. Consider the dip of the flank of a salt dome or a fold or the dip of a fault plane. Robust local dip filters discriminate among features that are vertical as well as horizontal, without special handling of infinities. They are best parameterized by dips θ instead of slopes σ.

Local dip filters should be invertible. From inverses we can construct better dip filters and notch filters that surgically remove features with a specified local dip without attenuating other coherent features having slightly different dips.

Figures 1 show an example. I first applied a local dip filter to the image of Figure 1a to obtain the image of Figure 1b. To this image I then applied the inverse of a slightly modified local dip filter to create a notch filter and the image of Figure 1c. Whereas both dip and notch filters have removed strong coherent events, the notch filter has preserved weaker but interesting coherent features in Figure 1c.

Inverses of local dip filters are also useful for regularization in seismic inverse problems. Instead of simply requiring that solutions to such problems be smooth, we may require that they be smooth in some spatially varying directions. For example, those directions might correspond to geologic dip (Clapp et al., 2004; Fomel and Guitton, 2006). Figure 1d shows an example of such anisotropic smoothing.

In this paper I describe invertible local dip filters that are based on approximations to directional derivatives of images. These robust filters handle features that are vertical as well as horizontal, and have inverses that can be used to construct notch filters. The directions for the derivatives and, hence, coefficients of the filters depend on estimates of dips of locally planar features.

1.1 Estimating local dips

To apply a local dip filter or its inverse, we need estimates of local dips. In all of the examples of this paper, I estimate local dips using local structure tensors, which are also called gradient-square tensors (van Vliet and

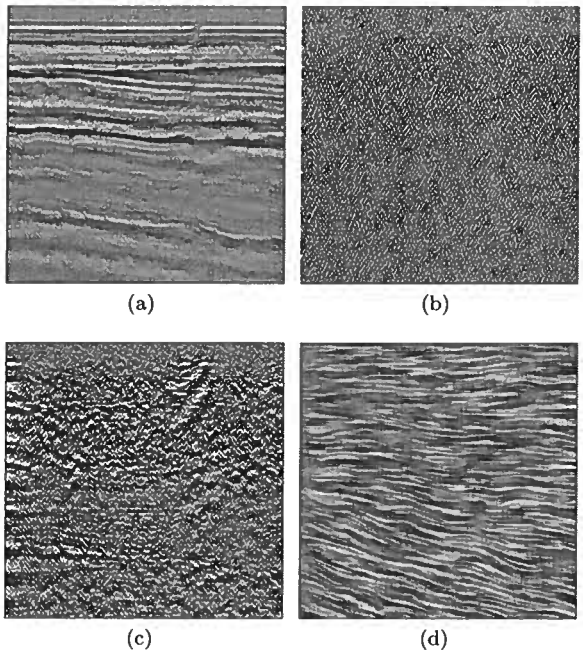

Figure 1. A seismic image (a) after local dip-filtering to remove the dominant locally linear feature found at each sample. Filtering a broad range of dips (b) eliminates these features and many others as well, leaving only high spatial frequencies. Local notch filtering (c) is more discriminate, preserving many weaker but locally coherent features of interest. Applying the inverse of a local dip-filter to random noise yields a texture (d) that shows the local orientation estimated for each sample in (a).

Verbeek, 1995). For 2-D images, a structure tensor is a 2×2 matrix:

$$G = \begin{bmatrix} < g_1^2 > & < g_1 g_2 > \\ < g_1 g_2 > & < g_2^2 > \end{bmatrix}, \quad (1)$$

where g_1 and g_2 denote vertical and horizontal components of the gradient of an image, and $< \cdot >$ denotes 2-D Gaussian smoothing.

As shown by van Vliet and Verbeek (1995), the orthogonal unit eigenvectors $\hat{\mathbf{u}}$ and $\hat{\mathbf{v}}$ of the positive-semidefinite matrix G describe the orientation of locally linear features. Specifically, for each sample the vector $\hat{\mathbf{u}}$ corresponding to the largest eigenvalue is orthogonal to the locally dominant linear feature at that sample.

Figures 2 show examples. The components of the unit vectors $\hat{\mathbf{u}}$ and $\hat{\mathbf{v}}$ are related to local dips θ by

$$u_1 = \cos\theta \quad \text{and} \quad u_2 = -\sin\theta,$$

$$v_1 = \sin\theta \quad \text{and} \quad v_2 = \cos\theta.$$

By convention the vertical component u_1 of $\hat{\mathbf{u}}$ is non-negative; that is, $-\pi/2 \le \theta \le \pi/2$.

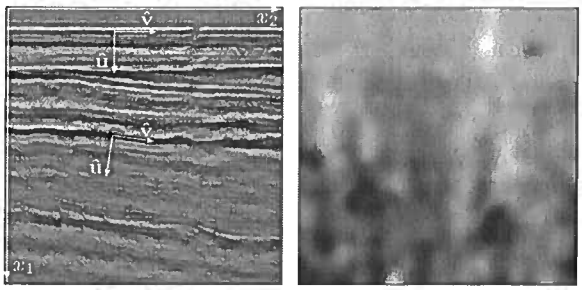

(a) (b)

Figure 2. Unit vectors $\hat{\mathbf{u}}$ and $\hat{\mathbf{v}}$ (a) define a coordinate system aligned with the dominant dip estimated for every image sample. By convention vertical components u_1 (not shown) of the local normal vectors $\hat{\mathbf{u}}$ are always non-negative and in this example are close to one for most samples. Horizontal components u_2 (b) are positive (white) for features dipping upward to the right ($\theta < 0$), and negative (black) for features dipping downward to the right ($\theta > 0$).

2 FOUR BASIC FILTERS

I begin by describing four basic local dip filters. The second and third filters are derived from the first filter, which was proposed by Claerbout (1992). The fourth filter is Fomel's (2002) plane-wave destruction filter, which I describe here for comparison and also because its implementation is almost identical to that of the third filter.

2.1 Claerbout's wavekill filter A

Let f denote a sampled image like that in Figure 2a, and let g denote the output of a local dip filter A applied to f. In directions parallel to the vectors $\hat{\mathbf{v}}$ in Figure 2a, the image f changes slowly, and so derivatives in those directions will be small. Hence, a simple local dip filter A can be constructed from a local directional derivative:

$$g = \hat{\mathbf{v}} \cdot \vec{\nabla} f,$$

or

$$A = \hat{\mathbf{v}} \cdot \vec{\nabla} = \hat{\mathbf{v}}^T \vec{\nabla}.$$

A simple finite-difference approximation to the gradient $\vec{\nabla}$ has components

$$\frac{\partial}{\partial x_1} \approx \begin{array}{|c|c|}\hline -\frac{1}{2} & -\frac{1}{2} \\ \hline \frac{1}{2} & \frac{1}{2} \\ \hline \end{array} \quad \text{and} \quad \frac{\partial}{\partial x_2} \approx \begin{array}{|c|c|}\hline -\frac{1}{2} & \frac{1}{2} \\ \hline -\frac{1}{2} & \frac{1}{2} \\ \hline \end{array}$$

where x_1 denotes the vertical spatial coordinate increasing downward and x_2 denotes the horizontal spatial coordinate increasing to the right. The filter A is then

$$A = \begin{array}{|c|c|}\hline -\frac{v_1+v_2}{2} & -\frac{v_1-v_2}{2} \\ \hline \frac{v_1-v_2}{2} & \frac{v_1+v_2}{2} \\ \hline \end{array},$$

where v_1 and v_2 are vertical and horizontal components of the unit vector $\hat{\mathbf{v}}$ aligned with the features that we wish to attenuate.

Alternatively, we can express the filter A in terms of vertical and horizontal components of the normal vector $\hat{\mathbf{u}}$:

$$A = \begin{array}{|c|c|} \hline -\frac{u_1-u_2}{2} & \frac{u_1+u_2}{2} \\ \hline -\frac{u_1+u_2}{2} & \frac{u_1-u_2}{2} \\ \hline \end{array} . \tag{2}$$

This is the stencil for the *wavekill filter* proposed by Jon Claerbout (1992). When applied to an image f, this filter attenuates features that are parallel to the vector $\hat{\mathbf{v}}$ and perpendicular to the vector $\hat{\mathbf{u}}$.

2.1.1 Implementing A

As the vectors $\hat{\mathbf{u}}$ and $\hat{\mathbf{v}}$ vary from sample to sample, so do the coefficients of this filter. The computational cost of computing those coefficients for each sample is small, due to their simplicity and the filter's compact 2×2 stencil.

If we let

$$m = \frac{u_1 - u_2}{2} \quad \text{and} \quad p = \frac{u_1 + u_2}{2}, \tag{3}$$

(m for minus, p for plus) then the wavekill filter stencil becomes

$$A = \begin{array}{|c|c|} \hline -m & p \\ \hline -p & m \\ \hline \end{array} . \tag{4}$$

An equation that implements this local dip filter is

$$\begin{aligned} g[i_1,i_2] &= m[i_1,i_2] \times f[i_1,i_2] \\ &+ p[i_1,i_2] \times f[i_1-1,i_2] \\ &- p[i_1,i_2] \times f[i_1,i_2-1] \\ &- m[i_1,i_2] \times f[i_1-1,i_2-1] \end{aligned} \tag{5}$$

for all image sample indices i_1 and i_2.

In this implementation I have chosen the lower-right corner of the filter stencil as the output sample for the filter. My choice is somewhat arbitrary. The stencil has no sample about which it is symmetric, so any corner will do.

Choosing the lower-right corner makes A a causal quarter-plane filter in the sense that the output $g[i_1,i_2]$ depends only on present and past input samples in the upper-left quarter plane.

2.1.2 Implementing A^{-1}

If a causal filter has a causal and stable inverse, then we say it is minimum-phase. (For an extension of the minimum-phase concept to multi-dimensional filters, see Claerbout, 1998.) The filter A is not minimum-phase; its causal inverse is unstable. We obtain that causal inverse by rewriting equation 5 to solve recursively for

$$\begin{aligned} f[i_1,i_2] = \big(& g[i_1,i_2] \\ & - p[i_1,i_2] \times f[i_1-1,i_2] \\ & + p[i_1,i_2] \times f[i_1,i_2-1] \\ & + m[i_1,i_2] \times f[i_1-1,i_2-1] \big) / m[i_1,i_2]. \end{aligned} \tag{6}$$

A necessary (but insufficient) condition for stability is that the divisor $m[i_1,i_2]$ is never zero. For a dip $\theta = -45$ degrees this inverse filter is clearly unstable, for then $u_1 = u_2$ and $m = 0$. In fact this causal inverse filter is unstable for all negative dips for which $m < p$.

2.1.3 Amplitude spectra of A

To assess the fidelity of the forward filter A we may look at its 2-D amplitude spectra for various dips, as shown in Figure 3.

For small wavenumbers less than half-Nyquist, these filters have the desired amplitude response, with the greatest attenuation along a (dark blue) line in the direction of the normal vector $\hat{\mathbf{u}}$. For higher wavenumbers, contours of constant amplitude are no longer linear, and the wavekill filter attenuates dips that are not parallel to $\hat{\mathbf{v}}$. This dispersion is caused by the finite-difference approximation to the gradient $\vec{\nabla}$.

2.2 Symmetric filter $A^T A$

From the simple wavekill filter $A = \hat{\mathbf{v}} \cdot \vec{\nabla} = \hat{\mathbf{v}}^T \vec{\nabla}$ we can construct a symmetric filter

$$\begin{aligned} A^T A &= \vec{\nabla}^T \hat{\mathbf{v}} \hat{\mathbf{v}}^T \vec{\nabla} \\ &= \vec{\nabla}^T (I - \hat{\mathbf{u}} \hat{\mathbf{u}}^T) \vec{\nabla}, \end{aligned} \tag{7}$$

where $I = \hat{\mathbf{u}}\hat{\mathbf{u}}^T + \hat{\mathbf{v}}\hat{\mathbf{v}}^T$ is a 2×2 identity matrix. Since A is a directional derivative, $A^T A$ is like a directional second derivative, or a *directional Laplacian*. More precisely, $A^T A$ is the negative of a directional Laplacian, because $\vec{\nabla}^T \vec{\nabla} = -\vec{\nabla}^2$.

2.2.1 Implementing $A^T A$

An obvious way to apply this filter is to first apply the linear filter A and then apply its transpose A^T. The transpose filter A^T is easy to implement if we think of equation 5 as multiplication by a sparse matrix, with the columns of the input and output images f and g arranged end to end in tall column vectors.

Thinking of the filter A^T in this way leads us to the following observation. Whereas equation 5 *gathers* four weighted input samples f to compute one output sample g, its transpose *scatters* one input sample into four output samples with the same weights. This gather-scatter symmetry can be seen in any software that carefully implements the transpose of a linear filter.

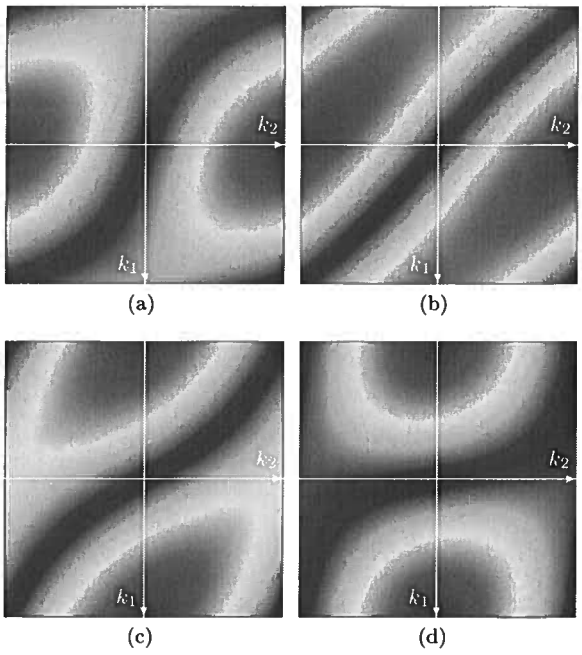

Figure 3. 2-D amplitude spectra of Claerbout's (1998) wavekill filters A for dips of (a) 20, (b) 40, (c) 60, and (d) 80 degrees, and for $-\pi \le k_1 \le \pi$ and $-\pi \le k_2 \le \pi$. Dark blue denotes zero. Dark red denotes the maximum amplitude, which varies for different filters.

Because the stencil for the filter A is small, the stencil for the filter A^TA is only slightly larger

$$A^TA = \begin{array}{|c|c|c|} \hline -m^2 & 2mp & -p^2 \\ \hline -2mp & 1 & -2mp \\ \hline -p^2 & 2mp & -m^2 \\ \hline \end{array}, \tag{8}$$

where m and p are defined by equations 3. This stencil is simply the 2-D auto-correlation of that in equation 4.

I have momentarily assumed that m and p are constants. When they vary spatially the coefficients in this stencil are not centrosymmetric (not symmetric about its center) and the central coefficient may not equal one.

It might be tempting to implement this filter by using $m[i_1, i_2]$ and $p[i_1, i_2]$ for the indices i_1 and i_2 of the central sample in this stencil to compute the filter coefficients for the eight adjacent image samples. But this approach does not yield a symmetric positive-semidefinite composite filter A^TA.

As described above, one proper way to implement A^TA is to first apply the filter A for variable coefficients, and then to apply the filter A^T for variable coefficients. The impulse response of the composite filter A^TA will vary with the location of the impulse, but it will not generally be centrosymmetric like the stencil of equation 8 above.

A more efficient way to achieve A^TA is suggested by equation 7. We may first apply the gradient filter $\vec{\nabla}$, then multiply by the 2×2 matrix $\hat{\mathbf{v}}\hat{\mathbf{v}}^T = I - \hat{\mathbf{u}}\hat{\mathbf{u}}^T$, and finally apply the transpose of the gradient filter $\vec{\nabla}^T$.

These three steps can all be performed in a single pass over the input and output images. Here is a fragment of a C, C++ or Java computer program that implements the filter of equation 7 in one-pass:

```
for (int i2=1; i2<n2; ++i2) {     // i2=0?
  for (int i1=1; i1<n1; ++i1) {   // i1=0?
    float u2i = u2[i2][i1];
    float u1i = sqrt(1.0f-u2i*u2i);
    float a11 = 1.0f-u1i*u1i;
    float a12 =     -u1i*u2i;
    float a22 = 1.0f-u2i*u2i;
    float fa = f[i2  ][i1  ]-f[i2-1][i1-1];
    float fb = f[i2  ][i1-1]-f[i2-1][i1  ];
    float f1 = 0.5f*(fa-fb);
    float f2 = 0.5f*(fa+fb);
    float g1 = a11*f1+a12*f2;
    float g2 = a12*f1+a22*f2;
    float ga = 0.5f*(g1+g2);
    float gb = 0.5f*(g1-g2);
    g[i2  ][i1  ]  = ga;
    g[i2-1][i1-1] -= ga;
    g[i2  ][i1-1] -= gb;
    g[i2-1][i1  ] += gb;
  }
}
```

This simple fragment does not compute the first row $i_1 = 0$ or first column $i_2 = 0$ of the output image g; those cases are easily handled by assuming zero values outside array bounds.

2.2.2 *Implementing* $(A^TA)^{-1}$

In applications requiring inverse filters, a symmetric positive-semidefinite A^TA is especially useful. For if we try to apply $(A^TA)^{-1} = A^{-1}A^{-T}$ using a cascade of fast recursions as in equation 6, we encounter the same instability that we have seen before.

However, because A^TA is symmetric positive-semidefinite and sparse, we can apply inverse filters by solving systems of equations $A^TAf = g$ by the iterative method of conjugate gradients. This method requires only three extra arrays, each the size of the images f and g. For 3-D images, this relatively low memory requirement can be an important consideration.

An alternative to conjugate-gradient iterations is Cholesky decomposition of A^TA. For variable coefficients this matrix decomposition may be more costly than the method of conjugate gradients.

However, an approximation to Cholesky decomposition may be adequate. The approximation is Wilson-Burg factorization (Fomel et al., 2003), a method for computing a minimum-phase filter from its auto-correlation. The Wilson-Burg method computes a minimum-phase filter $\bar{A}$ such that

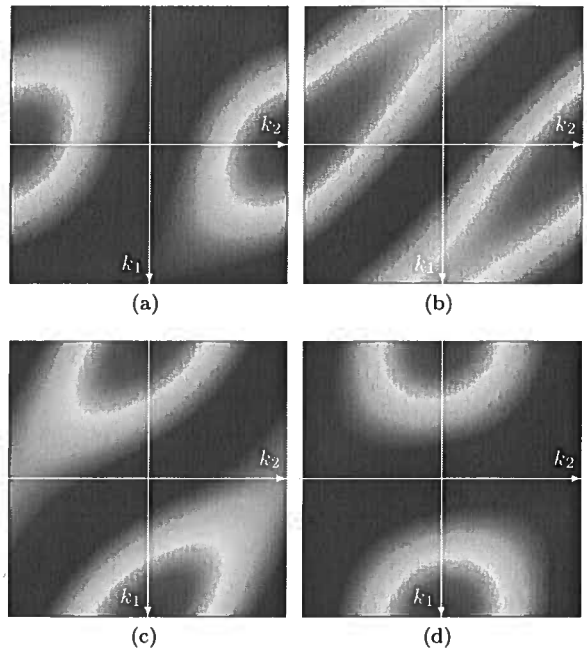

Figure 4. 2-D amplitude spectra of symmetric filters A^TA for dips of (a) 20, (b) 40, (c) 60, and (d) 80 degrees, and for $-\pi \le k_1 \le \pi$ and $-\pi \le k_2 \le \pi$. These amplitudes are the square of those in Figures 3. Dark blue denotes zero. Dark red denotes the maximum amplitude, which varies for different filters.

$$\tilde{A}^T\tilde{A} \approx A^TA. \tag{9}$$

In my approximations I computed minimum-phase filters $\tilde{A}$ with 14 non-zero coefficients such that $\tilde{A}^T\tilde{A}$ approximates A^TA in the stencil of equation 8 above.

I have tabulated such filters as a function of dip θ, and then applied $\tilde{A}$ for variable coefficients by selecting for each output sample the most appropriate filter from the table. Because each of the tabulated filters $\tilde{A}$ is minimum-phase, both $\tilde{A}$ and $\tilde{A}^T$ have stable inverses, and those inverses $\tilde{A}^{-1}$ and $\tilde{A}^{-T}$ can be implemented efficiently as recursive filters.

In practice the differences between A^TA and $\tilde{A}^T\tilde{A}$ are insignificant; the approximation in equation 9 is adequate. Differences in the inverses however may be more significant. Even then the filter $\tilde{A}^{-1}\tilde{A}^{-T}$ is useful as a preconditioner (approximate inverse) in the method of conjugate gradients when applying $(A^TA)^{-1}$.

2.2.3 Amplitude spectra of A^TA

For constant coefficients we may compute amplitude spectra of the centrosymmetric stencil A^TA of equation 8 for different dips. These are shown in Figures 4.

Amplitude spectra for A^TA are simply the square of those for A. (Compare Figures 3 and 4.) Squaring the amplitudes broadens the valleys of attenuation. The filter A^TA attenuates the specified dip but significantly attenuates many nearby dips as well. In this respect, the filter A^TA is less discriminant than A.

2.3 Folded filter B

A better filter would have the amplitude spectrum of A and a stable inverse that does not require solution of a sparse system of linear equations. I obtained such a filter by folding the stencil of A^TA in equation 8 from right to left symmetrically about its center:

$$B = \begin{array}{|c|c|c|} \hline -2m^2 & 2mp & \\ \hline -4mp & 1 & \\ \hline -2p^2 & 2mp & \\ \hline \end{array} .$$

In folding, I centrosymmetrically added coefficients on the right side of the stencil for A^TA to those on the left side, leaving the central column of coefficients unchanged.

To understand why such folding might provide a useful dip filter, imagine a dipping feature that passes through the central sample of the stencil for A^TA. Because this stencil is centrosymmetric, the products of the dipping feature and coefficents on the right are the same as products obtained for coefficients on the left. So we can simply double the left-side products and omit the right-side products.

Another way to derive the stencil for B is to construct a weighted sum of wavekill filters with the goal of making that sum invertible. Recall that the inverse filter of equation 6 is unstable for $m = 0$. In other words, for $m = 0$, the filter of equation 5 is not invertible. In this case, that wavekill filter has zero weight in the weighted sum:

$$B = 2m \times \begin{array}{|c|c|} \hline -m & p \\ \hline -p & m \\ \hline 0 & 0 \\ \hline \end{array} + 2p \times \begin{array}{|c|c|} \hline 0 & 0 \\ \hline -m & p \\ \hline -p & m \\ \hline \end{array} .$$

In this sum, the left-hand stencil handles the positive dips $\theta > 0$ for which $u_2 < 0$ and $m \neq 0$, while the right-hand stencil handles the negative dips $\theta < 0$ for which $u_2 > 0$ and $p \neq 0$. The scale factor 2 makes this sum the same as the stencil obtained by folding:

$$B = \begin{array}{|c|c|} \hline -2m^2 & 2mp \\ \hline -4mp & 1 \\ \hline -2p^2 & 2mp \\ \hline \end{array} . \tag{10}$$

2.3.1 Implementing B

Implementation of the folded filter B with six coefficients is much like that for the wavekill filter A with four coefficients. We let the middle-right coefficient with value 1 in this stencil be the central sample for the filter B. Then, for each output sample, we simply multiply coefficients in this stencil by corresponding input samples and sum the products.

When the coefficients vary spatially this operation is not convolution; but it is linear, and we may again think of B as a large sparse matrix with which we compute an output image $g = Bf$ from an input image f.

2.3.2 Implementing B^{-1}

Because the central sample for the filter B is 1, and therefore never 0, we might hope that this filter is easily inverted. Indeed, this potential motivated the weighted sum used to derive B. However, unlike the wavekill quarter-plane filter A, the folded half-plane filter B is not causal, due to the non-zero lower-right coefficient $2mp$ that is generally non-zero.

Therefore, given $g[i_1, i_2]$ we cannot simply solve for the central sample $f[i_1, i_2]$ in terms of previously computed adjacent samples, as I did in equation 6. Specifically, the sample $f[i_1, i_2]$ is coupled by the right column of the stencil for B to the samples above and below it.

However, if we have already computed $f[i_1, i_2 - 1]$ for all indices i_1, then we may compute $f[i_1, i_2]$ for all i_1 by solving a tridiagonal system of equations. Unlike more general sparse systems, tridiagonal systems can be solved efficiently without iterations.

In summary, we may apply the inverse filter B^{-1} to an image by recursively solving tridiagonal systems of equations from left to right. We begin with $i_2 = 0$ and assume that $f[i_1, -1] = g[i_1, -1] = 0$. We then solve recursively for $f[i_1, 0]$, $f[i_1, 1]$, and so on.

2.3.3 Amplitude spectra of B

Amplitude spectra for the filter B are shown in Figures 5. Let us again focus our attention on small wavenumbers near the centers of these spectra, where the filters should be most accurate.

For small dips the amplitude spectra for B resemble those for the wavekill filter A in Figures 3. For the largest dip $\theta = 80$ degrees the amplitude spectrum of B is more like that for $A^T A$ in Figure 4d.

These differences in amplitude spectra are caused by folding in one direction. Folding horizontally makes the horizontal part of the directional second-derivative $A^T A$ more like a first-derivative, but leaves the vertical part like a second-derivative.

One might wonder whether folding both horizontally and vertically would reduce these differences. However, the resulting quarter-plane filter would treat features with positive dips differently than those with negative dips. Therefore I folded only horizontally to obtain the half-plane filter B.

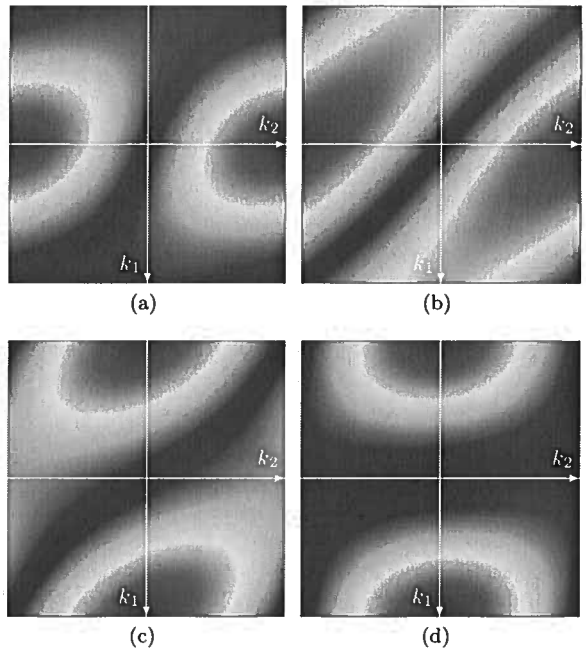

Figure 5. 2-D amplitude spectra of folded filters B for dips of (a) 20, (b) 40, (c) 60, and (d) 80 degrees, and for $-\pi \le k_1 \le \pi$ and $-\pi \le k_2 \le \pi$. Dark blue denotes zero. Dark red denotes the maximum amplitude, which varies for different filters.

2.4 Fomel's plane-wave destruction filter C

Our search for a filter with a stencil like that in equation 10 was motivated by Fomel's *plane-wave destruction filter* (2002), which has a similar stencil:

$$C = \begin{array}{|c|c|} \hline -\frac{(1+\sigma)(2+\sigma)}{12} & \frac{(1-\sigma)(2-\sigma)}{12} \\ \hline -\frac{(2+\sigma)(2-\sigma)}{6} & \frac{(2+\sigma)(2-\sigma)}{6} \\ \hline -\frac{(1-\sigma)(2-\sigma)}{12} & \frac{(1+\sigma)(2+\sigma)}{12} \\ \hline \end{array}. \tag{11}$$

where $\sigma = v_1/v_2 = -u_2/u_1 = \tan\theta$ is the slope of the feature to be attenuated.

The coefficients in the left and right columns of this stencil approximate quadratic interpolations of three samples with indices $i_1 - 1$, i_1, and $i_1 + 1$, evaluated at $i_1 - \sigma/2$ and $i_1 + \sigma/2$, respectively. By subtracting the interpolated value on the right from the one on the left, this filter annihilates features with slope σ.

The accuracy of the interpolation decreases with increasing $|\sigma|$. For vertical features, σ and the coefficients of C in equation 11 are infinite, and this filter is unstable.

Fomel describes higher order interpolations that could be used instead, but these too will fail for vertical or near vertical features. The problem here lies in choosing one direction for interpolation, the vertical x_1 direction. For features with slopes $|\sigma| > 1$ we should instead be interpolating in the horizontal x_2 direction.

2.4.1 Implementing C

Implementation of the plane-wave destruction filter for any slope is the same as that for filter B described above, and vice-versa. Indeed, one of my motives for designing filter B was to make it easy to insert B into any existing implementation of filter C.

Infinities for vertical features can be eliminated by simply multiplying the coefficients of this filter by u_1 to obtain

$$C_2 = \begin{bmatrix} -\frac{(u_1-u_2)(2u_1-u_2)}{12} & \frac{(u_1+u_2)(2u_1+u_2)}{12} \\ -\frac{(2u_1-u_2)(2u_1+u_2)}{6} & \frac{(2u_1-u_2)(2u_1+u_2)}{6} \\ -\frac{(u_1+u_2)(2u_1+u_2)}{12} & \frac{(u_1-u_2)(2u_1-u_2)}{12} \end{bmatrix}. \quad (12)$$

Coefficients of this normalized filter are finite for all dips.

2.4.2 Implementing C^{-1}

I have not used the normalized filters C_2 in the examples shown in this paper, partly because they are not the more familiar filters proposed by Fomel (2002), and also because normalization does not help with the implementation of inverse filters.

For slopes $|\sigma| < 1$ we can implement inverse filters C^{-1} the same way we implement B^{-1}. That is, we can recursively construct and solve tridiagonal systems of equations from left to right when applying C^{-1}.

However, for slopes $|\sigma| > 1$, the corresponding tridiagonal matrix is not diagonally dominant, and this left-to-right recursion becomes unstable.

2.4.3 Amplitude spectra of C

Amplitude spectra for the plane-wave destruction filter C of equation 11 are shown in Figures 6. For smaller dips, the amplitudes resemble those of the other filters described above.

For larger dips, these amplitude spectra are aliased. This aliasing may be useful when attempting to remove aliased dipping events from images, but in such cases the filter C will for some wavenumbers also remove unaliased events having different smaller dips.

3 EXAMPLES

Qualities of the four local dip filters described above are best illustrated with examples. To compare and contrast these filters, I applied them to images with small dips, large dips, and a test image with a complete range of all possible dips.

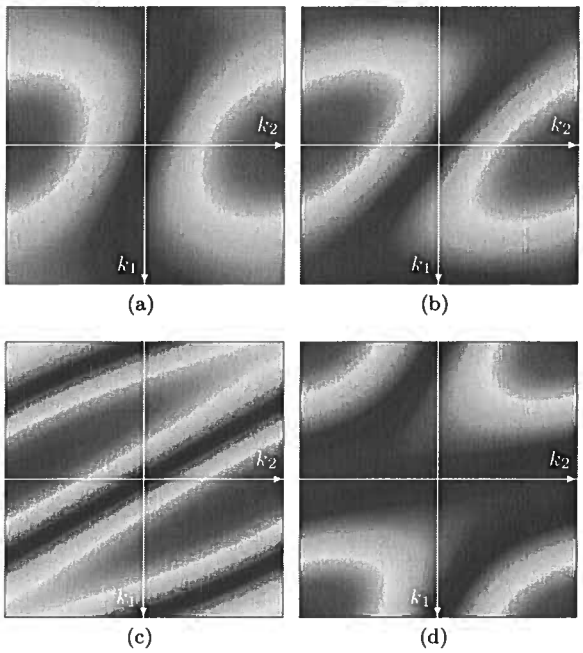

Figure 6. 2-D amplitude spectra of Fomel's plane-wave destruction filters C for dips of (a) 20, (b) 40, (c) 60, and (d) 80 degrees, and for $-\pi \le k_1 \le \pi$ and $-\pi \le k_2 \le \pi$. Dark blue denotes zero. Dark red denotes the maximum amplitude, which varies for different filters.

In all examples, I first estimated local dips from local structure tensors, and then used those dips to compute the coefficients for all four filters.

3.1 Small dips

The first example is the input image of Figure 1a (also Figure 2a). Dips of dominant features in this image are small, with $|\theta| < 45$ degrees.

Output images for all four filters — A, B, C and A^TA — are displayed in Figures 7. All filters attenuate the locally planar events in these images. The output images for filters A, B and C are almost identical as we would expect from similarities in their amplitude spectra for small dips.

The output for filter A^TA is notably different, as it effectively differentiates the input image twice instead of once. This filter therefore further amplifies high wavenumbers while attenuating a broader swath of dips for low wavenumbers. Again this output is consistent with the amplitude spectra for small dips shown in Figures 4a and 4b.

To test the inverses of the four filters for small dips, I applied them to an image containing isotropically ban-

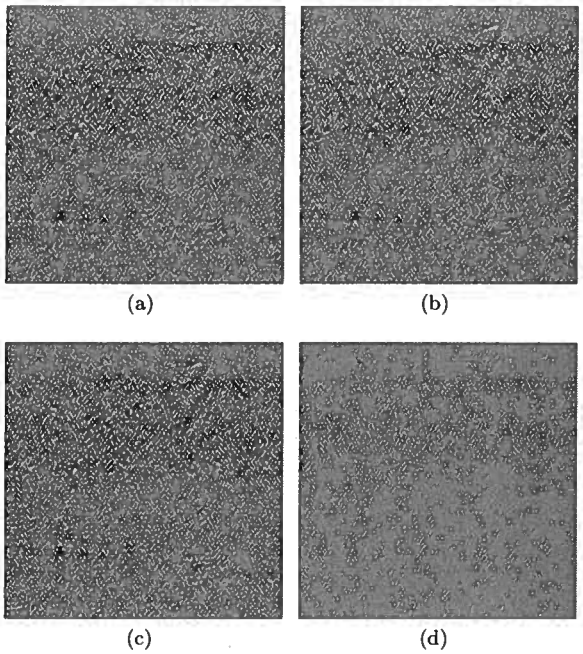

Figure 7. Output images for local dip filters (a) A, (b) B, (c) C and (d) A^TA applied to the image of Figure 1a. All filters attenuate locally coherent dipping features, but leave only features with dips that differ significantly from the predominate dip. For small dips, the outputs for the folded filter B and Fomel's plane-wave destruction filter C appear almost identical to that for the wavekill filter A.

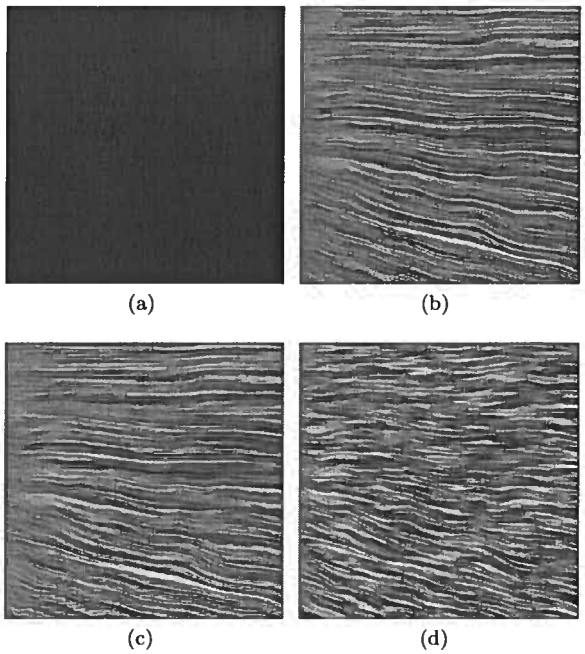

Figure 8. Application to a random-noise image of inverses of local dip filters (a) A, (b) B, (c) C and (d) A^TA. Causal inverses of wavekill filters A are unstable. Inverses for the folded filter B and Fomel's filter C are obtained by recursively solving tridiagonal systems of equations from left to right. The inverse of the symmetric filter A^TA is computed by conjugate-gradient iteration.

dlimited random noise. Inverses that are unstable for such random images are also unstable for real images, because pseudo-random rounding errors are created in the application of inverse filters to any real image.

The causal recursive inverse A^{-1} is unstable and produces no output. For the small dips in this example, the recursive tridiagonal inverses B^{-1} and C^{-1} produce almost identical textures.

Dips in the texture for the inverse $(A^TA)^{-1}$ are less well defined than those for B^{-1} and C^{-1}. Because the filter A^TA attenuates a wider range of dips, its inverse $(A^TA)^{-1}$ amplifies a wider range of dips instead of a single sharply defined dip at each sample.

3.2 Large dips

A simple way to test local dip filters for large dips is to transpose the image used in the previous examples, so that horizontal features become vertical. This transposed image is shown in Figure 9a.

Figure 9b shows a synthetic test image with small and large, negative and positive dips. For any sample in this image, there exists only one coherent event with one local dip, and the output for an ideal local dip filter should be zero.

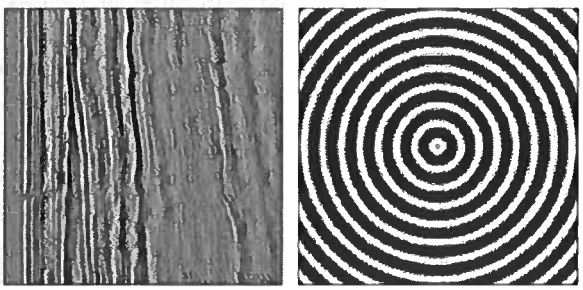

Figure 9. Test image (a) with vertical features is the transpose of the image of Figure 1a. Test image (b) is a synthetic image with all dips.

Filter outputs for the transposed input are shown in Figures 10. For this example, the coefficients of the plane-wave destruction filter C approach infinity, and this accounts for the high amplitudes in Figure 10c.

The similarity of the outputs for the folded filter B (Figure 10b) and the symmetric filter A^TA (Figure 10d) is consistent with their amplitude spectra for the largest dip in Figures 4d and 5d. For dips near 90 degrees, both

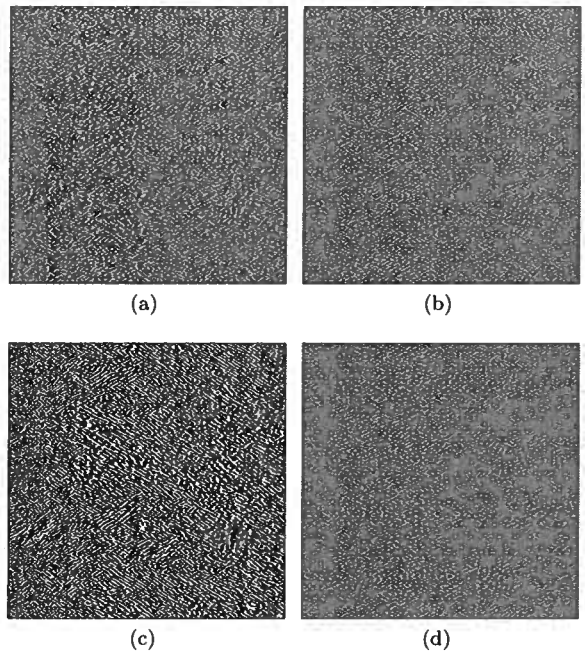

Figure 10. Output images for local dip filters (a) A, (b) B, (c) C and (d) A^TA applied to the transposed image in Figure 9a. For large dips, the output for Fomel's filter C goes to infinity.

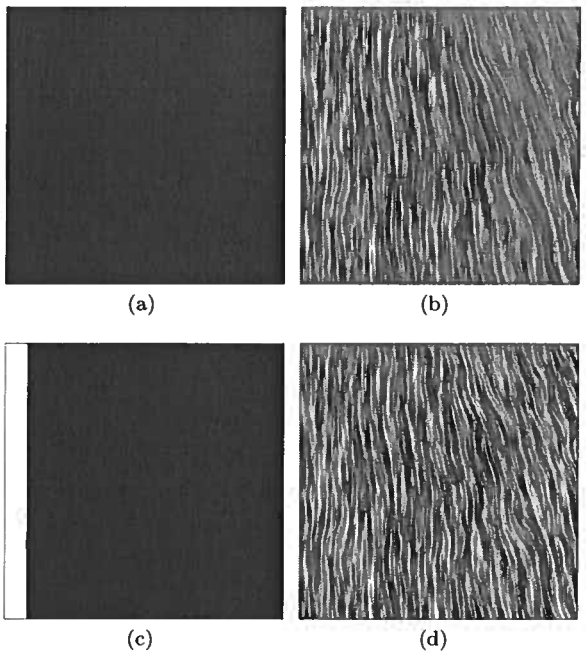

Figure 11. Application to a random-noise image of inverses of local dip filters (a) A, (b) B, (c) C and (d) A^TA for dips obtained from the transposed image in Figure 9a. Causal inverses of wavekill filters A are unstable. Inverses for the folded filter B and Fomel's filter C are obtained by recursively solving tridiagonal systems of equations from left to right. The inverse of the symmetric filter A^TA is computed by conjugate-gradient iteration.

of these filters approximate a second derivative in the vertical direction.

I applied the inverses of these four filters to a random-noise image to obtain the textures shown in Figures 11. The inverse A^{-1} for the wavekill filter is again unstable, as is the inverse C^{-1} for the plane-wave destruction filter.

For near-vertical events the inverses B^{-1} and $(A^TA)^{-1}$ exhibit similar textures in Figures 11b and 11d, consistent with the similarity of the filters outputs in Figures 10b and 10d.

Outputs for the circular synthetic input with all dips are shown in Figures 12. The most obvious difference in these output images is the instability of the plane-wave destruction filter C for large dips.

Textures for the four inverse filters are shown in Figures 13. The inverses A^{-1} and C^{-1} are again unstable. Texture for the inverse $(A^TA)^{-1}$ is most consistent for all dips.

4 USEFUL COMBINATIONS

We can combine basic filters like B and A^TA and their inverses to obtain notch filters or dip filters that are more useful than the basic filters alone.

To simplify notation, let H denote the filter A^TA defined by equation 7:

$$H \equiv A^TA = \vec{\nabla}^T\hat{\mathbf{v}}\hat{\mathbf{v}}^T\vec{\nabla} = \vec{\nabla}^T(I - \hat{\mathbf{u}}\hat{\mathbf{u}}^T)\vec{\nabla}.$$

If we neglect errors due to finite-difference approximations of derivatives, then the Fourier transform of this basic filter is

$$H(k_1, k_2) = (v_1k_1 + v_2k_2)^2.$$

Contours of constant amplitude $H(k_1, k_2)$ are parallel lines corresponding to constant $v_1k_1 + v_2k_2$. These parallel contours are apparent near the origins of the spectra in Figures 4, where wavenumbers and finite-difference errors are small.

4.1 Notch filters

To construct a notch filter, we first define a perturbed basic filter

$$H(\epsilon) \equiv \vec{\nabla}^T\hat{\mathbf{v}}\hat{\mathbf{v}}^T\vec{\nabla} + \epsilon I.$$

Then a notch filter is the composite filter defined by

$$H_n = H^{-1}(\epsilon)\, H(0).$$

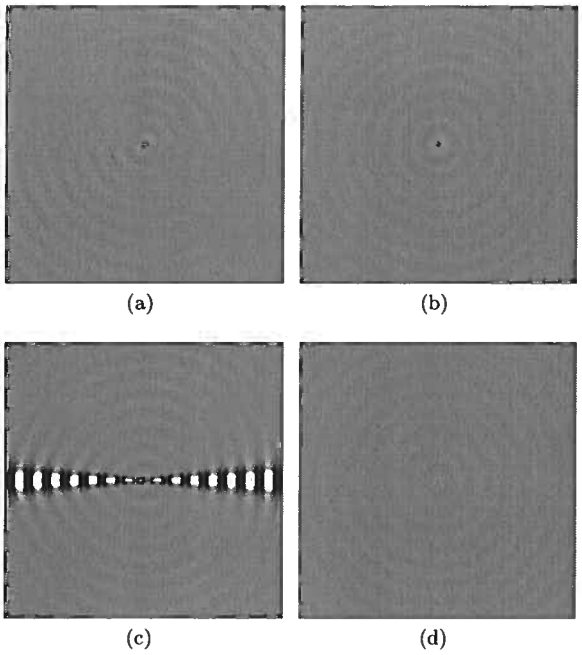

Figure 12. Output images for local dip filters (a) A, (b) B, (c) C and (d) A^TA applied to the test image in Figure 9b. For large dips, the output for Fomel's filter C goes to infinity.

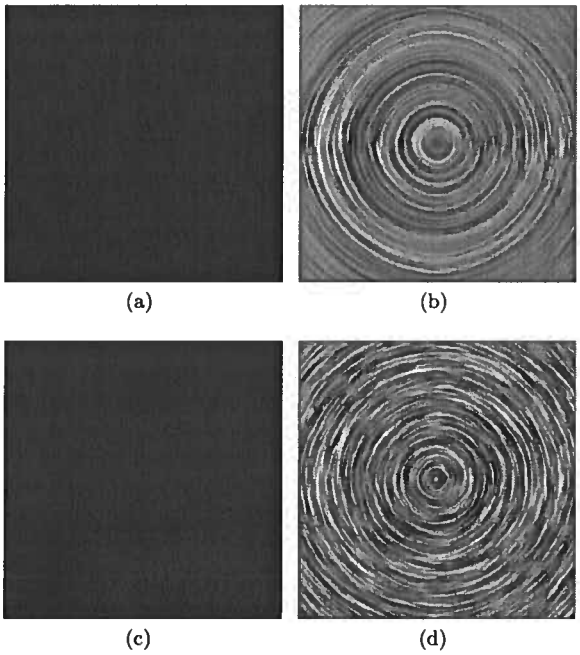

Figure 13. Application to a random-noise image of inverses of local dip filters (a) A, (b) B, (c) C and (d) A^TA for dips obtained from the synthetic test image in Figure 9b.

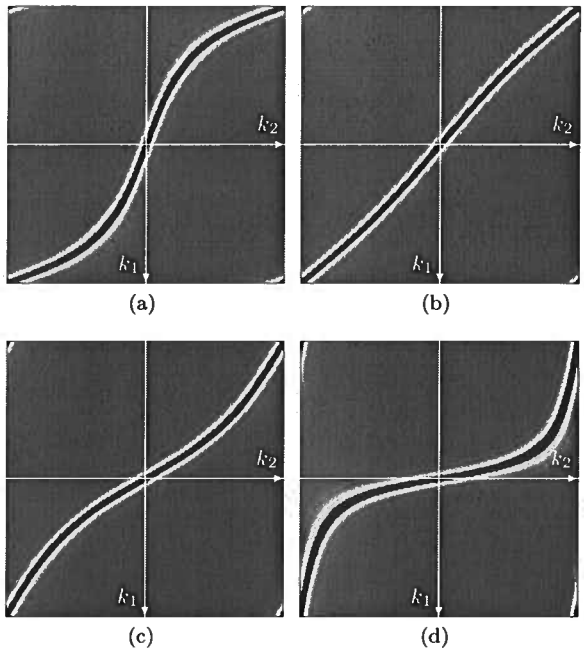

Figure 14. 2-D amplitude spectra of notch filters H_n for dips of (a) 20, (b) 40, (c) 60, and (d) 80 degrees, and $\epsilon = 0.01$. Dark blue and red denote amplitudes of zero and one, respectively.

Neglecting finite-difference errors, the Fourier transform of this notch filter is

$$H_n(k_1,k_2) = \frac{(v_1k_1+v_2k_2)^2}{(v_1k_1+v_2k_2)^2+\epsilon}.$$

Contours of constant amplitude $H_n(k_1,k_2)$ are again parallel lines corresponding to constant $v_1k_1+v_2k_2$.

Amplitude spectra for notch filters with $\epsilon = 0.01$ are displayed in Figures 14. Comparing these spectra with those of Figures 4, we see how notch filters H_n can be more discriminate than the basic filters $H = A^TA$ in their attenuation of specified dips.

The parameter ϵ controls the width of each notch. If we choose $\epsilon = 0$, then $H_n = 1$ and the filters do nothing. By increasing ϵ slightly we create a narrow notch at the dip to be zeroed, and the width of this notch grows with ϵ. Far from the notch, spectral amplitudes approach one.

A small positive ϵ has a side benefit. It increases the eigenvalues of $H(\epsilon)$, thereby reducing the number of iterations required when the method of conjugate gradients is used to apply $H^{-1}(\epsilon)$ in the notch filter H_n. We can easily modify any implementation of H^{-1} to implement $H^{-1}(\epsilon)$.

The difference between the basic filter $H = A^TA$ and the notch filter H_n is highlighted above in Figures 1b and 1c, respectively. Both filters attenuate the stronger coherent events in the image of Figure 1a. The basic filter H attenuates much more, leaving only high-

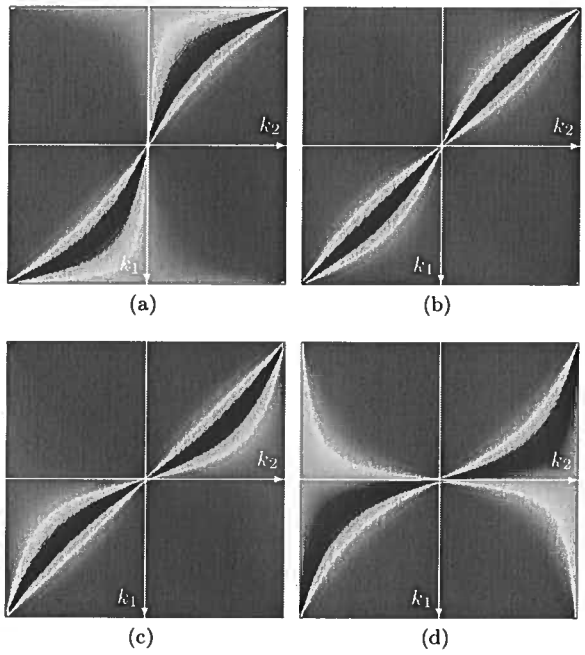

Figure 15. 2-D amplitude spectra of dip filters H_d for dips of (a) 20, (b) 40, (c) 60, and (d) 80 degrees, and $\epsilon = 0.05$. Dark blue and red denote amplitudes of zero and one, respectively.

wavenumber and mostly incoherent energy. The notch filter H_n is more discriminate, preserving many coherent and interesting features, while surgically removing the stronger events.

4.2 Better dip filters

To construct a better dip filter, we perturb our basic filter H in a slightly different way:

$$H(\epsilon) \equiv \vec{\nabla}^T \left[(1+\epsilon) I - \hat{\mathbf{u}}\hat{\mathbf{u}}^T \right] \vec{\nabla}.$$

Then the improved dip filter is the composite filter defined by

$$H_d = H^{-1}(\epsilon)\, H(0).$$

Neglecting finite-difference errors, the Fourier transform of this dip filter is

$$H_d(k_1, k_2) = \frac{(v_1 k_1 + v_2 k_2)^2}{(v_1 k_1 + v_2 k_2)^2 + \epsilon(k_1^2 + k_2^2)}.$$

Contours of constant amplitude $H_d(k_1, k_2)$ are lines radiating from the origin. Amplitude is a function of only the ratio k_2/k_1.

Amplitude spectra of this dip filter for $\epsilon = 0.05$ are displayed in Figures 15.

As their Fourier transforms suggest, our better dip filters H_d are simply notch filters for which the width of the notch grows with increasing wavenumbers k_1 and k_2. The parameter ϵ controls the rate at which the notch width grows or, equivalently, the range of dips attenuated.

4.3 3-D filters

Much of the design of local dip filters above can be extended to three (or more) dimensions.

We can estimate dips θ and azimuths ϕ of locally planar features from 3-D local structure tensors, 3×3 matrices computed from image gradients like those in equation 1 for two dimensions. For each image sample, the eigenvectors of these 3×3 matrices are orthogonal unit vectors $\hat{\mathbf{u}}$, $\hat{\mathbf{v}}$ and $\hat{\mathbf{w}}$. The vector $\hat{\mathbf{u}}$ is normal to the best-fitting plane and corresponds to the largest eigenvalue. The vectors $\hat{\mathbf{v}}$ and $\hat{\mathbf{w}}$ lie within that best-fitting plane.

In three dimensions

$$A^T A = \vec{\nabla}^T (I - \hat{\mathbf{u}}\hat{\mathbf{u}}^T) \vec{\nabla},$$

which is identical to equation 7, except that vectors now have three components instead of two, and $I = \hat{\mathbf{u}}\hat{\mathbf{u}}^T + \hat{\mathbf{v}}\hat{\mathbf{v}}^T + \hat{\mathbf{w}}\hat{\mathbf{w}}^T$ is a 3×3 identity matrix. In any number of dimensions, the directional Laplacian $A^T A$ is the isotropic Laplacian $\vec{\nabla}^T \vec{\nabla}$ minus the projection of that Laplacian onto the normal vector $\hat{\mathbf{u}}$.

By subtracting the component of an isotropic Laplacian that is orthogonal to a plane, we construct local dip filters that attenuate features lying within that plane.

As discussed above for two dimensions, the most efficient way to apply $A^T A$ for any number of dimensions is to

(i) apply the gradient filter $\vec{\nabla}$,
(ii) multiply by the matrix $I - \hat{\mathbf{u}}\hat{\mathbf{u}}^T$, and
(iii) apply the transpose of the gradient filter $\vec{\nabla}^T$.

Again, these three steps can be performed in a single pass over the input and output images.

Having generalized directional Laplacian filters $A^T A$ to three or more dimensions, we can generalize composites of these filters as well. Definitions and implementations of the notch filter H_n and the dip filter H_d are almost identical in any number of dimensions.

Note that 3-D local dip filters constructed as directional Laplacians are not equivalent to a cascade of 2-D filters. To understand the difference, consider a hypothetical example in which we wish to remove horizontal planar features from a 3-D image. For these features, the normal vector $\hat{\mathbf{u}}$ points vertically downward.

In this case, the amplitude spectrum of the required directional Laplacian filter is $k_2^2 + k_3^2$, where k_2 and k_3 are wavenumbers corresponding to horizontal spatial coordinates x_2 and x_3. As expected, this amplitude is zero when both $k_2 = 0$ *and* $k_3 = 0$.

If we instead apply a 2-D filter in the x_2 direction, followed by a 2-D filter in the x_3 direction, the amplitude

spectrum of the composite filter is $k_2^2 k_3^2$. This amplitude is zero when either $k_2 = 0$ *or* $k_3 = 0$.

The difference between a 3-D directional Laplacian and a cascade of two 2-D filters lies in the difference between *and* and *or*. The filter cascade will attenuate features that appear horizontal in either constant-x_2 *or* constant-x_3 slices of a 3-D image, even when those features may be dipping in directions perpendicular to those slices. The 3-D directional Laplacian will correctly attenuate only truly horizontal features.

5 CONCLUSION

By constructing basic dip filters from directional derivatives, we obtain filters that

- adapt easily to changes in local dip,
- handle robustly all (even vertical) dips,
- can be inverted to construct notch filters, and
- extend easily to any number of dimensions.

This paper highlights two such basic dip filters B and $A^T A$.

The folded filter B was designed to fit on the stencil of Fomel's plane-wave destruction filter C. Software that uses filter C can easily be modified to use filter B, which more robustly handles steeply dipping features and has a stable and efficient inverse. The efficiency of the inverse B^{-1} is due to the efficiency with which we can solve tridiagonal systems of equations.

Folding to obtain the filter B from the symmetric filter $A^T A$ is useful in two dimensions, but less so in higher dimensions. The limitation is that folding works for only one axis. In three or more dimensions, the inverse B^{-1} of a folded filter B requires solution of a sparse system of equations that is not tridiagonal.

For 3-D images it may be simpler and more efficient to use $A^T A$ instead. The symmetric filter $A^T A$ has only a slightly larger stencil and can be implemented efficiently in only one pass over input and output images. Inverse filters can be applied either by conjugate-gradient iterations or with tables of minimum-phase filters precomputed by Wilson-Burg factorization.

Although the examples of this paper show only 2-D images, extension of the filter $A^T A$ to three and higher numbers of dimensions is straightforward. We begin with a finite-difference approximation to an isotropic N-dimensional Laplacian, and then subtract away projections of that operator corresponding to the features that we wish to preserve.

The filter $A^T A$ is not discriminate enough to be useful by itself. However, by combining this filter with inverses of slightly modified filters, we obtain notch filters and better dip filters. These combinations attenuate strong coherent signals while preserving weaker signals with slightly different dips. Such combinations may be used to enhance as well as attenuate image features.

REFERENCES

Claerbout, J.F., 1992, Earth soundings analysis — processing versus inversion: Blackwell Scientific Publications.

Claerbout, J.F., 1998, Multidimensional recursive filters via a helix: Geophysics, **63**, 1532–1541.

Clapp, R.G., B. Biondi, and J.F. Claerbout, 2004, Incorporating geologic information into reflection tomography: Geophysics, **69**, 533–546.

Fomel, S., 2002, Applications of plane-wave destruction filters: Geophysics, **67**, 1946–1960.

Fomel, S., and P. Sava, J. Rickett, and J.F. Claerbout, 2003, The Wilson-Burg method of spectral factorization with application to helical filtering: Geophysical Prospecting, **51**, 409–420.

Fomel, S., and A. Guitton, 2006, Regularizing seismic inverse problems by model reparameterization using plane-wave construction: Geophysics, **71**, A43–A47.

van Vliet, L.J., and P.W. Verbeek, 1995, Estimators for orientation and anisotropy in digitized images: Proceedings of the first annual conference of the Advanced School for Computing and Imaging ASCI'95, Heijen (The Netherlands), 442–450.

A case study of azimuthal AVO analysis with anisotropic spreading correction

Xiaoxia Xu[1] and Ilya Tsvankin[2]

[1] *Formerly Colorado School of Mines, Department of Geophysics, Center for Wave Phenomena; presently ExxonMobil Upstream Research Company, Houston, TX 77252.*

[2] *Colorado School of Mines, Department of Geophysics, Center for Wave Phenomena, Golden, CO 80401-1887.*

ABSTRACT

Seismic methods play an important role in the development of tight fractured reservoirs with substantial spatial variability of fracture density. Here, we apply a comprehensive processing sequence designed for layered azimuthally anisotropic media to wide-azimuth P-wave data acquired over a fractured gas sand formation in the Rulison field, Colorado. The main processing steps include nonhyperbolic moveout inversion based on an orthorhombic velocity model, estimation of effective and interval normal-moveout (NMO) ellipses, anisotropic geometrical-spreading correction, and azimuthal amplitude-variation-with-offset (AVO) analysis.

The azimuthal AVO response, obtained by computing the azimuthally varying AVO gradient on common-midpoint supergathers, proved to be the most sensitive fracture-detection attribute. In particular, we have identified two areas of extremely high AVO ellipticity at the bottom of the reservoir. One of these AVO anomalies becomes much more pronounced and spatially coherent after application of the moveout-based anisotropic geometrical-spreading correction (MASC). In contrast, the interval NMO ellipticity in the reservoir is relatively weak, most likely because of the influence of vertical and lateral heterogeneity.

The two major AVO-gradient anomalies at the bottom of the reservoir coincide with the intersections of two wrenching fault systems, which suggests that the azimuthal AVO analysis helped to detect "soft spots" of high fracture density. Also, the dominant fracture direction (N70W) estimated from the AVO ellipses is aligned with one of the fault systems and is in good agreement with EMI logs.

Key words: case study, wide-azimuth data, AVO analysis, geometrical spreading, P-wave, azimuthal anisotropy, fracture characterization

1 INTRODUCTION

Geomechanical properties of tight, low-porosity reservoirs are largely governed by natural fracture networks. Therefore, reliable estimation of fracture density and orientation is extremely important for cost-effective hydraulic completion and hydrocarbon production. Direct information about fracturing can be obtained using borehole methods, such as image log analysis, which provide estimates of fracture counts and orientations on various scales. The main shortcoming of borehole measurements is that they are sensitive only to formation properties in the immediate vicinity of the well. In some cases, the spatial distribution of fractures can be inferred from fault maps obtained by coherence analysis of surface seismic data. However, the correlation between areas of high fracture density and fault locations is not always straightforward.

Therefore, fracture characterization increasingly re-

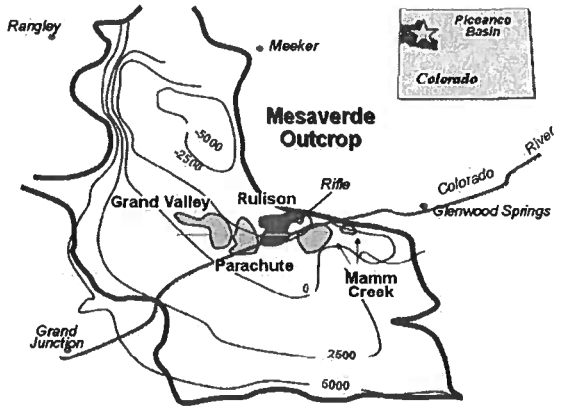

Figure 1. Location of the Rulison field in the Piceance Basin, Colorado.

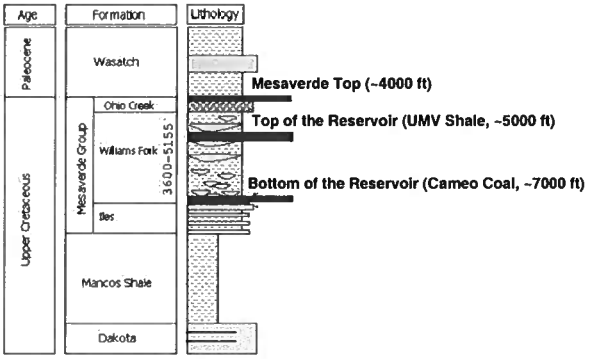

Figure 2. Stratigraphic column of the Rulison field. The gas-producing reservoir is bounded by the UMV shale and the Cameo coal. The Mesaverde Top is an unconformity that separates the Mesaverde group from the overlying Wasatch formation.

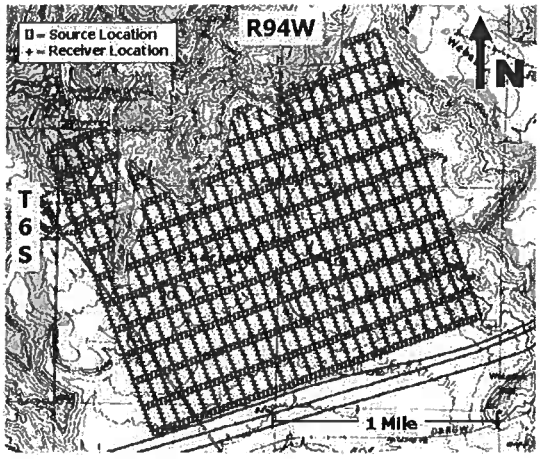

Figure 3. Seismic acquisition grid for the RCP nine-component 2003 survey.

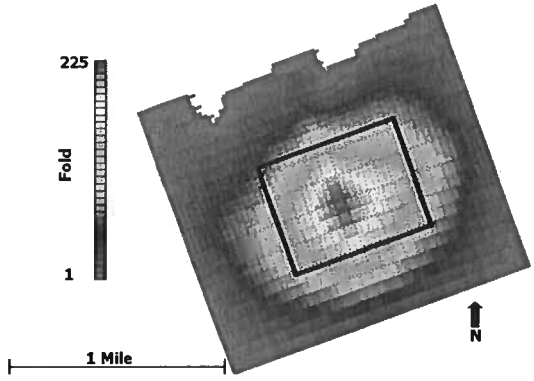

Figure 4. P-wave fold for the 55x55 ft bin size. The square in the center marks the study area of this paper.

lies on seimsic inversion methods that operate with both 3D wide-azimuth surface data and VSP (vertical seismic profiling) surveys (Hall and Kendall, 2003; Gray and Todorovic-Marinic, 2004). In particular, valuable information about fracture orientation and density is provided by the azimuthal variation of such P-wave signatures as moveout attributes and amplitude-variation-with-offset (AVO) response (Grechka and Tsvankin, 1999; Lynn et al. 1999; Bakulin et al., 2000; Li et al. 2003; Neves et al. 2003; Rüger, 2001). After cross-validation with borehole measurements, fracture maps obtained from azimuthal seismic attributes can serve as the input into reservoir simulation.

Both azimuthal moveout and AVO (often abbreviated as "AVAZ") analysis have their advantages and drawbacks. While the AVO response provides local, high-resolution information about fracturing at the top or bottom of the reservoir, moveout attributes (e.g., the NMO ellipse) depend on the average fracture properties for the whole reservoir layer. When combined together, azimuthal AVO and moveout attributes can offer improved understanding of the spatial distribution and physical properties of fractures.

From the processing standpoint, azimuthal moveout measurements usually are more robust and less distorted by standard preprocessing algorithms. On the other hand, reflection amplitudes are more sensitive to the presence of anisotropy and can provide higher vertical resolution, which is especially important for thin reservoirs. In addition to the difficulties caused by the near surface (e.g., statics errors and coupling problems), both moveout and amplitude methods have to account for the propagation phenomena in the overburden. In-

Survey type	3-D, 9-C
Subsurface bin size	55'x55'
Number of receiver locations	1500
Number of source locations	770
Receiver grid	110' inline spacing, 330' between lines
Source grid	110' inline spacing, 660' between lines
Receiver array	1, 3-C VectorSeis System Four
Source array	Mertz 18
P-wave sweep range	6-120 Hz

Table 1. Acquisition parameters of the survey.

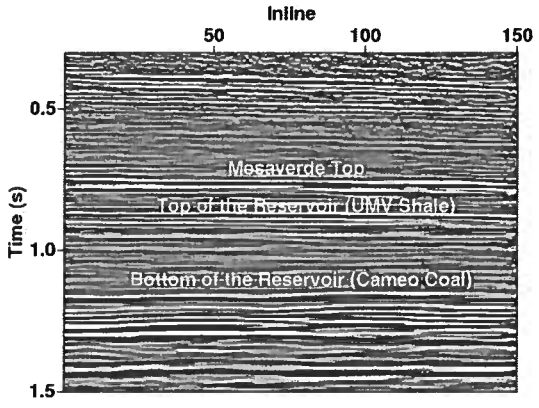

Figure 5. Seismic section across the middle of the survey area. The reflectors analyzed in the paper are marked on the plot.

terval NMO ellipses are obtained by applying the generalized Dix equation to the reflections from the top and bottom of the reservoir (Grechka and Tsvankin, 1998; Grechka et al. 1999; Neves, 2003). This procedure becomes unstable if the thickness of the reservoir layer is relatively small compared to its depth. Then it may become necessary for purposes of moveout analysis to combine the reservoir with a layer above or below it.

It is less common in seismic fracture characterization to properly account for amplitude distortions in the overburden, in particular those caused by anisotropic geometrical spreading. The high sensitivity of geometrical spreading to the presence of anisotropy along the raypath can cause serious errors in AVO analysis (Rüger and Tsvankin, 1997; Tsvankin, 2005). To remove the geometrical-spreading factor and accurately estimate the reflection coefficient, Xu et al. (2005) and Xu and Tsvankin (2006a) developed a methodology of moveout-based anisotropic spreading correction (MASC). The moveout parameters that provide the input to MASC are obtained by 3D nonhyperbolic moveout inversion of wide-azimuth data (Vasconcelos and Tsvankin, 2006). It should be emphasized that MASC does not require any additional information about the velocity field and fits in a straightforward way into the processing flow of azimuthal AVO analysis. Synthetic tests on realistic orthorhombic layered models show that application of MASC becomes necessary when the azimuthal variation of the geometrical spreading reaches at least 1/3 of that of the reflection coefficient (Xu and Tsvankin, 2006b).

Here, we carry out azimuthal moveout and AVO analysis of P-wave data acquired above a fractured reservoir at the Rulison field in Colorado. Prior to estimating the azimuthally varying AVO gradient, we apply MASC to correct reflection amplitudes for the geometrical spreading in the overburden. Comparison of our processing results with those obtained with a conventional gain correction shows that MASC made it possible to enhance and focus one of the two major azimuthal AVO anomalies. Analysis of the AVO gradients at the top and bottom of the reservoir provides important insight into the fracture distribution and helps to identify zones of intense fracturing.

2 GEOLOGIC BACKGROUND

The Rulison field is a basin-centered gas accumulation located in the South Piceance Basin, Garfield county, Colorado (Figure 1). Gas production comes primarily from the Williams Fork formation, which consists of channel sand lenses embedded in fine-grained levee deposition (Figure 2). The reservoir is capped by the UMV shale, while the Cameo coal beneath the reservoir is believed to provide the source for the gas accumulation. The unconformity at the top of the Mesaverde group underlies a massive shale formation.

The reservoir lithology is classified as tight sand with the matrix permeability on the order of micro-Darcies and porosity of 6–12%. The top several hundred feet of the reservoir formation are saturated with water, which is replaced by gas in the lower part of the reservoir (Cumella and Ostby, 2003). The pay section is relatively thick (about 1200 feet) and is considered to be normally pressured or slightly overpressured. Because of the low porosity and matrix permeability, characterization of natural fracture networks has vital importance for cost-effective development of the field.

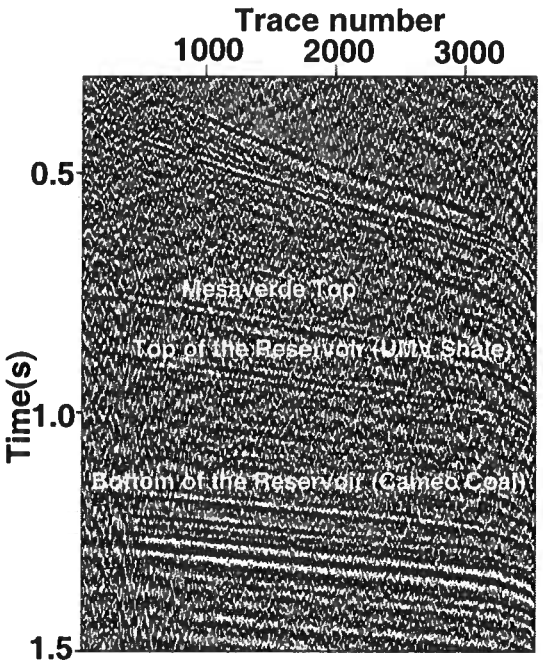

Figure 6. CMP supergather in the upper left corner of the study area. The maximum offset is 7700 feet.

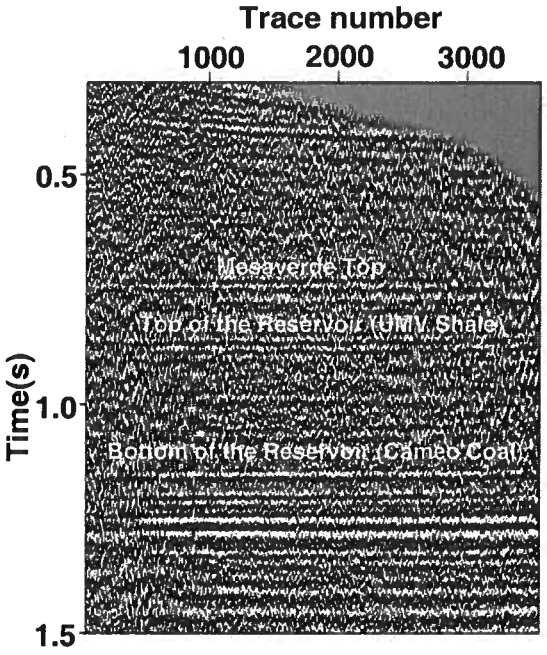

Figure 7. Supergather from Figure 6 after application of azimuthally-varying hyperbolic moveout correction. The maximum offset-to-depth ratios for the Mesaverde Top, the top of the reservoir (UMV shale), and the bottom of the reservoir (Cameo coal) are 1.9, 1.5, and 1.1, respectively.

3 DATA ACQUISITION AND PROCESSING

To map the spatial distribution and orientation of fractures and study the in-situ stress field, the Reservoir Characterization Project (RCP) at CSM acquired a 3D multicomponent seismic survey over a 2.2x2.5 km area of the Rulison field. The orthogonal acquisition geometry was designed to reach optimal balance between the uniformity of the azimuthal distribution and the economy of the layout (Figure 3). The data coverage is especially dense near the center of the survey area, with the highest fold of 225 for a small bin size of 55x55 ft (Table 1 and Figure 4).

Prior to the AVO processing described below, a statics correction was applied to the data by Veritas. As illustrated by the cross-section in Figure 5, the data quality is above average for land surveys. Also, the subsurface structure is close to layer-cake, which simplifies application of azimuthal moveout and AVO analysis and the anisotropic geometrical-spreading correction (MASC).

To improve azimuthal and offset coverage, we collected CMP gathers into superbins. The choice of the superbin size is nontrivial and requires conducting a number of tests. Relatively small superbins suffer from nonuniformity of the distribution of offsets and azimuths; on the other hand, using large superbins increases the influence of lateral heterogeneity. After experimenting with several bin sizes, we found 5x5 superbins to be optimal. Further increase in size reduces semblance values in 3D moveout analysis, which is likely caused by lateral heterogeneity.

Figure 6 displays a 5x5 superbin gather in the upper left corner of the study area. The ground roll was suppressed using the slope filter suggested by Vasconcelos and Grechka (2006), which is designed to minimize azimuthal distortions. The same gather after application of azimuthally-varying NMO correction using the best-fit NMO ellipse is shown in Figure 7. The bending at the far offsets (i.e., a "hockey stick") for the reflection from the top of the reservoir (UMV shale) indicates the presence of nonhyperbolic moveout generated in the overburden. The apparent flatness of the Cameo coal reflection is explained by the relatively small offset-to-depth-ratio (slightly larger than unity) at the bottom of the reservoir.

The azimuthally-varying NMO velocity is described by a quadratic function of the horizontal coordinates and typically traces out an ellipse in the horizontal plane (Grechka and Tsvankin, 1998). Similarly, the azimuthal variation of AVO gradient can be approximated by an

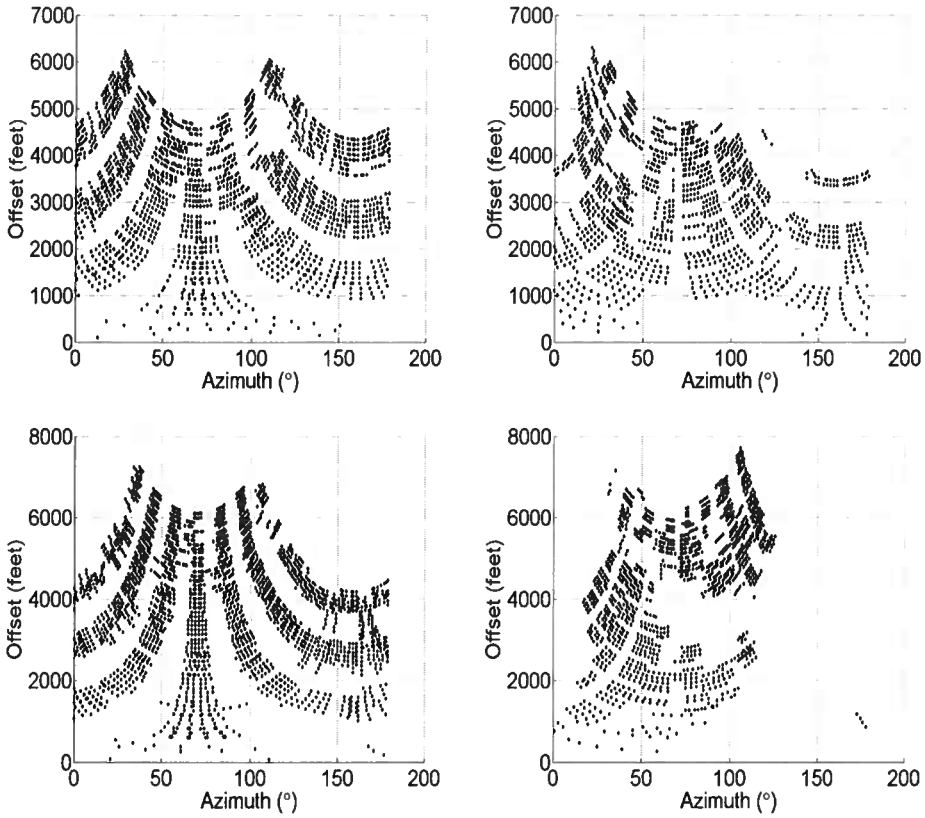

Figure 8. Distribution of offsets and azimuths for CMP superbins in the four corners of the study area. Note that full azimuthal coverage is achieved for offsets up to about 5000 ft.

elliptical curve, unless the gradient changes sign with azimuth (Rüger, 2001). For laterally homogeneous models, the orientation and eccentricity of both ellipses depend on the direction, density, and fluid saturation of subsurface fracture systems. To reconstruct NMO and AVO ellipses, it is common to divide 3D data into azimuthal sectors and estimate the NMO velocity and AVO gradient in each sector separately. Although implementation of this approach is facilitated by application of existing 2D algorithms, it suffers from bias caused by uneven distribution of offsets and azimuths (Grechka and Tsvankin, 1999; Li et al. 2003). Here, we adopted a more robust "global" algorithm that honors the azimuth of each trace and fits an ellipse to the data using all source-receiver pairs in a 3D CMP gather (Grechka and Tsvankin, 1999; Vasconcelos and Tsvankin, 2006).

Our processing sequence starts with multiazimuthal moveout analysis based on the algorithm of Vasconcelos and Tsvankin (2006). First, the NMO ellipse is estimated from conventional-spread data with the maximum offset-to-depth ratio close to unity. Second, this ellipse is used as the initial guess to carry out 3D nonhyperbolic moveout analysis of all traces in the gather. The estimated moveout parameters not only allow us to flatten reflection events in the multiazimuth gather, but also serve as the input to the geometrical-spreading correction. Third, we perform amplitude picking on conventional-length spreads along the traveltime surface defined by the 3D nonhyperbolic moveout parameters. Fourth, the picked amplitudes are corrected for the geometrical spreading using the method (MASC) of Xu and Tsvankin (2006a, 2006b). Finally, the corrected amplitudes are inverted for the azimuthally-varying AVO gradient (along with the AVO intercept) to obtain the AVO ellipse. To evaluate the impact of the anisotropic spreading correction on the azimuthal AVO analysis, we also repeated the last two processing steps with MASC replaced by the conventional t^2-gain.

The azimuthal moveout and AVO analyses were carried out for CMP locations inside a square area in the center of the RCP survey (Figure 4), where the fold per superbin varied from 1500 to 5000. Figure 8 shows the azimuthal and offset coverage for CMP superbins in the four corners of this study area; the coverage increases towards the center of the survey. It is evident that uniform azimuthal coverage, which is critical for our processing,

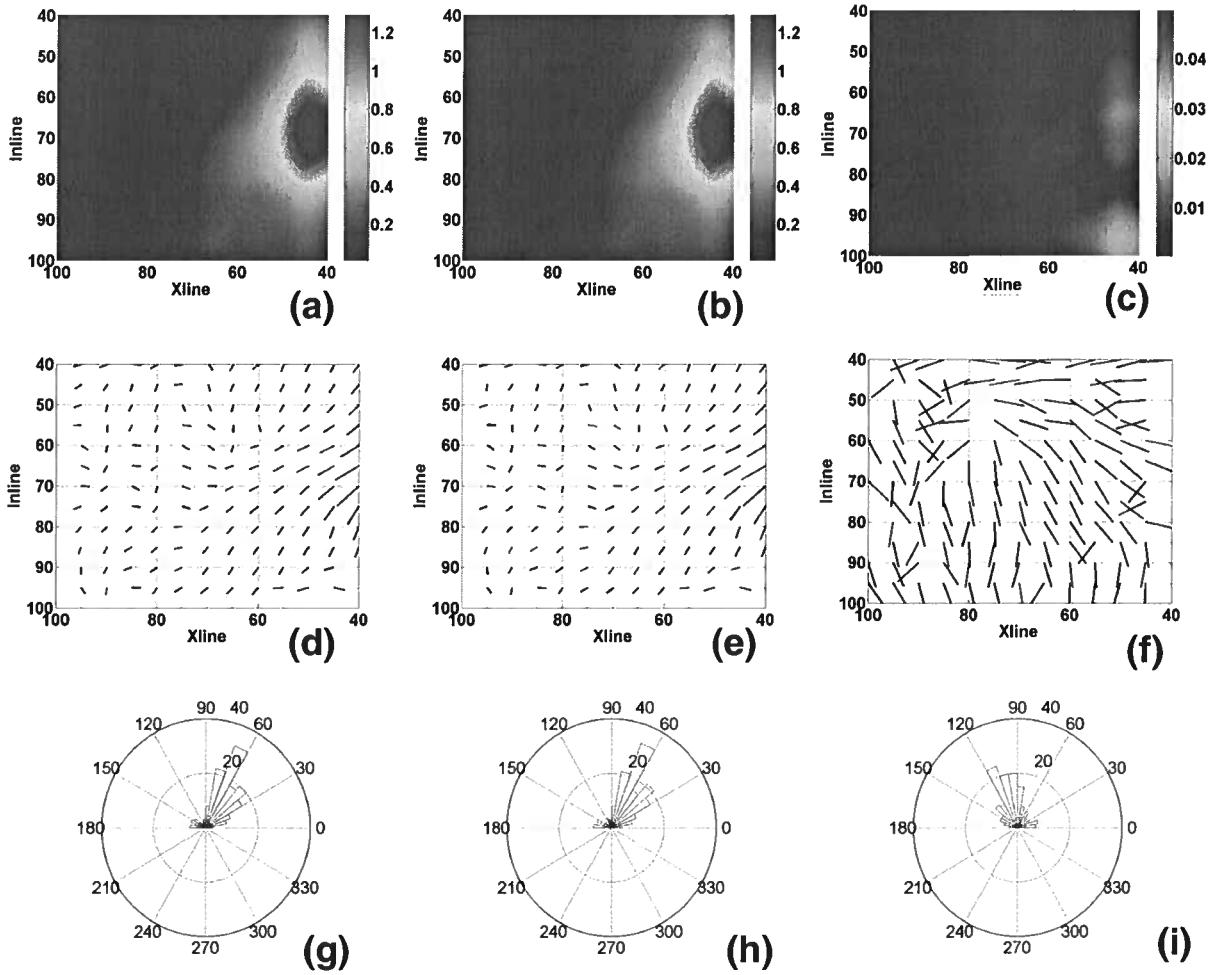

Figure 9. AVO and NMO ellipses estimated for the reflection from the Mesaverde Top. The first two columns display the AVO ellipses computed using MASC (left) and the conventional t^2 gain correction (center). The right column shows the effective NMO ellipses. The top row (panels a, b, and c) is the eccentricity of the ellipses calculated by subtracting unity from the ratio of the semi-major and semi-minor axes. The middle row (panels d, e, and f) is the azimuth of the semi-major axis; the length of the ticks is proportional to the eccentricity. The semi-major axis of the AVO ellipse corresponds to the larger absolute value of the AVO gradient.Panels g, h, and i in the bottom row are the rose diagrams of the azimuths from panels d, e, and f, respectively.

extends to offsets of about 5000 feet. This implies that estimation of the NMO and AVO ellipses for Mesaverde Top and the top of the reservoir should be free from the acquisition footprint. The processing results for the bottom of the reservoir (Cameo coal), however, may bear some acquisition footprint, particularly at the edges of the study area.

4 RESULTS OF AZIMUTHAL SEISMIC ANALYSIS

Here, we present the results of the azimuthal AVO and NMO analysis for three major reflectors: the top of the Mesaverde group, the top of the reservoir (UMV shale), and the bottom of the reservoir (Cameo coal). To minimize possible edge effects, some of the processed CMP superbins included source/receiver locations outside of the study area in Figure 4. Both AVO and NMO ellipses are represented by their eccentricity and the orientation (azimuth) of the semi-major axis computed for each common midpoint.

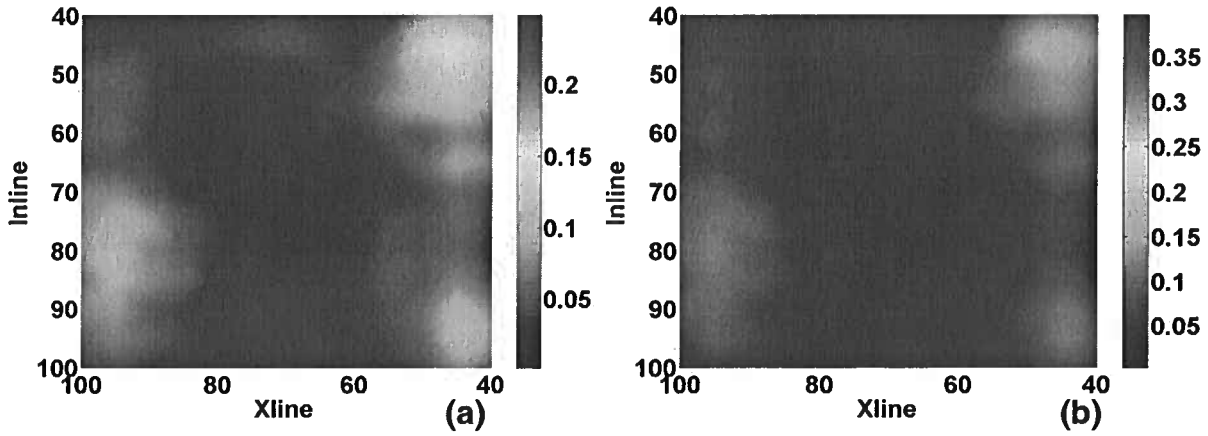

Figure 10. Azimuthal variation of the (a) geometrical spreading and (b) effective parameter η for the Mesaverde Top. Plot (a) shows the relative difference between the spreading values in the vertical symmetry planes for the offset-to-depth ratio equal to one; the symmetry planes correspond to the axes of the NMO ellipse. Plot (b) shows the difference between the parameters $\eta^{(1)}$ and $\eta^{(2)}$ in the vertical symmetry planes (for parameter definitions, see Tsvankin, 2005).

4.1 Mesaverde Top

The AVO ellipses for the Mesaverde Top exhibit a distinctive azimuthal AVO anomaly near the east boundary of the study area (Figures 9a,b). The eccentricity of the ellipses is defined as the ratio of the semi-major and semi-minor axes minus unity. Therefore, at the center of this anomaly the AVO gradient in one principal azimuthal direction is more than twice as large as in the orthogonal direction. In contrast, the NMO ellipticity for this reflector is close to zero, which suggests that the overburden is effectively azimuthally isotropic with respect to NMO velocity. The axes of the AVO ellipses in the area of the anomaly have azimuths close to 45° and 135°. Since the reflection coefficient responds to the local changes of rock properties at the interface, the azimuthal AVO anomaly in Figure 9 may be associated with an intensely fractured zone near the Mesaverde Top. The obtained AVO-gradient map offers potentially valuable information for the operating company, which is interested in using formations above the Mesaverde Top to store production water.

Although the anellipticity parameter η estimated from nonhyperbolic moveout inversion is substantial (0.15 on average), it is almost the same in both vertical symmetry planes of the model (Figure 10b). On the whole, the reflection moveout for the Mesaverde Top is weakly dependent on azimuth. Consequently, the azimuthal variation of the geometrical spreading is almost negligible (Figure 10a). Comparison of the first two columns of Figure 9 confirms that the impact of MASC (i.e., of the anisotropic spreading correction) on the azimuthal AVO response for the Mesaverde Top is small.

4.2 Top of the reservoir (UMV shale)

Similar to the Mesaverde Top, the only pronounced AVO-gradient anomaly at the top of the reservoir is located near the east boundary of the study area (Figure 11a). The magnitude of this anomaly, however, is about 30% higher than that for the Mesaverde Top, and the point of the maximum AVO ellipticity is shifted up by about 200 m. Since the UMV shale layer above the reservoir is likely to be transversely isotropic with a vertical symmetry axis (VTI; see below), the anomaly in Figure 11 may be caused by a "soft spot" of high fracture density in the upper reservoir. The influence of the anisotropic spreading correction on the azimuthal AVO response at the top of the reservoir is marginal for the same reason as for the Mesaverde Top.

The maximum effective NMO ellipticity for the top of the reservoir is only slightly larger than that for the Mesaverde Top. The right column in Figure 11 shows the interval NMO ellipses in the UMV shale layer computed from the generalized Dix equation of Grechka et al. (1999). The orientations of the ellipses are almost random, which suggests that either the shale formation is almost azimuthally isotropic, or the layer-stripping operation is not sufficiently stable because of the weak effective NMO ellipticity.

4.3 Bottom of the reservoir (Cameo coal)

The azimuthal seismic attributes for the bottom of the reservoir are shown in Figure 12. Two significant AVO-gradient anomalies appear in the upper right and lower left corners of the study area (Figures 12a,b). The magnitude of both anomalies is close to 1.5, which means that the semi-major axis of the AVO ellipse is 2.5 times

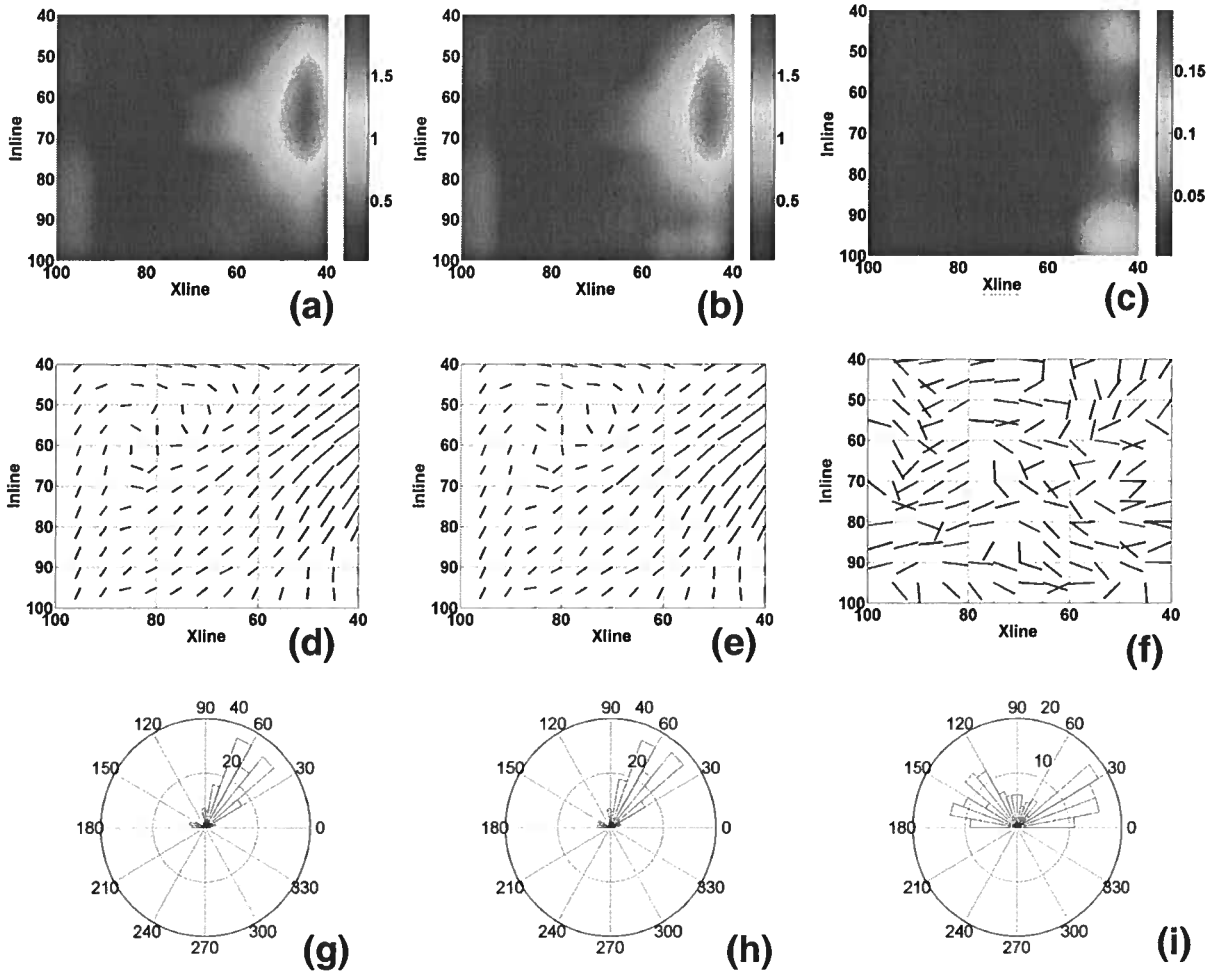

Figure 11. AVO ellipses for the top of the reservoir (the left and center columns) and the interval NMO ellipses in UMV shale (the right column); the same display as in Figure 9.

larger than the semi-minor axis. The azimuth of the semi-major axis (Figures 12d,e) exhibits a strikingly regular pattern that might be related to the geomechanical processes that produce wrenching faults in the area (Jansen, 2005). According to the AVO results in Figures 12g, h, the average fracture azimuth at the bottom of the reservoir should be close to N70W.

The large thickness of the reservoir ensures stable computation of the interval NMO ellipses (the right column in Figure 12). The only noticeable azimuthal NMO anomaly is located in the upper right corner of the area and partially overlaps with one of the azimuthal AVO anomalies described above. The magnitude of the NMO anomaly is close to 8%, which translates into a difference of about 0.08 between the anisotropy parameters $\delta^{(1)}$ and $\delta^{(2)}$ in the vertical symmetry planes (see Tsvankin, 2005).

In contrast to the results for the more shallow reflectors, the anisotropic spreading correction (MASC) makes a significant impact on the azimuthal AVO response for the bottom of the reservoir (compare Figures 12a and 12b). The AVO anomaly in the lower left corner of the study area is much more pronounced and spatially coherent after application of MASC. The strong azimuthal variation of the geometrical spreading (as well as the parameter η) in the lower part of the area is likely caused by the influence of subvertical fractures in the thick reservoir formation (Figure 13). Therefore, the anisotropic spreading correction becomes essential for computing an accurate AVO response from the bottom of the reservoir. The contribution of MASC is smaller for the second AVO anomaly (Figures 12a,b), probably because of the more limited vertical extent of fracturing near the right boundary of the area.

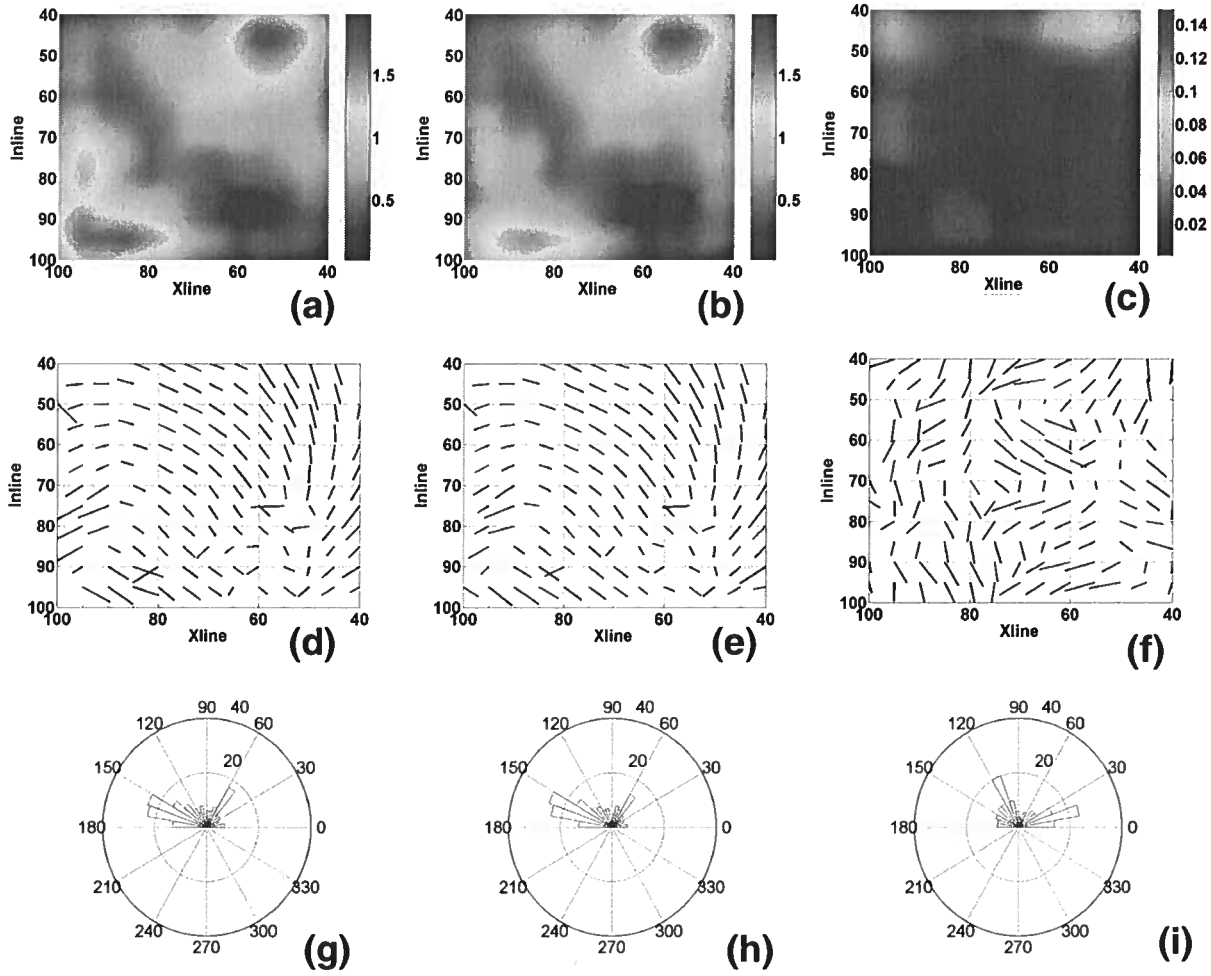

Figure 12. AVO ellipses for the bottom of the reservoir (the left and center columns) and the interval NMO ellipses in the reservoir (the right column); the same display as in Figure 9.

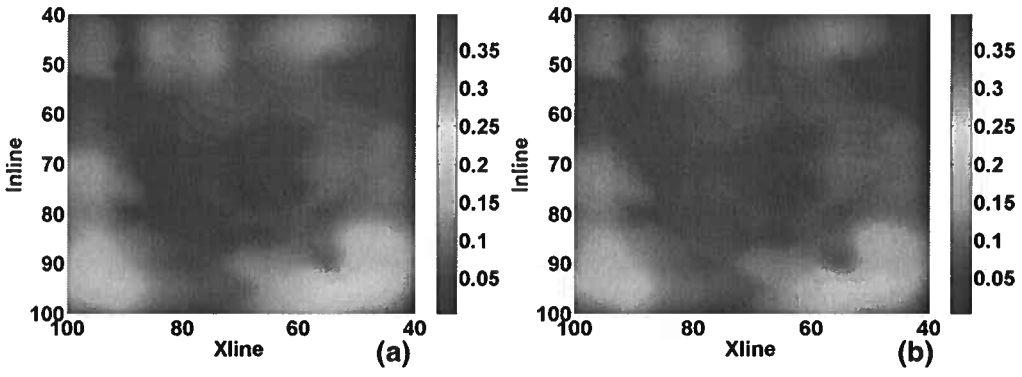

Figure 13. Azimuthal variation of the (a) geometrical spreading and (b) effective parameter η for the bottom of the reservoir (the same display as in Figure 10).

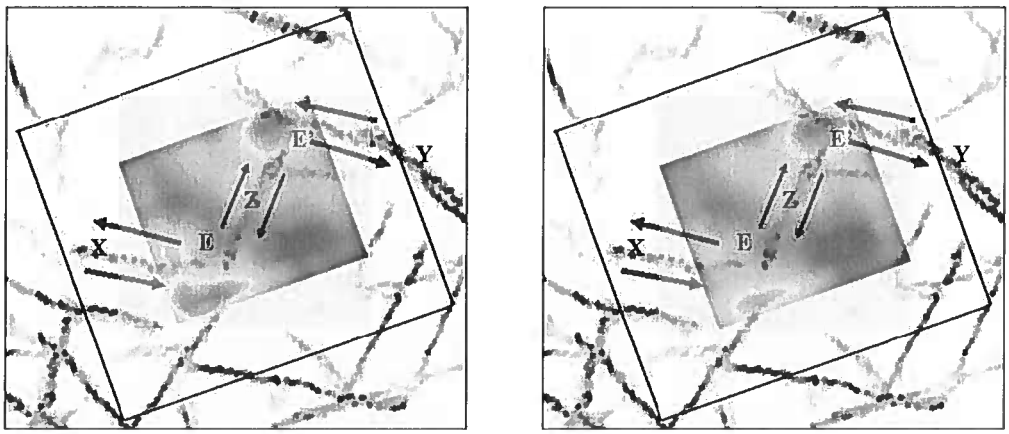

Figure 14. Comparison of the fault system and the eccenticity of the AVO ellipses for the bottom of the reservoir. The faults (blue lines), which are identical on plots (a) and (b), were mapped by Jansen (2005) using poststack P-wave images; the arrows indicate the slip movement. The azimuthal AVO attribute on plot (a) is computed using MASC (Figure 12a), and on plot (b) using the conventional spreading correction (Figure 12b). The black rectangle marks the RCP survey area. The AVO anomalies on plot (a) coincide almost exactly with the intersections E and E' of the two wrenching fault systems.

Most existing case studies of azimuthal AVO analysis are conducted for the top of the reservoir formation (e.g., Neves et al. 2003). Using synthetic modeling for fractured gas sands, Sayers and Rickett (1997) concluded that the bottom of the reservoir often produces a stronger azimuthal AVO anomaly. However, since Sayers and Rickett (1997) did not apply an anisotropic spreading correction, their modeled amplitudes were influenced by both the reflection coefficient and the azimuthally varying geometrical spreading inside the reservoir. Our results demonstrate that to take full advantage of the azimuthal AVO signature of events reflected beneath the reservoir, it is critically important to remove the anisotropic geometrical-spreading factor from recorded amplitudes. In addition, analysis of geometrical spreading and the input moveout parameters provides useful supplementary information for fracture characterization.

5 DISCUSSION

In this section we compare our processing results with available geologic and borehole information, estimate errors in the NMO velocities and AVO gradients, examine the correlation between the NMO and AVO ellipses, and outline some directions of future work.

5.1 Comparison with the fault distribution and EMI logs

Since both fractures and faults respond to subsurface stress fields, enhanced fracture zones are often associated with location of faults. It is, therefore, interesting to compare our fracture-characterization results with the fault distribution in the Rulison field. Cumella and Ostby (2003) suggest that the fault system in the area follows a wrenching pattern. Employing the wrenching fault model, Jansen (2005) mapped the fault system using automated curvature measurements. The background image in Figure 14 shows the faults at the bottom of the reservoir. The primary fault system is aligned along N70W, while a secondary step-over fault trends along N30E.

Interestingly, the AVO-gradient anomalies obtained after application of MASC are located at the intersections of the two wrenching fault systems, where stress concentration is likely to induce intense fracturing. Also, the orientation of the AVO ellipses (Figures 12d,e) exhibits a rotation pattern, which seems to support the wrenching fault model.

An electrical microimager (EMI) log is available in well RWF 542-20 in the center of our study area. Figure 15 compares the fracture directions obtained from the EMI log and the azimuthal AVO analysis for the bottom of the reservoir. The difference between the dominant fracture orientations estimated from the two methods is less than 10°.

5.2 Acquisition footprint

Since full azimuthal coverage is achieved for offsets up to approximately 5000 feet, the NMO and AVO ellipses at the Mesaverde Top and the top of the reservoir (UMV shale) should not be distorted by the acquisition footprint. The azimuthal and offset coverage in the four

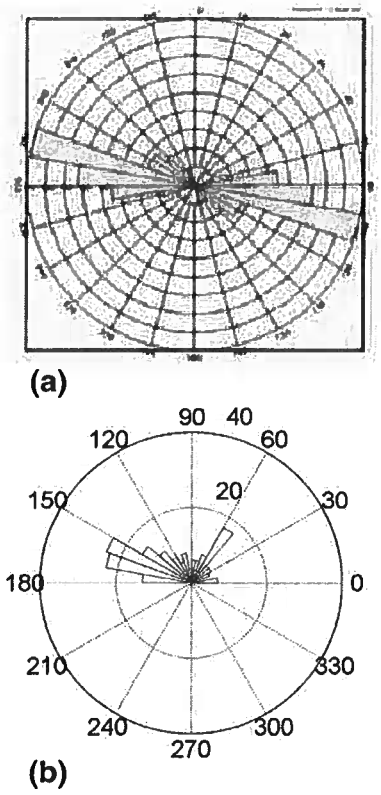

Figure 15. Rose diagrams of the fracture orientation obtained from EMI logs and azimuthal AVO analysis. The fracture directions were (a) counted in well RWF 542-20 within the reservoir; (b) estimated from the AVO ellipses at the bottom of the reservoir.

corners of our study area suggests that the azimuthal signatures for the bottom of the reservoir (Cameo coal) might be biased towards the dominant acquisition azimuths from 40° to 100°. The orientation of neither AVO nor NMO ellipses for the bottom of the reservoir, however, exhibits any noticeable bias (Figures 12d,e,f). In particular, the azimuths of the AVO ellipses are practically random in the lower right corner of the area where the AVO eccentricity is small (Figures 12d,e). The absence of the acquisition footprint can be explained by the orthogonality of the acquisition layout, which ensures that 80% of all traces fall into the offset range with complete azimuthal coverage.

5.3 Error analysis

Assuming that the uncertainty in traveltime picking does not exceed 8 ms, Vasconcelos and Grechka (2006) estimated the variance in the estimated NMO velocities to be close to 7%. The most serious problem in the estimation of the NMO ellipses, however, is the bias caused by varying superbin size. The NMO ellipticity systematically increases over the area when the superbin size changes from 5x5 to 9x9. Since this increase in ellipticity is accompanied by lower semblance values, the larger superbins seem to be more influenced by lateral heterogeneity. On average, the semblance value for the top of the reservoir decreases from around 0.6 for 5x5 superbins to 0.45 for 9x9 superbins, while the effective NMO ellipticity increases by 0.04. Evidently, 5x5 superbins used in our processing produce more reliable azimuthal seismic attributes.

The confidence interval for the eccentricity of the AVO ellipse can be inferred from the correlation between the magnitude of the AVO anomalies and the regularity of the ellipse orientation (Figures 9, 11, and 12). When the eccentricity is smaller than 0.3, the azimuths of the AVO ellipses are random, which is particularly clear in the upper left quarter of Figure 11d and the lower right quarter of Figure 12d. When the eccentricity exceeds 0.3, the azimuths of the AVO ellipses show a regular pattern. Since AVO ellipses are estimated independently at each CMP with no data overlap between adjacent gathers and no smoothing, the confidence level of the AVO eccentricity can be set at 0.3. The major azimuthal AVO anomalies discussed above should be significant because their magnitude is three times or more this confidence level.

Due to the relatively small offset-to-depth-ratio for the bottom of the reservoir (close to unity at the edges and 1.6 in the center of the study area), the estimated anellipticity parameters $\eta^{(1,2,3)}$ may contain large errors. The performance of MASC, however, is insensitive to trade-offs between the moveout parameters, as long as they give an accurate approximation for the traveltime surface (Xu and Tsvankin, 2006a). The high quality of the traveltime fit provided by our moveout-inversion algorithm is confirmed by the large semblance values (0.7 on average) for the bottom of the reservoir.

5.4 Correlation between the NMO and AVO ellipses

It has been suggested in the literature that combining the NMO ellipse with the azimuthally-varying AVO gradient can help to constrain the anisotropic velocity model and some physical fracture parameters (Rüger and Tsvankin, 1997; Bakulin et al. 2000a). This approach is feasible when the reservoir is thick enough for reliable estimation of the interval NMO ellipses, and the variation of major fracture properties (orientation, density, fluid saturation) with depth is not significant. In the presence of strong vertical heterogeneity, the difference in vertical resolution between amplitude and traveltime methods complicates joint analysis of AVO and NMO results.

Although the thickness of the reservoir formation in the Rulison field is sufficient for azimuthal moveout

inversion, there is no obvious correlation between the azimuthal NMO and AVO attributes. Most likely, the vertical and lateral heterogeneity of the Williams Fork formation has a strong impact on the interval NMO ellipses, which reflect the average properties of the reservoir. In contrast, azimuthal AVO response after the geometrical-spreading correction mostly depends on the local medium properties above and below the reflector. Still, further joint analysis of the NMO and AVO attributes may be helpful in improving our understanding of the reservoir.

5.5 Quantitative AVO inversion

The AVO gradient is estimated here by expressing the reflection coefficient as a quadratic function of the source and receiver coordinates. While this representation is justified for the NMO ellipse (Grechka and Tsvankin, 1998), it is not appropriate for quantitative inversion of the AVO response. Indeed, the plane-wave reflection coefficient obtained by amplitude processing has to be treated as a function of the incidence phase angle or horizontal slowness (ray parameter). Unfortunately, accurate computation of the phase angle at the reflector requires knowledge of the interval anisotropy parameters in the overburden. This issue deserves further investigation, which is outside of the scope of this paper.

6 CONCLUSIONS

Despite the complexity of the heterogeneous fractured reservoir in the Rulison field, P-wave reflection data provide valuable information for fracture characterization. Our processing sequence included advanced anisotropic traveltime and amplitude inversion methods designed for wide-azimuth, long-offset data. Nonhyperbolic moveout analysis for several major horizons helped to flatten the long-spread reflection events and estimate the effective NMO ellipses. Then the generalized Dix equation was used to remove the influence of the overburden and compute the interval NMO ellipses in the reservoir and the layer above it (UMV shale). The estimated nonhyperbolic moveout parameters also provided the input to the moveout-based anisotropic geometrical-spreading correction (MASC), which was applied prior to azimuthal AVO analysis.

The azimuthal variation of the AVO gradient (AVO ellipse) proved to be the most sensitive fracture-detection attribute. Significant azimuthal AVO anomalies were observed for all three processed horizons, which indicates that fracturing is not limited to the reservoir formation. It should be emphasized that the AVO response for the bottom of the reservoir is substantially distorted by the azimuthally varying geometrical spreading. The AVO-gradient anomaly in the lower left corner of the study area becomes much more pronounced and spatially coherent after application of MASC. It is clear that an accurate spreading correction is even more important for quantitative inversion of the azimuthal AVO attributes. Note that implementation of MASC is entirely based on the results of azimuthal moveout analysis and, therefore, involves almost no extra computational cost.

The two strong AVO-gradient anomalies at the bottom of the reservoir coincide with the intersections of two wrenching fault systems, where one can expect concentration of stress. This geologic evidence suggests that the anomalies indeed correspond to "soft spots" of high fracture density. While the fracture orientation estimated from the AVO ellipses varies over the field, the dominant fracture azimuth (N70W) is in good agreement with the EMI logs and the direction of one of the fault systems.

The weak NMO ellipticity for the interval between the Mesaverde Top and the top of the reservoir indicates that this shaly layer is azimuthally isotropic (likely to be VTI). Thus, the AVO anomalies at the top and bottom of this layer are likely caused by enhanced fractured zones in the formation immediately above the Mesaverde Top and in the upper reservoir, respectively.

The interval NMO ellipticity in the reservoir is much less pronounced compared to the azimuthal variation of the AVO gradient for the reservoir boundaries. Also, the azimuthal AVO and NMO attributes are not well correlated, which may be explained by the inherent difference between these two measurements. Reflection coefficient is governed by the local contrasts in the elastic parameters across interfaces, whereas NMO velocity reflects the average medium properties over coarse intervals. Since the reservoir horizon in the Rulison field is thick and strongly heterogeneous, the weak correlation between the AVO and NMO ellipses is not surprising.

ACKNOWLEDGMENTS

We are grateful to Tom Davis, Bob Benson, Michael Rumon, Eldar Guliyev, and Matthew Casey (all of CSM/RCP) for providing the seismic data and valuable additional information for this study. We also thank Ken Larner, Ivan Vasconcelos, Carlos Pacheco, Rodrigo Fuck, Jyoti Behura, and John Stockwell (all of CSM/CWP) for stimulating discussions and technical help. Shannon Higgins (RCP, now Schlumberger) helped us with the image logs and Kjetil Jansen (RCP, now Occidental) shared his fault maps. The support for this work was provided by the Consortium Project on Seismic Inverse Methods for Complex Structures at the Center for Wave Phenomena and by the Chemical Sciences, Geosciences and Biosciences Division, Office of Basic Energy Sciences, Office of Science, U.S. Department of Energy.

REFERENCES

Bakulin, A., V. Grechka, and I. Tsvankin, 2000a, Estimation of fracture parameters from reflection seismic data – Part I: HTI model due to a single fracture set: Geophysics, **65**, 1788–1802.

Bakulin, A., V. Grechka, and I. Tsvankin, 2000b, Estimation of fracture parameters from reflection seismic data – Part II: Fractured models with orthorhombic symmetry: Geophysics, **65**, 1803–1817.

Cumella, S. P., and D. B. Ostby, 2003, Geology of the basin-centered gas accumulation, Piceance Basin, Colorado. Piceance Basin 2003 Guidebook: Rocky Mountain Association of Geologists, 171–193.

Grechka, V., and I. Tsvankin, 1998, 3-D description of normal moveout in anisotropic inhomogeneous media: Geophysics, **63**, 1079–1092.

Grechka, V., and I. Tsvankin, 1999, 3-D moveout inversion in azimuthally anisotropic media with lateral velocity variation: Theory and a case study: Geophysics, **64**, 1202–1218.

Grechka, V., I. Tsvankin, and J. K. Cohen, 1999, Generalized Dix equation and analytic treatment of normal-moveout velocity for anisotropic media: Geophysical Prospecting, **47**, 117–148.

Gray, F. D., and D. Todorovic-Marinic, 2004, Fracture detection using 3D azimuthal AVO: CSEG Recorder, **29**, 5–8.

Hall, S., and J. M. Kendall, 2003, Fracture characterization at Valhall: Application of P-wave amplitude variation with offset and azimuth (AVOA) analysis to a 3-D ocean-bottom data set: Geophysics, **68**, 1150–1160.

Jansen, K., 2005, Seismic investigation of wrench faulting and fracturing at Rulison field, Colorado: M.S. thesis, Colorado School of Mines.

Li, X., Y. Liu, E. Liu, F. Shen, L. Qi, and S. Qu, 2003, Fracture detection using land 3D seismic data from the Yellow River delta, China: The Leading Edge, 680–683.

Lynn, H. B., W. E. Beckham, K. M. Simon, C. R. Bates, M. Layman, and M. Jones, 1999, P-wave and S-wave azimuthal anisotropy at a naturally fractured gas reservoir, Bluebell-Altamont Field, Utah: Geophysics, **64**, 1312–1328.

Neves, F. A., A. Al-Marzoug, J. J. Kim, and E. L. Nebrija, 2003, Fracture characterization of deep tight sands using azimuthal velocity and AVO seismic data in Saudi Arabia: The Leading Edge, **22**, 469–475.

Perez, M. A., V. Grechka, and Michelena, R. J., 1999, Fracture detection in a carbonate reservoir using a variety of seismic methods: Geophysics, **64**, 1266–1276.

Rüger, A., 2001, Reflection coefficients and azimuthal AVO analysis in anisotropic media: Society of Exploration Geophysics.

Rüger, A., and Tsvankin, I., 1997, Using AVO for fracture detection: Analytic basis and practical solutions: The Leading Edge, **16**, 1429–1434.

Sayers, C. M., and J. E. Rickett, 1997, Azimuthal variation in AVO response for fractured gas sands: Geophysical Prospecting, **45**, 165–182.

Tsvankin, I., 2005, Seismic signatures and analysis of reflection data in anisotropic media: Elsevier Science Publ. Co., Inc. (second edition).

Vasconcelos, I., and V. Grechka, 2006, Seismic characterization of multiple fracture sets from multicomponent, multiazimuth, 3D data: Rulison Field, CO: CWP Project Review Volume.

Vasconcelos, I., and I. Tsvankin, 2006, Non-hyperbolic moveout inversion of wide-azimuth P-wave data for orthorhombic media: Geophysical Prospecting, **54**, 535–552.

Xu, X., and I. Tsvankin, 2006a, Anisotropic geometrical-spreading correction for wide-azimuth P-wave reflections: Geophysics, **71**, D161–D170.

Xu, X., and I. Tsvankin, 2006b, Azimuthal AVO analysis with anisotropic spreading correction: A synthetic study: The Leading Edge, **24**, 1336–1342.

Xu, X., I. Tsvankin, and A. Pech, 2005, Geometrical spreading of P-waves in horizontally layered, azimuthally anisotropic media: Geophysics, **70**, D43–D53.